Novel Group IV Alloy Semiconductor Materials

Thesis by

Gang He

In Partial Fulfillment of the Requirements

for the Degree of

Doctor of Philosophy

California Institute of Technology

Pasadena, California

1997

(Submitted August 23, 1996)

ACKNOWLEDGMENTS

I have greatly enjoyed my five years of graduate study at Caltech and have benefited tremendously from interacting with all the wonderful people in this environment.

I would first like to thank my advisor, Professor Harry A. Atwater, for all his encouragement, support, and guidance which helped me through my graduate study. He introduced me to the fascinating scientific world of electronic materials, and his great enthusiasm and optimism for scientific pursuit have been my source of inspiration and courage in my graduate research. His broad knowledge and deep insight in science have guided me through various difficulties during my research, and his encouragement and trust have helped me establish my confidence in independent scientific research. His influence has benefited me tremendously during my graduate study and will continue to do so in my future career.

My interaction with Professor Thad Vreeland was short but very enjoyable. He helped me in understanding high resolution x-ray diffraction and gave me a lot of encouragement in experimental research. I would also like to thank Professor Marc-Aurele Nicolet for the helpful scientific discussions. Many thanks to Dr. Channing Ahn who taught me transmission electron microscopy and has given me

numerous helps in my graduate research. Working with him on the parallel electron energy loss spectroscopy system has been a great learning experience for me.

I would like to thank Michael P. Easterbrook for setting up the Pelletron for Rutherford backscattering experiments and sometimes even spending extra hours to help me finish experiments in time. I would also like to thank Rob Gorris for helping me fix various parts for my experiments. I am grateful to Carol M. Garland for teaching me how to use the transmission electron microscopes in the Keck Laboratory. She spent a lot of time showing me all the small details from preparing cross-sectional samples to operating the microscopes and to finally printing images in the dark room. Thanks to Reynold E. Johnson for his help when I was a teaching assistant for the Integrated Circuit Device Fabrication laboratory. And thanks to Richard Borup for teaching me the basics of machining.

I would especially like to thank Dr. M.V. Ramana Murty for showing me the molecular beam epitaxy system and teaching me all the experimental details with great patience. He is extremely knowledgeable and always ready to help. I am truly obliged for his generosity in spending a lot of his time answering my endless questions and helping me with my various experiments during the early years of my graduate study. I can never thank Chih-Ming Yang too much for spending so much of his precious time as a graduate student taking care of all the computers in our lab. Without his unselfish efforts and help, my work could not have been done so smoothly. Chih-Ming is also a very good personal friend of mine and I have

greatly enjoyed his company and friendship over the years. I am very glad that I have had the opportunity to work closely with Maggie E. Taylor on several overlapping projects. She is thoughtful and intelligent, and I have truly enjoyed her friendship and the various wonderful social events that she organized for our lab. Our working together on the SnGe projects during the summer research in the FOM institute in Amsterdam, the Netherlands has been a great experience for me. I would also like to thank Dr. Selmer Wong for giving me various help with my experiments and I have really enjoyed working with her on the parallel electron energy loss spectroscopy system. I would like to thank Dr. Imran Hashim and Dr. Winston Saunders who gave me a lot of help when I was a teaching assistant for the Integrated Circuit Device Fabrication laboratory, which was a great learning experience for me. Thanks to Dr. Shouleh Nikzad who also helped me a lot on molecular beam epitaxy. I would like to express my thanks to Dr. Hyun Sung Joo, who is very knowledgeable and experienced in scientific research and is always ready to offer his valuable help. I would like to thank Kirill Shcheglov for all the exciting and fruitful discussions that we had in our office, as well as all the experimental help I received from him. Also thanks to Joseph Christopher who has done a great job organizing the molecular beam epitaxy system. Thanks to Kyu Sung Min and Renato P. Camata for their numerous helpful discussions as well as their great friendships. Thanks to Robert B. Lee for analyzing my samples with atomic force microscopy late at night. Thanks to Dr. Donald Lie for helping me with my work on the high-resolution x-ray diffraction system. I have also enjoyed and benefited from the interactions with Dr. Ruth Brain, Dr. Jung Shin, Susan M. Melnik, Regina Ragan, Claudine Chen, Heather Frase, Hiroshi Yoshino, and

Seongil Im, who have all given me valuable help in various ways. During my graduate study, I have had the great pleasure to work closely with several undergraduate students in our lab: Mark Savellano, Lisa Moesker, Zu Xin Yu, and Kay Saipetch. They are all very intelligent and energetic in their research and have given me a lot of help in many ways.

Many graduate courses I took at Caltech were extremely valuable and exciting. I greatly enjoyed taking the incredible course of Application of Classical Physics taught by Professor Kip S. Thorne and Professor Roger D. Blandford. The course of Electronic Material taught by Professor Harry A. Atwater has been very valuable for my graduate research. I also enjoyed the course of Electronic Circuit and Application in Physics Research by Professor Ronald W.P. Drever, the course of Micro Fabrication Technology by Professor Yu-Chong Tai, the course of Solid State Physics by Professor William L. Johnson, the course of Semiconductor Device Physics by Professor Marc-Aurele Nicolet, the course of Ion Beam Material Modification and Analysis by Professor Harry A. Atwater and Professor Marc-Aurele Nicolet, the course of Diffraction Theory and Applications by Professor Brent T. Fultz, and the laboratory course of Transmission Electron Microscopy by Dr. Channing Ahn.

My summer research in the FOM institute in Amsterdam, the Netherlands has been a great experience for me both scientifically and personally. I must thank Professor Albert Polman for his generous invitation and his detailed arrangements for all the aspects of working and living in Amsterdam. During the summer

research he gave me tremendous help and inspiration in my research. I would also like to thank Mark L. Brongersma and Gerlas van den Hoven for their countless help in both research and living and for their friendship which I enjoyed so much during my stay in Amsterdam.

I would especially like to thank our secretary, Rosalie Rowe, who has been a great help in handling all kinds of paperwork and arranging all the conference travels.

Last, but not least, I must thank my family. Thanks to my parents, grandparents, sister, and all the members of my extended families, for their sacrifices, supports, and encouragement both emotionally and financially during all the years of my education and scientific study. Without their total commitment, I could not have reached so far. And most of all, I must give my thanks to my wife, Haiyun Zhang, whose love, support and encouragement has been the greatest driving force behind my graduate study. She not only is my dearest companion and best friend in life, but also is the greatest inspiration in my scientific pursuit.

ABSTRACT

Novel group IV alloy semiconductor materials were investigated to explore their potential applications in silicon-based optoelectronic devices and high speed electronic devices. One system investigated is the ternary $Si_{1-y}(Sn_{1-x}C_x)_y$ alloy. Epitaxial $Si_{1-y}(Sn_{1-x}C_x)_y$ alloy films with tin and carbon concentrations of up to y=0.02 (x=0.5) were synthesized successfully on silicon substrates by molecular beam deposition followed by solid phase epitaxy. The effect of strain compensation from tin and carbon greatly reduced the epitaxial strain and produced dislocation-free heteroepitaxial films on silicon substrates which may enable high-speed silicon-based low-strain heterojunction devices. Another system investigated is the binary Sn_xGe_{1-x} alloy. Tight-binding and pseudopotential calculations predicted that Sn_xGe_{1-x} has a direct energy band gap that is continuously tunable in the mid and long wavelength infrared region (E_g = 0.55 eV ~ 0 eV) for tin concentrations in the range of x=0.2 to x=0.6, which makes it an attractive material system for silicon-based integrated infrared optoelectronic devices. Epitaxial Sn_xGe_{1-x} films were synthesized successfully on silicon substrates by conventional molecular beam epitaxy with tin concentrations of up to x=0.2, beyond which severe tin surface segregation caused a breakdown of epitaxy. To overcome the problem of surface segregation, ion-assisted molecular beam epitaxy was studied. Low energy, high flux ion irradiation of the sample surface during growth greatly reduced tin surface segregation and achieved

tin concentrations up to x=0.34. An analytical model was developed to describe surface segregation during energetic beam epitaxial growth and was applied to ion-assisted molecular beam epitaxy growth of Sn_xGe_{1-x}. Infrared absorption measurements of the Sn_xGe_{1-x} samples showed that the decrease of Sn_xGe_{1-x} energy band gap with increasing tin concentration was much faster than predicted by tight-binding and pseudopotential calculations. The measured absorption onset was as low as 0.25 eV for a tin concentration of x=0.15, and the measured absorption strength was comparable to the typical direct band gap infrared semiconductors such as InAs and InSb. The results of the absorption measurements suggest that full access to the tunable Sn_xGe_{1-x} energy band gap from mid infrared to far infrared may be obtained with a maximum tin concentration of about x=0.25 instead of x=0.6 as predicted by tight-binding and pseudopotential calculations.

LIST OF PUBLICATIONS

Parts of this thesis have been published, or will be published under the following titles:

G. He, M.D. Savellano, and H.A. Atwater, Synthesis of Dislocation-Free $Si_y(Sn_xC_{1-x})_{1-y}$ Alloys by Molecular-Beam Deposition and Solid-Phase Epitaxy, Material Research Society Symposium Proceedings 298, 229 (1993)

G. He, M.D. Savellano, and H.A. Atwater, Synthesis of Dislocation-Free $Si_y(Sn_xC_{1-x})_{1-y}$ Alloys by Molecular-Beam Deposition and Solid-Phase Epitaxy, Applied Physics Letters 65, 1159 (1994)

G. He, M.D. Savellano, and H.A. Atwater, Section X2.15 Electronic Materials: $Si_y(Sn_xC_{1-x})_{1-y}$, Handbook of Thin Film Process Technology, Ed. D.A. Golcker and S.I. Shah, Institute of Physics Publishing Ltd. (Bristol and Philadelphia) (1995)

S.S. Wong, G. He, S. Nikzad, C.C. Ahn, and H.A. Atwater, Local Order Measurement in Sn_xGe_{1-x} Alloys and Monolayer Sn Films on Si with reflection Electron-Energy-Loss Spectrometry, Journal of Vacuum Science and Technology 13, 216 (1995)

H.A. Atwater, G. He, and K. Saipetch, Epitaxial Growth of Metastable Sn_xGe_{1-x} Alloy Films by Ion-Assisted Molecular Beam Epitaxy, Material Research Society Symposium Proceedings 355, 123 (1995)

G. He and H.A. Atwater, Synthesis of Epitaxial Sn_xGe_{1-x} Alloy Thin Films by Ion-Assisted Molecular Beam Epitaxy, Nuclear Instruments and Methods B 106, 126 (1995)

G. He and H.A. Atwater, A Model for Ion-Assisted Molecular Beam Epitaxy and Application to Synthesis of Epitaxial Sn_xGe_{1-x} Alloy Films, Material Research Society Symposium Proceedings 399, 89 (1995)

G. He and H.A. Atwater, Synthesis of Epitaxial Sn_xGe_{1-x} Alloy Films by Ion-Assisted Molecular Beam Epitaxy, Applied Physics Letters 68, 664 (1996)

G. He and H.A. Atwater, Structure and Interband Transitions in Sn_xGe_{1-x} Alloys, in preparation

Contents

List of Figures

List of Tables

Chapter 1

INTRODUCTION

Semiconductor devices based on silicon technology have been a major driving force behind the electronics revolution in the past few decades. However, the inherent electronic properties of silicon have limited its applications in the areas of optoelectronic devices and very high speed electronic devices. To explore these areas of device applications, while preserving the advantage of the highly advanced and efficient silicon processing technology, novel group IV alloy semiconductor materials are being investigated. Group IV elements include carbon, silicon, germanium, tin, and lead. Except for lead, all the first four group IV elements have stable or metastable phases in diamond-cubic crystal structure, which is the crystal structure of the semiconductor silicon. As atomic number increases, energy band gaps decrease while lattice constants increase. Thus group IV alloys are interesting candidates for new semiconductor materials which may have a wide range of potential electronic properties for future high-performance and optoelectronic devices. Compared with III-V or II-VI compound semiconductors, group IV alloy semiconductors are easier to integrate with the silicon technology since they are isoelectronic elemental materials and, as a result, have similarities in their physical and chemical properties. For example, binary alloys of silicon and germanium have been widely studied as a semiconductor material for high-performance silicon-based heterojunction devices. High-speed heterojunction devices based on such alloys have been demonstrated on silicon

with operation frequencies much higher than that can be achieved with silicon-only devices [1].

In this study, two specific group IV alloy systems were investigated – the $Si_{1-y}(Sn_{1-x}C_x)_y$ [2]-[4] and the Sn_xGe_{1-x} [8]-[5] alloy systems. The ternary $Si_{1-y}(Sn_{1-x}C_x)_y$ alloys are interesting materials that may allow flexible strain and band-gap engineering for high-performance silicon-based heterojunction devices. The binary Sn_xGe_{1-x} alloys have been predicted to have continuously tunable direct energy band gaps in the infrared region (from $Eg = 0.55$ eV to 0 eV for tin concentration from x=0.2 to 0.6) [8]-[14] which may enable monolithic silicon-based integrated optoelectronic devices. These novel alloy materials also raise interesting questions about the physics involved in their structural and electronic properties as well as in their growth processes. Both materials exhibit elastic and compositional metastability, so that novel processes of material synthesis (e.g., ion-assisted molecular beam epitaxy) were investigated.

In the ternary $Si_{1-y}(Sn_{1-x}C_x)_y$ alloy system (chapter 2), epitaxial $Si_{1-y}(Sn_{1-x}C_x)_y$ alloy films with tin and carbon concentrations of up to y=0.02 (x=0.5) were synthesized successfully on silicon substrates by molecular beam deposition followed by solid phase epitaxy. The effect of strain compensation from tin and carbon greatly reduced the epitaxial strain and produced dislocation free heteroepitaxial films on silicon substrates which may enable high-speed silicon-based low-strain heterojunction devices.

In the Sn_xGe_{1-x} alloy system (chapter 3), epitaxial Sn_xGe_{1-x} films were grown successfully on silicon substrates by conventional molecular beam epitaxy with tin concentrations of up to x=0.2, beyond which severe tin surface segregation caused a breakdown of epitaxy. To overcome the problem of surface segregation, ion-assisted molecular beam epitaxy was studied. Low energy, high flux ion irradiation of the sample surface during growth greatly reduced tin surface segregation and achieved tin concentration up to x=0.34.

The local structure of the Sn_xGe_{1-x} alloys was investigated by first-principle density functional theory calculations (chapter 3). The calculations indicated a small metastability of the Sn_xGe_{1-x} alloys relative to decomposition, and suggested that while Vegard's law is good description for the Sn_xGe_{1-x} alloys, the local bond arrangements in the alloy deviate significantly from the virtual crystal approximation, which has been the basis of most tight-binding and pseudopotential calculations of Sn_xGe_{1-x} electronic structure.

To understand the suppression of surface segregation during ion-assisted molecular beam epitaxy, an analytical model for surface segregation in energetic beam epitaxial growth was developed (chapter 4). The model described quantitatively the effect of energetic beam irradiation on alloy surface segregation during energetic beam epitaxial growth in general, and was applied to the ion-assisted molecular beam epitaxy growth of Sn_xGe_{1-x}.

The most interesting electronic property of Sn_xGe_{1-x} is its predicted tunable band gap in the infrared region. To characterize the Sn_xGe_{1-x} band gap, thin film optical analyses were performed to measure the absorption spectra of Sn_xGe_{1-x} (chapter 5). The results showed that the decrease of Sn_xGe_{1-x} band gap with increasing tin concentration was much faster than tight-binding and pseudopotential calculations predicted [15]. The measured absorption strength was comparable to the typical direct band gap infrared semiconductors such as InAs and InSb, suggesting a promising semiconductor material for silicon-based infrared optoelectronic devices.

Bibliography

[1] G.L. Patton, J.H. Comfort, B.S. Meyerson, E.F. Crabbe, G.J. Scilla, E. Defresart, J.M.C. Stork, J.Y.C Sun, D.L. Harame, et al., IEEE Elec. Dev. Lett. 11, 171 (1990).

[2] G. He, M.D. Savellano, and H.A. Atwater, Mat. Res. Soc. Symp. Proc. 298, 229 (1993).

[3] G. He, M.D. Savellano, and H.A. Atwater, Appl. Phys. Lett. 65, 1159 (1994).

[4] G. He, M.D. Savellano, and H.A. Atwater, Section X2.15 Electronic Materials: SiSnC, Handbook of Thin Film Process Technology, Ed. D.A. Golcker and S.I. Shah, Institute of Physics Publishing Ltd. (Bristol and Philadelphia) (1995).

[5] G. He and H.A. Atwater, Appl. Phys. Lett. 68, 664 (1996).

[6] G. He and H.A. Atwater, Nucl. Instrum. Methods B 106, 126 (1995).

[7] G. He and H.A. Atwater, Mat. Res. Soc. Symp. Proc. 399, 380 (1996).

[8] H.A. Atwater, G. He, K. Saipetch, Mat. Res. Soc. Symp. Proc. 355, 123 (1995).

[9] D.W. Jenkins and J.D. Dow, Phys. Rev. B 36, 7994 (1987).

[10] B. Bouhafs, F. Benkabou, M. Ferhat, B. Khelifa, J.P. Dufour, H. Aourag, Infrared Phys. & Tech. 36, 967 (1995).

[11] Na. Amrane, S. Ait Abderrahmane, H. Aourag, Infrared Phys. & Tech. 36, 843 (1995).

[12] K.A. Mader, A. Baldereschi, H. von Kanel, Solid State Comm. 69, 1123 (1989).

[13] T. Brudevoll, D.S. Citrin, N.E. Christensen, M. Cardona, Phys. Rev. B 48,17128 (1993).

[14] E. Kaxiras, unpublished.

[15] G. He and H.A. Atwater, in preparation.

Chapter 2

SOLID PHASE EPITAXY OF $Si_{1-y}(Sn_{1-x}C_x)_y$ ALLOY FILMS

2 .1 Introduction

The group IV ternary alloys, including diamond-cubic $Si_{1-y}(Sn_{1-x}C_x)_y$, hold promise in fabricating silicon-based devices with novel electronic and optoelectronic properties. For example, fabrication of unstrained or modestly strained group IV single-crystal heterojunction devices on silicon substrate may be achieved with the ternary alloys. It has also been shown that relatively efficient electroluminescence at 1.28 μm wavelength can be achieved from a carbon-related isovalent impurity complex [1][2]; thus silicon-based optoelectronic devices are among possible applications. The effect of strain compensation by adding carbon and tin into silicon together not only reduces strain in heterojunction devices but also may enhance the mutual solubility of tin and carbon in silicon, since the solubility of isovalent impurities in silicon is most likely dominated by the strain-induced changes in free energy. Among the possible techniques to synthesize $Si_{1-y}(Sn_{1-x}C_x)_y$ are molecular beam epitaxy, chemical vapor deposition, ion implantation [3], and solid phase epitaxy. In this study, high-quality single-crystal $Si_{1-y}(Sn_{1-x}C_x)_y$ alloy films on silicon (100) substrates were synthesized by molecular beam deposition in ultrahigh vacuum from solid sources, followed by

solid phase epitaxy [4]-[6]. When compared with molecular beam epitaxy and chemical vapor deposition, solid phase epitaxy is relatively simple and compatible with silicon VLSI technology. Alloy synthesis by molecular beam deposition was chosen because it permits greater control over film thickness, composition, and composition profile than does ion implantation. Compared with the ternary $Si_{1-y}(Ge_{1-x}C_x)_y$ system [7]-[10], tin compensates the carbon-related strain in silicon more efficiently owing to its larger atomic radius, and $Si_{1-y}(Sn_{1-x}C_x)_y$ may allow access to a wider range of strain and band gap combinations.

2 .2 Potential Device Applications

One potential application of the ternary diamond-cubic $Si_{1-y}(Sn_{1-x}C_x)_y$ alloy system is the independent strain and band-gap engineering for silicon-based high-performance heterojunction devices. The lattice parameter varies from 0.355 nm for carbon (diamond) to 0.543 nm for silicon to 0.649 nm for tin (diamond-cubic α-phase), while the band gap varies from 5.5 eV for carbon (diamond) to 1.12 eV for silicon to -0.4 eV for tin (diamond-cubic α-phase) (Figure 2.1) . Alloying silicon with carbon and tin may thus enable access to a very wide range of lattice parameters and band gap combinations.

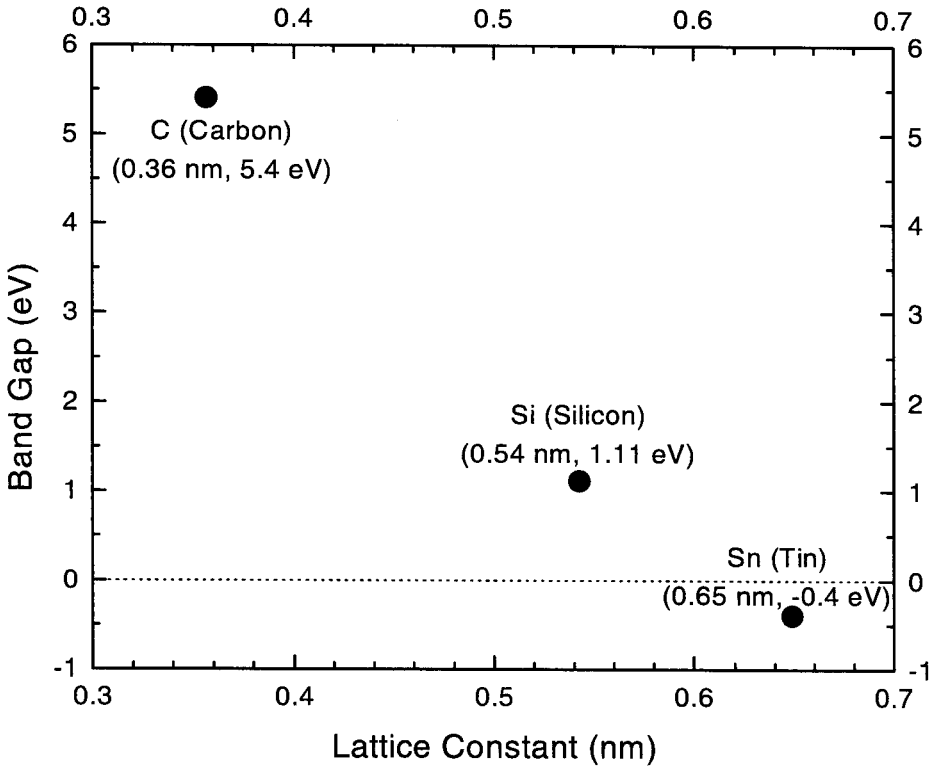

Figure 2.1 Band gap and lattice parameter of Si, Sn, and C.

Such capabilities in strain and band-gap engineering may potentially enable unstrained or low strained heterojunction transistors (Figure 2.2). Device reliability of heterojunction transistors is in general closely related to the lattice misfit strain in the heteroepitaxial layers. However, epitaxial strain is unavoidable in the case of current heterojunction transistors based on the $Si_{1-x}Ge_x$ binary alloy system grown on silicon substrates. On the other hand, a ternary alloy system such as $Si_{1-y}(Sn_{1-x}C_x)_y$ may produce lattice-matched heterojunction layers on silicon

substrates by careful strain compensation. If Vegard's law is obeyed, it is expected that $Si_{1-y}(Sn_{0.6}C_{0.4})_y$ will be lattice-matched to silicon.

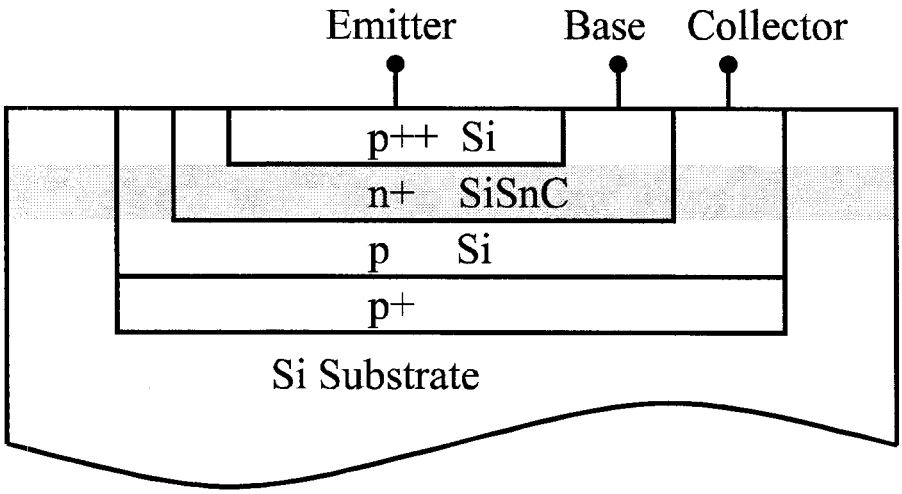

Figure 2.2 Potential silicon-based low-strain heterojunction bipolar transistor using epitaxial $Si_{1-y}(Sn_{1-x}C_x)_y$ alloy layers.

Another interesting potential device application of $Si_{1-y}(Sn_{1-x}C_x)_y$ is related to a carbon-related isovalent impurity complex in silicon, which has been shown to produce relatively efficient electroluminescence at 1.28 μm wavelength [1][2] – an important wavelength for fiber optical communications since it is close to the 1.3 μm window for minimum dispersion in optical fibers. Since $Si_{1-y}(Sn_{1-x}C_x)_y$ alloy films contain relatively high concentrations of carbon, silicon-based light emitting diodes may be possible using this carbon-related isovalent impurity complex (Figure 2.3). Since this impurity complex contain interstitial atoms, careful defect engineering would be required in order to produce a high

concentration of such light emitting complexes without generating other non-radiative defects. Electron beam irradiation is one potential method to satisfy such a requirement since it selectively generates vacancy/interstitial pairs versus other defects such as divacancies [1].

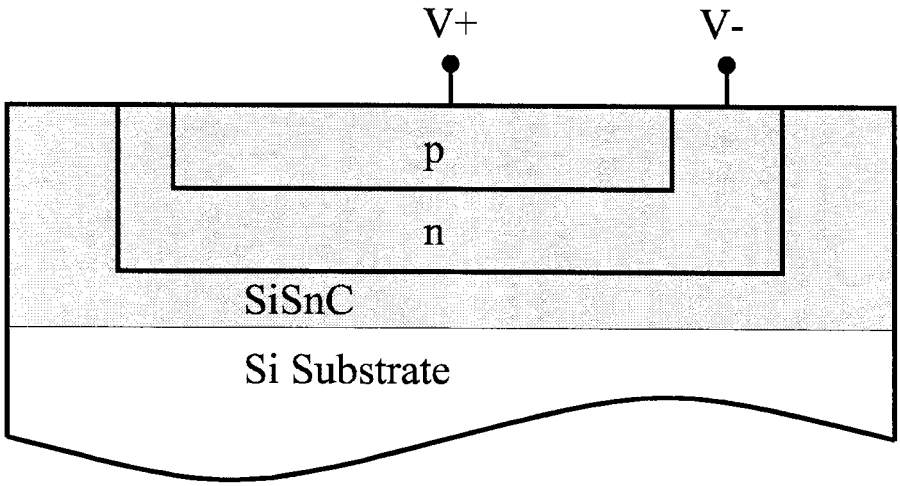

Figure 2.3 Potential silicon-based light emitting diode using epitaxial $Si_{1-y}(Sn_{1-x}C_x)_y$ alloy layers.

2 .3 Thermodynamics

The equilibrium phase diagrams of the binary Si-Sn (Figure 2.4) and Si-C (Figure 2.5) systems [11] revealed that the equilibrium solid solubilities of tin and carbon in silicon are extremely small – about 10^{-4} for tin [12] and 10^{-6} for

carbon [2]. Since the $Si_{1-y}(Sn_{1-x}C_x)_y$ alloys of interest have tin and carbon concentrations far exceed their equilibrium solid solubility, these alloys are thermodynamically metastable. At high temperatures, tin will have a tendency to segregate out of the alloy matrix and carbon will have a tendency to form silicon carbide precipitates. Studies on the binary $Si_{1-x}C_x$ alloy system have suggested that silicon carbide precipitation may occur at temperatures above 800°C with carbon concentrations up to 0.014 [13]. The metastability of $Si_{1-y}(Sn_{1-x}C_x)_y$ alloys suggests that the epitaxial growth process must be performed far from equilibrium.

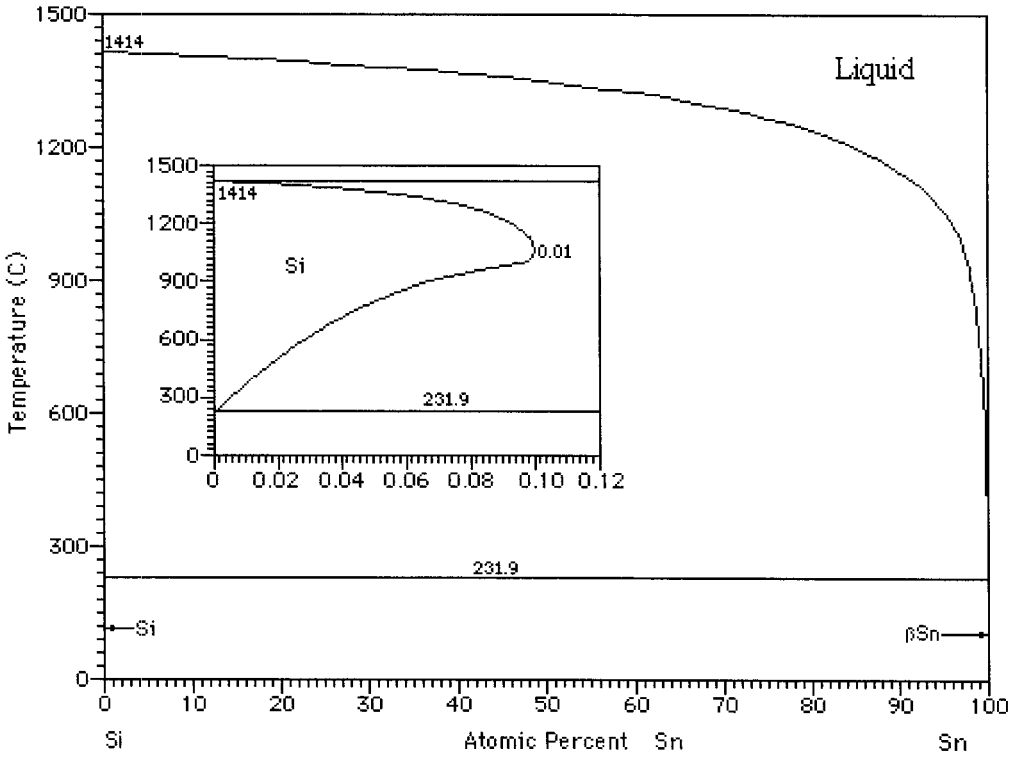

Figure 2.4 Binary phase diagram of Si-Sn [11].

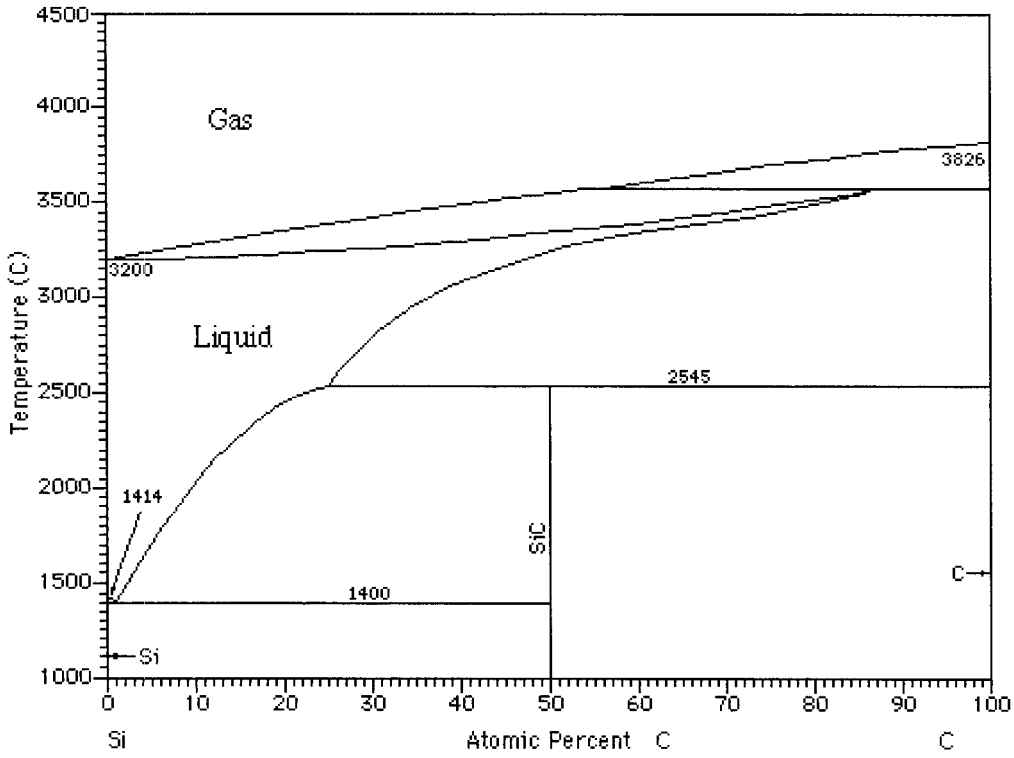

Figure 2.5 Binary phase diagram of Si-C [11].

2 .4 Molecular Beam Deposition

The two step process of $Si_{1-y}(Sn_{1-x}C_x)_y$ synthesis consists of first deposition of amorphous $Si_{1-y}(Sn_{1-x}C_x)_y$ alloy films by molecular beam deposition and then solid phase epitaxial regrowth by annealing at higher temperatures. The amorphous $Si_{1-y}(Sn_{1-x}C_x)_y$ alloy films were deposited on (100) silicon wafers in a custom-designed molecular beam epitaxy system (Figure 2.6) with a base pressure

of around 1×10^{-9} Torr. The main deposition chamber was pumped by a 1600 l/sec cryopump and the load lock was pumped by a 330 l/sec turbopump. The residual gas in the chamber consists of mostly H_2, CO, and H_2O. Solid sources were used for the deposition and the film thickness and growth rate were monitored by a quartz crystal monitor. Electron beam evaporation was used for silicon and carbon deposition, while tin was deposited by thermal effusion from a Knudsen cell.

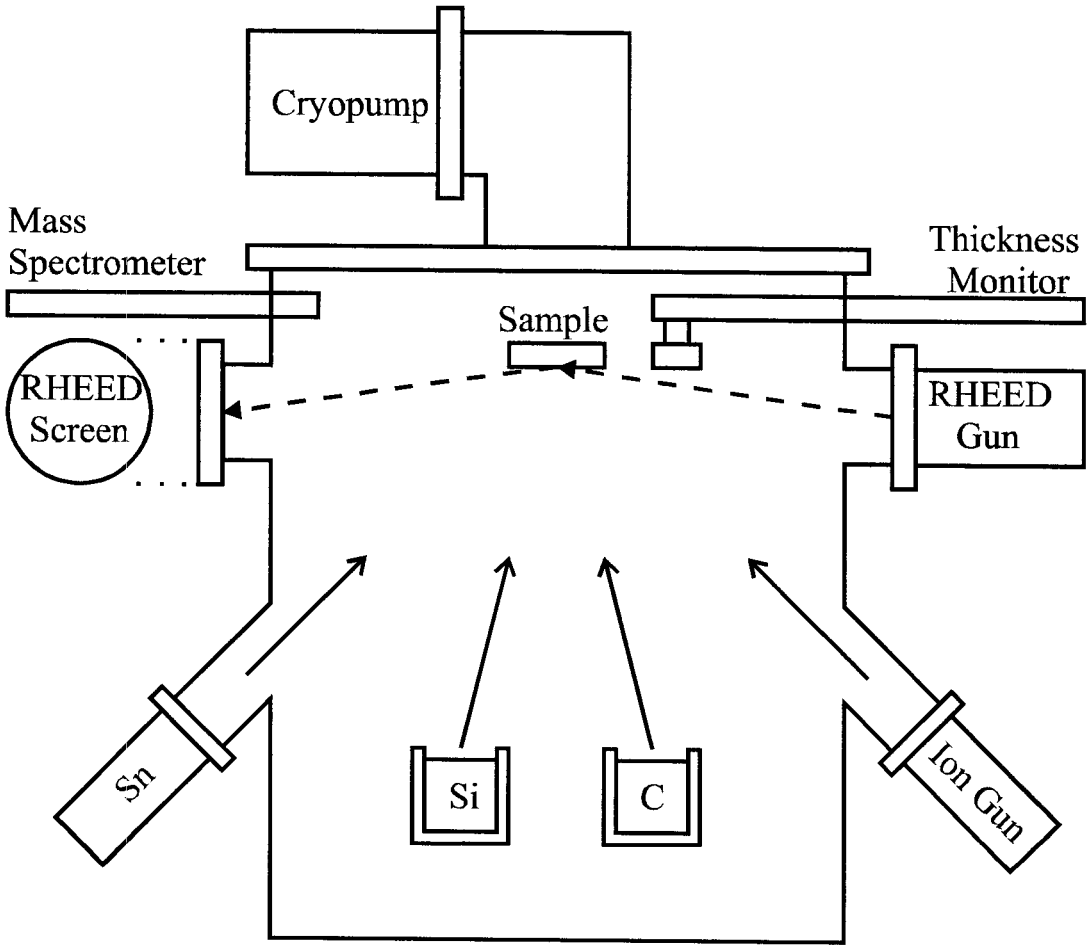

Figure 2.6 Schematic of the $Si_{1-y}(Sn_{1-x}C_x)_y$ molecular beam deposition chamber.

Silicon (100) wafers were first chemically cleaned by alternately placing the wafers in H_2O:H_2O_2:NH_4OH 5:1:1 at 80°C for 10 minutes and HF 5% for 30 seconds for a total of three times. The first solution removes organic contamination as well as particulates and metals from the wafer surface and form a thin oxide layer on the surface at the same time. The second solution etches away the surface oxide layer and produces a dihydride-terminated silicon (100) surface. After the final HF treatment the sample surfaces were highly hydrophobic and can be picked out of the solution with no liquid droplets on the front surface. The back side of the wafer were dried on lint free paper. The sample was then immediately mounted on the molybdenum substrate holder without a subsequent water rinse and transferred into the growth chamber within five minutes. A two hour *in situ* prebake at 200°C in ultrahigh vacuum was performed prior to film growth in order to desorb any remaining hydrocarbon-based contamination which can inhibit solid phase epitaxy.

Assurance of a high quality clean interface between the amorphous layers and the single crystal substrate is one of the most critical conditions for the success of subsequent solid phase epitaxy. Two methods were used to prepare such interface following the 200°C *in situ* prebake. In the first method, the substrate was cooled to 70°C and sputter cleaned by 500 eV Ar^+ ion beam generated by a Kaufman ion source at 0.1 mA/cm^2 for 5 minutes. In the second method, an epitaxial silicon buffer layer of about 100 nm was grown at 550°C and the sample was then cooled back to 200°C. The base pressure of the deposition

chamber is critical for this method since it takes approximately one hour for the sample to cool down after the deposition of the epitaxial silicon buffer layer. The second method is a simpler and potentially cleaner process since no ion source is needed. In this method it is desirable to ramp the substrate temperature down more rapidly after the growth of the epitaxial buffer layer so that the surface has less contamination and the subsequent amorphous layer can be deposited at a lower temperature to obtain a sharper crystal-to-amorphous transition with less or no defects [14]. A 200~300 nm amorphous silicon layer was then deposited at a rate of approximately 0.2 nm/sec on the prepared surface. This amorphous silicon layer serves as a buffer layer for the subsequent solid phase epitaxy and can be used to determine the quality of the initial crystal-amorphous interface. Following the amorphous silicon buffer a 100 nm $Si_{1-y}(Sn_{1-x}C_x)_y$ alloy film was deposited at a rate of approximately 0.2 nm/sec. Finally a low temperature anneal at 200°C for one hour was carried out in ultrahigh vacuum to improve the density of the amorphous layers before the sample was removed from the growth chamber. The resulting samples have a layer structure of a-$Si_{1-y}(Sn_{1-x}C_x)_y$/a-Si/epi-Si/Si(100) (Figure 2.7).

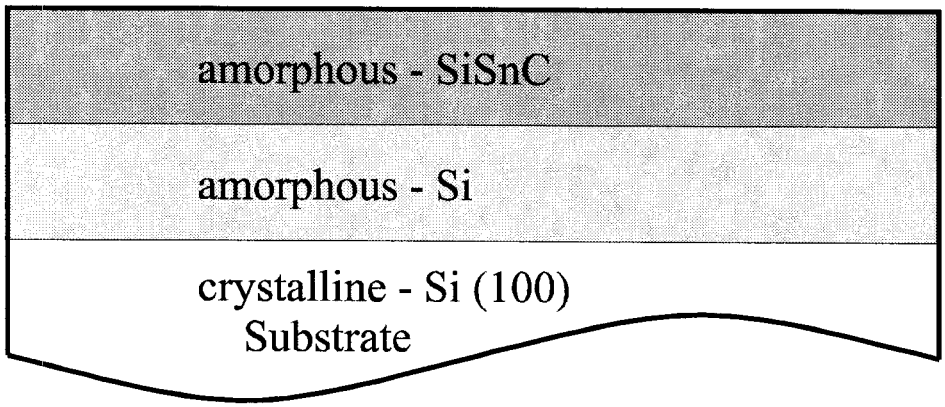

Figure 2.7 Layer structure of the amorphous $Si_{1-y}(Sn_{1-x}C_x)_y$ samples after the molecular beam deposition.

2 .5 Solid Phase Epitaxy

Solid phase epitaxy of a-$Si_{1-y}(Sn_{1-x}C_x)_y$/a-Si/epi-Si/Si(100) was performed at 580°C in an annealing crucible in air and was monitored by *in situ* time resolved reflectivity measurement using a 670 nm diode laser (Figure 2.8). Due to the slight difference in refractive index between the amorphous phase and crystalline phase, a fraction of the incident laser beam was reflected at the crystal-amorphous interface. The time resolved reflectivity measures the alternating constructive and destructive interference between the reflected laser beam from the sample surface and crystal-amorphous interface as the interface moves toward the surface during solid phase epitaxy. The measured reflectivity as a function of time provides

important real time information regarding the mode and rate of the amorphous to crystalline transition during the anneal [15].

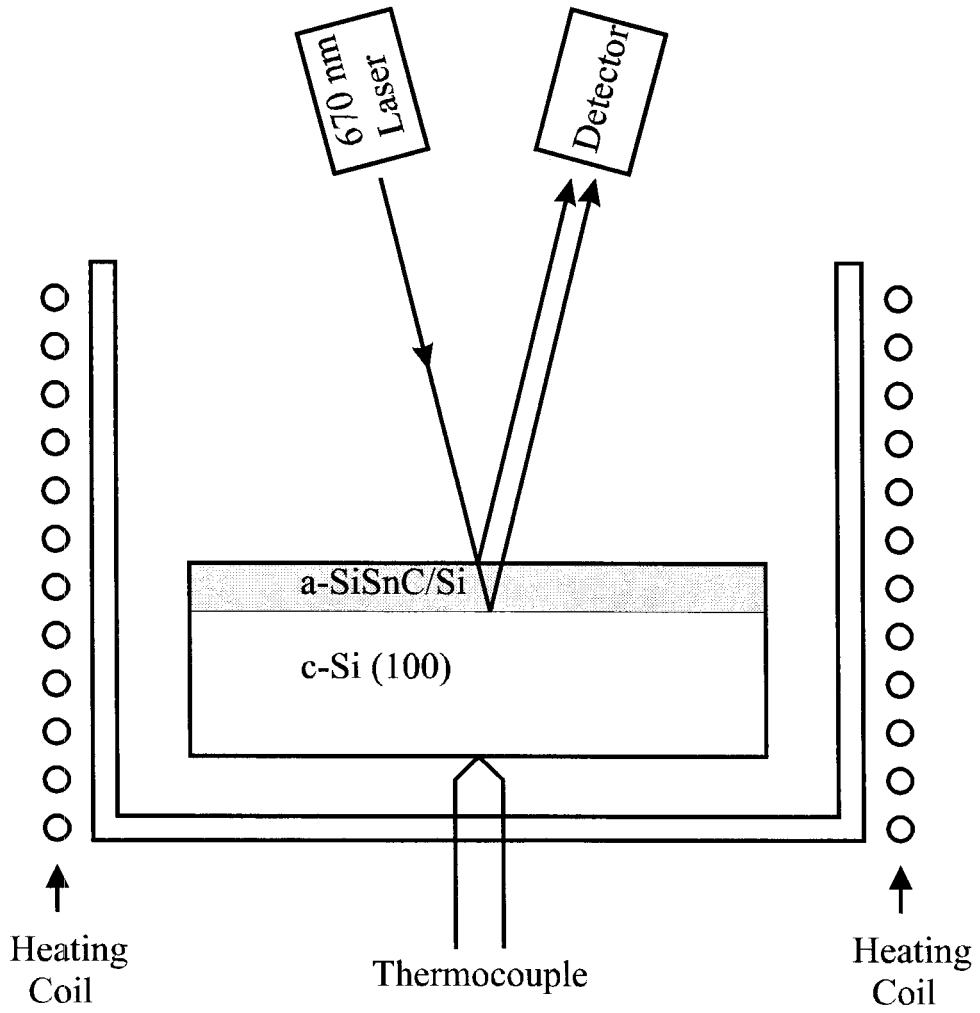

Figure 2.8 Schematic of the solid phase epitaxy system with *in situ* time resolved reflectivity monitoring.

Among the various $Si_{1-y}(Sn_{1-x}C_x)_y$ film compositions with a range of tin and carbon concentrations (up to 0.1), $Si_{0.98}Sn_{0.01}C_{0.01}$ showed very good planar solid phase epitaxy during the anneal. Other lattice mismatched samples with either tin or carbon concentrations exceeding these values resulted in polycrystalline films or no crystallization, as indicated by the time resolved reflectivity signals during the anneal (Figure 2.9).

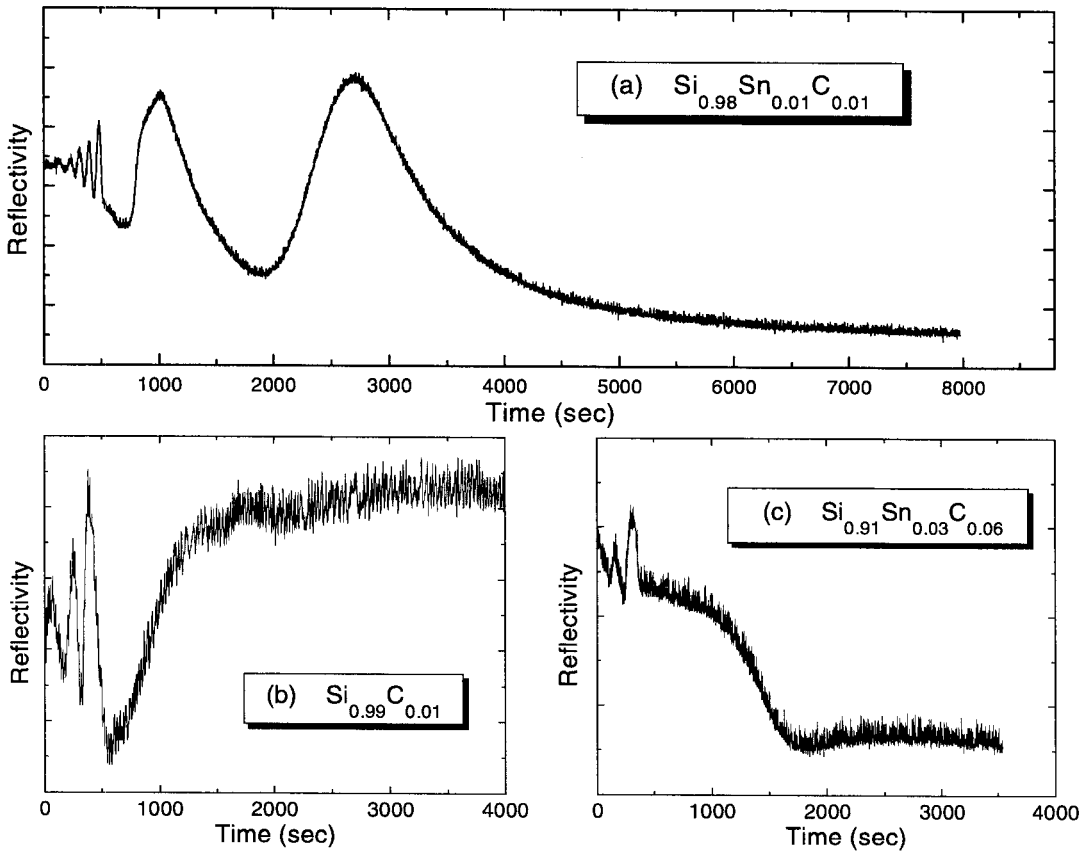

Figure 2.9 Time resolved reflectivity signals during the annealing of amorphous $Si_{1-y}(Sn_{1-x}C_x)_y$ samples.

The first few relatively fast oscillations in the time resolved reflectivity signals from all the samples shown in Figure 2.9 corresponded to the planar solid phase epitaxy growth of the amorphous silicon buffer layer. Note that only samples that showed normal planar solid phase epitaxy regrowth in the amorphous silicon buffer layer were included in the experimental results to assure that the initial crystal-amorphous interface was contamination free. The subsequent slower oscillations in Figure 2.9(a) indicated the planar solid phase epitaxy growth of the 100 nm $Si_{0.98}Sn_{0.01}C_{0.01}$ film, which had a solid phase epitaxy rate of approximately 2.9 nm/min, about 20 times slower than that of the pure silicon buffer layer. The time resolved reflectivity signal in Figure 2.9(b) showed stopped crystallization regrowth in the $Si_{0.99}C_{0.01}$ film since the oscillation of the signal stopped shortly after the solid phase epitaxy regrowth of the amorphous silicon buffer layer and remained constant after that. The time resolve reflectivity signal in Figure 2.9(c) indicated amorphous to polycrystalline transformation through non-planar random nucleation in the $Si_{0.91}Sn_{0.03}C_{0.06}$ sample since the signal decreased monotonically to the level of crystalline film without any oscillation after the initial solid phase epitaxy regrowth of the amorphous silicon buffer layer. Other samples with high tin concentrations showed similar transitions in their time resolved reflectivity signals during their annealing. However, none of these high tin concentration samples have compositions close to the lattice matched compositions with silicon (Table 2.1). The results of these solid phase epitaxy experiments suggest that excess carbon in $Si_{1-y}(Sn_{1-x}C_x)_y$ tends to inhibit

crystallization, while excess tin tends to induce an amorphous to polycrystalline transformation. Note that the $Si_{0.99}C_{0.01}$ sample did not show complete solid phase epitaxy regrowth while the $Si_{0.98}Sn_{0.01}C_{0.01}$ sample did. This suggested that careful strain compensation may enhance the solid phase epitaxy rate and increase the maximum impurity concentration without inhibition of solid phase epitaxy through a reduction of the strain energy component in the total energy barrier of solid phase epitaxy.

$Si_{0.98}Sn_{0.01}C_{0.01}$	Good SPE
$Si_{0.99}C_{0.01}$	No Crystallization
$Si_{0.96}Sn_{0.005}C_{0.035}$	Polycrystalline Transformation
$Si_{0.91}Sn_{0.03}C_{0.06}$	Polycrystalline Transformation

Table 2.1 Results of solid phase epitaxy of $Si_{1-y}(Sn_{1-x}C_x)_y$ samples during annealing at 580°C

2.6 Elimination of Misfit Dislocations by Strain Compensation

Rutherford backscattering spectra for the $Si_{0.98}Sn_{0.01}C_{0.01}$ sample were taken both before and after the solid phase epitaxy regrowth. The spectra showed no significant tin redistribution (Figure 2.10). The carbon and tin concentrations were also confirmed by electron microprobe measurements and were in good agreement with the deposition rate controls and the Rutherford backscattering results. Ion channeling spectrum in Figure 2.11 showed good epitaxial crystal quality. A minimum yield of about 0.08 was obtained from the spectrum, a significant portion of which can be attributed to a surface oxide layer which can also be seen in the same channeling spectrum. This is consistent with the annealing of the $Si_{1-y}(Sn_{1-x}C_x)_y$ samples in air at 580°C. The channeling feature of the tin signal indicated good substitutionality of tin in silicon. Taking the experimental uncertainties into account, it is estimated that 90~100% of tin is substitutional in the epitaxial silicon matrix.

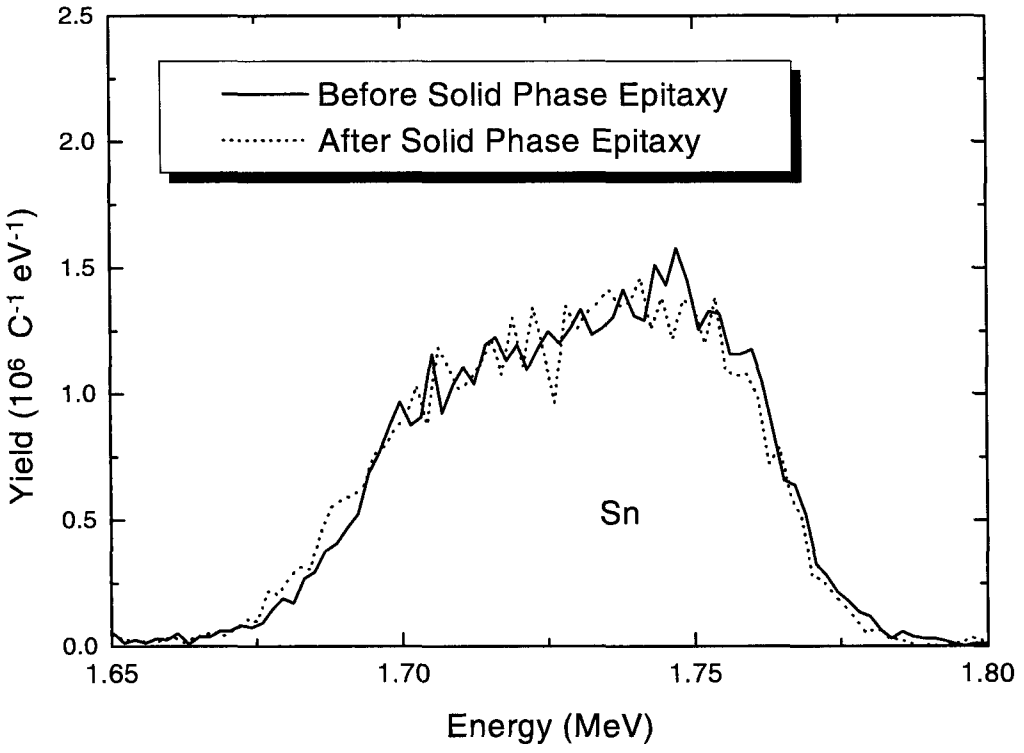

Figure 2.10 Rutherford backscattering spectra of the $Si_{0.98}Sn_{0.01}C_{0.01}$ sample before and after the solid phase epitaxy.

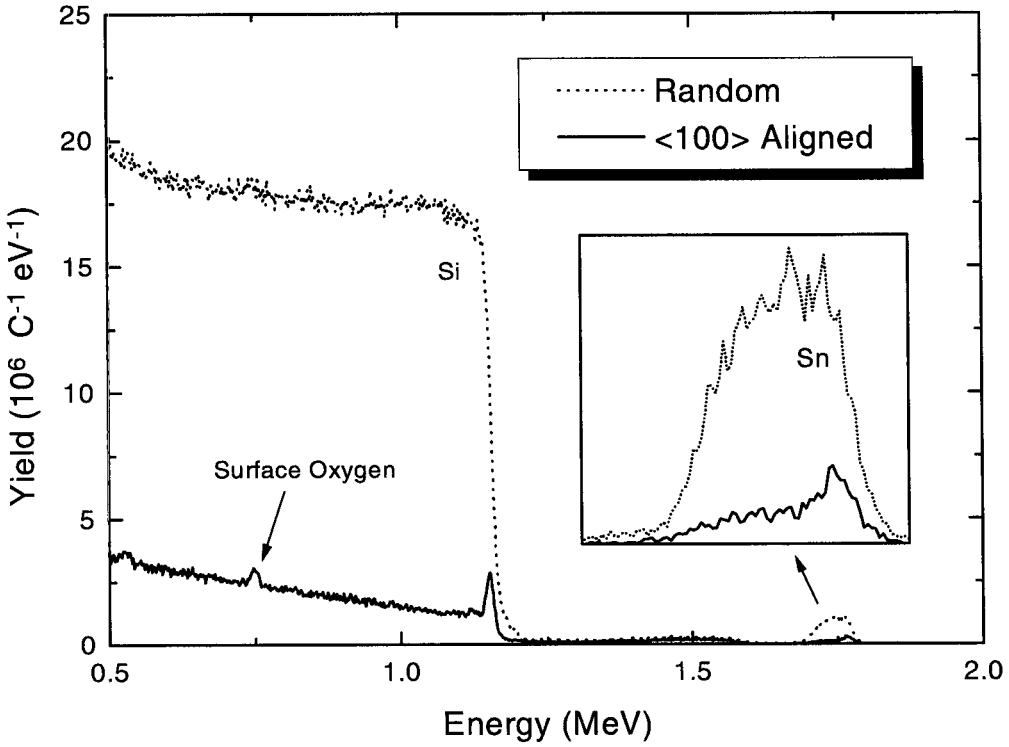

Figure 2.11 Rutherford backscattering and channeling spectra of the $Si_{0.98}Sn_{0.01}C_{0.01}$ sample.

A high resolution x-ray diffraction scan around the silicon (440) diffraction peak is shown in Figure 2.12. Scans taken at different azimuthal angles around the surface normal showed no azimuthal dependence, indicating that there was no misfit accommodation by epitaxial tilt of the film crystal orientation relative to the substrate. The peak position of the $Si_{0.98}Sn_{0.01}C_{0.01}$ film in the diffraction curve was shifted relative to that of the substrate, so that the lattice parameter of the film was

slightly smaller than that of pure silicon and the film was under tensile strain. This suggested that carbon was substitutional in the $Si_{0.98}Sn_{0.01}C_{0.01}$ film, and was consistent with the fact that 1 at.% carbon is more than enough to compensate the strain induced by 1 at.% tin. A comparison of (440) and (400) diffraction curves showed that the $Si_{0.98}Sn_{0.01}C_{0.01}$ film was coherently strained. Assuming Vegard's law to be valid, the amount of strain measured from x-ray diffraction corresponds to about 1.0 at.% substitutional carbon, which is good agreement with the 1.0 at.% total carbon concentration from the deposition rate control as well as electron microprobe measurement.

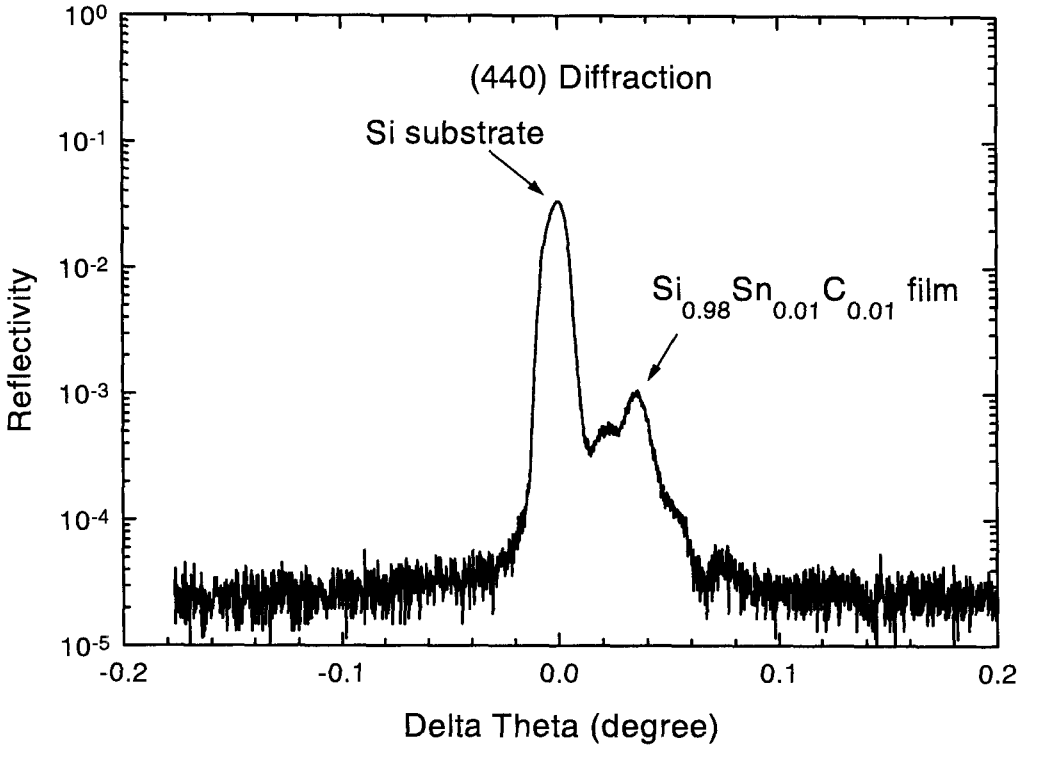

Figure 2.12 High resolution x-ray diffraction of the $Si_{0.98}Sn_{0.01}C_{0.01}$ sample after solid phase epitaxy regrowth.

Cross sectional transmission electron microscopy analysis indicated that the regrown $Si_{0.98}Sn_{0.01}C_{0.01}$ sample was epitaxial and dislocation free (Figure 2.13). The sample was also examined by plan view transmission electron microscopy analysis and was found to have no dislocations in a sample region larger than 100 μm by 100 μm, implying a threading dislocations density of less than 10^4 cm^{-2}. The residual lattice mismatch calculated from the amount of shift in the x-ray

diffraction curves was about 0.001. This small lattice mismatch is consistent with the absence of dislocations in the transmission electron microscopy analysis, since the 100 nm film thickness was below the thermodynamic critical thickness of dislocation formation as a result of the strain compensation between carbon and tin. Assuming Vegard's law to be valid, the concentration of substitutional carbon in the film was calculated from the high resolution x-ray diffraction curve to be about 0.01, which was in good agreement with the total carbon concentration obtained from the deposition rate controls and the electron microprobe measurements.

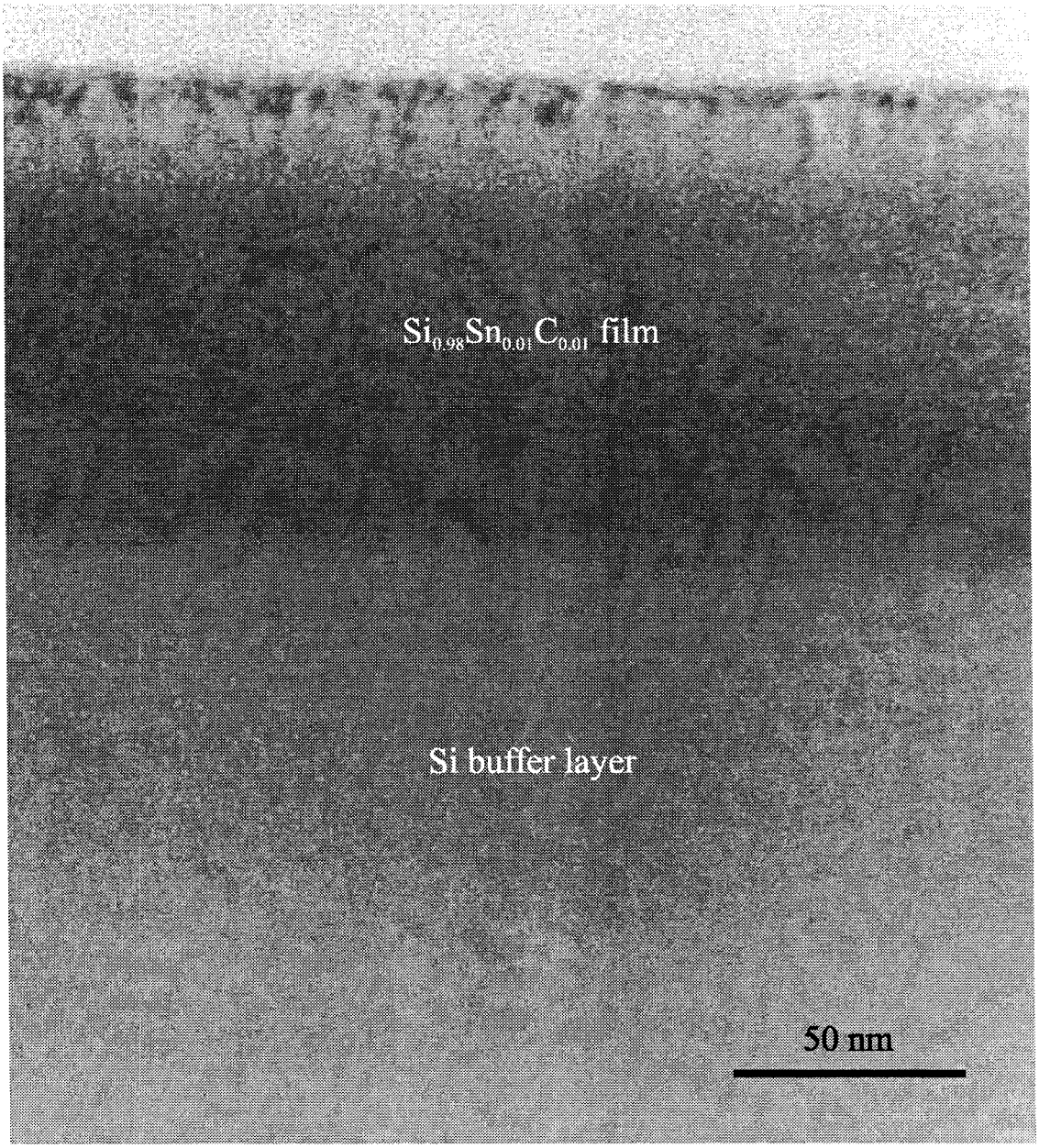

Figure 2.13 Cross sectional transmission micrograph of the $Si_{0.98}Sn_{0.01}C_{0.01}$ sample after solid phase epitaxy regrowth.

2 .7 $Si_{1-x}Sn_x$ Alloy Growth by Ion-Assisted Molecular Beam Epitaxy

To further increase the maximum tin concentration in silicon, growth of $Si_{1-x}Sn_x$ on silicon (100) substrates was performed by ion-assisted molecular beam epitaxy in the same molecular beam epitaxy system. The system was equipped with a 250W electron cyclotron resonance ion source with excitation at 2.45 GHz. The ion source was connected to a source of argon gas with a 99.9995% purity. Prior to growth, silicon substrates were first chemically cleaned by the same process in the molecular beam deposition of $Si_{1-y}(Sn_{1-x}C_x)_y$. After a 200°C *in situ* prebake for 2 hours the substrate temperature was raised to 550°C to produce a (2×1) reconstructed clean silicon surface. A 100 nm epitaxial silicon buffer layer was first grown with a growth rate of 0.05 nm/sec. During the growth of the silicon buffer layer the substrate temperature was decreased continuously from 550°C at the beginning to 410°C at the end. An epitaxial $Si_{1-x}Sn_x$ layer was then grown at 410°C at a growth rate of 0.05 nm/sec. During the growth of the $Si_{1-x}Sn_x$ alloy layer the sample surface was irradiated by an Ar^+ ion beam (40~50 eV, 0.05 mA/cm^2 at substrate) to suppress surface segregation of tin. The ion beam was generated by the electron cyclotron resonance ion source with an 5 sccm argon gas flow which introduced a 7×10^{-5} Torr argon background pressure in the growth chamber. Samples with tin concentrations of up to 0.04 were grown. *In situ* reflection high energy electron diffraction pattern showed that the resulting

$Si_{0.96}Sn_{0.04}$ sample was epitaxial and the alloy film surface was atomically smooth. The diffraction pattern also showed a possible (4×n) surface reconstruction pattern on the $Si_{0.96}Sn_{0.04}$ (45 nm thick) sample surface (Figure 2.14) [16] [17] in contrast to the (2×1) reconstruction pattern on pure silicon buffer layer surface. Rutherford backscattering spectrum confirmed the tin concentration and showed that tin was uniformly distributed inside the alloy film with a small surface peak (Figure 2.15) which may indicate some degree of tin surface segregation during the growth.

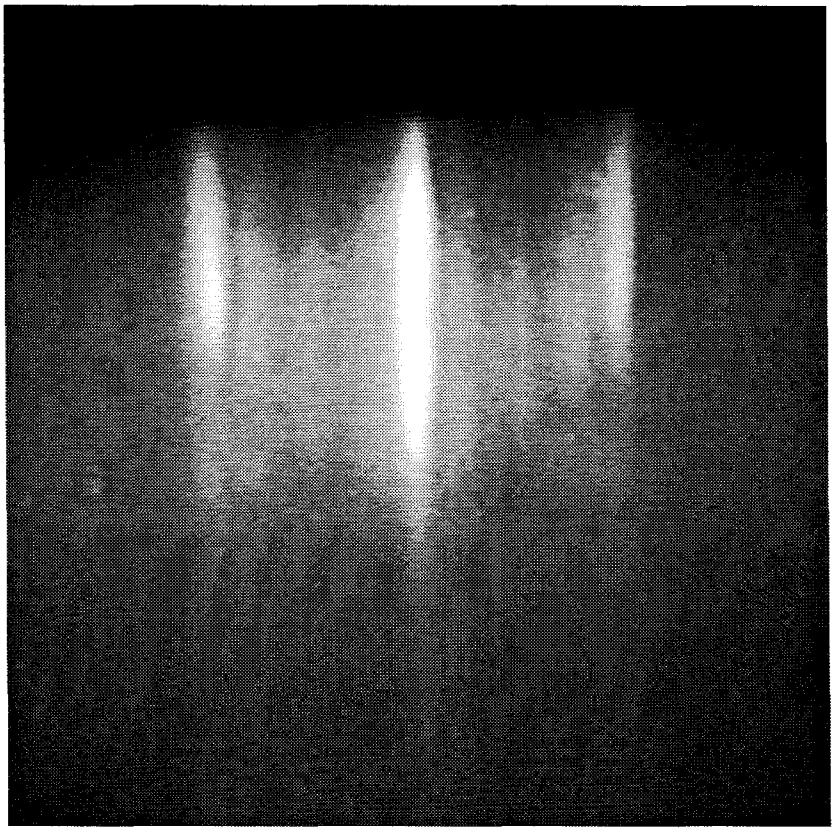

Figure 2.14 Reflection high energy electron diffraction pattern along (011) direction of the $Si_{0.96}Sn_{0.04}$ sample surface during molecular beam epitaxy growth.

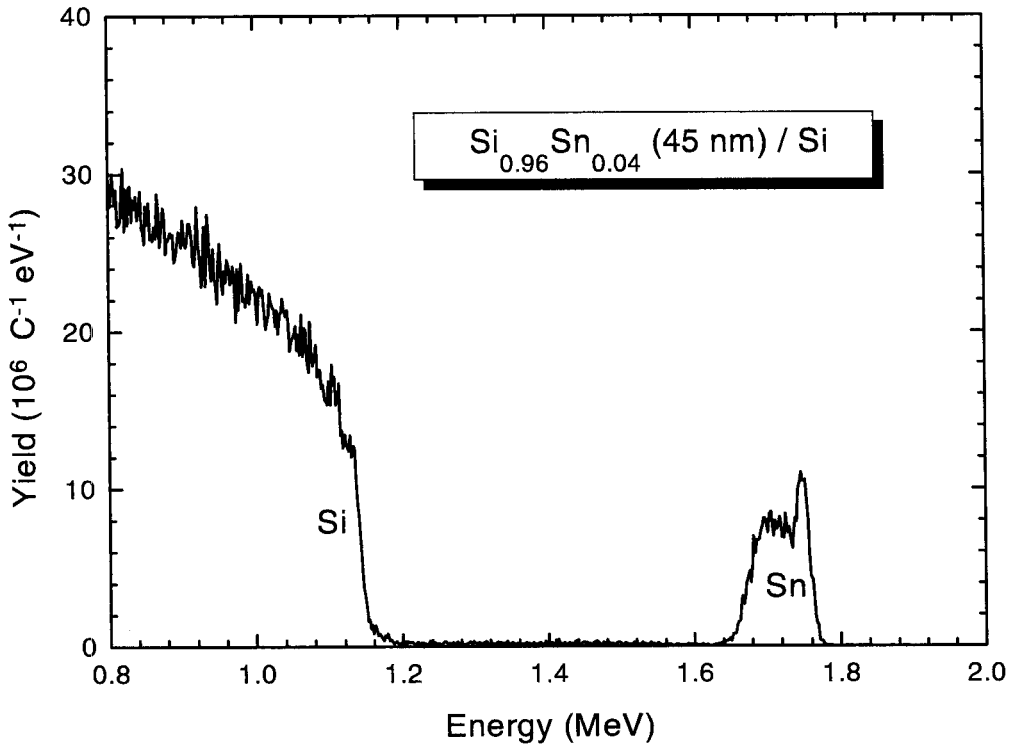

Figure 2.15 Rutherford backscattering spectrum of the $Si_{0.96}Sn_{0.04}$ sample grown by molecular beam epitaxy.

2 .8 Conclusions

High crystal quality epitaxial $Si_{1-y}(Sn_{1-x}C_x)_y$ alloy thin films were synthesized on silicon (100) substrates by molecular beam deposition and solid phase epitaxy with tin and carbon concentrations of about y=0.02 (x=0.5), well above their solid solubility in silicon. The epitaxial film was found to be dislocation free, with good substitutionality of tin and carbon. The experiments also suggest that strain compensation may increase the maximum impurity concentrations without inhibiting solid phase epitaxy. Also, epitaxial $Si_{1-x}Sn_x$ alloy films were successfully synthesized by ion-assisted molecular beam epitaxy on silicon (100) substrates with tin concentrations of up to 0.04. Reflection high energy electron diffraction pattern suggested a possible 4× surface reconstruction on the $Si_{0.96}Sn_{0.04}$ surfaces during ion-assisted molecular beam epitaxy. The successful synthesis of these silicon-based epitaxial alloy thin films presents potentially attractive processes for fabrication of silicon-based high performance heterojunction devices as well as silicon-based optoelectronic devices using the carbon-related impurity complex centers with electroluminescence at 1.28 μm.

Bibliography

[1] L.T. Canham, K.G. Barraclough, and D.J. Robbins, Appl. Phys. Lett. 51, 1509 (1987).

[2] L.T. Canham, M.R. Dyball, and K.G. Barraclough, Mat. Sci. Eng. B4, 95 (1989).

[3] P. Mei, M.T. Schmidt, E.S. Yang, and B.J. Wilkens, J. of Appl. Phys., 69, 8417 (1991).

[4] G. He, M.D. Savellano, and H.A. Atwater, Mat. Res. Soc. Symp. Proc. 298, 229 (1993).

[5] G. He, M.D. Savellano, and H.A. Atwater, Appl. Phys. Lett. 65, 1159 (1994).

[6] G. He, M.D. Savellano, and H.A. Atwater, Section X2.15 Electronic Materials: SiSnC, Handbook of Thin Film Process Technology, Ed. D.A. Golcker and S.I. Shah, Institute of Physics Publishing Ltd. (Bristol and Philadelphia) (1995).

[7] R.A. Soref, J. Appl. Phys. 70, 2407 (1991).

[8] K. K. Eberl, S.S. Iyer, S. Zollner, J.C. Tsang, and F.K. LeGoues, Appl. Phys. Lett., 60, 3033 (1992).

[9] A.R. Powell, K. Eberl, B.A. Ek, and S.S. Iyer, J. Cryst. Growth 127, 425 (1993).

[10] J.W. Strane, W. Edwards, J.W. Mayer, H.S. Stein, S.R. Lee, B.L. Doyle, and S.T. Picraux, Mater. Res. Soc. Symp. Proc. 280, 609 (1992).

[11] T.B. Massalski, et al., Binary Alloy Phase Diagrams, Second Edition, Am. Soc. Metals, Materials Park, 1990.

[12] M. Vergnat, M. Piecuch, G. Marchal, and M. Gerl, Phil. Mag., B51, 327 (1985).

[13] J.W. Strane, H.J. Stein, S.R. Lee, S.T. Picraux, J.K. Watanabe, and J.W. Mayer, J. Appl. Phys. 76, 3656 (1994).

[14] M.V.R. Murty, H.A. Atwater, Phys. Rev. B 49, 8483 (1994).

[15] G.L. Olsen and J.A. Roth, Mat. Sci. Rep., 3, 1 (1988).

[16] A.A. Baski, C.F. Quate, and J. Nogami, Phys. Rev. B 44, 11167 (1991).

[17] L. Li, Y. Wei, and I.S.T. Tsong, J. Vac. Sci. Tech. A 13, 1609 (1995).

Chapter 3

MOLECULAR BEAM EPITAXY OF Sn_xGe_{1-x} ALLOY FILMS

3 .1 Introduction

The diamond-cubic Sn_xGe_{1-x} alloy system is an interesting group IV semiconductor material with potential applications in the fabrication of silicon-based long wavelength infrared optoelectronic devices and high performance heterojunction devices. Band structure calculations have suggested that, while tin is a semi-metal and germanium is an indirect band gap semiconductor, diamond-cubic Sn_xGe_{1-x} alloys may have a direct band gap that is continuously tunable from E_g=0.55 eV to E_g=0 eV for compositions from x=0.2 to x=0.6, with a very low electron effective mass, and hence high electron mobility [1]-[7].

Many growth techniques, including molecular beam epitaxy of alloy films and superlattices [10]-[18], sputter deposition [19] and solid phase recrystallization [20]-[22], have been used to synthesize both epitaxial and polycrystalline Sn_xGe_{1-x} thin films. However, synthesis of epitaxial Sn_xGe_{1-x} alloy films in the predicted direct gap composition range has proved to be difficult due to the severe tin surface segregation during conventional thermal growth [17]. Although decreasing the growth temperature can reduce surface segregation, the

temperature has a lower limit at which surface kinetic roughening is strong enough to cause a breakdown of epitaxy through a crystal to amorphous transition. Similar breakdown of epitaxy caused by surface kinetic roughening has been studied in low temperature silicon homoepitaxy [23] [24]. In the case of Sn_xGe_{1-x} growth for alloy compositions in the predicted direct band gap range, however, the surface segregation of tin is too strong to be completely suppressed even when the growth temperature is decreased to the limit where epitaxy breakdown occurs rapidly through surface kinetic roughening [2][25].

To overcome the conflicting requirements posed by tin surface segregation and surface kinetic roughening during conventional thermal growth, growth of epitaxial Sn_xGe_{1-x}/Ge/Si(100) by ion-assisted molecular beam epitaxy was studied [2][25]. When the growing surface of a thin film is irradiated by a high flux of low energy ions, the surface atoms undergo subsurface recoil-implantation and generate collisional mixing between the surface and subsurface layers, hence incorporating surface atoms into the growing film. Single-crystal epitaxial Sn_xGe_{1-x} alloy films with tin concentrations up to x=0.34 were successfully synthesized using an electron cyclotron resonance ion source which generates high flux Ar^+ ion beams in the 30 eV to 50 eV energy range to produces near-surface collisional mixing while avoiding ion damage to the bulk crystal.

3 .2 Electronic Properties and Potential Device Applications

One of the most interesting electronic features of Sn_xGe_{1-x} is its predicted continuously tunable direct energy band gap in the infrared region. Tight-binding and pseudopotential calculations have predicted that diamond-cubic Sn_xGe_{1-x} alloys may have a direct band gap that is continuously tunable from E_g=0.55 eV to E_g=0 eV for tin concentrations in the range of approximately x=0.2 to x=0.6 [1]-[4]. This can be illustrated by a schematic plot of the Sn_xGe_{1-x} energy band gap (relative to the valence band energy) as a function of the alloy composition in Figure 3.1 [1]. A small direct band gap was also suggested by tight-binding, pseudopotential, and density functional theory calculations for ordered zinc-blende structure SnGe [4]-[7]. Quantum-size effect on energy band gap of pure diamond-cubic tin was also investigated theoretically [8] [9].

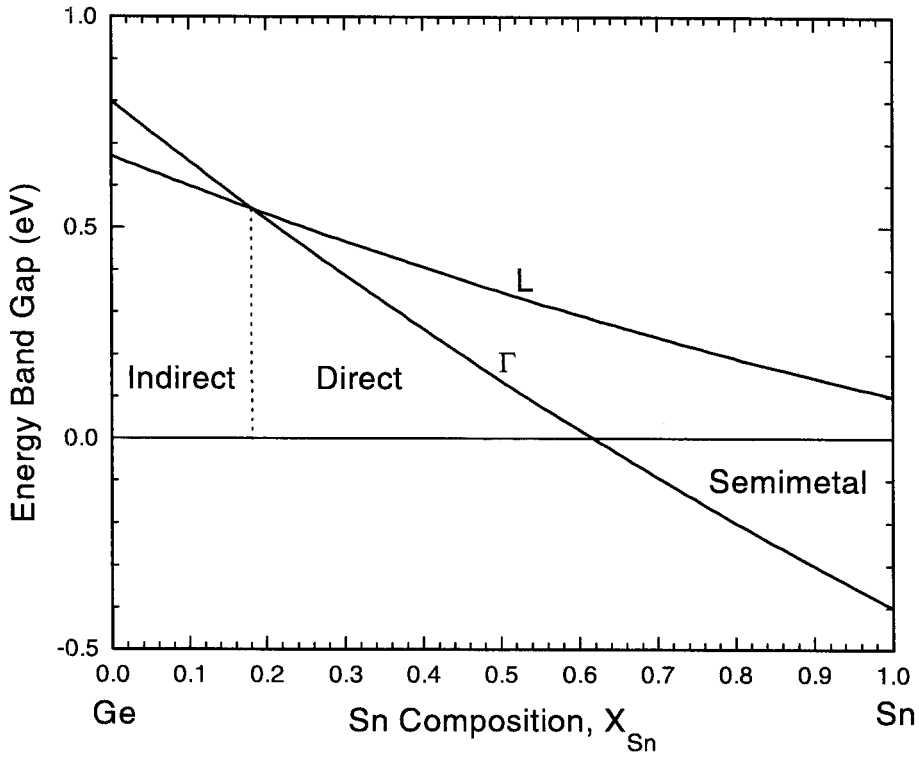

Figure 3.1 Schematic of Sn_xGe_{1-x} energy band gap (relative to the valence band energy) as a function of the alloy composition [1].

Plotted in Figure 3.1 are the energies of the Γ-point (k = (0, 0, 0) in the Brillouin zone) and the L-point (k = $(2\pi/a)$ (½, ½, ½) in the Brillouin zone) of the lowest conduction band relative to the valence band. Pure germanium is an indirect band gap semiconductor with a conduction band minimum at the L-point. Pure diamond-cubic tin is a semi-metal with a conduction band minimum at the Γ-point below the valence band. When tin is added into germanium, both the Γ-point

and the L-point of the conduction band decrease, but the Γ-point is predicted to decrease faster than the L-point. When the tin concentration is increased to about x=0.2, the Γ-point and the L-point cross over each other and the alloy material becomes a direct band gap semiconductor. A further increase of tin concentration decreases the direct band gap of Sn_xGe_{1-x} until the tin concentration reaches about x=0.6 where the Γ-point of the conduction band moves below the valence band and the alloy material becomes a semi-metal. The predicted tunable band gap of Sn_xGe_{1-x} corresponds to an optical wavelength longer than approximately 2 μm. This makes Sn_xGe_{1-x} an interesting semiconductor material for potential applications of silicon-based monolithic infrared optoelectronic devices. One potential device application is a silicon-based monolithic infrared detector array which uses an epitaxial Sn_xGe_{1-x} layer grown on silicon as the active detector element with integrated supporting electronic circuits (e.g., read-out driving circuit) built in silicon on the same chip (Figure 3.2). The ability to grow epitaxial Sn_xGe_{1-x} alloy films on silicon substrates at very low growth temperatures allows the growth of Sn_xGe_{1-x} layers on nearly fully processed wafers where the supporting silicon circuits are already fabricated.

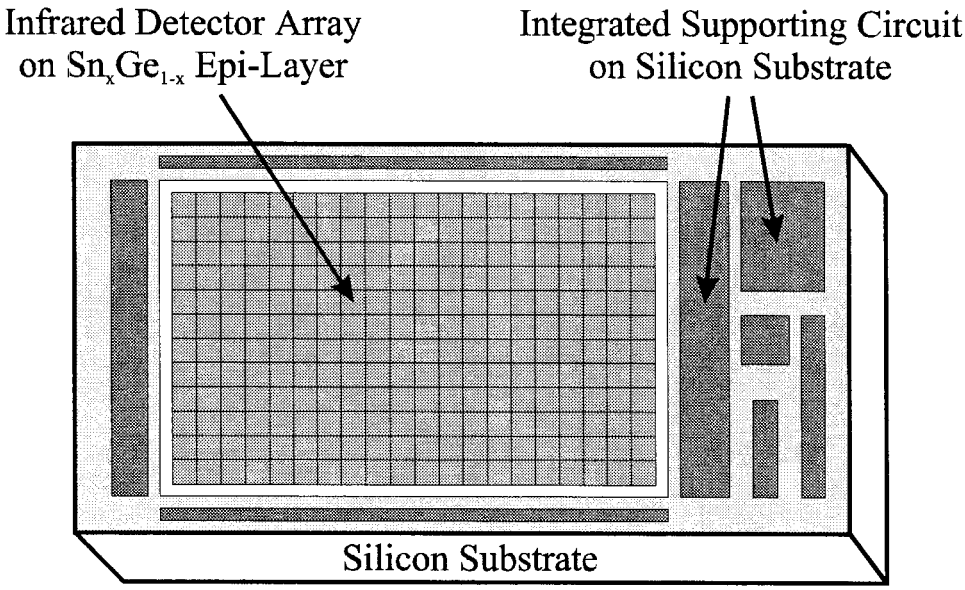

Figure 3.2 Schematic of a silicon-based monolithic infrared detector array using Sn_xGe_{1-x} epitaxial layers grown on silicon substrates.

Another interesting electronic feature of Sn_xGe_{1-x} is the low electron effective mass, hence high mobility, predicted by tight-binding calculations [1]-[2]. This prediction is consistent with the fact that the electron effective masses of diamond-cubic tin and germanium (0.02 m_e and 0.08 m_e) are much smaller than that of silicon (0.18 m_e). One potential device application is silicon-based high mobility field-effect transistors (Figure 3.3), where the epitaxial Sn_xGe_{1-x} layers are used as the high-speed conduction channels.

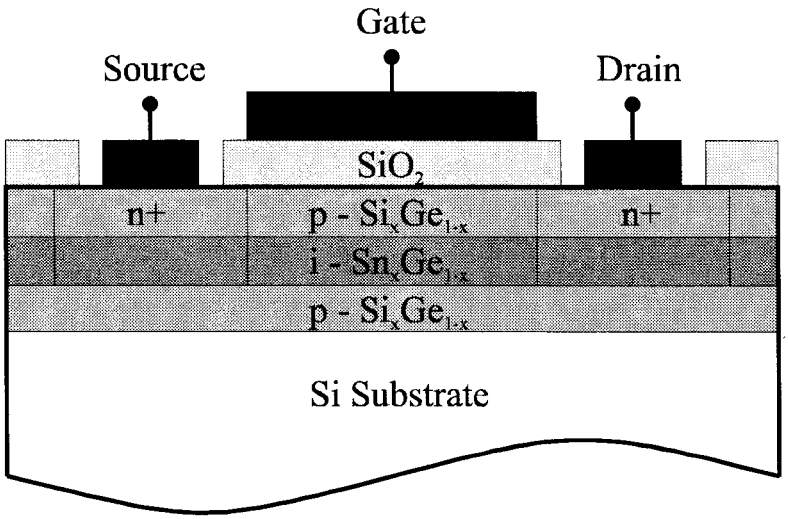

Figure 3.3 Schematic of a silicon-based SnGe high-speed modulation-doped field-effect transistor.

3 .3 Thermodynamics

The equilibrium phase diagram of Sn-Ge (Figure 3.4) shows a simple binary eutectic system (eutectic temperature ~ 231°C) [26] [27] with mutual equilibrium solubilities no more than 0.01 [28] [29]. Since the Sn_xGe_{1-x} alloy compositions required for a predicted direct band gap are much higher than the equilibrium bulk solid solubility, the alloys of interest are thermodynamically metastable. Driven by the limited bulk solid solubility and the difference in surface free energy between tin and germanium, tin tends to segregate to the surface during growth [10]-[19]. The difference in atomic radii between Sn and Ge (about

13%) may also play a role in the surface Sn segregation when Sn_xGe_{1-x} is deposited on a lattice mismatched substrate which generates a coherency strain field.

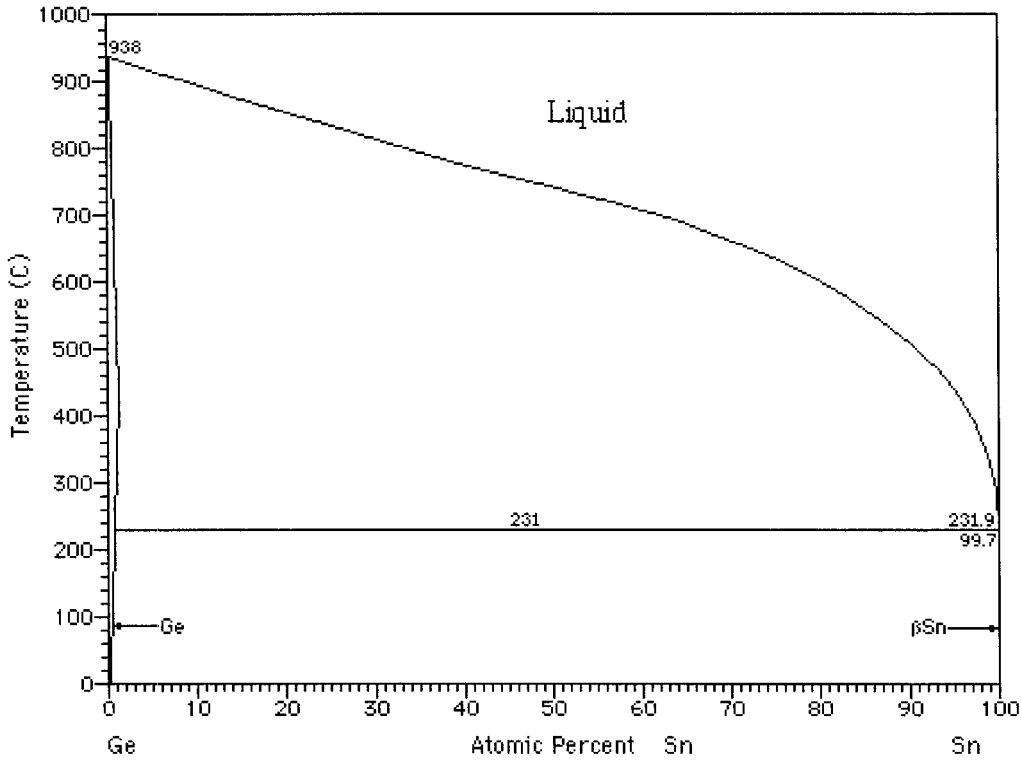

Figure 3.4 Binary phase diagram of Sn-Ge [27].

The predicted Sn_xGe_{1-x} electronic properties are based on band structure calculations that assume a diamond-cubic crystal structure. While bulk germanium is only stable in a diamond-cubic phase, bulk tin transforms from the diamond-cubic α-phase (gray tin) to the body-centered-tetragonal β-phase (white tin) above 13.2°C at thermodynamic equilibrium [30]. Nevertheless, it has been shown that

thin film α-tin can be epitaxially stabilized on single crystal substrates with similar lattice constants at much higher temperatures (~130°C) [31]-[34]. The diamond-cubic structure may be further stabilized by the addition of germanium which has a diamond-cubic crystal structure [35].

3 .4 First-Principles Calculation of Alloy Local Structure

Electronic properties of semiconductors are directly affected by their crystal structures. In the case of disordered alloys where the atomic species are randomly distributed among the crystalline lattice sites, the perfectly periodic crystalline lattice structure is perturbed by the alloy disorder. The overall (average) lattice constant of a disordered substitutional alloy is often estimated empirically by Vegard's Law as the linear average of the lattice constants of all the alloy constituents weighted by their atomic concentrations in the alloy. In most tight-binding and pseudopotential calculations, such as the ones predicted the electronic properties of Sn_xGe_{1-x} [1]-[4], the crystal structure of a disordered alloy is described by the virtual crystal approximation, which approximates the crystal structure of a disordered substitutional alloy as a perfectly periodic crystalline lattice with lattice constants as described by Vegard's law and identical virtual "alloy" atoms at the lattice sites each carrying an atomic potential as the average of the atomic potentials of all the alloy constituents, weighted by their atomic concentrations. Deviations from the virtual crystal approximation as a result of

alloy disorder have been shown to cause significant deviations from the results of tight-binding and pseudopotential calculations [36]. Such deviations are usually small in alloys whose constituents have closely matched atomic radii. However, note that for Sn_xGe_{1-x} alloys, tin and germanium have a difference in atomic radii of about 13%, compared to a difference of about 4% for germanium and silicon in Ge_xSi_{1-x} alloys.

To estimate the qualities of the approximations of Vegard's law and the virtual crystal approximation for Sn_xGe_{1-x} alloys, calculation of local crystal structures of the Sn_xGe_{1-x} alloys were performed by first-principles ground state density functional theory calculations under the local density approximation using the norm-conserving pseudopotentials through self-consistent total-energy minimization [37]. The calculations were performed using the Plane-Wave version 3.0.0 software package which is commercially available from Biosym Technologies, Inc.. Density functional theory calculations have been shown to reproduce structural and elastic properties of materials, including solids of group IV elements, with very good accuracy, but face some difficulties in reproducing the electronic energy band structures of solids with good accuracy since it is fundamentally a ground state theory while electronic energy band structure is an excited state property [38]. Due to limitations in the total number atoms for the calculation to finish in reasonable amounts of time and computational resources, the 8-atom conventional cubic unit cell of the diamond-cubic lattice was used as the "super cell" building block under the periodic boundary condition (Figure 3.5). The super cell resembles the conventional cubic unit cell of the diamond-cubic

lattice, but is subject to a simple cubic symmetry instead of a diamond-cubic or face-centered-cubic symmetry. Therefore, 9 different alloy compositions, ranging from x=0/8 to x=8/8 at every 1/8 interval, can be potentially constructed. While such an approach still implies a perfect long-range order in the crystal structure, short-range local structure can nevertheless be estimated from the calculation. In this way better estimations can be consistently approached by increasing the size of the super cell building block when increased computation powers are available.

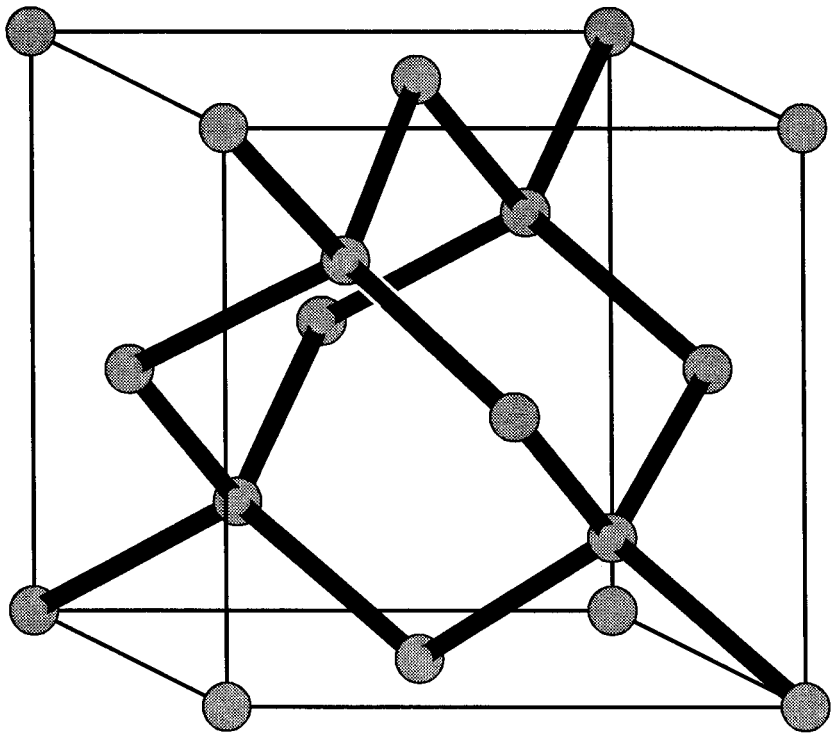

Figure 3.5 Conventional cubic unit cell of diamond-cubic crystals.

Since in this study the Sn_xGe_{1-x} alloys are experimentally approached from the germanium rich alloy compositions, structures of germanium rich Sn_xGe_{1-x} alloys with tin concentrations of x=1/8 (Sn_1Ge_7) and x=2/8 (Sn_2Ge_6) are calculated in particular. In addition, structures for pure diamond-cubic germanium and tin were also calculated as references. In the 8-atom super cell configuration, there is only one nonequivalent configuration for Sn_1Ge_7, and there are two nonequivalent configurations for Sn_2Ge_6 (labeled as Sn_2Ge_6 (a) and Sn_2Ge_6 (b) for configurations with and without tin-tin bonds, respectively) (Figure 3.6).

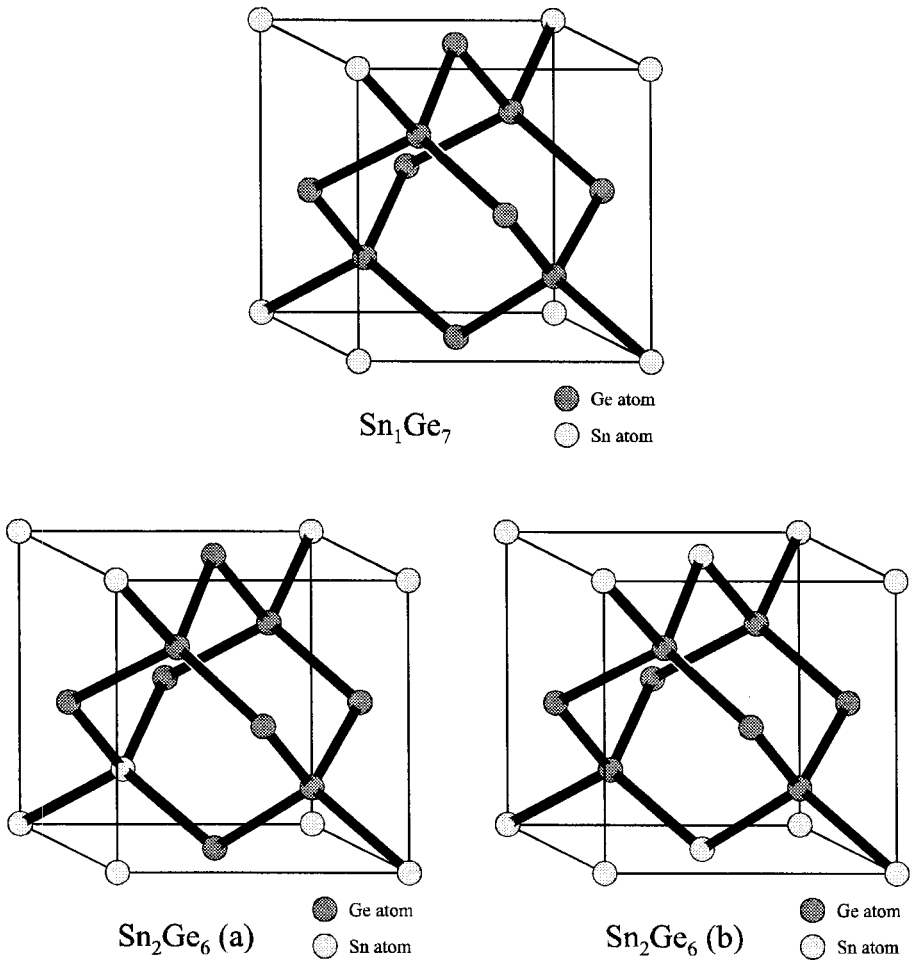

Figure 3.6 Cubic unit cell for Sn_1Ge_7, Sn_2Ge_6 (a), and Sn_2Ge_6 (b).

One useful parameter to characterize the local bonding arrangements of these configurations is the short-range order parameter r which can be defined as

$$r = \frac{q}{2x(1-x)} - 1 \quad = \quad \begin{cases} -1 & \textit{phase separated} \\ 0 & \textit{random alloy} \\ 1 & \textit{greatest short range order} \end{cases}$$

where x is the alloy composition, and q is the fraction of unlike nearest-neighbor bonds (in this case, tin-germanium bonds) among all nearest-neighbor bonds. In general the short-range order parameter indicates the degree of local ordering with a value ranging from $r=-1$ to $r=1$, with larger values of the order parameter r indicating stronger ordering in the alloy. For example, in completely phase separated materials, $q=0$, therefore the order parameter $r=-1$; In completely random disordered alloys, $q=2x(1-x)$, therefore the order parameter $r=0$; In perfectly ordered zinc-blende (zinc-sulfide) structures, $x=0.5$ and $q=1$, therefore $r=1$. The short-range order parameters for the Sn_xGe_{1-x} super cell configurations are $r=\frac{1}{7}$ for Sn_1Ge_7, $r=0$ for Sn_2Ge_6 (a) (with tin-tin bonds), and $r=\frac{1}{3}$ for Sn_2Ge_6 (b) (without tin-tin bonds).

Calculations of all the alloy structures were performed on a IBM RS6000 computer. For each super cell configuration, total system energies for various lattice constants were calculated. The optimal lattice constants were then determined at the minimum of total energy through a parabolic fit as a function of lattice constant for each configuration (Figure 3.7). For each calculation, all the atoms were originally positioned at the diamond-cubic lattice sites. During the calculations, the atoms were allowed to move along the directions of the net forces from all other atoms (gradients of total energy with respect to atom positions) to minimize the total system energy and obtain the optimal local crystal structure. All

the cutoff parameters and convergence criteria used in the calculations exceeded the recommended default values provided by the Plane Wave software package to assure good calculation quality. The cutoff energy for plane wave basis was set to 0.27 keV (default 0.23 keV); The Brillouin zone integration cutoff length was set to 1 nm (default 0.8 nm); The wave-function convergence criteria was set to 10^{-15} (default 10^{-10}); The atomic-position convergence criteria was set to 1×10^{-3} eV/nm (default 1 eV/nm). The results of the calculations are summarized in Table 3.1.

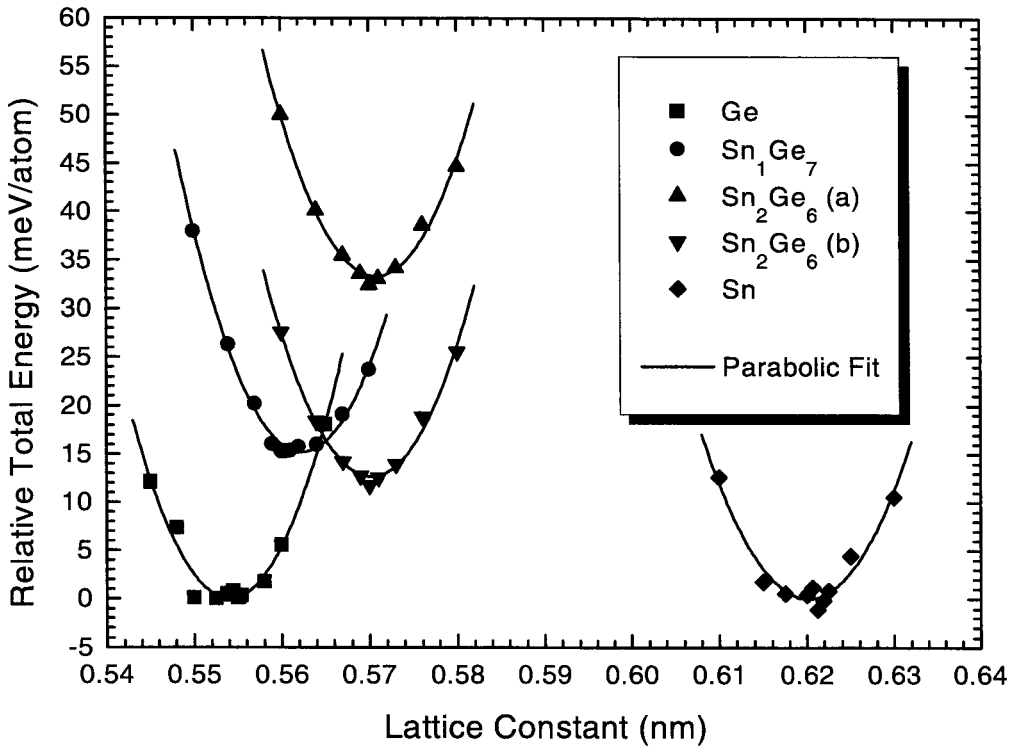

Figure 3.7 Calculated total energy as a function of cubic lattice constant for various Sn_xGe_{1-x} alloy compositions relative to the minimum total energies of pure diamond-cubic germanium and tin.

Alloy Configuration	Ge	Sn_1Ge_7	Sn_2Ge_6(a)	Sn_2Ge_6(b)	Sn
Sn Concentration, x	0	0.125	0.250	0.250	1
Order Parameter, r	N/A	1 / 7	0	1 / 3	N/A
Lattice Constant (nm)	0.554	0.562	0.571	0.570	0.620
Bulk Modulus (GPa)	77.6	76.7	71.1	71.0	53.1
H_{mix} (meV)	0	15.2	33.3	12.6	0
S_{mix} (meV/K)	0	0.0325	0.0485	0.0485	0
Super-Cell Bond (nm)	0.240	0.244	0.247	0.247	0.269
Ge-Ge Bond (nm)	0.240	0.241	0.243	0.243	N/A
Sn-Sn Bond (nm)	N/A	N/A	0.259	N/A	0.269
Ge-Sn Bond (nm)	N/A	0.249	0.251	0.251	N/A
Ge-Ge-Ge Angle (°)	109.5	110.7	116.5	116.9	109.5

Table 3.1 Summary of the density functional theory calculations for $Sn_{1-x}Ge_x$, including alloy configuration, average tin concentration (x), short-range order parameter (r), overall cubic lattice constant, bulk elastic modulus, enthalpy of mixing (H_{mix}), configurational entropy of mixing for random alloys of the same composition (S_{mix}), overall nearest-neighbor bond length of the super cell, average Ge-Ge nearest-neighbor bond length, average Sn-Sn nearest-neighbor bond length, average Ge-Sn nearest-neighbor bond length, and Ge-Ge-Ge bond angle where the center Ge atom is a nearest neighbor of a Sn atom in case of alloys.

The calculations suggested a positive enthalpy of mixing for Sn_xGe_{1-x} alloys relative to the decomposed phases of pure germanium and tin, indicating that Sn_xGe_{1-x} alloys are thermodynamically metastable relative to phase separation. This is consistent with the binary phase diagram of Sn_xGe_{1-x}. However, it is interesting to note that the calculated enthalpy of mixing is of the order of room temperature thermal energy, suggesting that the thermodynamic metastability of Sn_xGe_{1-x} alloys with respect to phase separation is quite small, especially considering that at nonzero temperatures the contribution of the configurational entropy of mixing ($S_{mix} = -k\left[x\ln(x) + (1-x)\ln(1-x)\right]$) in the total free energy of the system for random alloys is always energetically in favor of alloy mixing (against phase separation).

The calculated cubic lattice constants at total energy minimum for pure diamond-cubic germanium and tin are 0.554 nm and 0.620 nm, which are in good agreement with the expected values of 0.563 nm and 0.648 nm (low temperatures), respectively. The calculated total energy as a function of lattice constant yielded bulk elastic moduli of 77.1 GPa and 53.1 GPa for pure germanium and tin, which are in good agreement with the experimental values of 78 GPa and 53 GPa (room temperature), respectively. The calculated lattice constants as a function of the alloy composition are within 0.06% of the predictions from Vegard's law using the calculated lattice constants for pure diamond-cubic germanium and tin (Figure 3.8), indicating that Vegard's law is a good approximation for Sn_xGe_{1-x} alloys.

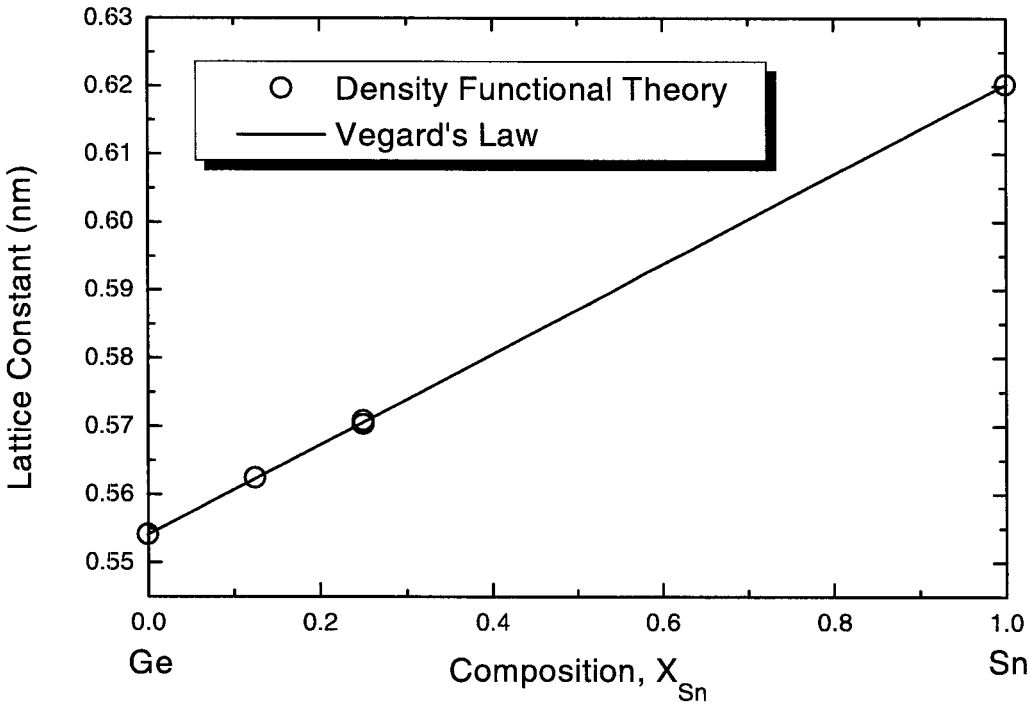

Figure 3.8 Calculated cubic lattice constant as a function of Sn_xGe_{1-x} alloy composition compared with Vegard's law.

On the other hand, the calculated nearest-neighbor bond lengths of the germanium-germanium, tin-tin, and germanium-tin bonds in the alloy configurations showed significant differences (up to 5%) from that of the virtual crystal approximation (Figure 3.9), suggesting that the local alloy structure deviates significant from the virtual crystal approximation. It is interesting to note that although the nearest-neighbor bond lengths deviate significantly (up to 5%)

from the virtual crystal approximation, the combination of the variations in both the bond lengths and bond angles produced overall cubit unit cell lattice parameters that are very well described (within 0.06%) by Vegard's law (Table 3.1). Similar effects have been observed in ternary $In_xGa_{1-x}As$ alloys experimentally [39].

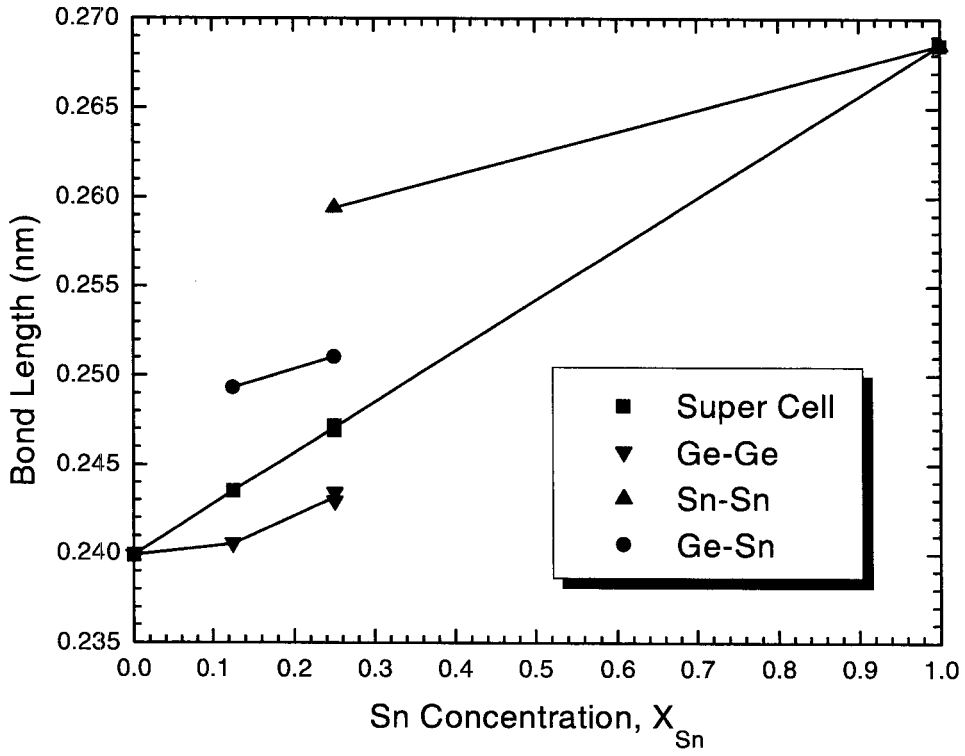

Figure 3.9 Calculated average nearest-neighbor bond length as a function of Sn_xGe_{1-x} alloy composition.

In summary, the calculations produced results for pure diamond-cubic germanium and tin that are in good agreement with the known experimental values of these materials. The calculations suggested the thermodynamic instability of the Sn_xGe_{1-x} alloys with respect to phase separation is relatively small (of the order of room temperature thermal energy). The calculations also suggested that, while the overall lattice constant of the Sn_xGe_{1-x} alloys can be described by Vegard's law quite well, the local structures (including bond lengths and angles) of the Sn_xGe_{1-x} alloys have significant deviations from the virtual crystal approximation as a result of alloy disorder.

3 .5 Conventional Molecular Beam Epitaxy

The growth of Sn_xGe_{1-x} alloy films by conventional molecular beam epitaxy were performed in a custom-designed molecular beam epitaxy system. The system is pumped by a 1600 l/sec cryopump and has a base pressure of about 3×10^{-10} Torr. A 30 keV reflection high energy electron diffraction (RHEED) system was used for *in situ* surface analysis. High purity (99.9999%) germanium and tin solid sources were used for deposition by electron beam evaporation and Knudsen effusion, respectively. The film thickness and deposition rate were controlled by quartz crystal thickness monitors. The substrate temperature was measured by a thermocouple attached to the side of the substrate holder. Note that while the substrate temperature measurements are consistent for samples grown in the same

system, the absolute value of the measured temperature may have a systematic error from the true temperature due to a possible temperature nonuniformity in the substrate holder. The temperature nonuniformity is usually small at low temperatures since the heat loss through radiation is small.

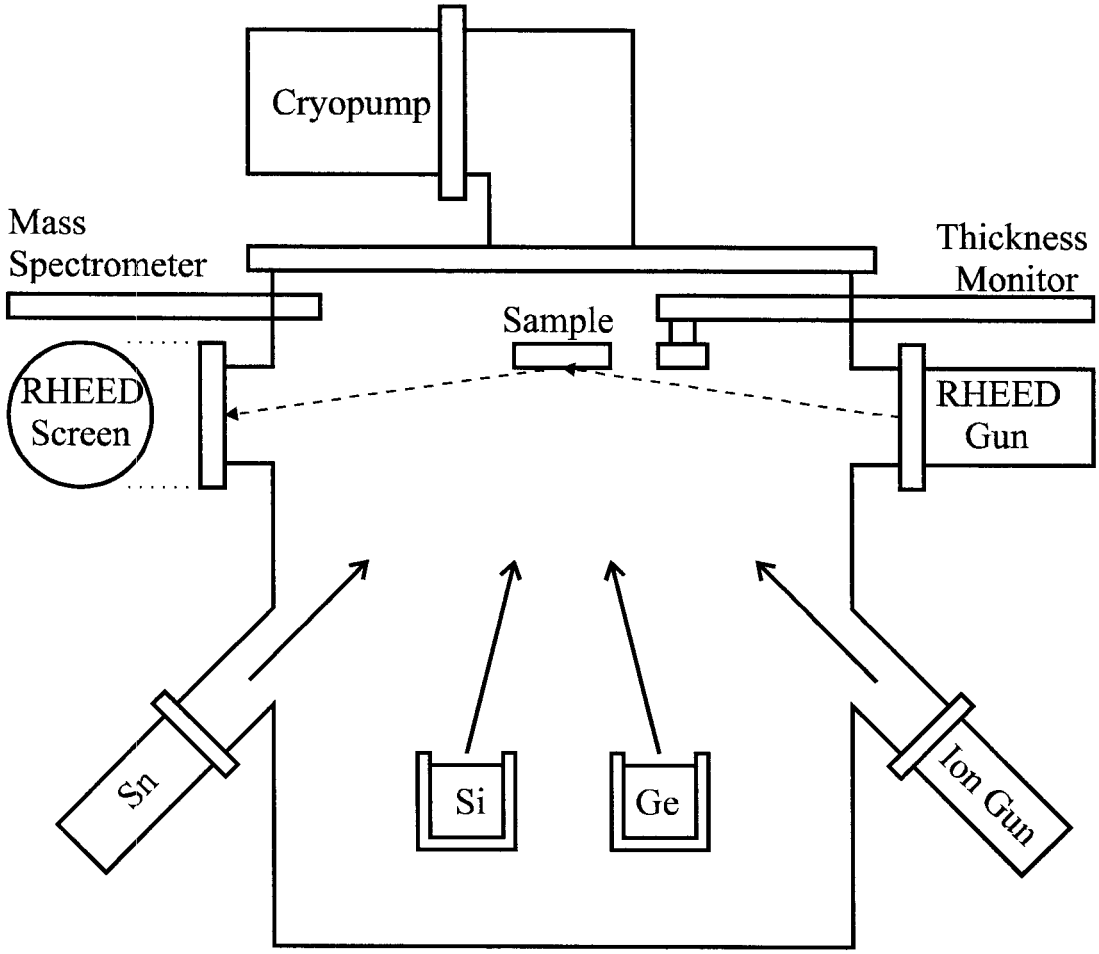

Figure 3.10 Schematic of the Sn_xGe_{1-x} molecular beam epitaxy system.

The substrates for Sn_xGe_{1-x} growth were Si (100) wafers and were chemically cleaned (in H_2O: H_2O_2:NH_4HNO_4 5:1:1 for 10 min) and hydrogen terminated (by dipping in 10% HF/H_2O) prior to being transferred into the ultrahigh vacuum deposition chamber. Following an *in situ* prebake at 200°C for 2 hours, the substrates were heated to 550°C to desorb the surface hydrogen and produce a (2×1) reconstructed clean Si (100) surface. Epitaxial Ge buffer layers of 50 to 100 nm were then deposited at 400°C to 450°C (without silicon buffer layers). The finished Ge buffer layer surfaces were also (2×1) reconstructed and smooth (as judged qualitatively by *in situ* reflection high energy electron diffraction). The substrates were then cooled to temperatures ranging from 120°C to 200°C and Sn_xGe_{1-x} layers were deposited at growth rates of about 0.05 nm/sec. *In situ* reflection high energy diffraction patterns along the (011) direction were recorded throughout growth by video data acquisition. Samples were characterized following growth by optical microscopy, Rutherford backscattering spectroscopy with 2 MeV He^{++}, high resolution x-ray diffraction with Cu-$K_{\alpha 1}$ x-ray, and transmission electron microscopy.

3 .5 .1 Growth of Sn_xGe_{1-x} Alloy Films

Sn_xGe_{1-x} alloy films with nominal tin concentrations ranging from x=0.1 to x=0.4 were grown by conventional molecular beam epitaxy at substrate temperatures of 120°C and 200°C. At 120°C growth temperature, Sn_xGe_{1-x} alloy

films with tin concentrations ranging from x=0.2 to x=0.3 were grown at growth rates ranging from 0.03 nm/sec to 0.05 nm/sec. During the growths of all the samples, *in situ* reflection high energy electron diffraction pattern turned spotty within 2 ~ 5 nm of alloy film growth and then amorphous after 5 ~ 10 nm of growth, indicating a breakdown of epitaxy (Figure 3.11). Optical microscopy showed that all the sample surfaces were optically clear (Figure 3.12).

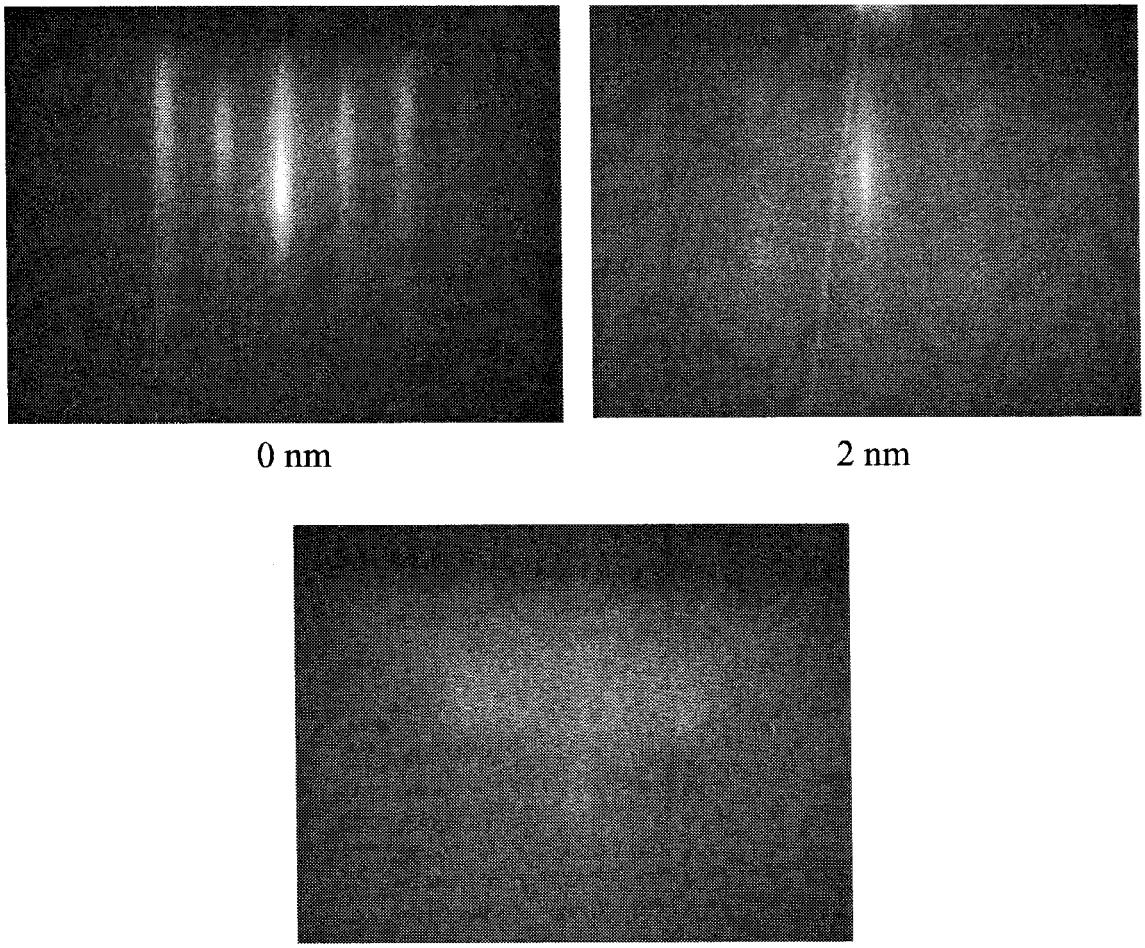

Figure 3.11 Evolution of reflection high energy electron diffraction pattern during the growth of $Sn_{0.25}Ge_{0.75}$ / Ge (100nm) / Si by conventional molecular beam epitaxy at 120°C.

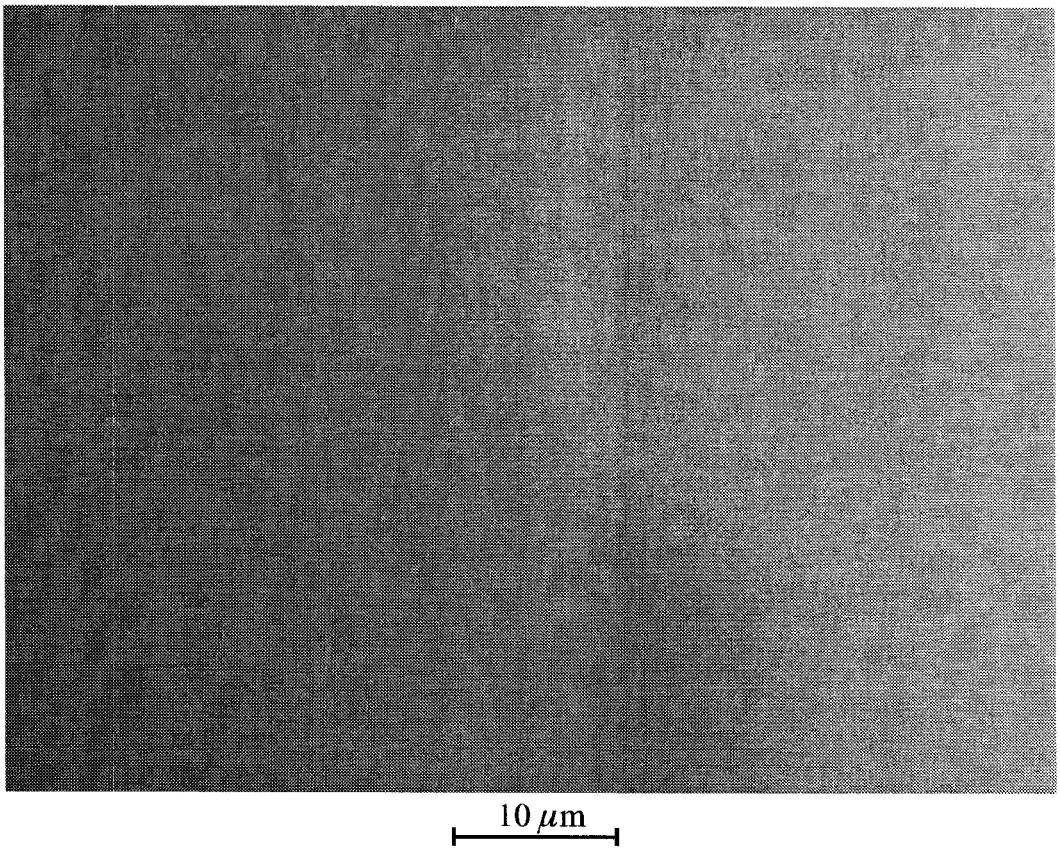

Figure 3.12 Optical micrograph of the sample surface of $Sn_{0.25}Ge_{0.75}$ (60nm) / Ge (100nm) / Si grown by conventional molecular beam epitaxy at 120°C.

At 200°C growth temperature, Sn_xGe_{1-x} alloy films with tin concentrations ranging from x=0.1 to x=0.3 were grown at growth rates of 0.05 nm/sec. During the growth of all the samples, *in situ* reflection high energy electron diffraction pattern turned spotty within 5 nm of film growth, indicating an atomically rough surface. The diffraction pattern stayed epitaxial with constant intensity throughout the growth for samples with tin concentrations of up to x=0.2. When the tin concentration is larger than x=0.2, however, the Bragg rod and Bragg spot

intensities in the diffraction pattern decreased continuously throughout the growth, suggesting a corresponding decrease of the total epitaxial area on the surface. For example, during the growth of a sample with four consecutive Sn_xGe_{1-x} alloy layers with tin concentrations of x=0.10 (60nm), x=0.15 (60nm), x=0.20 (60nm), and x=0.25 (50nm) on a 110 nm germanium buffer layer on silicon substrate, the *in situ* reflection high energy electron diffraction pattern was spotty throughout the growth of the alloy layers, with approximately constant diffraction intensity in the first three layers (up to x=0.20) and gradually decreasing diffraction intensity in the fourth layer (x=0.25) (Figure 3.13).

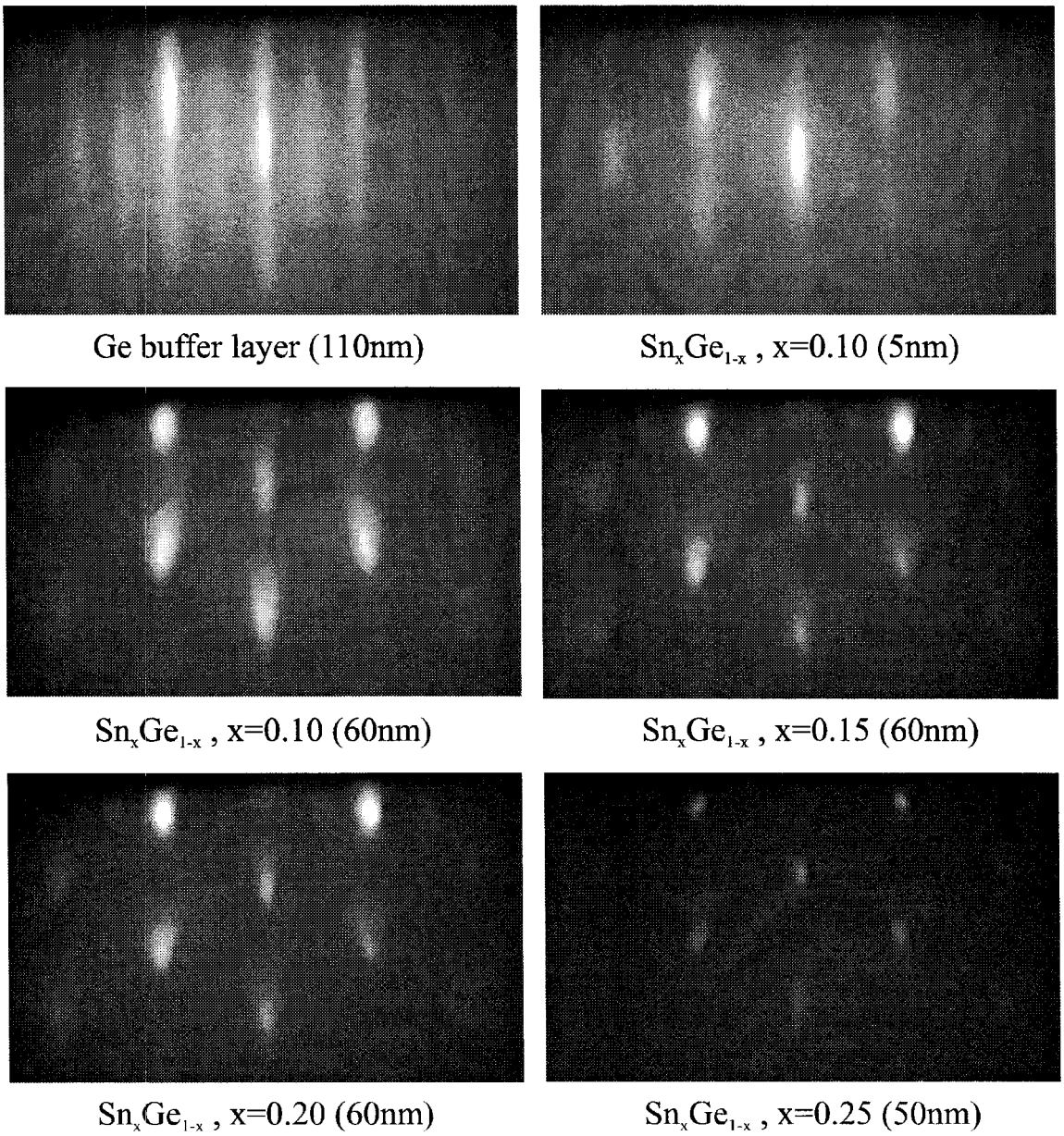

Figure 3.13 Evolution of reflection high energy electron diffraction pattern during the growth of $Sn_{0.25}Ge_{0.75}$ / $Sn_{0.20}Ge_{0.80}$ / $Sn_{0.15}Ge_{0.85}$ / $Sn_{0.10}Ge_{0.90}$ / Ge / Si by conventional molecular beam epitaxy with alloy layers grown at 200°C.

Optical microscopy of the samples grown at 200°C showed that the sample surfaces were optically clear for tin concentrations of up to x=0.2, and the sample surfaces were optically rough and covered with islands for tin concentrations larger than x=0.2. For example, due to the small nonuniformity of the tin growth flux across the wafer (since the tin source is oriented 45° toward the substrate), one sample with tin concentration close to x=0.2 showed two regions of both optically clear and rough surfaces with a relatively small transition region (about 5 mm) (Figure 3.14), and the exact tin concentration of these two regions were determined later by Rutherford backscattering to be x=0.20 and x=0.22, respectively. The transition from optically clear to optically rough regions occurred along the direction of the tin source, indicating that the transition was a result of nonuniformity of the tin growth flux. It is interesting to note that the islands on the optically rough surfaces can be easily scratched off by plastic tweezers, leaving a trace of scratch mark with a lump at the end (Figure 3.15). The lump may be a result of the accumulation of the island material that is scratched off from the trace. This suggests that the islands are mechanically soft and do not have very good adhesion to the sample surface. Also notice that thicker alloy films result in larger islands (Figure 3.15), indicating a growth of the islands during the alloy film growth. These observations are consistent with the assumption that the islands may be tin rich material formed as a result of accumulation of surface segregation of tin during the growth.

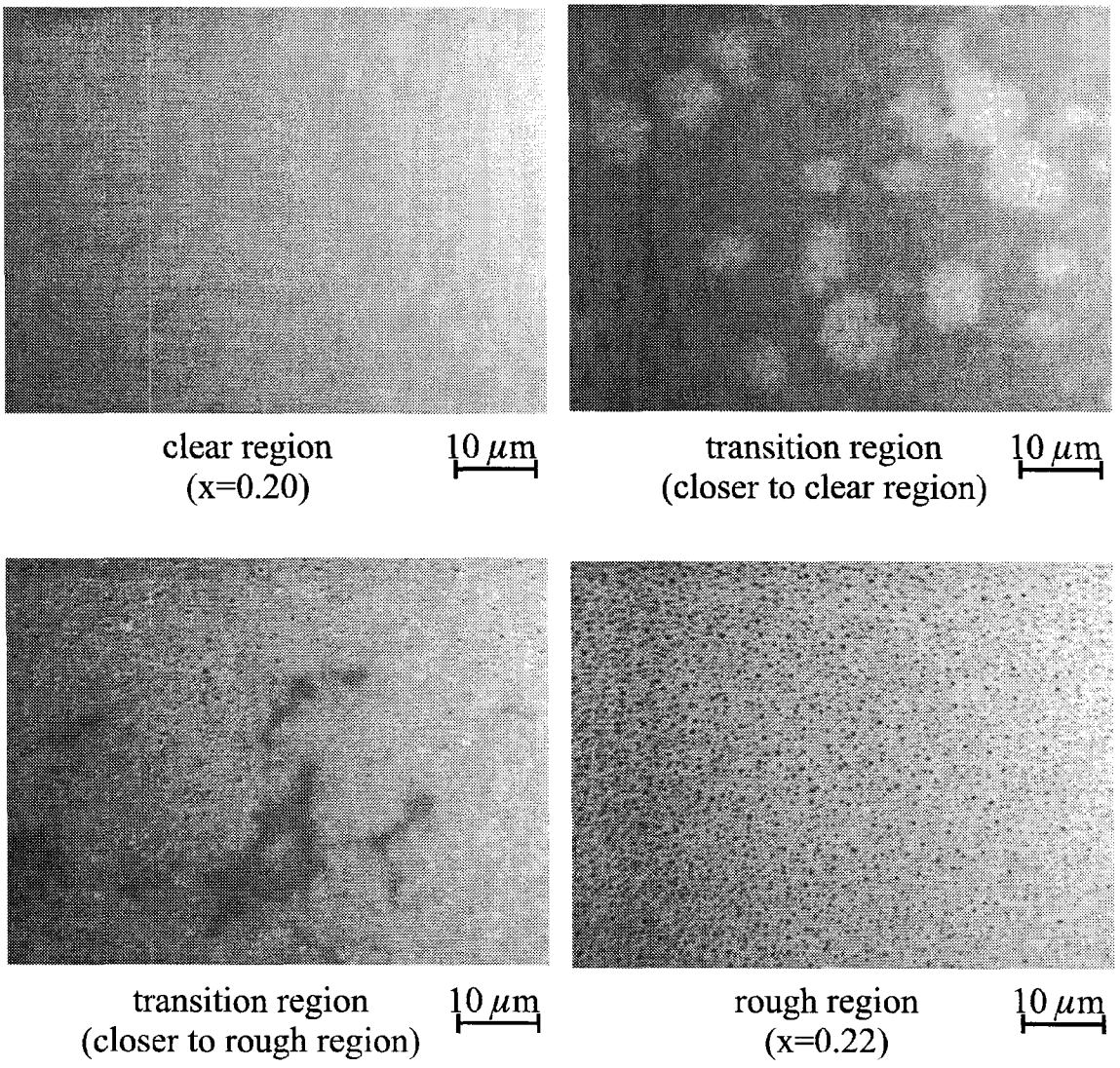

Figure 3.14 Optical micrograph of transition from optically clear surface region (x=0.20) to optically rough (with islands) surface region (x=0.22) across a distance of approximately 5 mm on a Sn_xGe_{1-x} (60 nm) sample grown by conventional molecular beam epitaxy at 200°C.

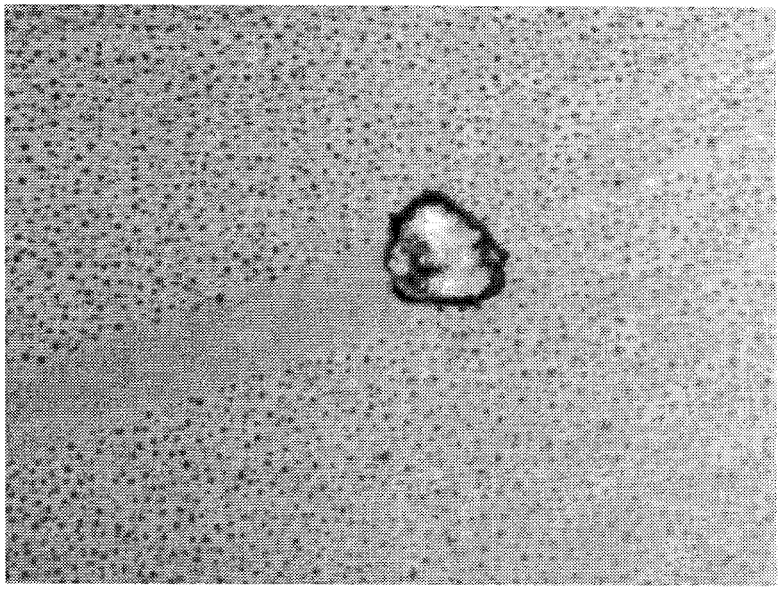

Figure 3.15 Optical micrograph of optically rough Sn_xGe_{1-x} sample surfaces after being scratched by plastic tweezers.

Scanning electron microscopy revealed that the optically rough sample surfaces also contained islands smaller than the resolution limit of the optical microscope (Figure 3.16), while the optically clear sample surfaces were free of islands within the resolution limit of the scanning electron microscope (which was about 10 nm). Energy dispersive spectroscopy (EDS) analysis showed that the islands were much more tin rich than the normal surfaces, although quantitative results were difficult to obtain in this case because the penetration volume of the electron beam (a few microns) was much larger than the island size and film thickness. These results indicated that the islands are results of accumulation of surface segregation of tin.

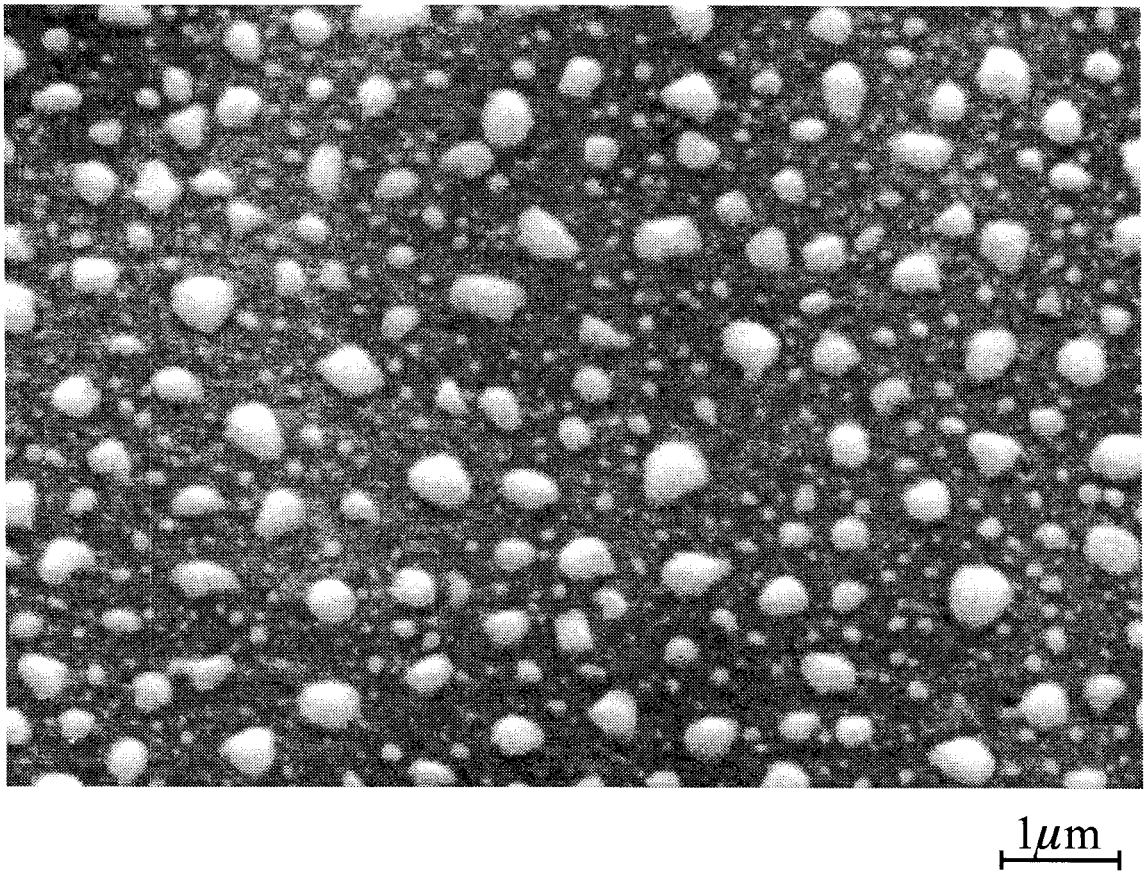

Figure 3.16 Scanning electron micrograph of the sample surface of Sn_xGe_{1-x} (60nm) / Ge (55nm) / Si grown by conventional molecular beam epitaxy at 200°C with nominal tin concentration of $x \approx 0.22$.

Rutherford backscattering indicated uniform alloy composition profile without surface segregation for samples with tin concentrations up to x=0.2 (Figure 3.17), and strong surface segregation of tin for tin concentrations larger than x=0.2 (Figure 3.18). The gradually decreasing tail of the tin signal and the gradually increasing germanium signal in the backscattering spectra of samples

with tin concentrations larger than x=0.2 are results of tin surface segregation and lateral composition nonuniformity as a result of island formation. The backscattering results of uniform and segregated alloy films correlate with the optical microscopy results of optically clear and rough surfaces very well. High resolution x-ray diffraction of the Sn_xGe_{1-x} samples showed that the uniform alloys films are epitaxial and diamond-cubic, and the diffraction peak intensity and peak width from the Sn_xGe_{1-x} alloy films are similar to those of the germanium reference films of similar thickness grown by conventional molecular beam epitaxy at 450°C on silicon (100) substrates (Figure 3.19). The x-ray diffraction peak locations are consistent with alloy lattice constants calculated from the alloy compositions measured by Rutherford backscattering assuming Vegard's law.

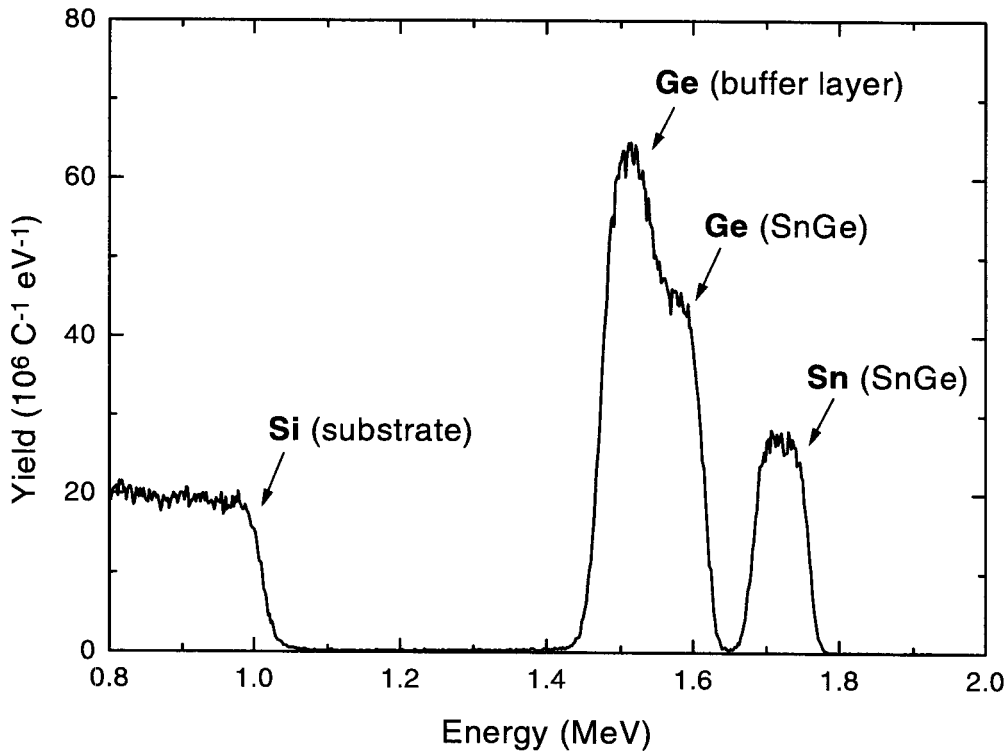

Figure 3.17 Rutherford backscattering spectrum of an epitaxial $Sn_{0.20}Ge_{0.80}$(58nm) / Ge(55nm) / Si(100) sample grown by conventional molecular beam epitaxy at 200°C.

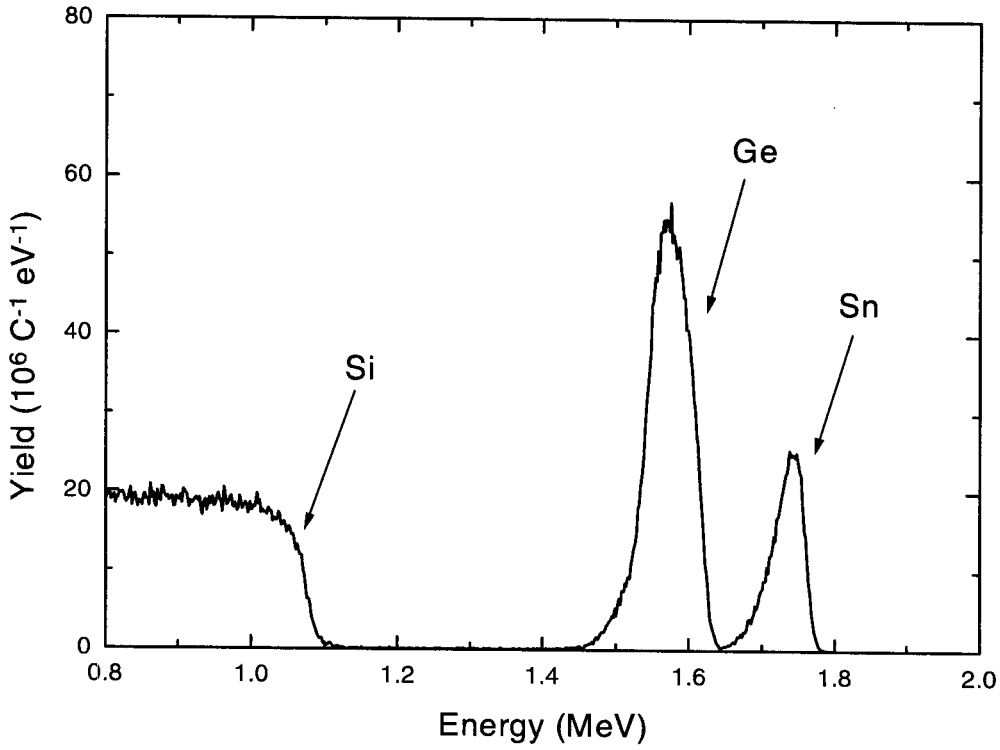

Figure 3.18 Rutherford backscattering spectrum of a Sn_xGe_{1-x}(60nm) / Ge(55nm) / Si(100) sample with a nominal tin concentration of x=0.22 grown by conventional molecular beam epitaxy at 200°C.

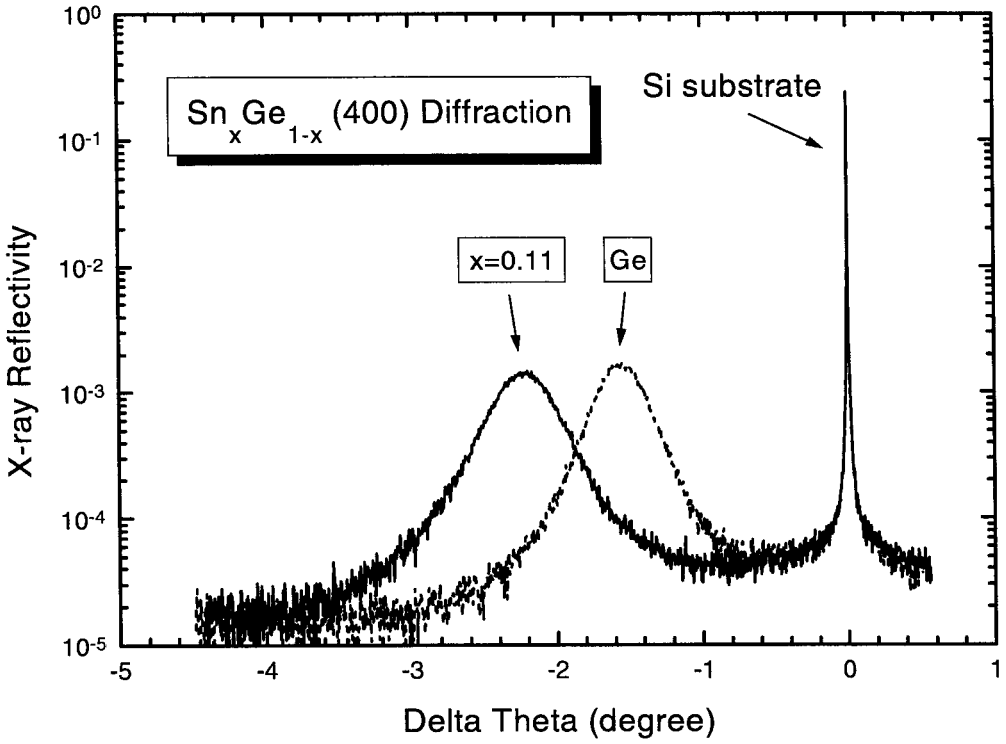

Figure 3.19 High-resolution x-ray diffraction of $Sn_{0.11}Ge_{0.89}$ (330nm) / Ge (10nm) / Si (100) compared with that of Ge (330nm) / Si (100), both grown by conventional molecular beam epitaxy at 200°C.

It is also interesting to note an unusual surface morphology observed on one $Sn_{0.18}Ge_{0.88}$ sample. During the growth of the sample there was a hot spot of approximately 2 mm size on the sample surface which appeared red hot during the growth of germanium buffer layer at 500°C. The hot spot may be a result of contamination on the molybdenum substrate holder block resulting in more

efficient thermal conduction at that spot relative to the other parts of the block. The sample has a 5 nm germanium buffer layer grown at 500°C, and then another 5 nm germanium buffer grown at 190°C, followed by a 20 nm $Sn_{0.18}Ge_{0.88}$ layer grown at 190°C. All the layers were grown at 0.05 nm/sec. Optical microscopy of the resulting sample showed an overall optically clear surface except at the location of the hot spot where segments preferentially oriented along the two orthogonal (011) directions were observed (Figure 3.20). The exact origin of these segments are not yet clear. *In situ* reflection high energy electron diffraction showed that all the layers were epitaxial with atomically rough surfaces (Figure 3.21), although most of the diffraction did not come from the small hot spot area. The hot spot may have raised the local growth temperature significantly above the overall sample temperature during the growth of the germanium buffer layers as well as the $Sn_{0.18}Ge_{0.88}$ alloy layer. One possibility is that the higher local growth temperature may locally enhance strain relaxation and tin diffusion, which may in turn generate extended structural and compositional defect (such as facets and dislocations). However, it is still unknown whether (and how) the observed segments in the hot spot correlate with such extended defects.

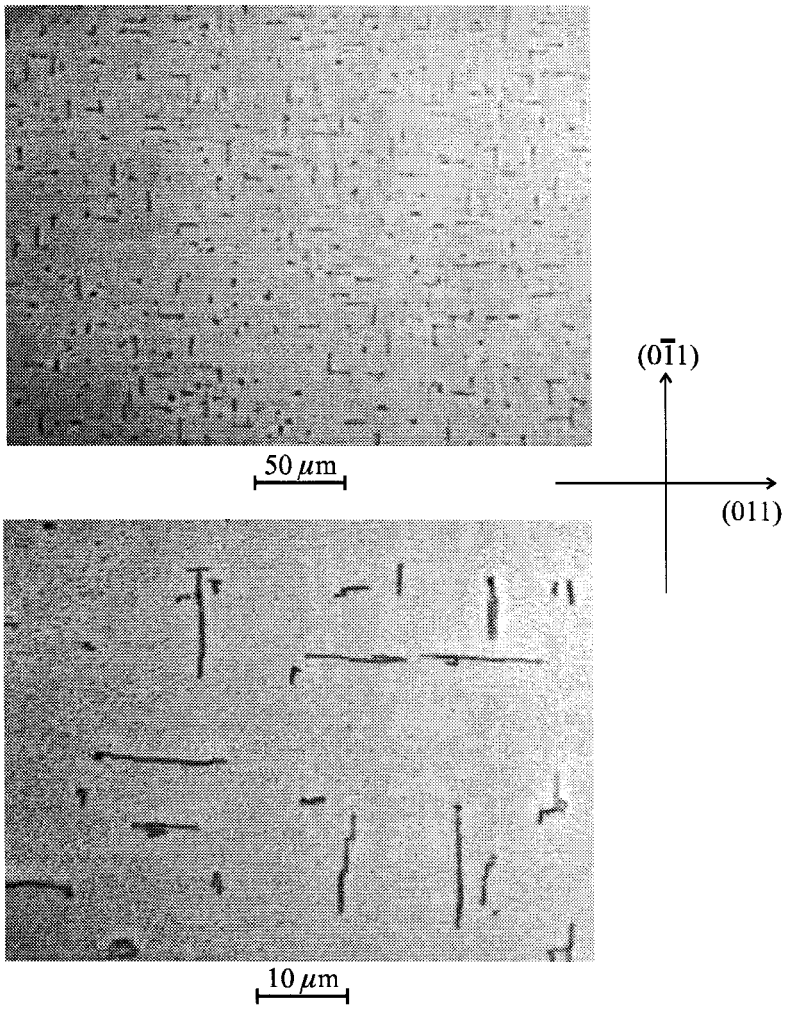

Figure 3.20 Optical microscopy of an area of hot spot on a $Sn_{0.18}Ge_{0.88}$ (20nm) / Ge (10nm) / Si (100) sample grown by conventional molecular beam epitaxy.

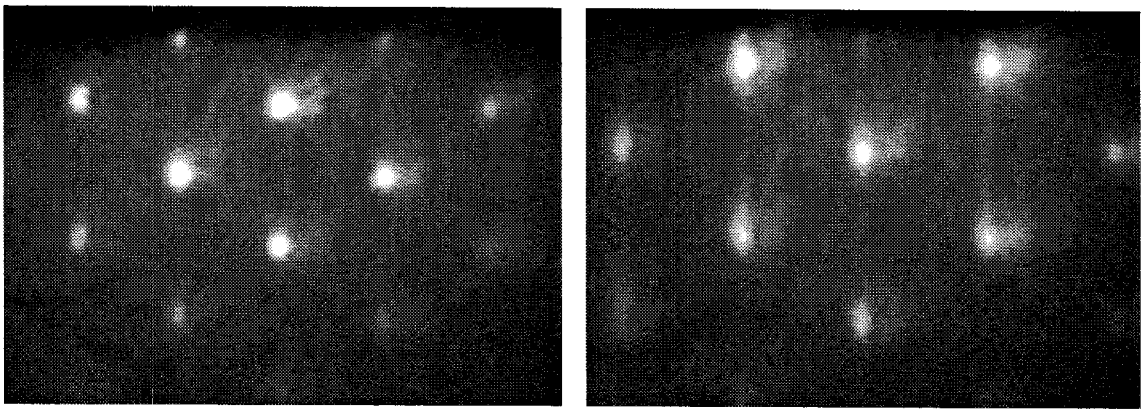

Ge buffer layer (5nm) Ge buffer layer (10nm)

$Sn_{0.18}Ge_{0.88}$ (20nm)

Figure 3.21 Evolution of reflection high energy electron diffraction pattern during the growth of $Sn_{0.18}Ge_{0.88}$ (20nm) / Ge(10nm) / Si (100) by conventional molecular beam epitaxy with alloy layers grown at 200°C.

3 .5 .2 Growth of $Ge/Sn_xGe_{1-x}/Ge$ Quantum Wells

Conventional molecular beam epitaxy was also used to study the growth of $Ge/Sn_xGe_{1-x}/Ge$ quantum-well structures. The growths were performed at substrate temperatures 120°C with growth rates of 0.05 nm/sec. Two quantum well samples were grown with quantum well thicknesses of 2 nm and 5 nm with nominal tin concentrations of x=0.4 to x=0.5. *In situ* reflection high energy electron diffraction pattern disappeared within about 0.5 nm growth of Sn_xGe_{1-x} layers for both samples, suggesting that the sample surfaces may be covered almost completely by segregated tin. During the subsequent growths of the germanium cap layer, the diffraction pattern slowly recovered with weak intensity after about 10 to 20 nm of the germanium cap layer growth, suggesting that epitaxy may still occur with the strongly segregated surface tin layers. The weak diffraction intensity indicated that the surfaces were not completely epitaxial. Optical microscopy indicated that the final sample surfaces were optically rough for both samples (Figure 3.22), which is consistent with a local breakdown of epitaxy as a result of island formation from the tin surface segregation during growth. These results suggest that tin surface segregation alone may not directly result in epitaxial breakdown. Instead, the breakdown of epitaxy may occur locally as a direct consequence of surface tin island formation which follows the surface segregation of a planar layer of tin. The results also suggest that the disappearance of Bragg rod and Bragg Spot diffraction features in the reflection high energy electron diffraction alone does not necessarily indicate a complete breakdown of epitaxial growth as evidenced by the recovery of the Bragg features in the diffraction pattern with germanium growth after the Sn_xGe_{1-x} alloy growth. However, once relatively large islands are formed on the film surface, complete epitaxial growth can not be recovered even if the

subsequent layer is pure germanium. Therefore, to achieve complete epitaxial growth of Sn_xGe_{1-x} alloys, formation of large surface island must be suppressed throughout the growth of all layers. In addition to reflection high energy electron diffraction, analysis by optical microscopy, backscattering, and x-ray diffraction are required to confirm a complete epitaxial growth.

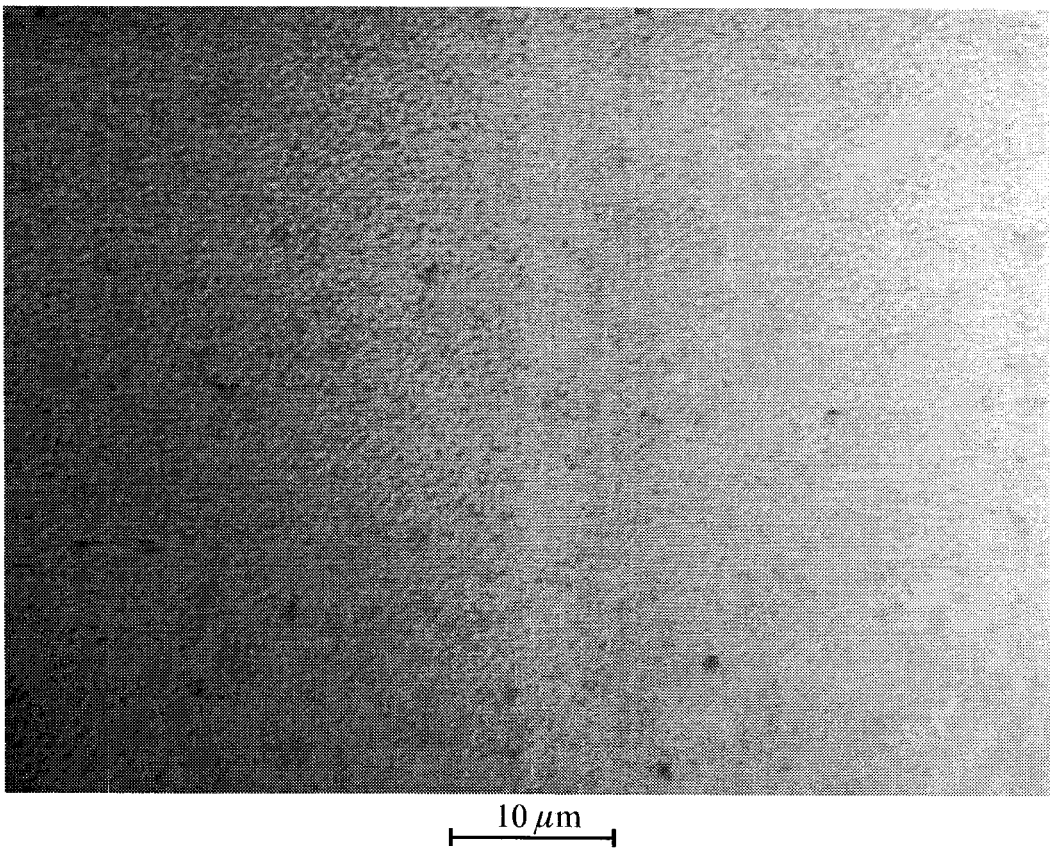

Figure 3.22 Optical micrograph of the sample surface of Ge (23nm) / Sn_xGe_{1-x} (2nm) / Ge (100nm) / Si grown by conventional molecular beam epitaxy at 120°C with nominal tin concentration of $x \approx 0.4$.

3 .5 .3 Summary of Conventional Epitaxial Growth

Epitaxial Sn_xGe_{1-x} alloy films can be grown by conventional molecular beam epitaxy with tin concentrations up to about x=0.2. At higher tin concentrations, epitaxy of the alloy films broke down either through a crystal to amorphous transition at low temperatures or through a severe surface segregation at high temperature. These results are consistent with the previous works on the molecular beam epitaxy of Sn_xGe_{1-x} [17]. The surface segregation of tin leads to island formation and growth which directly cause the local breakdown of epitaxy. Such surface segregation and island formation are indicated by a weak and decreasing reflection high energy electron diffraction pattern, a segregated Rutherford backscattering spectrum, or an optically rough surface by optical microscopy. Notice that the observation of surface islands by optical microscopy is limited by the sensitivity limit of optical microscopy. The island size may be well below the sensitivity limit of the optical microscopy at the early stage of island formation, and the observation of such islands may require techniques such as scanning probe microscopy and scanning electron microscopy. For example, formation of tin islands on silicon (100) surfaces has been observed by scanning tunneling microscopy [40]. To overcome the limitations of any single analysis techniques, a combination of analyses, such as reflection high energy electron diffraction, Rutherford backscattering spectroscopy, surface optical microscopy,

and high-resolution x-ray diffraction, is required to confirm a complete epitaxial growth of Sn_xGe_{1-x} alloy films.

3 .6 Ion-Assisted Molecular Beam Epitaxy

In order to achieve epitaxial Sn_xGe_{1-x} alloys with higher tin concentrations, ion-assisted molecular beam epitaxy was used to suppress the surface segregation of tin during the alloy growth [2] [25]. When the growing surface of the alloy film is irradiated by low energy ions, the surface atoms undergo subsurface recoil-implantation and generate collisional mixing between the surface and subsurface layers, hence incorporate surface atoms into the growing film. The irradiating ion energy should be low enough to avoid extended damage to the bulk crystal [41], and the ion flux should be high enough to generate sufficient surface mixing effect [42] [43]. Suppression of segregation by collisional mixing through low energy ion irradiation has been used for dopant incorporation [44] and was also demonstrated in the sputter deposition of Sn_xGe_{1-x} [19].

The ion-assisted epitaxial growth was performed in the same molecular beam epitaxy system used for thermal growth. The system was equipped with both a Kaufman ion source and an electron cyclotron resonance ion source. The Kaufman ion source has a limited capability in ion flux (~ 1 $\mu A/cm^2$ at substrate) when the ion energy is below about 100 eV. The electron cyclotron resonance ion

source, on the other hand, is capable of delivering high flux (~ 0.1 mA/cm^2 at substrate) ion beams with low energies (less than 50 eV). Both ion sources were connected to a high-purity (99.9995%) argon gas source through a 20 sccm mass flow controller. Flow rates of 10 sccm to 20 sccm were used which introduced argon background pressures of the order of 10^{-4} Torr in the growth chamber. The substrate can be electrically biased relative to ground to alter the irradiating ion energy as well as to measure the ion current.

Silicon (100) substrates were cleaned by the same method used for thermal growth. Sn_xGe_{1-x} layers with tin concentration ranging from 0.2 to 0.4 were grown on germanium buffer layers at growth temperatures ranging from 150°C to 200°C with growth rates of about 0.05 nm/sec under ion irradiation. *In situ* reflection high energy diffraction patterns along the (011) direction were recorded throughout growth by video data acquisition. Samples were characterized following growth by optical microscopy, Rutherford backscattering spectroscopy with 2 MeV He^{++}, high resolution x-ray diffraction with Cu-$K_{\alpha 1}$ x-ray, and transmission electron microscopy.

3 .6 .1 Growth with Kaufman Ion Source

The Kaufman ion source operates by DC discharge ionization (Figure 3.23) and is suitable for high energy or low flux ion beams. An argon flow rate of

4 sccm was used which resulted in a argon background pressure of about 10^{-5} Torr. The Ar^+ ion energy used for the growth was about 80 eV and the ion flux was about 1 $\mu A/cm^2$ at substrate measured by the substrate current and averaged over the 3 inch substrate area. At a film growth rate of 0.05 nm/sec, such an ion flux corresponds to an ion-flux to growth-flux ratio of the order of 10^{-2}.

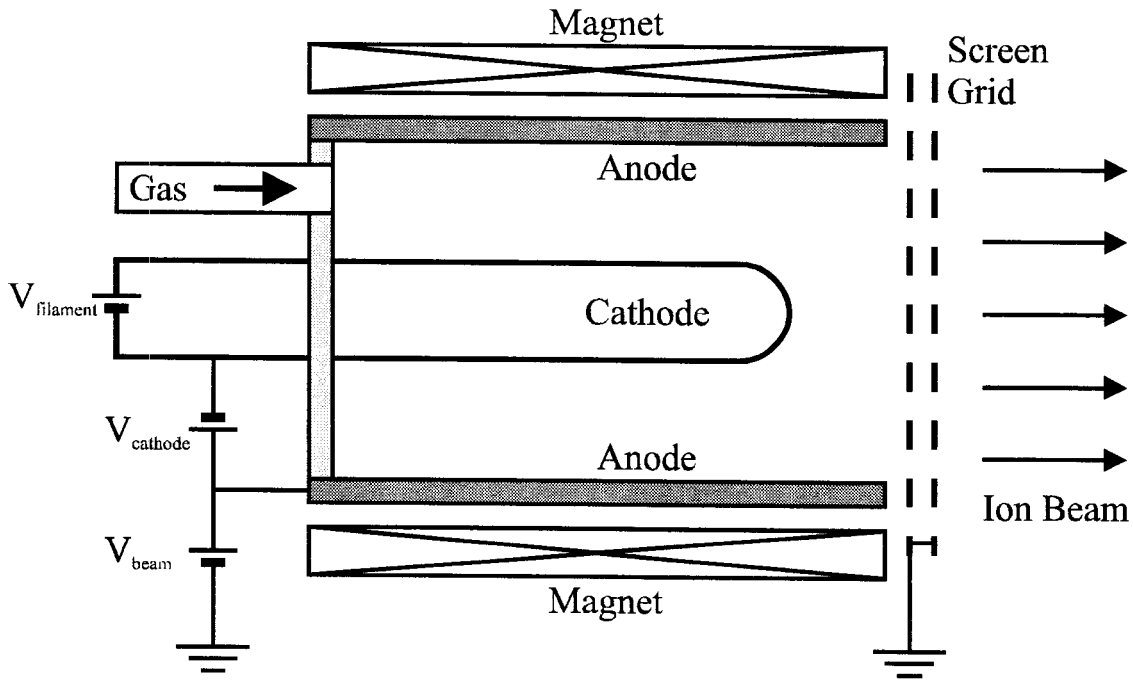

Figure 3.23 Schematic of the Kaufman ion source.

The Sn_xGe_{1-x} sample was grown at 150°C with a nominal tin concentration of x=0.30. During growth of the alloy layer the *in situ* reflection high energy electron diffraction pattern first turned spotty within 5 nm of film growth; then the diffraction intensity decreased continuously throughout the growth, suggesting a

corresponding decrease of the total epitaxial area on the surface. Optical microscopy unveiled optically rough sample surfaces covered with islands on the sample surface (Figure 3.24), and Rutherford backscattering indicated strong surface segregation of tin (Figure 3.25). These results are very similar to the results of thermal Sn_xGe_{1-x} growth at 200°C, suggesting that the ion flux from the Kaufman ion source is too low to sufficiently suppress the surface segregation of tin.

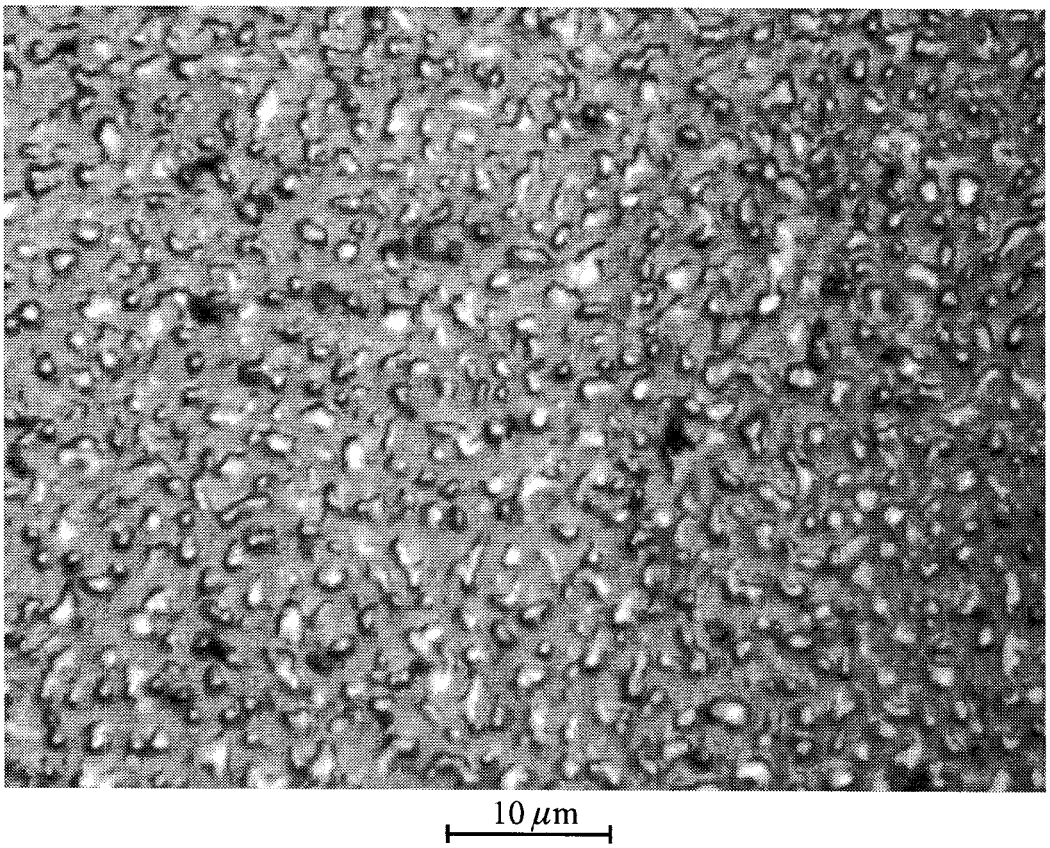

Figure 3.24 Optical micrograph of the sample surface of a Sn_xGe_{1-x}(200nm) / Ge(200nm) / Si(100) sample with a nominal tin concentration of x=0.30 grown by ion-assisted molecular beam epitaxy at 150°C with 80 eV Ar^+ from a Kaufman ion source, with an ion/atom flux ratio of the order of 10^{-2}.

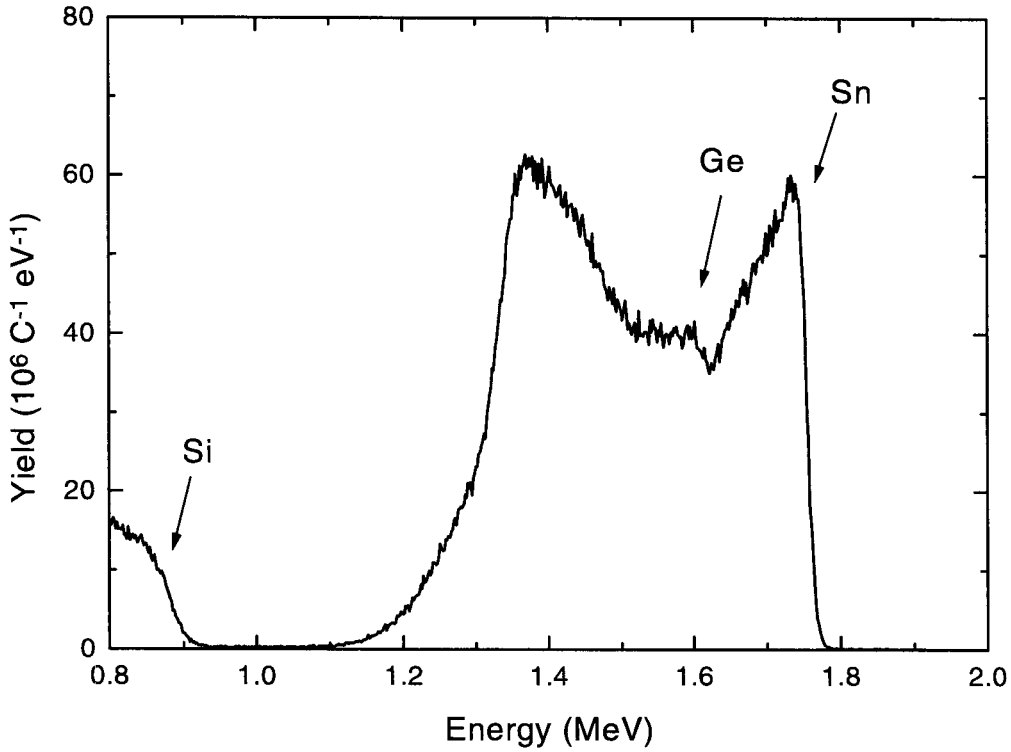

Figure 3.25 Rutherford backscattering spectrum of a Sn_xGe_{1-x}(200nm) / Ge(200nm) / Si(100) sample with a nominal tin concentration of 0.30 grown by ion-assisted molecular beam epitaxy at 150°C with Kaufman ion source.

3 .6 .2 Growth with Electron Cyclotron Resonance Ion Source

Electron cyclotron resonance ion sources operates by microwave-discharge ionization in electron cyclotron resonance mode (Figure 3.26) and are capable of generating high-flux (more than milliampere total) low-energy (less than 50 eV) ion beam at very low pressure (less than 10^{-4} Torr). The sources can also work at higher pressures (e.g., 10^{-3} Torr) in a downstream mode where the plasma can be sustained even without electron cyclotron resonance since the collision cross section is much higher at these higher pressures. The ion source is excited with 2.45 GHz right-hand circularly polarized microwave radiation with a 200 W maximum power. The ion source has an opening of about 5 cm diameter and was about 20 cm away from the substrate at a 45° angle. For electrically grounded substrates, the typical Ar^+ ion energy is in the range of 20 eV to 50 eV and the typical ion flux is about 0.05 mA/cm^2 (averaged over the 3 inch substrate area) at substrate. At a film growth rate of 0.05 nm/sec, such an ion flux corresponds to an ion-flux to growth-flux ratio of the order of unity. Note that the ion beam generated by the electron cyclotron resonance ion source is quasi-neutral, so that the ion current measured at the substrate is the total current of both ions and electrons. The ratio of measured ion current and electron flux depends on the bias voltage of the substrate. At large positive substrate bias the total current is dominated by the electron current, and at large negative substrate bias the total current is dominated by the ion current. The total ion current at substrate is measured by linearly extrapolating the voltage-dependent total current at large negative biases (-100 V to -200 V). The ion energy distribution as a function of the excitation microwave power was factory measured with an multi-grid ion energy analyzer and was supplied in the calibration data sheet of the ion source. The peak

ion energy ranges from 17 eV to 42 eV for microwave powers of 82 W to 164 W at a pressure of 3×10^{-4} Torr for argon, with a typical energy distribution of about 10 eV (full width half maximum).

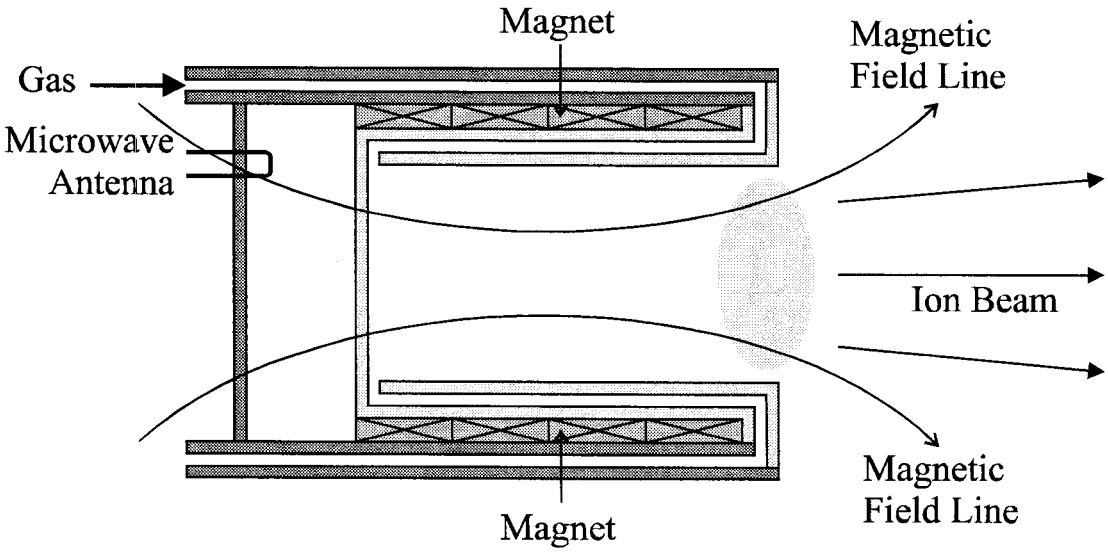

Electron cyclotron motion:

$\omega = e B / m$

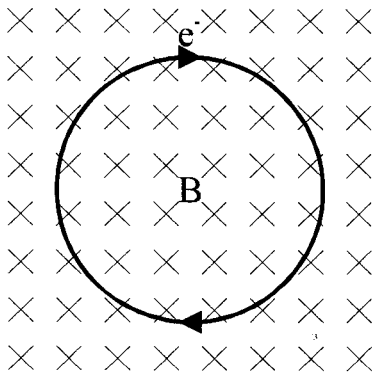

Figure 3.26 Schematic of the electron cyclotron resonance ion source.

Optimized operation of the electron cyclotron resonance ion source requires very fine tuning of the microwave resonant cavity in the ion source. The microwave excitation occurs in a tunable microwave resonant cavity which is mechanically adjusted with a micrometer to maximize absorption (or minimize reflection measured by a reflection power meter) of the microwave power. A very fine tuning is required at every operation of the ion source in order to obtain maximum ion current. Due to instabilities such as thermal drift of the microwave resonant cavity during the operation of the ion source, small adjustments of the cavity tuning are required during the operation in order to maintain optimum operation conditions. Such instabilities are usually indicated by a change in the reflected microwave power. The operation of the ion source also strongly depends on the operation pressure of the processing gas. The ion current in general increases with increasing operation pressure. When the operation pressure is less than about 10^{-3} Torr, the ion source operates in an electron cyclotron resonance mode where the excitation of the plasma is sustained by the electron cyclotron resonance. When the operation pressure is above about 10^{-3} Torr, the ion source operates in an non electron cyclotron resonance mode where the ionization cross-section in the gas phase is so large that the excitation of the plasma can be sustained even without electron cyclotron resonance. However, notice that the pressure measured by the ion gauge or mass spectrometer in the growth chamber reflect the background pressure of the chamber, which may be different from the local pressure at the ion source where the processing gas is introduced. The ion current density at the substrate also strongly depend on the down stream distance from the ion source to the substrate. A factor of 5 increase in ion current at

substrate was obtained when the ion source was moved from about 20 cm away from the substrate to about 5 cm away from the substrate.

A set of Sn_xGe_{1-x} samples with nominal tin concentrations in the range of x=0.3 to 0.4 were grown at 150°C substrate temperature with ion irradiation. The electron cyclotron resonance ion source was operated at 100 W microwave power with 10 sccm argon gas flow which resulted in an argon partial pressure of about 10^{-4} Torr. The substrates were electrically grounded during the growths. The irradiating ion flux was approximately 0.05 mA/cm^2, and the ion energy was approximately 30 eV. The growth rate of the alloy films were 0.05 nm/sec. During the ion-assisted growths, the ratio of the deposition rate at substrate to the deposition rate at the thickness monitor close to the germanium source was approximately half the normal value of conventional molecular beam epitaxy. This indicated a reduction of growth flux efficiency due to the gas-phase collisions between the growth flux and the argon background pressure. The *in situ* reflection high energy electron diffraction can be operated at pressures as high as 10^{-3} Torr since it was differentially pumped by a turbopump. The sharpness of the diffraction pattern degrades slightly at very high pressures, especially when the ion source is in operation. The i*n situ* reflection high energy electron diffraction during these Sn_xGe_{1-x} growth showed a gradual transition from surface roughening (at 10 nm film thickness) to twinning (at 20 nm film thickness) and eventually to polycrystalline transformation (at 50~100 nm film thickness) for tin concentrations less than x=0.35 (Figure 3.27). For tin concentrations larger than x=0.35, the diffraction intensity slowly decreased and eventually led to very low

diffraction contrast, which was similar to that of the conventional molecular beam epitaxy growth of Sn_xGe_{1-x} alloy films at 200°C when the tin concentrations were larger than x=0.2. The gradual decrease of diffraction intensity indicated a decrease of total epitaxial area, suggesting local breakdown of epitaxy during the growth.

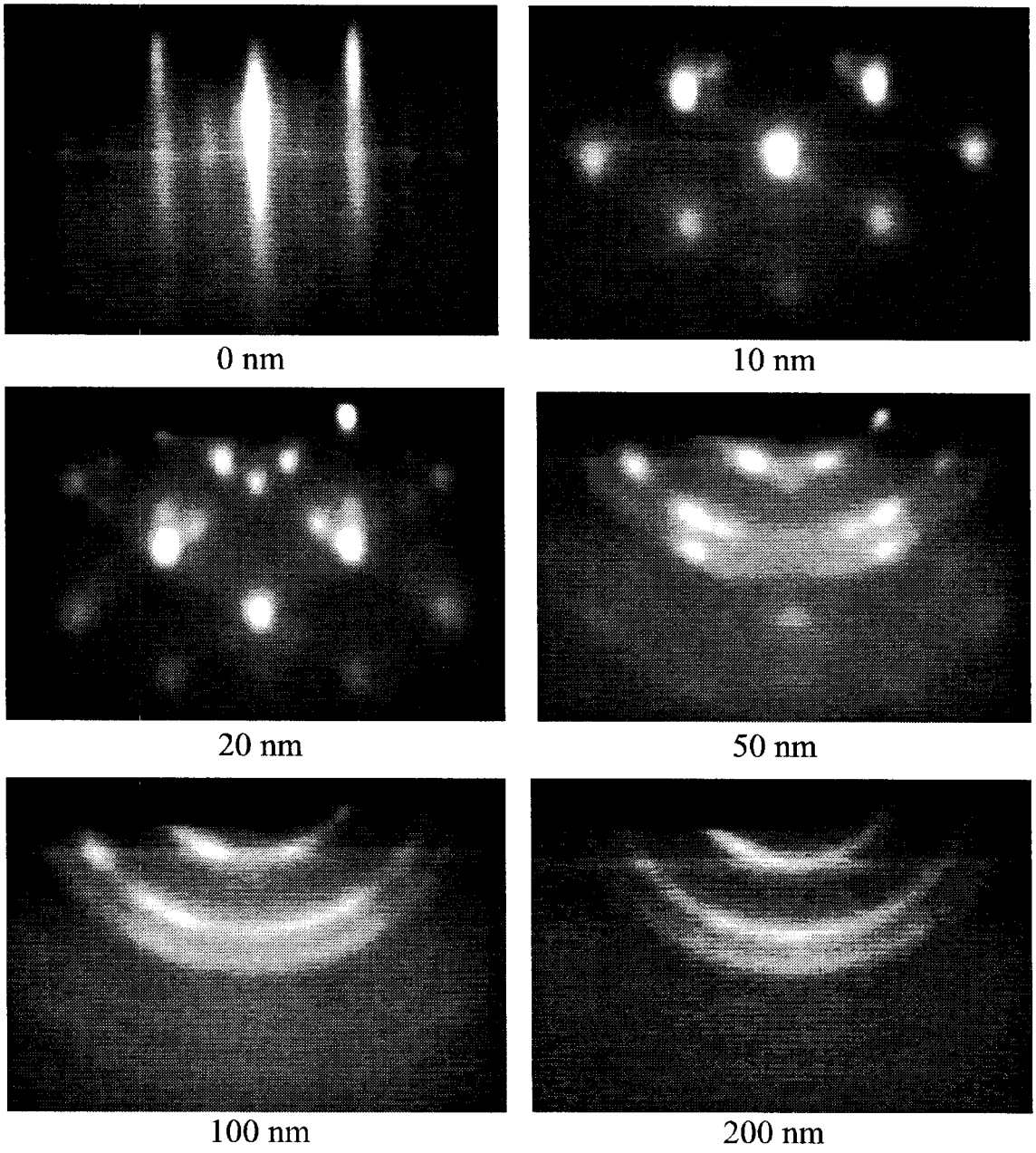

Figure 3.27 Evolution of reflection high energy electron diffraction pattern during growth of $Sn_{0.30}Ge_{0.70}$ by ion-assisted molecular beam epitaxy at 150°C with electron cyclotron resonance ion source.

Optical microscopy showed optically clear sample surfaces for tin concentrations of up to x=0.35 and optically rough sample surfaces covered with islands for tin concentrations larger than x=0.35. For example, due to the small nonuniformity of the tin growth flux across the wafer (since the tin source is oriented 45° toward the substrate), one sample with tin concentration close to x=0.35 showed two regions of both optically clear and rough surfaces with a relatively small transition region (about 5 mm) (Figure 3.28), and the exact tin concentration of these two regions were determined later by Rutherford backscattering to be x=0.34 and x=0.40, respectively. This was very similar to the observations of Sn_xGe_{1-x} samples grown by conventional molecular beam epitaxy at 200°C with tin concentrations close to x=0.2. The islands on the tin rich side of the sample are formed as a result of accumulation of surface-segregated tin. The formation and growth of these islands led to local breakdown of epitaxy, which was consistent with the decreasing intensity of reflection high energy electron diffraction as a result of a decreased fraction of film in which epitaxial growth occurred.

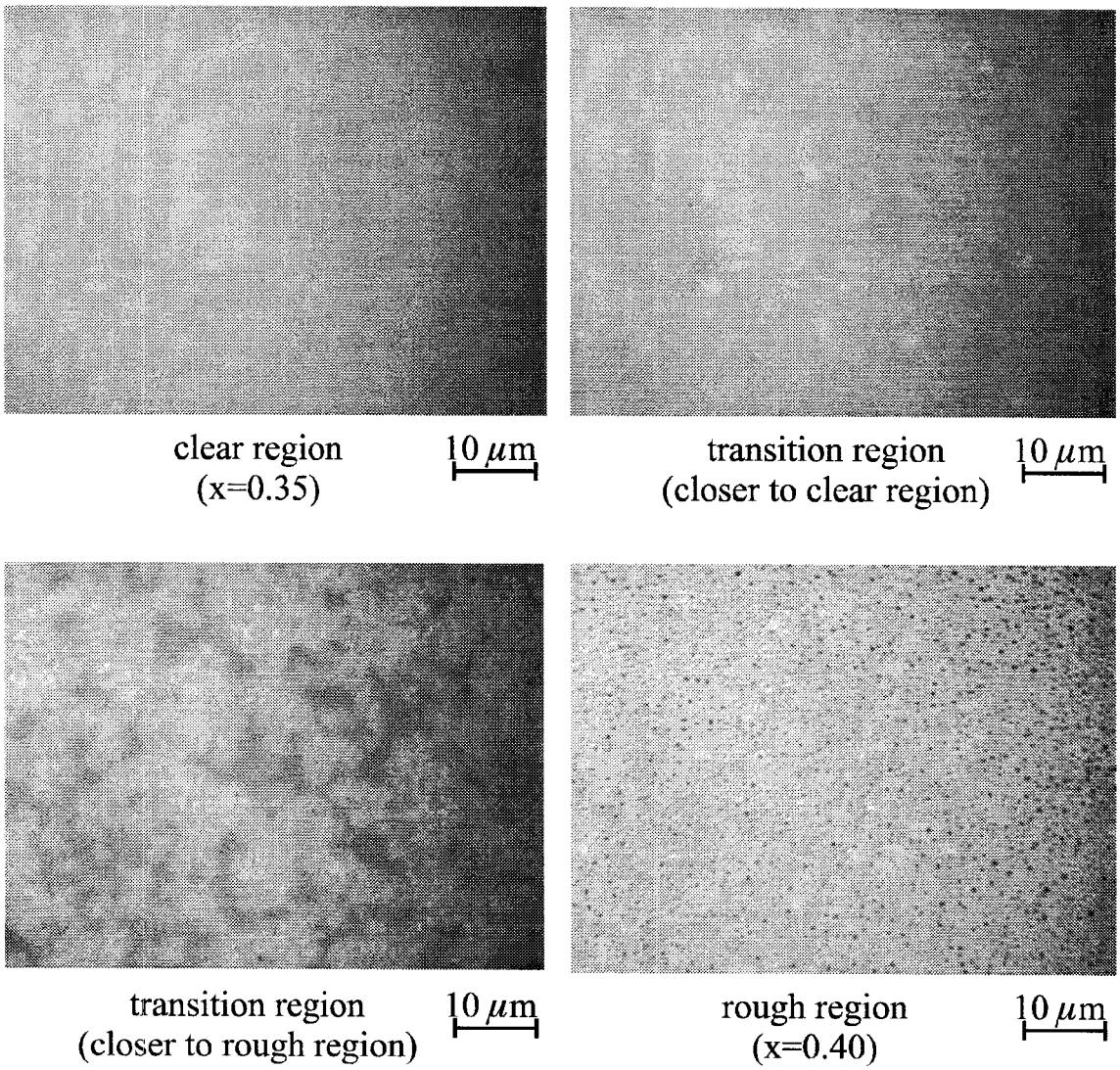

Figure 3.28 Optical micrograph of transition from optically clear surface region (x=0.34) to optically rough (with islands) surface region (x=0.40) across a distance of approximately 5 mm on a Sn_xGe_{1-x} (20 nm) sample grown by ion-assisted molecular beam epitaxy at 150°C.

The results of reflection high energy electron diffraction and surface optical microscopy were confirmed by Rutherford backscattering spectroscopy, which showed uniform alloy composition profile without surface segregation for tin concentrations up to x=0.35, including single crystal epitaxial $Sn_{0.34}Ge_{0.66}$ 23 nm thick (Figure 3.29) and polycrystalline $Sn_{0.30}Ge_{0.70}$ 250 nm thick (Figure 3.30). For tin concentrations larger than x=0.35, Rutherford backscattering showed strong surface segregation of tin (Figure 3.31), similar to that of conventional molecular beam epitaxy of Sn_xGe_{1-x} alloy films at 200°C when the tin concentrations were larger than x=0.2.

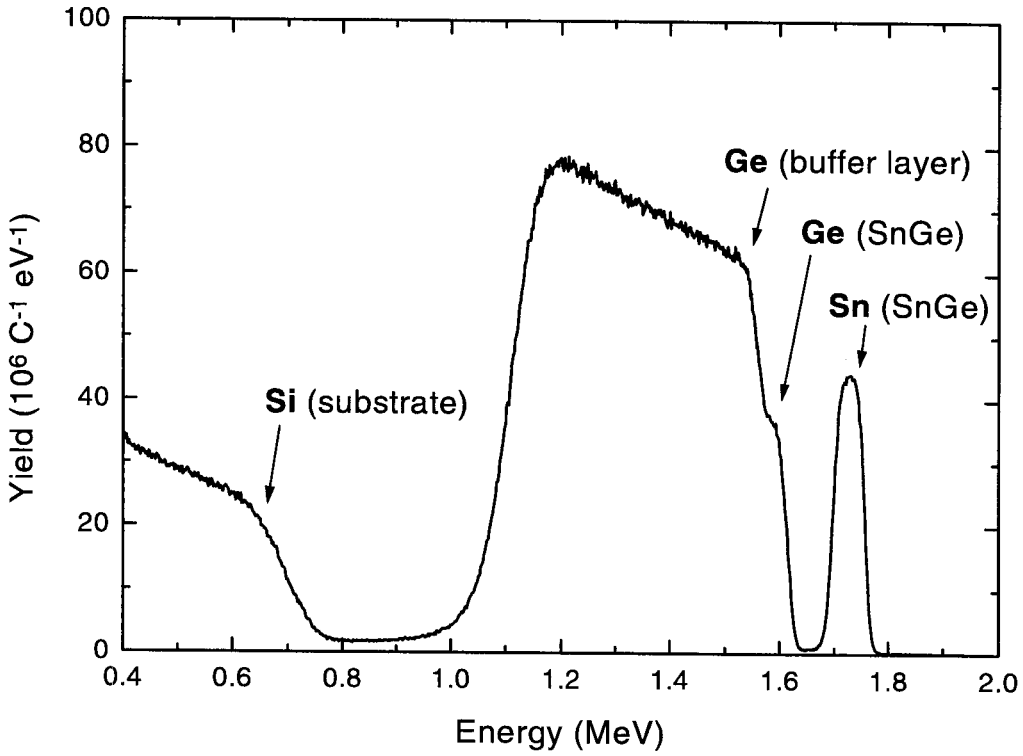

Figure 3.29 Rutherford backscattering spectrum of an epitaxial $Sn_{0.34}Ge_{0.66}$(23nm) / Ge(205nm) / Si(100) sample grown by ion-assisted molecular beam epitaxy at 150°C with electron cyclotron resonance ion source.

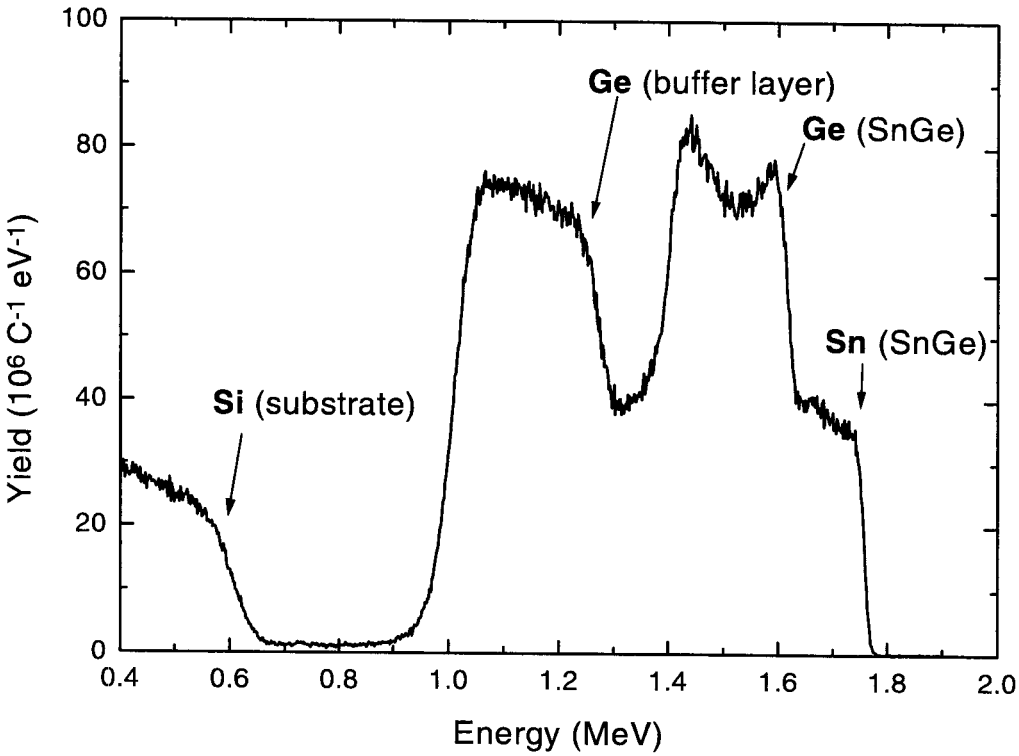

Figure 3.30 Rutherford backscattering spectrum of a polycrystalline $Sn_{0.30}Ge_{0.70}$(250nm) / Ge(200nm) / Si(100) sample grown by ion-assisted molecular beam epitaxy at 150°C with electron cyclotron resonance ion source.

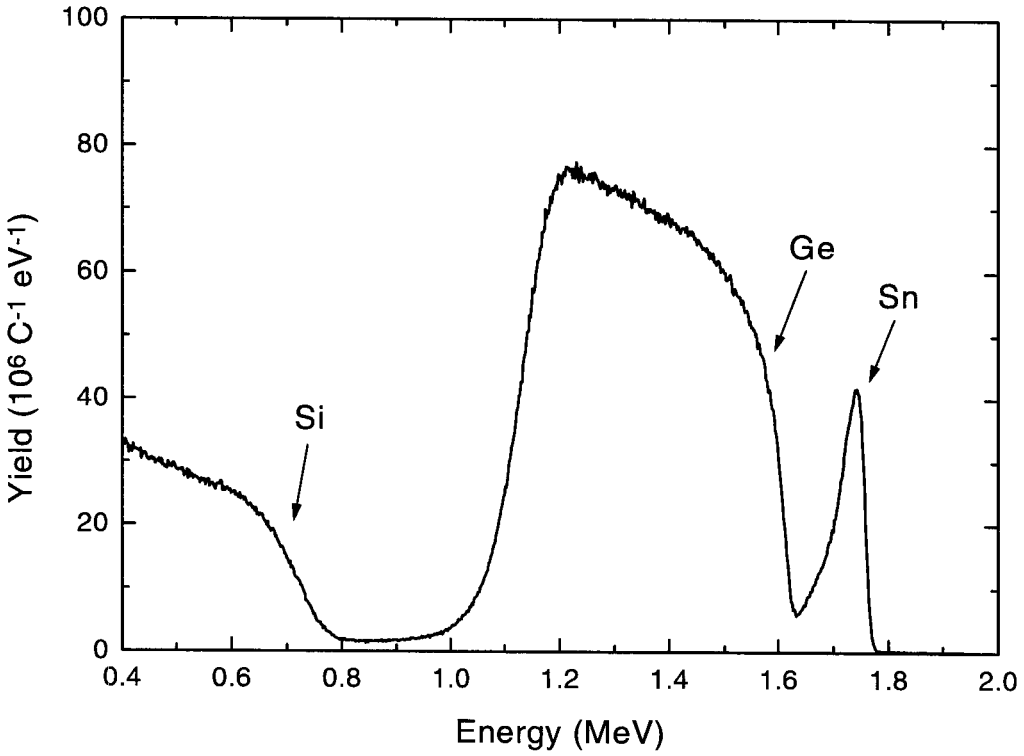

Figure 3.31 Rutherford backscattering spectrum of a Sn_xGe_{1-x}(23nm) / Ge(205nm) / Si(100) sample with a nominal tin concentration of 0.40 grown by ion-assisted molecular beam epitaxy at 150°C with electron cyclotron resonance ion source.

In order to grow thicker epitaxial Sn_xGe_{1-x} alloy films without polycrystalline transformation, ion-assisted growths of Sn_xGe_{1-x} were also performed at 200°C growth temperature with nominal tin concentrations in the range of 0.2 to 0.3 using the electron cyclotron resonance ion source. The growth conditions were similar to those of the 150°C growth. The growth rate was

0.05 nm/sec. The argon flow rate was about 10 sccm which produced an argon background pressures of about 10^{-4} Torr. The ion source microwave power was about 200 W, and the ion flux was about 0.05 mA/cm^{-2} at the substrate with ion energies of about 40 eV to 50 eV. For a series of samples with tin concentrations in the range of x=0.2 to 0.3, *in situ* reflection high energy electron diffraction indicated atomically rough surfaces, but a single crystal diffraction pattern persisted with no evidence of twinning throughout the growth of Sn_xGe_{1-x} layers more than 90 nm thick (Figure 3.32) (Figure 3.33). For samples with tin concentrations larger than x=0.3, on the other hand, the diffraction intensity started to decrease after about 90 nm of Sn_xGe_{1-x} film growth, indicating a reduction of epitaxial area.

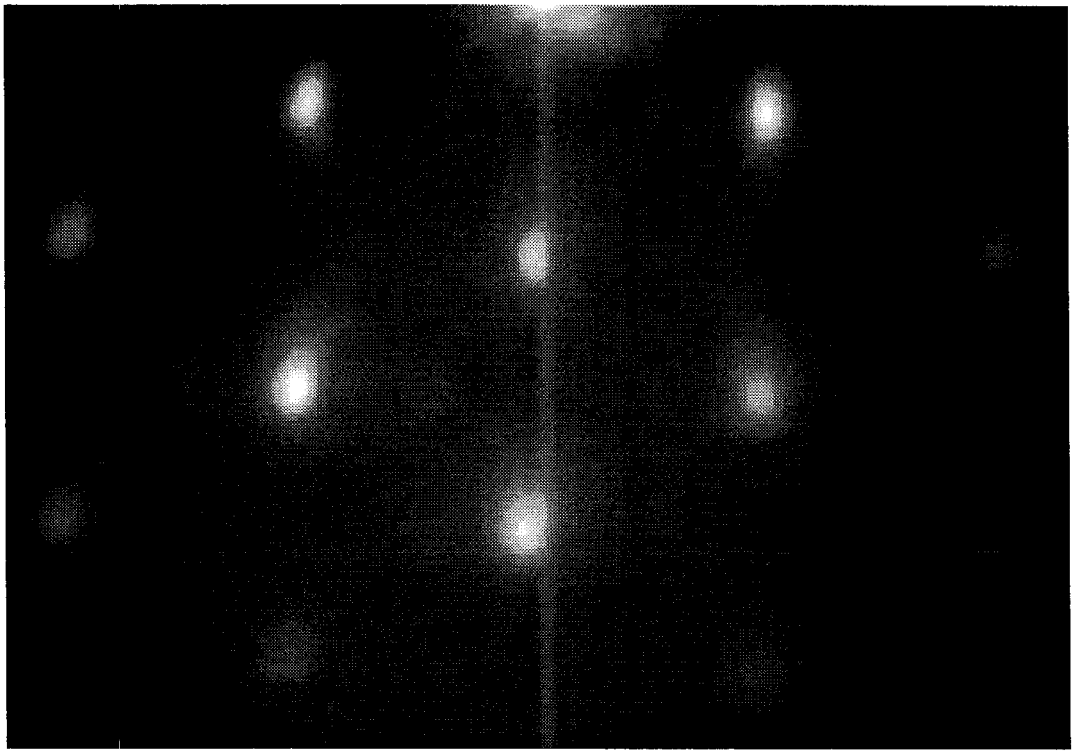

Figure 3.32 *In situ* reflection high energy electron diffraction of an epitaxial $Sn_{0.30}Ge_{0.70}$(95nm) / Ge(110nm) / Si(100) sample grown by ion-assisted molecular beam epitaxy at 200°C with electron cyclotron resonance ion source.

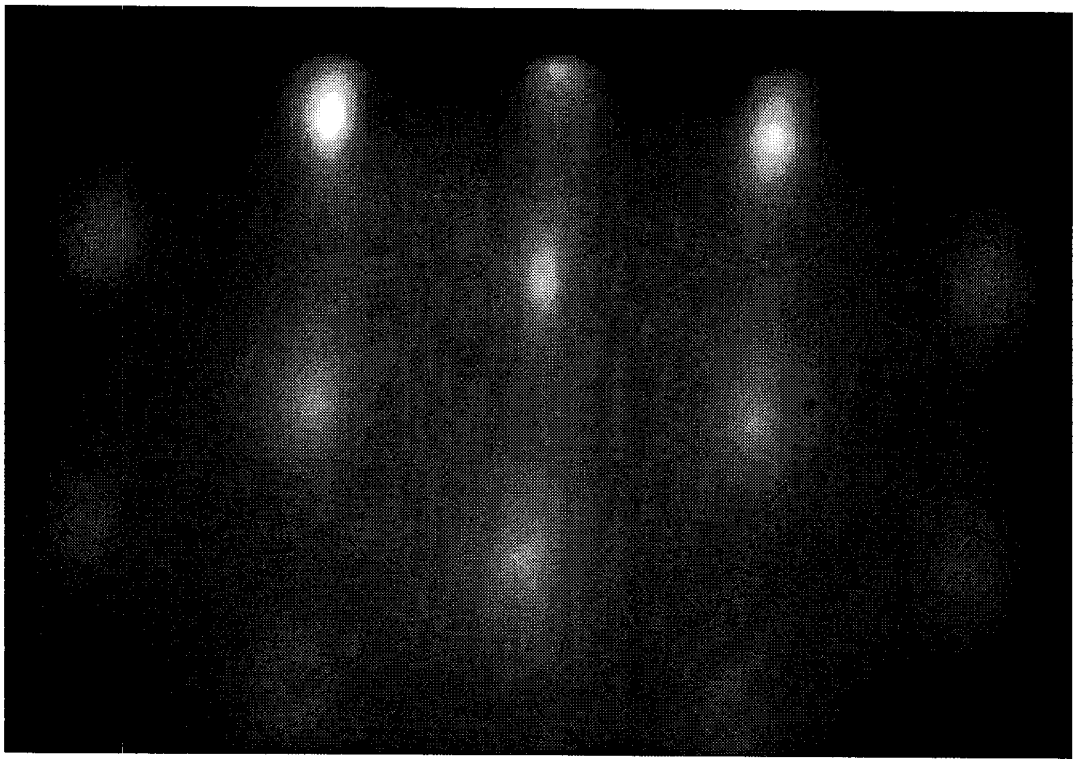

Figure 3.33 *In situ* reflection high energy electron diffraction of an epitaxial $Sn_{0.26}Ge_{0.74}$(230nm) / Ge(105nm) / Si(100) sample grown by ion-assisted molecular beam epitaxy at 200°C with electron cyclotron resonance ion source.

Optical microscopy inspections revealed optically smooth sample surfaces for tin concentrations less than x=0.3 and optically rough surfaces covered with islands for tin concentrations larger than x=0.3. It is interesting to note that a different surface morphology was observed on samples with optically rough surfaces by optical microscopy. For example, on samples that showed both optically clear and rough surface regions due to nonuniformity in the growth process, in addition to the morphologies observed on similar samples grown by

conventional molecular beam epitaxy at 200°C, a flower-like dendritic surface morphology was observed in a relatively wide (about 5 ~ 20 mm) transition region between the optically clear regions on one side and optically rough regions on the other (Figure 3.34). Scanning electron microscopy with energy dispersive spectroscopy showed that the flower-like morphology consisted of dendritic clusters of tin rich islands, and the outer peripherals of the structures were found to be especially tin rich (Figure 3.35). Such flower-like dendritic morphologies may be the traces of long range motion of the surface islands starting from some center locations and moving outward during the growth. The exact origin of such morphologies is not clear. One possibility is that the ion irradiation enhanced the mobility of the surface islands. The ion irradiation may also produce local heating of the substrate so that the actual local sample temperature may be raised. Note that in addition to the composition nonuniformity across the wafer, there is also a nonuniformity in the irradiating ion flux across the wafer due to the orientation of the ion source. The coexistence of two different island morphologies on the same samples from ion-assisted growth may be the result of the addition of ion-flux nonuniformity to the composition nonuniformity. For a few samples grown with the ion source positioned very close to the substrate (5~10 cm) for enhanced ion flux (~ 0.2 mA/cm^2) which also produced a larger ion-flux nonuniformity, the transition from optically rough to optically clear surface regions across a 3 inch substrate was strongly oriented toward the direction of the ion source where the ion flux is higher, whereas for samples grown without ion irradiation the transition was strongly oriented away from the direction of the tin source where the tin growth rate is higher (Figure 3.36). These directional orientations were results of

the spatial nonuniformity in ion-flux and alloy composition across the substrate and showed clearly the effect of segregation-inhibition by high-flux ion irradiation during epitaxial growth.

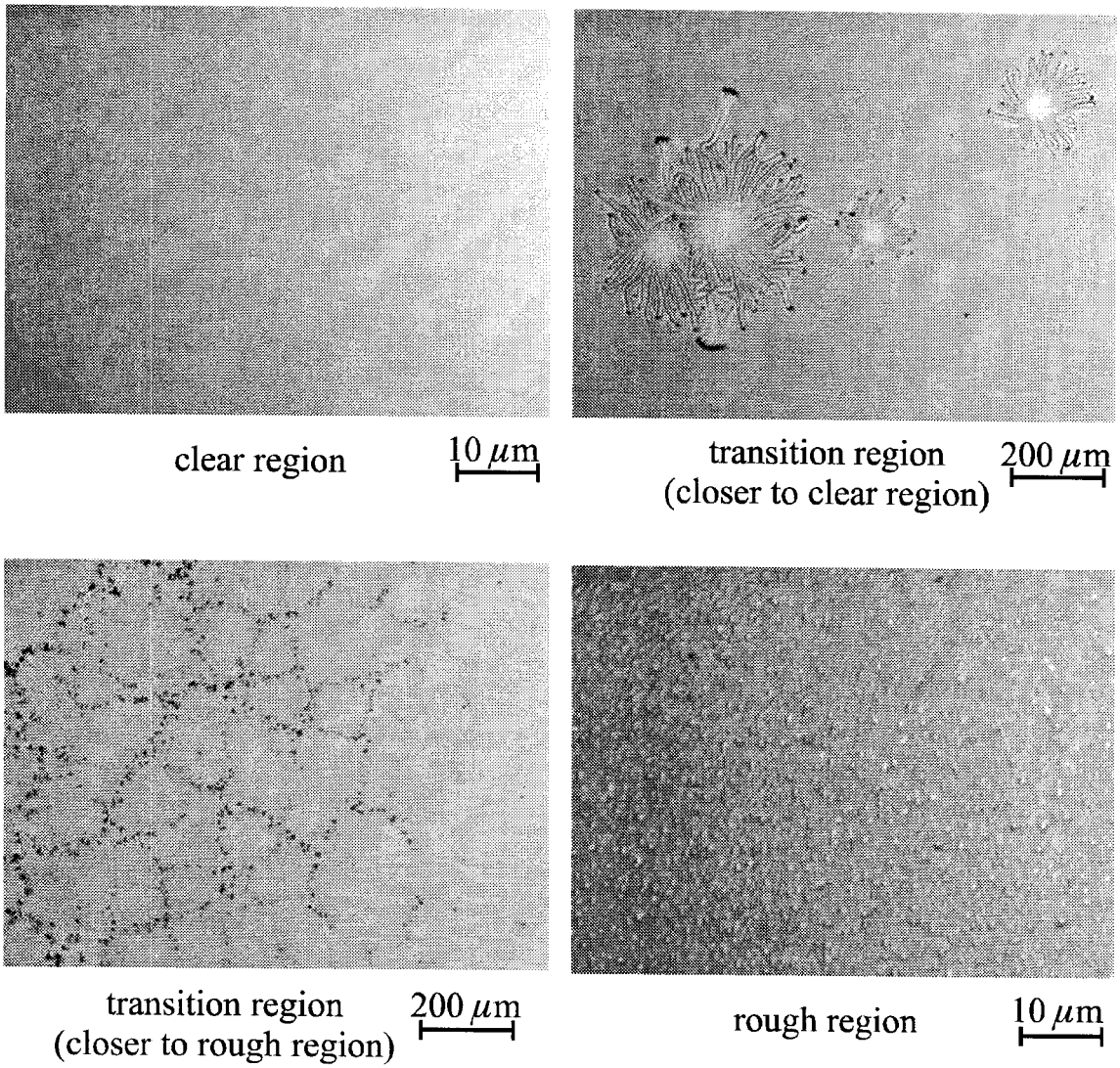

Figure 3.34 Optical micrograph of transition from optically clear surface region to optically rough (with islands) surface region across a distance of approximately 20 mm on a Sn_xGe_{1-x} (95 nm) sample with nominal tin concentration of $x \approx 0.3$ grown by ion-assisted molecular beam epitaxy at 200°C.

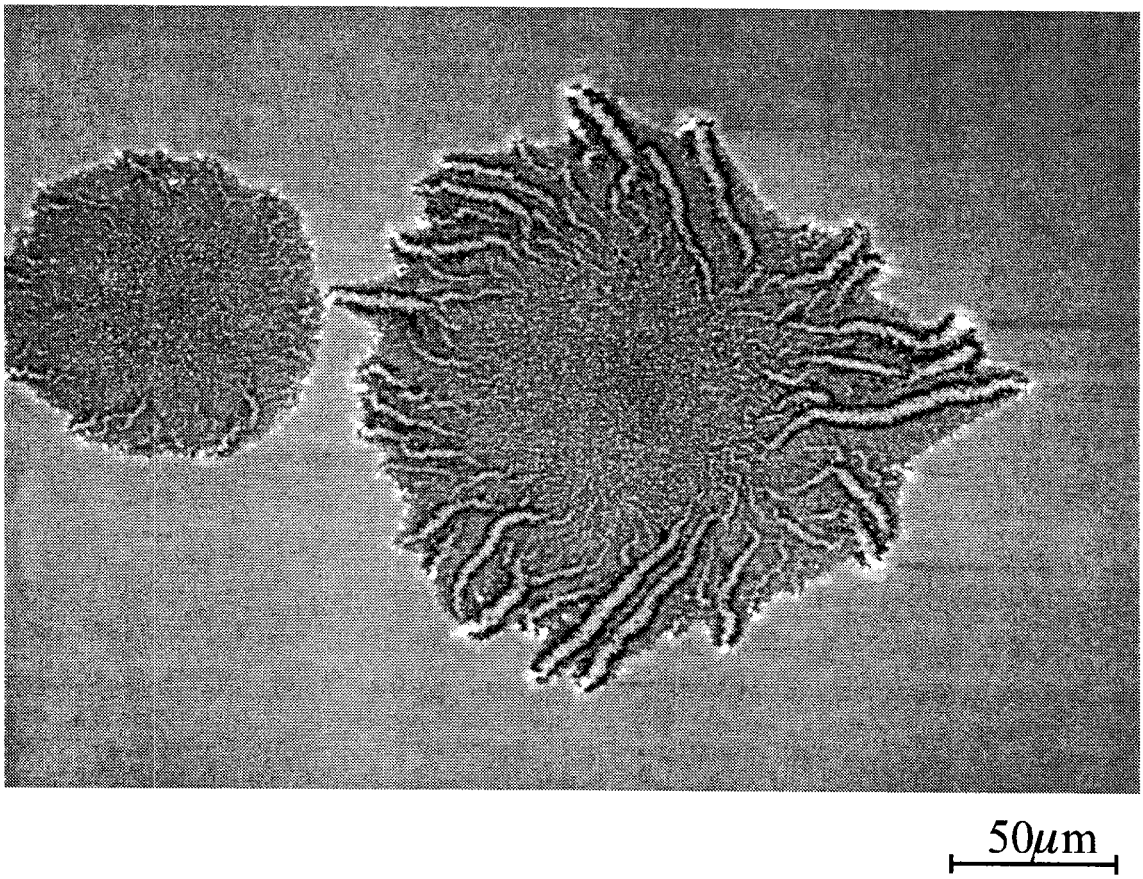

Figure 3.35 Scanning electron micrograph of the sample surface of Sn_xGe_{1-x} (95nm) / Ge (110nm) / Si grown by ion-assisted molecular beam epitaxy at 200°C with nominal tin concentration of $x \approx 0.3$. The image was obtained from a backscattering detector for better Z-contrast, so that the brighter areas of the image corresponds to higher concentration of the heavier elements (which is tin in this case).

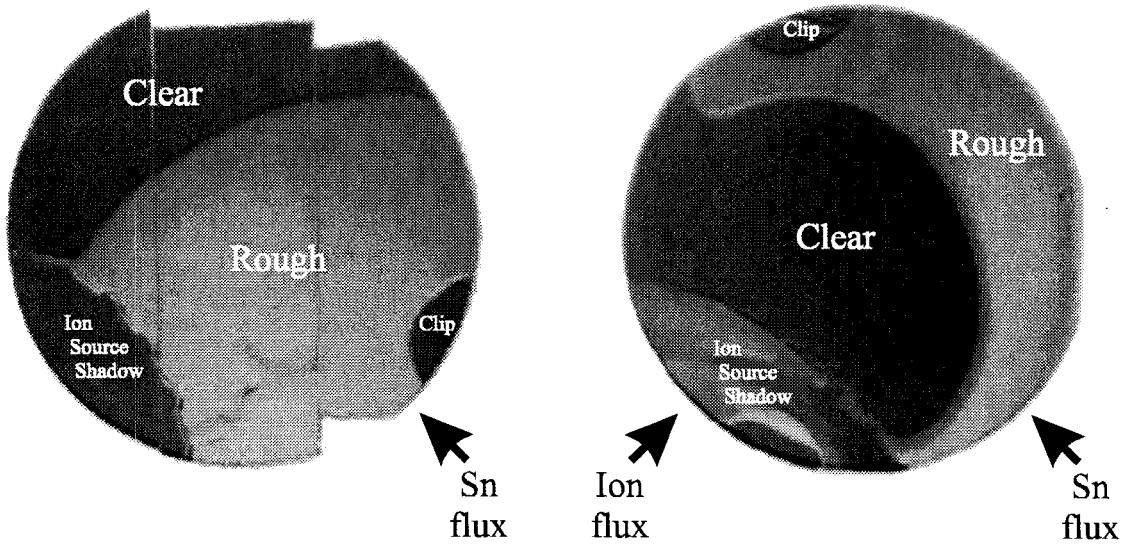

(a) Sn_xGe_{1-x} (x=0.20, 50nm) without ion irradiation

(b) Sn_xGe_{1-x} (x=0.25, 50nm) with ion irradiation

Figure 3.36 Orientation of optically clear and optically rough surface regions across a substrate of 3 inch diameter as a result of spatial nonuniformity in alloy composition and irradiating ion flux for samples (a) of nominal tin concentration x=0.20 (50nm) grown without ion irradiation and (b) of nominal tin concentration x=0.25 (50nm) grown with ion irradiation (Ar^+, 40~50 eV, ~ 0.2 mA/cm^2). The tin growth rate was higher toward the direction of the tin source. The irradiating ion flux was higher toward the direction of the ion source. Note that sample (a) has been cut and part of the sample has been used for other analyses.

Backscattering spectra of the alloy samples showed that tin incorporated uniformly into the Sn_xGe_{1-x} alloy films for the samples with optically clear surfaces. Epitaxial $Sn_{0.30}Ge_{0.70}$ films 95 nm thick (Figure 3.37) and $Sn_{0.26}Ge_{0.74}$ films 230 nm thick (Figure 3.38) were obtained with uniform composition profiles

by ion-assisted growth at 200°C. For a few samples grown with substrate biased at -50 eV which corresponded to an increase of irradiating ion energy to about 90 eV to 100 eV, backscattering spectra showed argon inclusions of approximately 1 at.% in the epitaxial Sn_xGe_{1-x} films. No argon inclusions were detectable by backscattering for samples grown with grounded substrates (i.e., ion energies less than about 50 eV).

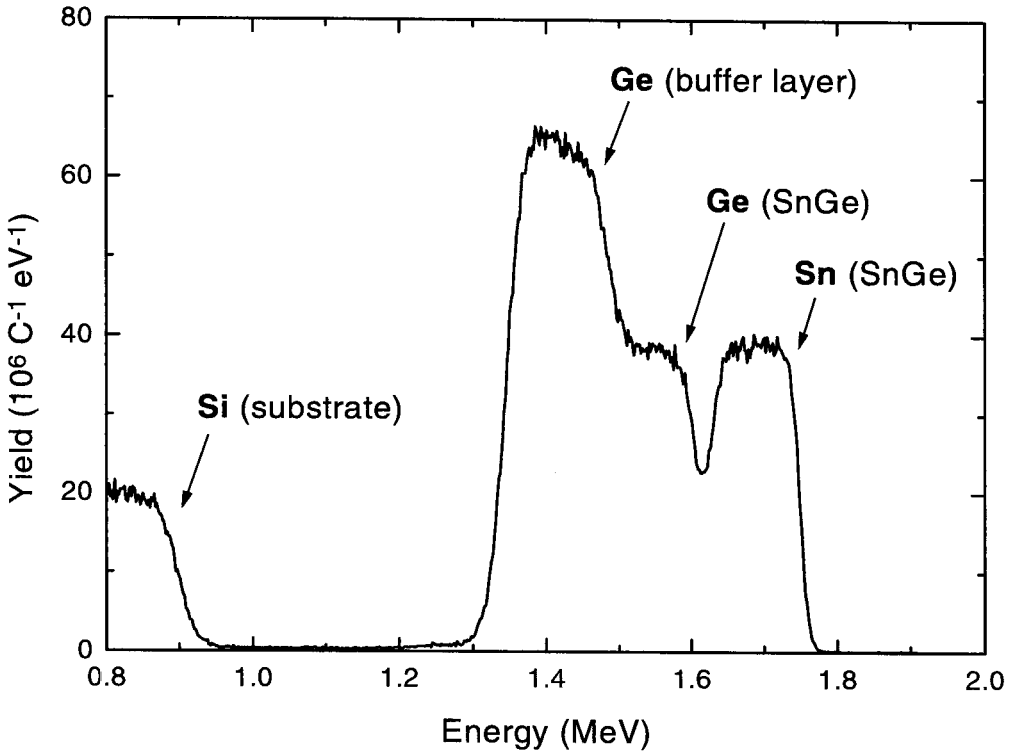

Figure 3.37 Rutherford backscattering spectrum of an epitaxial $Sn_{0.30}Ge_{0.70}$(95nm) / Ge(110nm) / Si(100) sample grown by ion-assisted molecular beam epitaxy at 200°C with electron cyclotron resonance ion source.

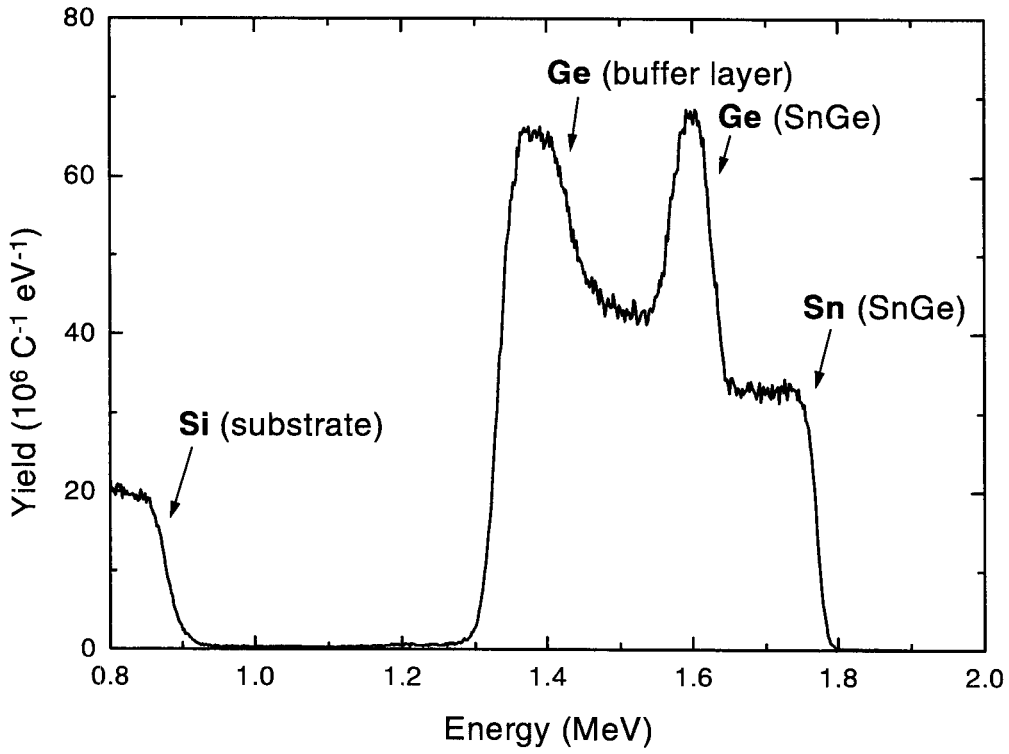

Figure 3.38 Rutherford backscattering spectrum of an epitaxial $Sn_{0.26}Ge_{0.74}$(230nm) / Ge(105nm) / Si(100) sample grown by ion-assisted molecular beam epitaxy at 200°C with electron cyclotron resonance ion source.

High resolution x-ray diffraction of the (400) diffraction peak from the Sn_xGe_{1-x} films produced peak shifts consistent with epitaxial diamond cubic Sn_xGe_{1-x} with lattice constants consistent with Vegard's law for strain relaxed films (Figure 3.39, Figure 3.40). However, notice that the diffraction peak widths

from the Sn_xGe_{1-x} films were significantly wider than that of the germanium buffer layers although the Sn_xGe_{1-x} film thicknesses were similar or larger than that of the germanium buffer layer. This indicated that these Sn_xGe_{1-x} films may contain a larger density of structural or compositional defects, such as misfit dislocations or composition fluctuations, than that of the germanium buffer layers.

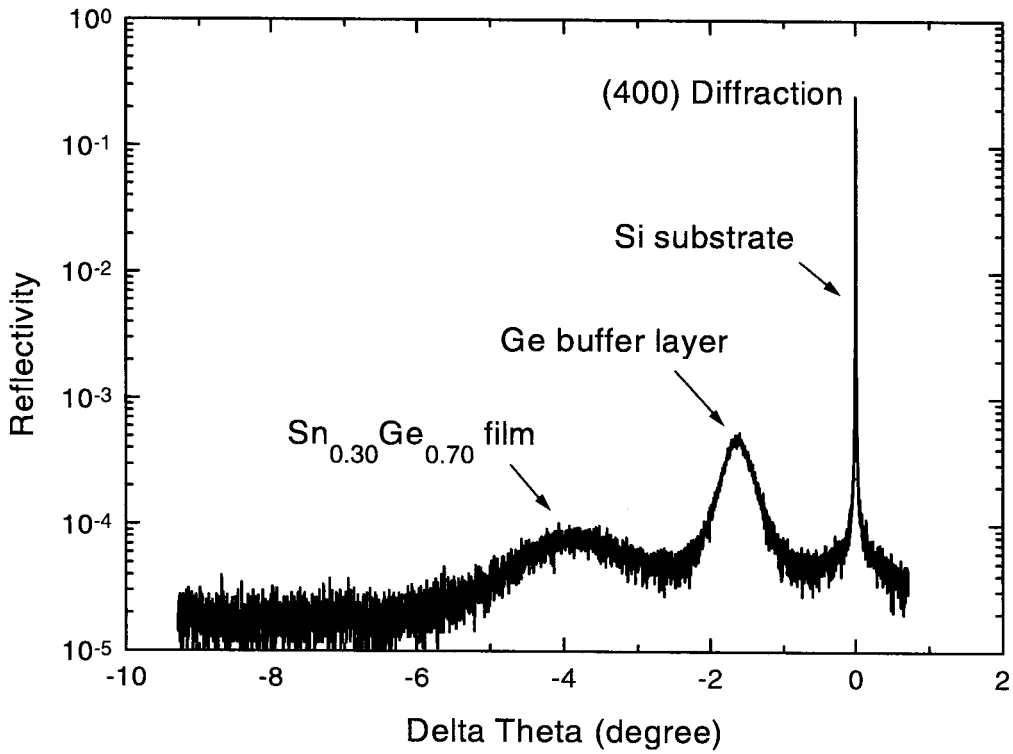

Figure 3.39 High resolution x-ray diffraction of an epitaxial $Sn_{0.30}Ge_{0.70}$(95nm) / Ge(110nm) / Si(100) sample grown by ion-assisted molecular beam epitaxy at 200°C with electron cyclotron resonance ion source.

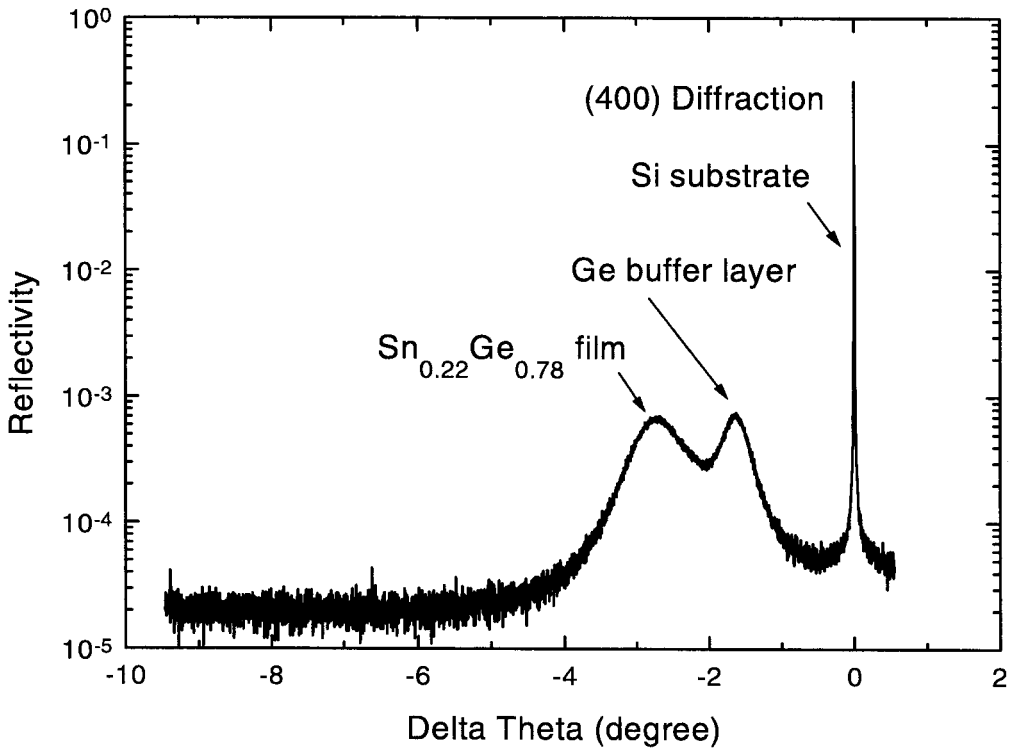

Figure 3.40 High resolution x-ray diffraction of an epitaxial $Sn_{0.22}Ge_{0.78}$(350nm) / Ge(150nm) / Si(100) sample grown by ion-assisted molecular beam epitaxy at 200°C with electron cyclotron resonance ion source.

Cross-sectional transmission electron microscopy analysis confirmed epitaxial Sn_xGe_{1-x} films with sharp interfaces but containing misfit dislocations which was expected as a result of strain relaxation.. Selected area electron diffraction patterns from the Sn_xGe_{1-x} films and the Ge buffer layers are consistent

with their lattice parameter differences expected from Vegard's law for strain relaxed films (Figure 3.41). Note that while the typical threading dislocation densities in relaxed germanium layers grown on silicon substrates are of the order of 10^8 cm^{-2}, much smaller dislocation densities have been demonstrated in compositionally graded $Si_{1-x}Ge_x$ layers as well as layers grown on ultra-thin silicon-on-insulator substrates [45] - [48].

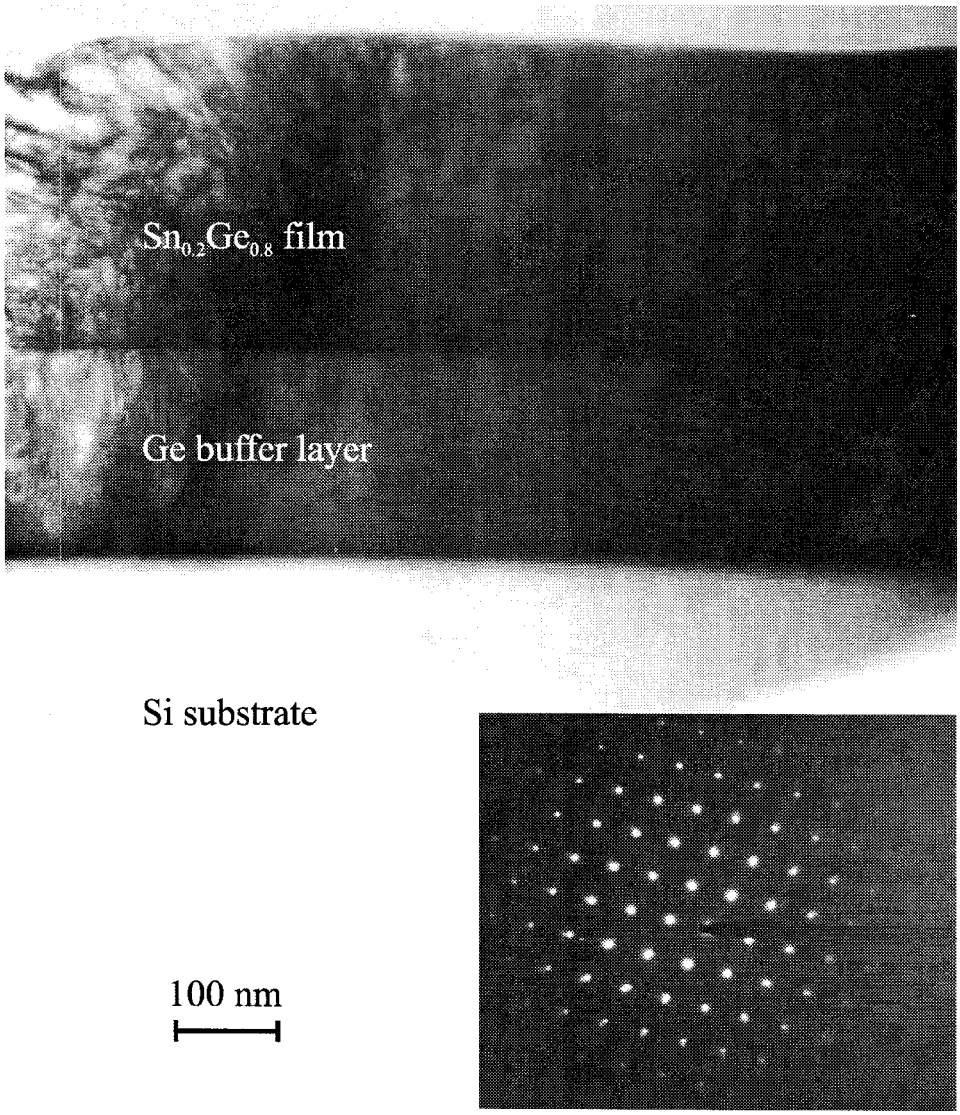

Figure 3.41 Bright-field cross-sectional transmission electron micrograph and selected area diffraction of an epitaxial $Sn_{0.20}Ge_{0.80}$(300nm) / Ge(200nm) / Si(100) sample grown by ion-assisted molecular beam epitaxy at 200°C with electron cyclotron resonance ion source. The film interfaces are relatively sharp. The films contain misfit dislocations as a result of strain relaxation. The selected area diffraction pattern indicated epitaxial films.

A Sn_xGe_{1-x} sample with a tin concentration of x=0.22 grown by ion-assisted molecular beam epitaxy was annealed at temperatures up to about 270°C while monitored by *in situ* reflection high energy electron diffraction. The single crystal diffraction pattern persisted throughout the anneal. Post-anneal Rutherford backscattering analysis indicated no redistribution of the alloy composition profile, and optical microscopy showed optically clear sample surfaces after the annealing. These results suggested that the alloy sample was stable at the annealing temperatures. Note that the maximum stable temperature is in general composition dependent.

3 .6 .3 Summary of Ion-Assisted Epitaxial Growth

Irradiation of the film surface with low energy (30~100 eV) high flux (ion flux / atom flux ~ 1) argon ion beams efficiently suppressed tin surface segregation during ion-assisted molecular beam epitaxy of Sn_xGe_{1-x}. While ion-assisted growth using the Kaufman ion source did not significantly affect the tin surface segregation due to its limited ion current density (~ 1 μA/cm^2), growth using the electron cyclotron resonance ion source significantly suppressed the tin surface segregation due to its much higher ion current density (~ 0.1 mA/cm^2). Compositionally homogeneous epitaxial diamond cubic Sn_xGe_{1-x} alloy films with tin concentration up to x=0.3 were successfully synthesized by ion-assisted

molecular beam epitaxy using Ar^+ ion beams produced by an electron cyclotron resonance ion source. Sn_xGe_{1-x} alloy films with tin concentration as high as x=0.34 were also achieved for a limited epitaxial film thickness (about 20 nm). A brief summary of the results of molecular beam epitaxy of Sn_xGe_{1-x} with and without ion irradiation is given in Table 3.2.

X_{Sn}	**Thick. (nm)**	**Ion beam**	**Temp. (°C)**	***In situ* RHEED**	**Surface**	**RBS**	**X-ray**
0.1~0.3	10~50	No	120	amorphous	smooth	segregate	N/A
0.2~0.3	20~50	No	200	weak	rough	segregate	N/A
0.34	20	Yes	150	epitaxial twinned	smooth	incorporate	N/A
0.30	200	Yes	150	poly-crystalline	smooth	incorporate	N/A
0.40	20	Yes	150	weak	rough	segregate	N/A
0.30	90	Yes	200	epitaxial	smooth	incorporate	epi.
0.26	230	Yes	200	epitaxial	smooth	incorporate	epi.

Table 3.2 Summary of molecular beam epitaxy of Sn_xGe_{1-x} with and without ion irradiation. The samples were characterized by *in situ* reflection high energy electron diffraction (*in situ* RHEED), optical microscopy surface imaging (surface), Rutherford backscattering spectroscopy (RBS), and high resolution x-ray diffraction (x-ray).

3 .7 Conclusions and Prospects

Epitaxial Sn_xGe_{1-x} alloys films were grown on silicon substrates by conventional molecular beam epitaxy with tin concentrations up to about x=0.2. For higher tin concentrations, thermal epitaxial growth faced great difficulty due to a breakdown of epitaxy caused by either surface Sn segregation at high temperatures or surface kinetic roughening at low temperatures. Irradiation of the film surface with a low energy (30~100 eV) high flux (ion/atom~1) ion beam efficiently suppressed tin surface segregation. Compositionally homogeneous epitaxial diamond cubic Sn_xGe_{1-x} alloy films with Sn compositions as high as x=0.30~0.34 were achieved with ion-assisted molecular beam epitaxy using electron cyclotron resonance argon ion source. Note that epitaxial Sn_xGe_{1-x} films with even higher compositions may be possible by optimizing the ion-assisted molecular beam epitaxy growth parameters, including growth temperature, growth rate, ion energy, ion flux, and ion species. For example, use of heavier ion species (such as xenon) may further improve the tin incorporation by better mass-matched energy transfer to the surface tin atoms since, in the case of head-on elastic recoil where the energy transfer efficiency is $\eta_E = 4m_1m_2/(m_1+m_2)^2$, the energy transfer efficiencies from argon to tin and germanium are 0.754 and 0.916,

respectively, while the energy transfer efficiencies from xenon to tin and germanium are 0.997 and 0.917, respectively.

Bibliography

[1] D.W. Jenkins and J.D. Dow, Phys. Rev. B 36, 7994 (1987).

[2] H.A. Atwater, G. He, K. Saipetch, Mat. Res. Soc. Symp. Proc. 355, 123 (1995).

[3] B. Bouhafs, F. Benkabou, M. Ferhat, B. Khelifa, J.P. Dufour, H. Aourag, Infrared Phys. & Tech. 36, 967 (1995).

[4] K.A. Mader, A. Baldereschi, H. von Kanel, Solid State Comm. 69, 1123 (1989).

[5] Na. Amrane, S. Ait Abderrahmane, H. Aourag, Infrared Phys. & Tech. 36, 843 (1995).

[6] T. Brudevoll, D.S. Citrin, N.E. Christensen, M. Cardona, Phys. Rev. B 48,17128 (1993).

[7] E. Kaxiras, unpublished.

[8] B.I. Craig and B.J. Garrison, Phys. Rev. B 33, 8130 (1986).

[9] B.I. Craig, Superlattices and Microstructures 12, 1 (1992).

[10] A. Harwit, P.R. Pukite, J. Angilello and S.S. Iyer, Thin Solid Films 184, 395 (1990).

[11] J. Piao, R. Beresford, T. Licata, W.I. Wang and H. Homma, J. Vac. Sci. Technol. B 8, 221 (1990).

[12] W. Wegscheider, K. Eberl, U. Menczigar and G. Abstreiter, Appl. Phys. Lett. 57, 875 (1990).

[13] H.-J. Gossmann, J. Appl. Phys. 68, 2791 (1990).

[14] E.A. Fitzgerald, P.E. Freeland, M.T. Asom, W.P. Lowe, R.A. Macharrie, JR., B.E. Weir, A.R. Kortan, F.A. Thiel, Y.-H. Xie, A.M. Sergent, S.L. Cooper, G.A. Thomas and L.C. Kimerling, J. Elec. Mat. 20, 489 (1991).

[15] K. Eberl, W. Wegscheider and G. Abstreiter, J. Crystal Growth 111, 882 (1991).

[16] P. Vogl, J. Olajos, W. Wegscheider and G. Abstreiter, Surface Science 267, 83 (1992).

[17] W. Wegscheider, J. Olajos, U. Menczigar, W. Dondl and G. Abstreiter, J. Crystal Growth 123, 75 (1992).

[18] O. Gurdal, M.-A. Hasan, M.R. Sardela, Jr., J.E. Green, H.H. Radamson, J.E. Sundgren, G.V. Hasson, Appl. Phys. Lett. 67, 956 (1995).

[19] S.I. Shah, J.E. Greene, L.L. Abels, Q. Yao and P.M. Raccah, J. Crystal Growth 83, 3 (1987).

[20] S. Oguz, W. Paul, T.T. Deutsch, B-Y. Tsaur and D.V. Murphy, Appl. Phys. Lett. 43, 848 (1983).

[21] I.T.H Chang, B. Cantor and A.G. Cullis, J. Non-Crystalline Solids 117/118, 263 (1990).

[22] S.M. Lee, J. Appl. Phys. 75, 1987 (1994).

[23] D.J. Eaglesham, H.-J. Gossmann, M. Cerullo, Phys. Rev. Lett. 65, 1227 (1990).

[24] M.V.R. Murty, H.A. Atwater, Phys. Rev. B 49, 8483 (1994).

[25] G. He and H.A. Atwater, Appl. Phys. Lett. 68, 664 (1996).

[26] T. Soma, H. Matsuo and S. Kagaya, Phys. Stat. Solid. 105, 311 (1981).

[27] T.B. Massalski, et al., Binary Alloy Phase Diagrams, Second Edition, Am. Soc. Metals, Materials Park, 1990.

[28] C.D. Thurmond, J. Phys. Chem. 57, 827 (1953).

[29] C.D. Thurmond, F.A. Trumbore and M. Kowalchik, J. Chem. Phys. 24, 799 (1956).

[30] W. Klemm and H. Stöhr, Z. Anorg. Allg. Chem. 241, 305 (1939).

[31] R.F.C Farrow, D.S. Robertson, G.M. Williams, A.G. Cullis, G.R. Jones, I.M. Young and P.N.J. Dennis, J. Crystal Growth 54, 507 (1981).

[32] J.L. Reno and L.L. Stephenson, Appl. Phys. Lett. 54, 2207 (1989).

[33] M.T. Asom, A.R. Kortan, L.C. Kimerling and R.C. Farrow, Appl. Phys. Lett. 55, 1439 (1989).

[34] T. Ito, Jpn. J. Appl. Phys. 31, L920 (1992).

[35] G.A. Busch, R. Kern, Solid State Physics, ed. F. Seitz, D. Thurnbull, Vol. 11, Academic Press, New York, 1960.

[36] A. Zunger and J.E. Jaffe, Phys. Rev. Lett. 51, 662 (1983).

[37] M.C. Payne, M.P. Teter, D.C. Allan, T.A. Arias, J.D. Joannopoulos, Rev. Mod. Phys. 64, 1045 (1992).

[38] R.O. Jones, O. Gunnarsson, Rev. Mod. Phys. 61, 689 (1989).

[39] J.C. Mikkelsen, Jr., J.B. Boyce, Phys. Rev. Lett. 49, 1412 (1982).

[40] L. Li, Y. Wei, and I.S.T. Tsong, J. Vac. Sci. Tech. A 13, 1609 (1995).

[41] M.V.R. Murty, H.A. Atwater, Phys. Rev. B 45, 1507 (1992).

[42] G. He and H.A. Atwater, Nucl. Instrum. Methods B 106, 126 (1995).

[43] G. He and H.A. Atwater, Mat. Res. Soc. Symp. Proc. 399, 380 (1996).

[44] J. Knall, J.-E. Sundgren, L.C. Markert and J.E. Greene, Surface Science 214, 149 (1989).

[45] E.A. Fitzgerald, Y.H. Xie, M.L. Green, D. Brasen, A.R. Kortan, J. Michel, Y.J. Mii, B.E. Weir, Appl. Phys. Lett. 59, 811 (1991).

[46] F.K. Legoues, B.S. Meyerson, J.F. Morar, Phys. Rev. Lett. 66, 2903 (1991).

[47] D.P. Malta, J.B. Posthill, R.J. Markunas, T.P. Humphreys, Appl. Phys. Lett. 60, 844 (1992).

[48] A.R. Powell, S.S. Iyer, F.K. Legoues, Appl. Phys. Lett. 64, 1856 (1994).

Chapter 4

MODELING OF SEGREGATION IN ION-ASSISTED EPITAXY

4 .1 Introduction

Tight-binding and pseudopotential calculations predicted that diamond cubic Sn_xGe_{1-x} alloys may have a direct band gap continuously tunable from E_g=0.55 eV to E_g=0 eV for compositions from x=0.2 to x=0.6, with very low electron effective mass and hence high electron mobility [1]-[4]. These predicted properties make Sn_xGe_{1-x} a potential semiconductor material for the fabrication of Si-based long-wavelength infrared optoelectronic devices and high performance heterojunction devices. However, Sn_xGe_{1-x} alloys in this composition range were difficult to synthesize due to the Sn surface segregation and phase separation during growth [5]-[16]. Driven by the limited solid solubility and the surface free energy difference between Sn and Ge, Sn tends to segregate to the surface with its relatively high diffusivity during the growth (Figure 4.1). The coherency strain may also play a role in the surface Sn segregation when Sn_xGe_{1-x} is deposited on a lattice mismatched substrate. As shown in the last chapter, alloy growth by ion-assisted molecular beam epitaxy can efficiently suppress surface segregation and achieve alloys with wider ranges of compositions [2][17] (Figure 4.2). Suppression of segregation by collisional mixing through low energy ion irradiation has also

been used for dopant incorporation [18] and was demonstrated in the sputter deposition of Sn_xGe_{1-x} [13]. In order to gain insights of these ion-induced mixing processes and provide guidelines for choosing the optimum growth parameters, we developed an analytical model to quantitatively describe the surface segregation and its suppression during energetic beam deposition in general [19] [20]. This model expands the existing kinetic model that describes the partitioning processes during conventional epitaxial growth [21]-[24] by including the effect of energetic beam induced adatom incorporation into alloys. The model includes the effect of both recoil implantation and direct implantation and predicts the degree of segregation as a function of irradiating ion flux. The model was also applied to the ion-assisted molecular beam epitaxy of Sn_xGe_{1-x} and compared with our experimental results.

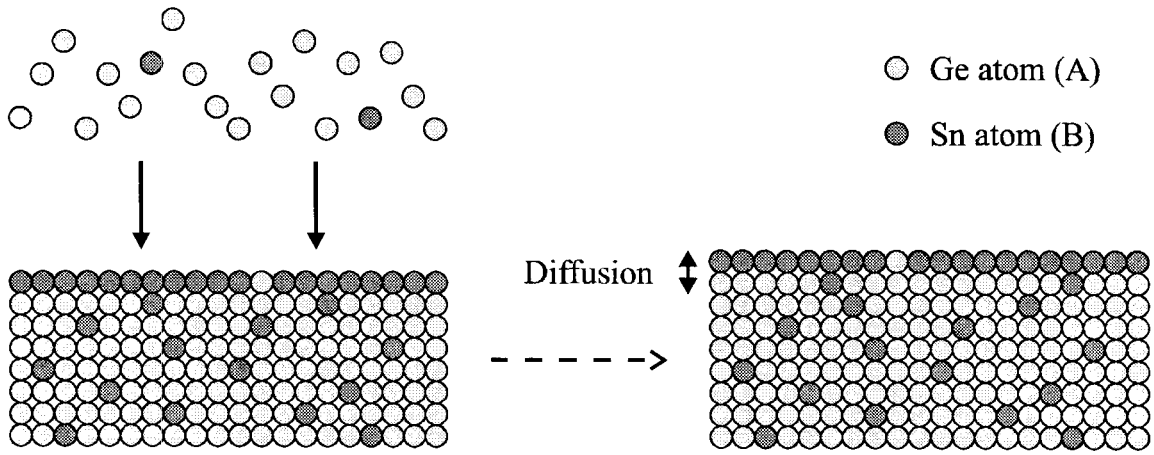

Figure 4.1 Schematic of surface segregation as a result of surface-subsurface diffusion.

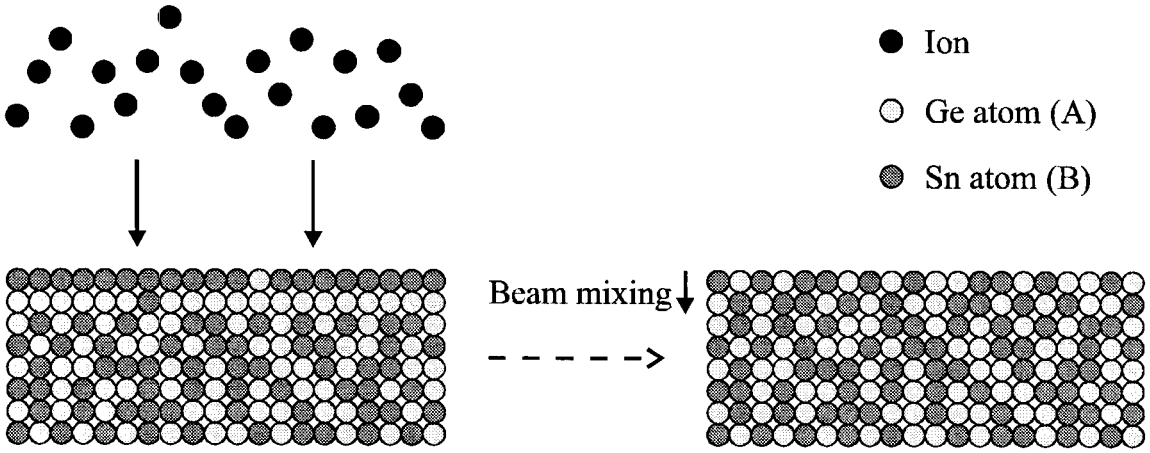

Figure 4.2 Schematic of suppression of surface segregation as a result of ion irradiation.

4 .2 Segregation Model for Thermal Epitaxy

In the conventional treatment of surface segregation during step-wise thermal growth [21]-[24], a segregation coefficient k of atomic species B is defined in alloy B_xA_{1-x} as the ratio of bulk composition x^{β} to surface composition x^{σ}:

$$k = x^{\beta} / x^{\sigma} .$$

In our experimental application, A and B correspond to Ge and Sn, respectively. At thermodynamic equilibrium, the segregation coefficient k_e of a regular solution can be expressed in terms of the partition parameter κ_e which depends on the difference in surface free energy γ^A and γ^B between the two chemical species A and B and the difference of the interaction parameters Ω^β and Ω^σ between the bulk and surface phases β and σ, respectively:

$$k_e = \frac{1-x^\beta}{1-x^\sigma}\kappa_e,$$

where

$$\kappa_e = e^{-\left(\gamma^A-\gamma^B+\Omega^\beta-\Omega^\sigma\right)/kT}$$

is the driving force for segregation. Note that epitaxial strain may also play a role in the driving force of segregation when the epitaxial film is lattice mismatched with the substrate. But strain effects was not explicitly considered here as distinct from the chemical driving forces for segregation. Assuming a step-wise growth mode [22] with thermal diffusion occurring only between the surface and subsurface monolayers (Figure 4.3), the surface and subsurface atoms may exchange positions in both the forward and backward directions, so that the diffusion flux between the two monolayers is:

$$J_D = J_D^+ - J_D^-,$$

where:

$$J_D^+ = \frac{D}{a^2}x^\beta\left(1-x^\sigma\right),$$

$$J_D^- = \frac{D}{a^2}\kappa_e x^\sigma \left(1 - x^\beta\right),$$

$$D = f\nu\, e^{-E_D/kT}.$$

Here J_D^+ and J_D^- are the forward and backward diffusion fluxes from bulk to surface, respectively; a is the atomic monolayer spacing; D is the subsurface-surface monolayer inter-diffusion coefficient; f is a geometric site factor; ν is the attempting frequency; and E_D is the atomic exchange activation energy barrier between the surface layer and the first subsurface (bulk) layer.

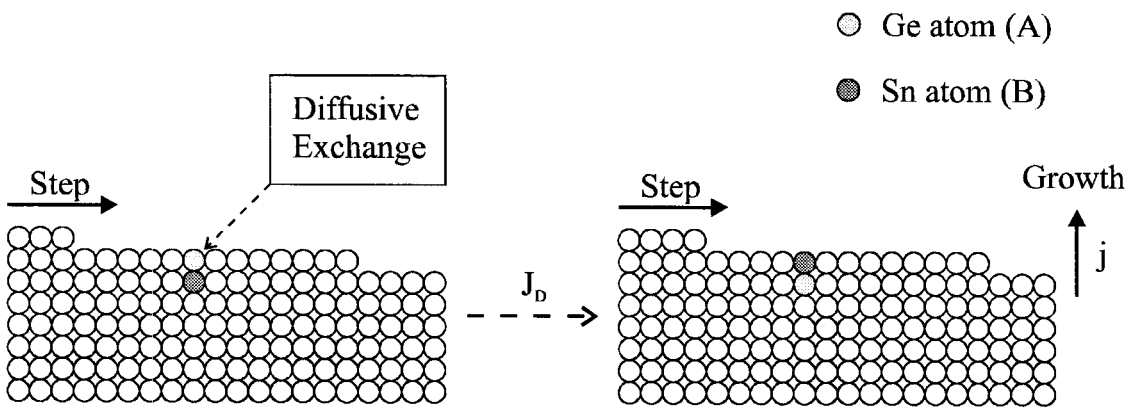

Figure 4.3 Schematic of surface-subsurface diffusion during thermal epitaxial growth

Assuming a constant surface composition x^σ, for step-wise growth between time $t = 0$ when a step just passes a surface layer and time $t = \tau_{monolayer}$

when the next step passes the same point, the change of surface layer composition $x(t)$ can be described by the first-order rate equation:

$$\begin{aligned}\frac{d}{dt}x(t) &= -J_D \\ &= -\left(J_D^+ - J_D^-\right) \\ &= -\frac{D}{a^2}\left[x(t)\left(1-x^\sigma\right) - \kappa_e x^\sigma\left(1-x(t)\right)\right]\end{aligned}$$

with boundary conditions

$$\left\{x(t)_{t=0} = x^\sigma,\, x(t)_{t=\tau_{monolayer}} = x^\beta\right\}.$$

Also define a time-dependent segregation coefficient

$$k(t) = x(t)/x^\sigma$$

and film thickness in terms of monolayers:

$$l = j\,t$$

where j is the growth rate in terms of monolayers per unit time. Rearranging the rate equation to obtain a form similar to the dilute solution situation yields

$$\frac{d}{dl}k(l) = -P_D\left[k(l) - k_e^*\right]$$

with boundary conditions

$$\left\{k(l)_{l=0} = 1,\, k(l)_{l=1} = k\right\}$$

where

$$P_D = \frac{D^*}{a^2 j},$$

$$D^* = D\left(1 - x^{\sigma} + \kappa_e x^{\sigma}\right),$$

$$k_e^* = \kappa_e / \left(1 - x^{\sigma} + \kappa_e x^{\sigma}\right).$$

Here D^* and k_e^* are the composition-dependent effective thermal diffusion coefficient and thermal segregation coefficient. For dilute solutions where x^{σ} and x^{β} are small, D^* and k_e^* approaches D and κ_e, respectively. P_D is a dimensionless Péclet number which describes the diffusion-flux to atom-flux ratio. This central rate equation can be solved analytically with the following steady-state solutions [21]:

$$k_{per} = k_e^* + \frac{1 - k_e^*}{e^{P_D}} \qquad \text{(periodic steps).}$$

Note that this is the steady-state solution for growth with perfectly periodic step flow where the steps on the surface are equally spaced so that they pass over the surface at constant time intervals. In the case of aperiodic step flow, where the steps on the surface are totally randomly spaced so that they pass over the surface at time intervals with a random Poisson distribution, the effective steady-state segregation coefficient would be the average of the segregation coefficient of periodic step flow weighted by the Poisson distribution [21]:

$$k_{aper} = \int_0^{\infty} k_{per}\left(t_{monolayer} = \tau\right) j e^{j\tau} d\tau$$

$$= k_e^* + \frac{1 - k_e^*}{1 + P_D} \qquad \text{(aperiodic steps).}$$

Note that the solution for aperiodic step flow is mathematically the same as the solution for continuous media [24].

The periodic and aperiodic solutions represent two rather extreme growth conditions. In practice, the surface step flow is usually neither perfectly periodic nor totally random as characterized by a Poisson distribution. In either case, one very important parameter in the solution of steady-state segregation coefficient is the dimensionless Péclet number defined as the ratio of diffusion flux and growth atom flux. A plot of steady-state segregation coefficient k during thermal epitaxial growth as a function of the Péclet number P_D is shown in Figure 4.4. When the Péclet number P_D is much larger than unity so that the diffusion flux is much larger than the growth atom flux, the steady-state segregation coefficient approaches the equilibrium segregation coefficient (strong segregation). This corresponds to either very small growth rate or very high growth temperature hence large diffusion flux. When the Péclet number P_D is much smaller than unity so that the diffusion flux is much smaller than the growth atom flux, the steady-state segregation coefficient approaches unity (no segregation). This corresponds to either very large growth rate or very low growth temperature hence small diffusion flux. In practice, however, the approach of suppressing segregation using larger growth rate and lower growth temperature is limited by the effect of surface kinetic roughening that occurs under the same conditions. This process of surface kinetic roughening eventually leads to a breakdown of epitaxy through a crystal-to-amorphous transition [25] [26]. In the case of Sn_xGe_{1-x} growth by conventional

molecular beam epitaxy, the experimental results discussed in the previous chapter suggested that, in order to avoid the crystal-to-amorphous transition for an epitaxial film of reasonable thickness (e.g., 10 nm), the growth temperature must sufficiently high that the surface tin segregation would be too strong for the epitaxial growth of Sn_xGe_{1-x} films with tin concentrations above x=0.2.

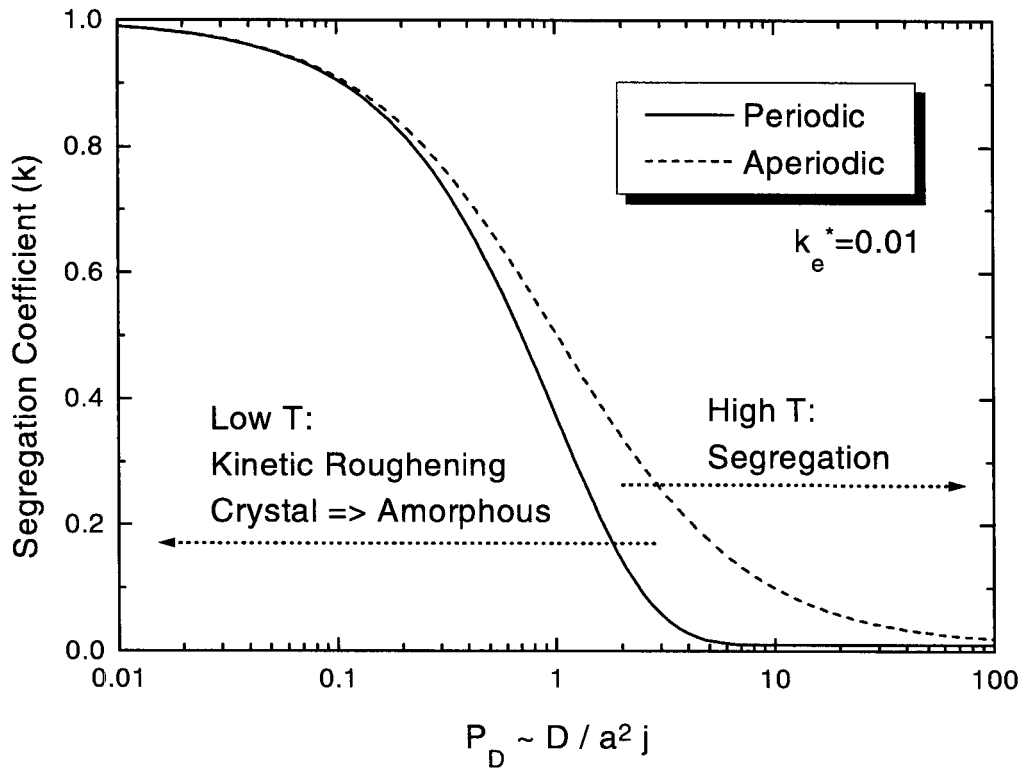

Figure 4.4 Steady-state segregation coefficient as a function of the ratio of diffusion-flux to growth-atom-flux during thermal epitaxial growth.

A plot of the steady-state segregation coefficient as a function of growth temperature of growth rate can be obtained if the temperature-dependent subsurface-surface diffusion coefficient D is be known. In the case of epitaxial growth of Sn_xGe_{1-x} alloy films, an estimation of the diffusion coefficient D can be obtained from the temperature-dependent steady-state segregation coefficients measured experimentally by W. Wegscheider, et al. [12]. The estimated diffusion coefficients are calculated using an average of the periodic and aperiodic step-flow solutions and are then fit to an Arrhenian form of $D = D_0 \exp(-E_D/kT)$ which yielded an activation energy of $E_D \approx 0.47$ eV (Figure 4.5), from which the steady-state segregation coefficient as a function of growth temperature at 0.05 nm/sec growth rate (Figure 4.6) as well as a function of growth rate at 200°C growth temperature (Figure 4.7) are obtained. Here the equilibrium segregation coefficient is assumed to be negligibly small compared to the steady-state segregation coefficient (since the equilibrium solubility is only about 0.01), so that the segregation process is diffusion limited and is not strongly affected by the temperature dependent equilibrium segregation coefficient.

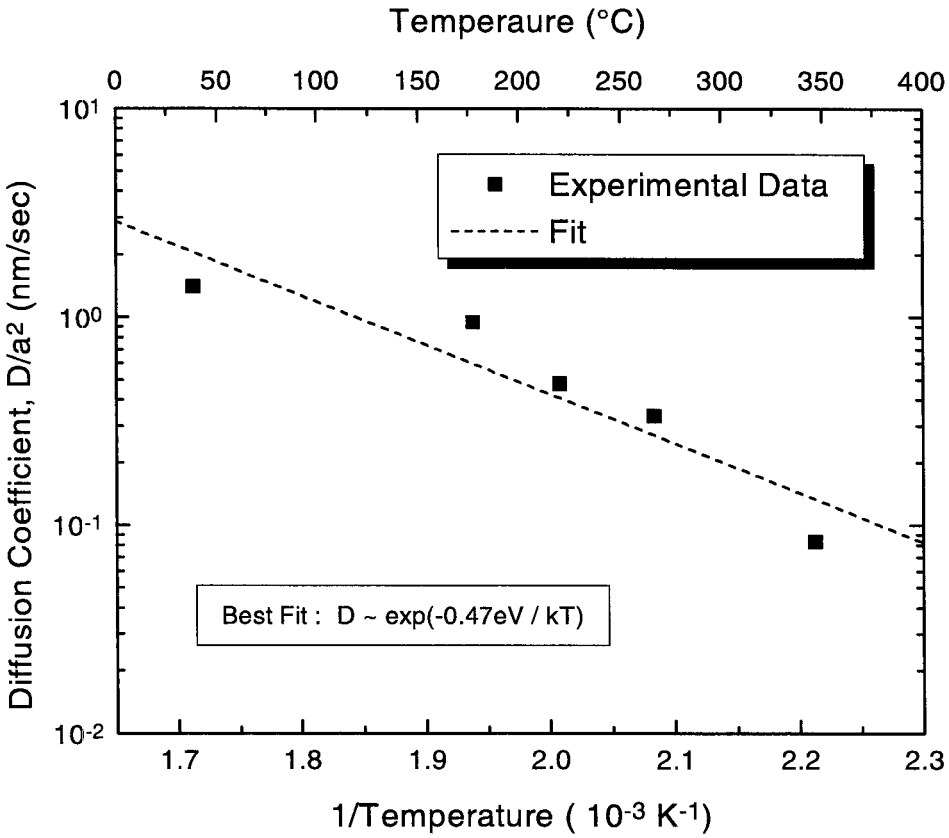

Figure 4.5 Temperature dependent subsurface-surface diffusion coefficient averaged from calculations based on periodic and aperiodic step-flow solutions using the experimentally measured steady-state segregation coefficients from W. Wegscheider, et al. [12].

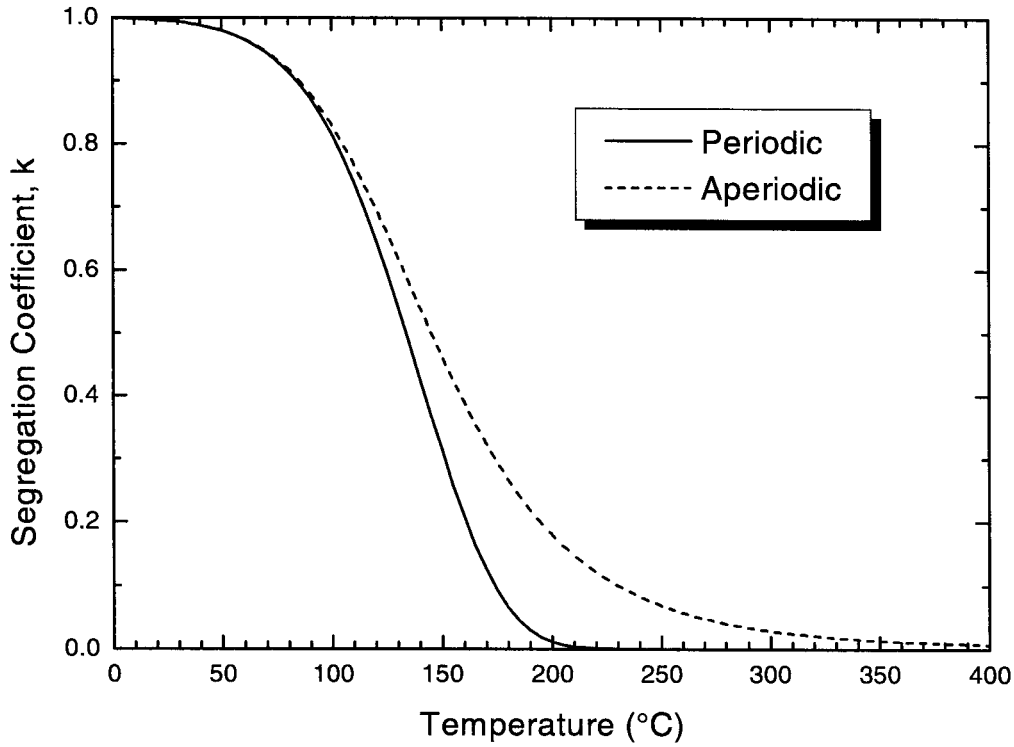

Figure 4.6 Steady-state segregation coefficient of Sn_xGe_{1-x} epitaxial growth as a function of growth temperature at 0.05 nm/sec growth rate (derived from the subsurface-surface diffusion coefficient in Figure 4.5 using data of W. Wegscheider, et al. [12]).

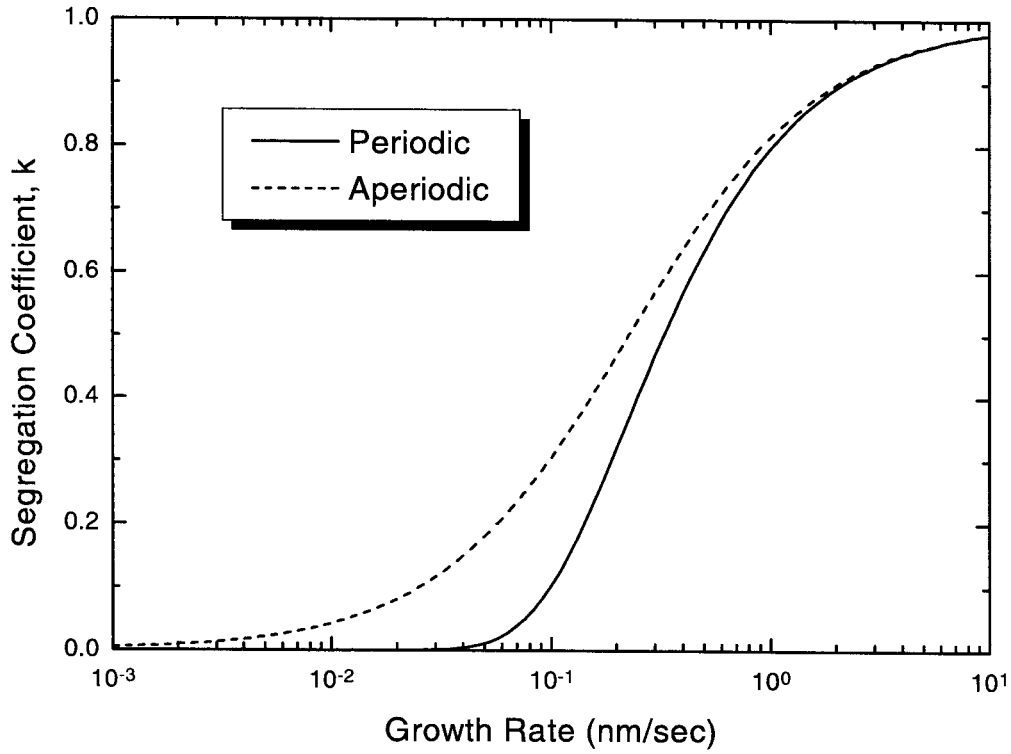

Figure 4.7 Steady-state segregation coefficient of Sn_xGe_{1-x} epitaxial growth as a function of growth rate at 200°C growth temperature (derived from the subsurface-surface diffusion coefficient in Figure 4.5 using data of W. Wegscheider, et al. [12]).

In the case of non-steady-state growth, where the growth flux and its composition vary with time, the surface and bulk compositions become time-dependent. The rate of change of the surface composition is then the net flux into the surface layer which includes the growth flux from the vapor and the trapping

flux to the bulk, so that the time-dependent (or thickness-dependent) surface composition can be determined as [21]

$$\frac{d}{dl}x^{\sigma}(l) = x_j(l) - k(l)x^{\sigma}(l)$$

where $x_j(l)$ is the composition of the growth flux. The time-dependent (or thickness-dependent) bulk composition is therefore

$$x^{\beta}(l) = k(l)x^{\sigma}(l).$$

Here $k(l)$ is the non-equilibrium steady-state segregation coefficient and is in general dependent on the surface composition $x^{\sigma}(l)$. In the case of dilute solution, $k(l)$ become composition independent so that $k(l) = k$, and the time-dependent (or thickness-dependent) bulk composition profile can be solved analytically for an sharp step of growth flux composition from $x_j = 0$ to $x_j = x_{steady}$ at time $t = 0$ (or thickness $l = 0$) (Figure 4.8):

$$x^{\beta}(l) = x_{steady}\left[1 - \exp(-k\,l)\right].$$

Note that $x^{\beta}(\infty) = x_{steady}$. For a non-dilute solution where the steady-state segregation coefficient k is composition-dependent (i.e., lower k for lower surface composition), the initial increase of the bulk composition profile will be slower due to the stronger initial segregation, but the approach to steady state will be faster because the surface composition builds up faster with a stronger initial segregation.

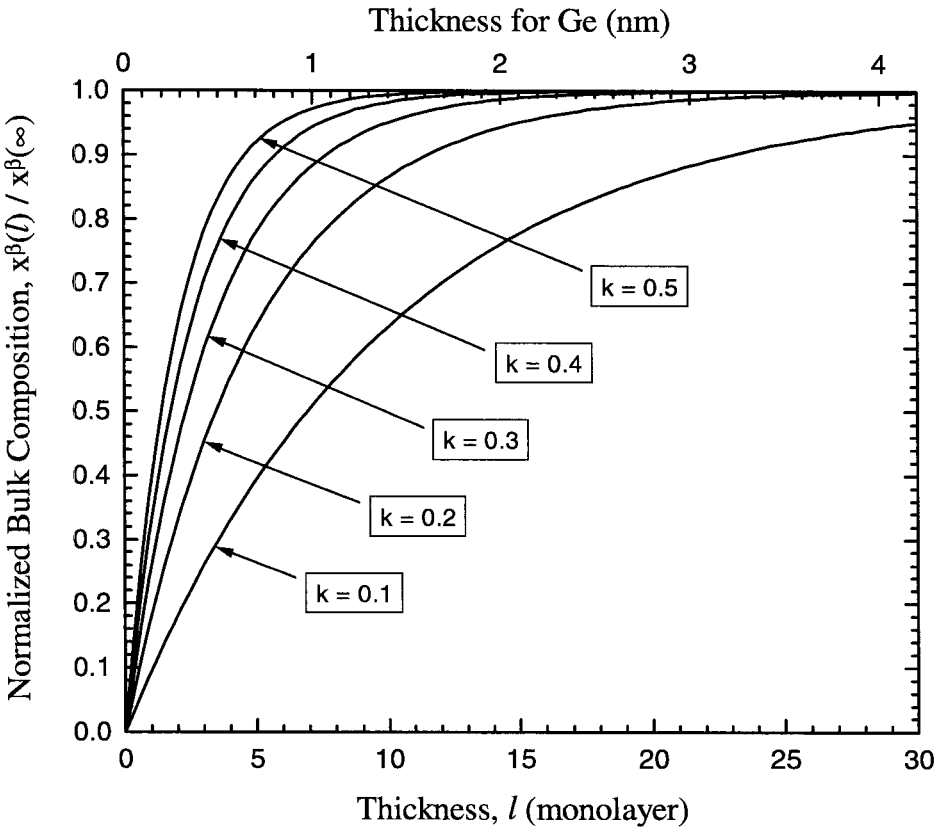

Figure 4.8 Bulk composition profile as a function of germanium thickness for an sharp step change of growth flux composition from $x_j = 0$ to $x_j = x_{steady}$ at time $t = 0$ (or thickness $l = 0$), normalized by the steady-state composition $x^{\beta}(\infty) = x_{steady}$, for various steady-state segregation coefficients k.

4 .3 Segregation Model for Ion-Assisted Epitaxy

For energetic beam deposition, there is beam-induced mixing between the surface and subsurface monolayers which inhibits the surface segregation. The irradiating ion energy should be low enough to avoid extended damage in the bulk crystal [27] while high enough to produce mixing effect between the surface and subsurface layers. Such beam-induced mixing effects can be caused by the processes of subsurface recoil-implantation and direct subsurface implantation. In the process of subsurface recoil-implantation, the incoming energetic ions impinge on the surface atoms and produce recoil events that implant the surface atoms into the subsurface layer. This process occurs for most energetic beam deposition growth methods (e.g., ion-assisted epitaxial growth). In the process of direct subsurface implantation, the deposition flux itself contains energetic components that may directly implant the deposition species into the subsurface layer. This process occurs for growth methods such as direct ion beam deposition, sputter deposition, and pulsed laser deposition.

In the process of subsurface recoil implantation, the surface and subsurface atoms may exchange positions in both the forward and backward directions as a result of the recoil events (Figure 4.9), so that the recoil-mixing flux between the two monolayers can be expressed as:

$$J_R = J_R^+ - J_R^-,$$

where

$$J_R^+ = I\eta\, x^{\beta}\left(1 - x^{\sigma}\right),$$

$$J_R^- = I\eta\,\kappa_R\, x^{\sigma}\left(1 - x^{\beta}\right).$$

J_R^+ and J_R^- are the forward and backward recoil-mixing fluxes from bulk to surface, respectively; I is the irradiating ion flux; η is the recoil-mixing efficiency; and κ_R is the recoil-mixing partition parameter defined as the ratio of backward to forward recoil exchange probability which describes the selectivity of recoil-implantation between the two atomic species in the film.

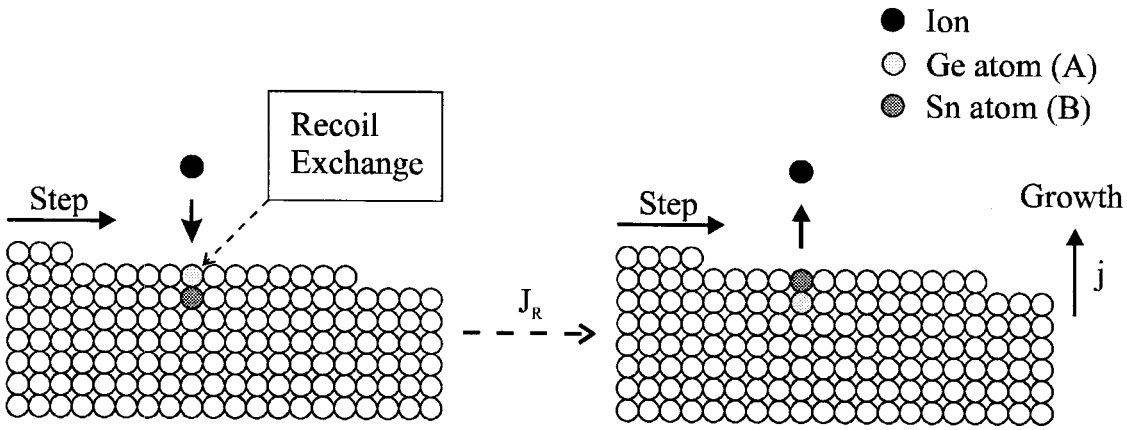

Figure 4.9 Schematic of subsurface recoil-mixing during energetic beam epitaxial growth.

In the process of direct subsurface implantation, depending on the species of the implanted and replaced atom, the net implantation flux also contains a forward component and a backward component (Figure 4.10), so that the direct-implant-mixing flux can be expressed as:

$$J_I = J_I^+ - J_I^-,$$

where

$$J_I^+ = I_A \eta_A x^\beta,$$

$$J_I^- = I_B \eta_B \left(1 - x^\beta\right).$$

J_I^+ and J_I^- are the forward and backward implant-mixing fluxes from bulk to surface, respectively; I_A and I_B are the direct implantation ion fluxes of the A and B species, respectively; and η_A and η_B are the direct-implant efficiencies of the A and B species, respectively. Two convenient parameters that characterize this direct implant process are the effective total direct implantation flux defined as

$$I_{AB}^* = I_A \eta_A + I_B \eta_B \tag{8}$$

and the effective direct implantation composition defined as

$$x_I^* = \frac{I_B \eta_B}{I_A \eta_A + I_B \eta_B}. \tag{9}$$

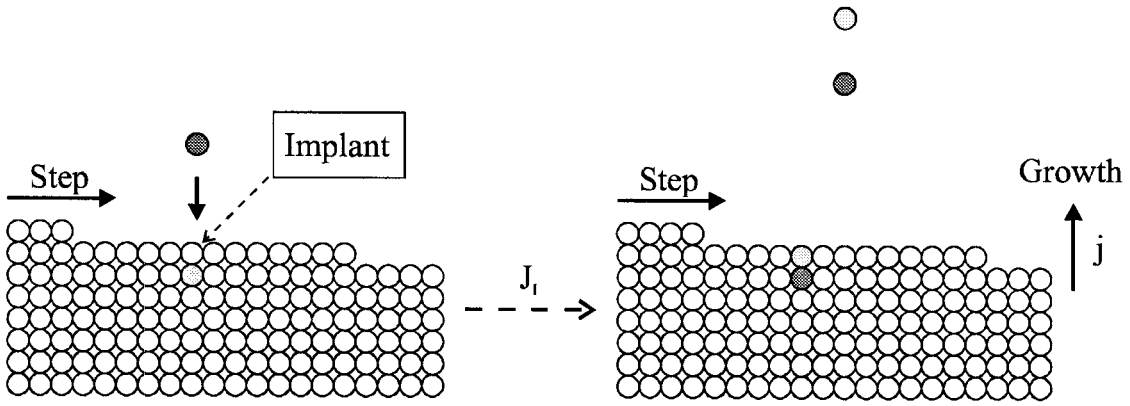

Figure 4.10 Schematic of direct subsurface implantation during energetic beam epitaxial growth.

Similar to the treatment of surface segregation during thermal deposition, for a step wise growth between a step just passing a surface layer and the next step passing the same point, the change of surface layer composition x(t) can be described by the rate equation:

$$\frac{d}{dt}x(t) = -J_D - J_R - J_I,$$

with boundary conditions

$$\left\{x(t)_{t=0} = x^{\sigma}, x(t)_{t=\tau_{moolayer}} = x^{\beta}\right\}.$$

The first term in the equation above describes the thermal diffusion driven by the thermodynamic driving force toward the equilibrium partitioning, which promotes surface segregation. This is the only term in the rate equation for thermal growth. For energetic beam deposition, however, the second and third terms that describe ion-mixing are also present in the rate equation. They drive the system away from

thermodynamic equilibrium partitioning, hence suppressing surface segregation. Replacing $x(t)$ with $k(t)=x(t)/x^{\sigma}$ and t with $l=j\,t$ yields a rate equation similar to the dilute situation:

$$\frac{d}{dl}k(l)=-P_D\left[k(l)-k_e^*\right]-P_R\left[k(l)-k_R^*\right]-P_I\left[k(l)-k_I^*\right],$$

with boundary conditions

$$\left\{k(l)_{l=0}=1, k(l)_{l=1}=k\right\}$$

where

$$P_R = I\eta^*,$$

$$\eta^* = \eta\left(1-x^{\sigma}-\kappa_R\,x^{\sigma}\right),$$

$$k_R^* = \kappa_R/\left(1-x^{\sigma}-\kappa_R\,x^{\sigma}\right),$$

$$P_I = I_{AB}^*,$$

$$k_I^* = x_I^*/x^{\sigma}\,.$$

Here η^* and k_R^* are the composition-dependent effective parameters of recoil-mixing efficiency and recoil-mixing segregation parameter. For dilute solutions where x^{σ} and x^{β} are small, η^* and k_R^* approaches η and κ_R, respectively. The parameter P_R is a dimensionless Péclet number which describes the effective recoil-flux to atom-flux ratio. The parameter k_I^* is the composition-dependent effective direct-implant-mixing segregation parameter. The parameter P_I is a dimensionless Péclet number which describes the effective direct-implant-flux to

atom-flux ratio. Note that the direct-implant-mixing is especially efficient in suppressing thermal segregation when the surface coverage x^{σ} is small since $k_I^* = x_I^*/x^{\sigma}$ becomes large. Rearranging this rate equation yields the central equation for energetic beam epitaxial growth which is very similar to the thermal segregation rate equation:

$$\frac{d}{dl}k(l) = -P^*\left[k(l) - k^*\right],$$

with boundary conditions

$$\left\{k(l)_{l=0} = 1, k(l)_{l=1} = k\right\}$$

where

$$P^* = P_D + P_R + P_I,$$

$$k^* = \left(P_D k_e^* + P_R k_R^* + P_I k_I^*\right)/P^*.$$

Here P^* is an effective Péclet number of total flux ratio which is the sum of the Péclet number of the thermal diffusion process, the recoil mixing process, and the implant-mixing process. The parameter k^* is an effective segregation coefficient, which is the average of k_e^* , k_R^* and k_I^* weighted by their respective Péclet numbers. This central rate equation can be solved in analogy to the thermal segregation rate equation with the following steady-state solutions:

$$k_{per} = k^* + \frac{1-k^*}{e^{P^*}},$$

$$k_{aper} = k^* + \frac{1-k^*}{1+P^*},$$

where k_{per} is the solution for perfectly periodic step flow growth and k_{aper} is the solution for totally random aperiodic step flow growth. They are the general solutions for segregation rates during energetic beam epitaxial growth. They have the same mathematical form as the analysis for conventional growth except that the Péclet number and the segregation coefficient are replaced by values that reflects the combination of the thermal diffusion, recoil-mixing, and implant-mixing processes. They can also be used to describe the ion-assisted dopant incorporation during epitaxial growth, where in most cases the solutions are dilute and D^*, k_e^*, η^*, k_R^* approach the values of D, κ_e, η, κ_R in this limit. For non-dilute solutions, D^*, k_e^*, η^*, k_R^* are in general dependent on the surface composition x^σ: the parameters D^* and η^* decrease with increasing x^σ, while the parameters k_e^* and k_R^* increase with increasing x^σ. Note that in this model of energetic beam epitaxial growth the effect of ion energy on surface segregation is included implicitly through the values of the recoil-mixing and implant-mixing efficiencies which are ion-energy dependent. In practice, the optimal ion energy should be low enough to avoid damage to the bulk crystals and high enough to produce significant surface-subsurface mixing.

In the case of ion-assisted molecular beam epitaxy without direct-implantation (i.e., recoil-mixing only), an important parameter in the steady-state

solutions is the dimensionless recoil-mixing Péclet number P_R (effective ion-flux to atom-flux ratio). A plot of steady-state segregation coefficient k as a function of P_R calculated from the model with a set of specifically chosen parameters is shown in Figure 4.11. As expected, the model predicts that the segregation coefficient k approaches $k_{thermal}$, that of the thermal growth without ion irradiation, when P_R is much less than unity. The segregation coefficient k approaches the recoil-mixing segregation coefficient k_R^* when P_R is much larger than unity. The transition occurs over a P_R range of one or two orders of magnitude. The exact transition point also depends on the value of the diffusion-flux to atom-flux ratio (P_D). The model suggests that in order to significantly suppress segregation by ion irradiation, an actual ion-flux to atom-flux ratio of approximately unity or greater is required.

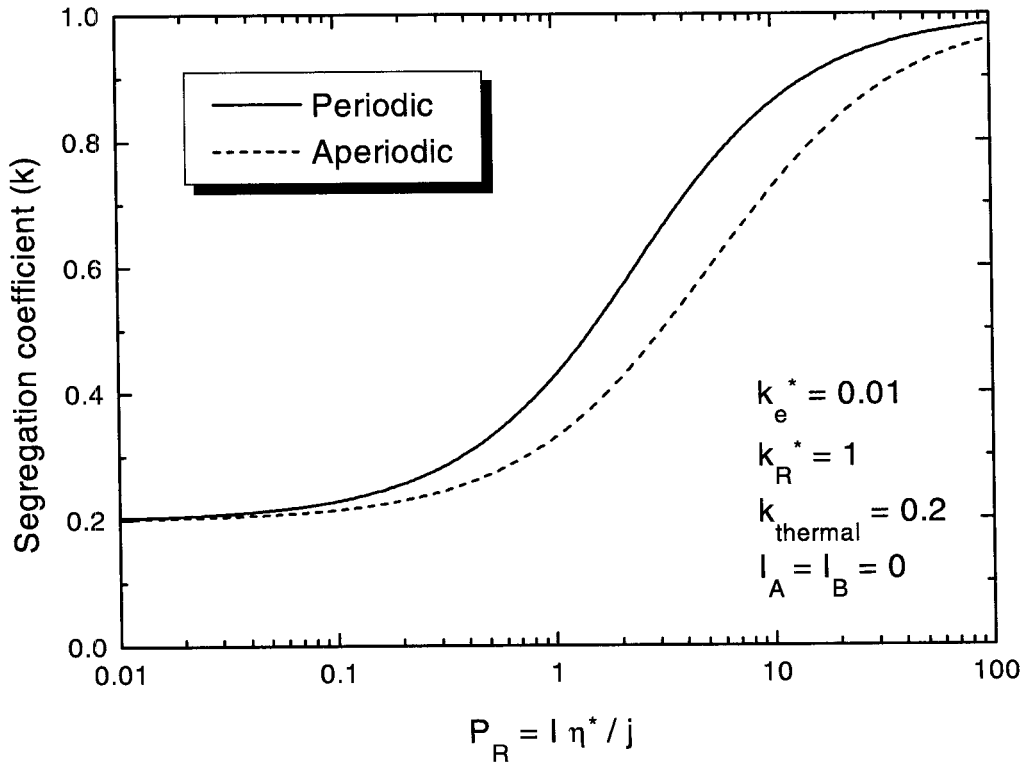

Figure 4.11 Steady-state segregation coefficient as a function of ion flux to growth atom flux ratio during ion-assisted epitaxial growth.

For non-steady-state growth where the composition of the growth flux and ion flux varies with time, the surface and bulk compositions become time dependent and can be determined in the same way as in the thermal epitaxial growth:

$$\frac{d}{dl}x^{\sigma} = x_j - k\,x^{\sigma}$$

$$x^{\beta} = k\,x^{\sigma},$$

where k is the steady-state segregation coefficient for energetic beam epitaxial growth.

4 .4 Surface Segregation in Ion-Assisted Sn_xGe_{1-x} Epitaxy

To compare the model of energetic beam epitaxial growth with ion-assisted molecular beam epitaxy of Sn_xGe_{1-x}, a set of Sn_xGe_{1-x} (50nm) / Ge / Si (100) samples were grown by ion-assisted molecular beam epitaxy with various irradiating Ar^+ ion flux (~ 50 eV) and alloy film composition. The irradiating ion flux was generated by an electron cyclotron resonance ion source and the growth temperature was 200°C. The details of the growth were described in the previous chapter. The resulting samples were characterized by *in situ* reflection high energy electron diffraction, optical microscopy, and Rutherford backscattering spectroscopy. Note that the 50 nm thickness of the Sn_xGe_{1-x} alloy films were well above the minimum thickness for steady-state segregation (which is less than 5 nm for steady-state segregation coefficients above k=0.1). One set of the samples were found to have uniformly incorporated Sn in the Sn_xGe_{1-x} film while the others were found to have surface segregated Sn. For the Sn segregated samples, *in situ*

reflection high energy electron diffraction showed decreasing diffraction intensity during growth. Optical microscopy inspection revealed that the sample surfaces were optically rough with micron-sized droplets, and Rutherford backscattering analysis indicated severe surface segregation of Sn. For the samples without tin segregation, *in situ* reflection high energy electron diffraction showed constant diffraction intensity during growth. Optical microscope inspection showed optically smooth sample surfaces, and Rutherford backscattering analyses indicated uniform incorporation of the Sn_xGe_{1-x} alloy. If we assume that the film surface is almost completely covered by the segregated tin when epitaxy breaks down as a result of severe segregation, then the maximum bulk tin concentration at this transition can be estimated as $x^{\beta} = k\, x^{\sigma} \approx k$. The experimentally measured values of bulk tin concentration x^{β} from these samples grown with different ion fluxes are summarized in Figure 4.12 and compared with a plot of calculated steady-state segregation coefficient k as a function of the effective ion-flux to atom-flux ratio using the proposed model with a set of specifically chosen parameters. The calculation assumed that epitaxy breakdown occurs, possibly through island formation and growth, when the surface tin concentration exceeds an ion-flux-independent critical concentration. The effective diffusion-flux to atom-flux ratio was chosen such that a segregation coefficient of about k=0.2 was obtained for thermal growth (zero ion flux). This corresponds to the Sn segregation during our thermal Sn_xGe_{1-x} growth at a substrate temperature of 200°C. The equilibrium segregation coefficient k_e^* (for $j \to 0$ and $I \to 0$) was chosen to be 0.01 which corresponds to a Sn_xGe_{1-x} alloy film covered by a tin rich

surface with a bulk tin concentration close to the equilibrium solid solubility. The effective recoil-mixing segregation coefficient k_R^* was set to unity (note that with a segregated Sn rich surface layer $x^\sigma \to 1$ so that $k_R^* \to 1$ as long as $\kappa_R >> 1 - x^\sigma$). The calculation was fitted to the experimental data yielding effective ion-mixing efficiency of $\eta^* \approx 0.2$ for 50 eV Ar^+ irradiation. The experimental results presented in the figure were consistent with the proposed segregation model, although the range of the experimental growth conditions was limited by the maximum ion flux obtainable with our current experimental setup.

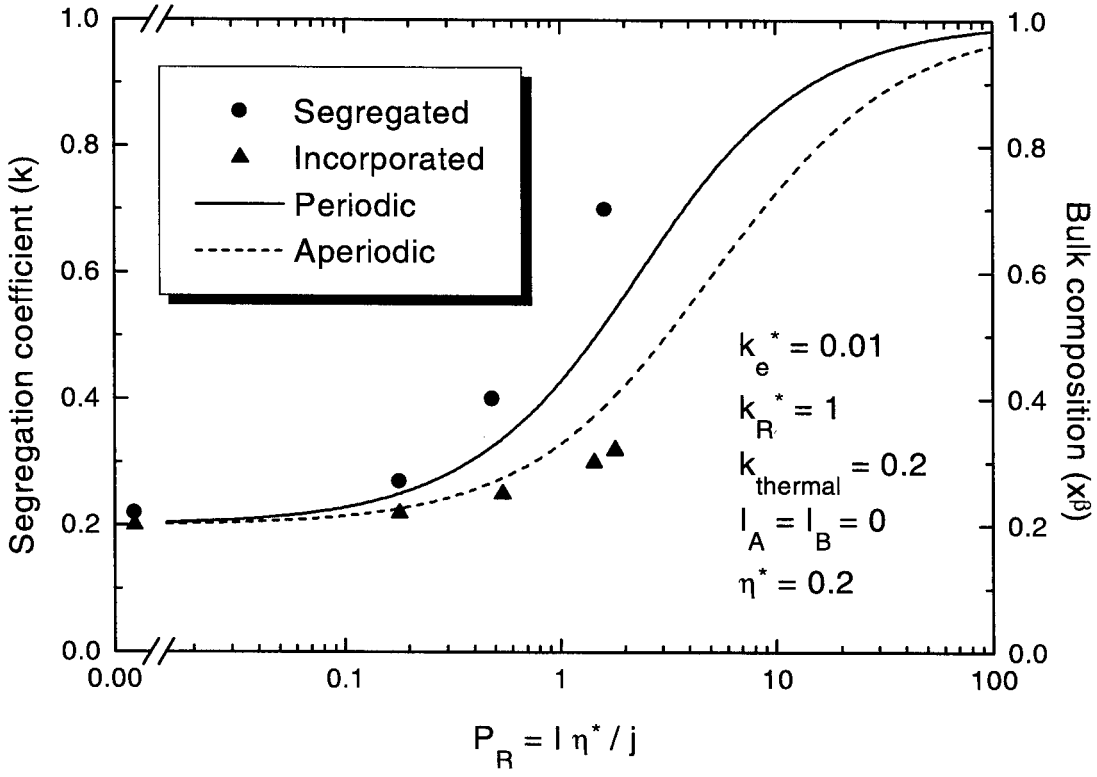

Figure 4.12 Comparison of the segregation model for energetic beam epitaxy with experimental results of Sn_xGe_{1-x} ion-assisted molecular beam epitaxy.

4 .5 Conclusions

By extending a partitioning model for conventional epitaxial growth, an analytical model is developed to describe the segregation behavior during energetic beam

deposition using a partition rate equation that incorporates both direct and recoil mixing induced by energetic beams. The experimental results from ion-assisted Sn_xGe_{1-x} growth were consistent with the proposed model. The model suggests that the tin concentration in the Sn_xGe_{1-x} film can be significantly increased when the effective irradiating ion flux is increased so as to be large compared to the growth flux. The tin concentration can also be increased by incorporation via direct ion beam deposition, or by optimizing the other growth parameters such as growth temperature, growth rate, ion energy, ion flux, ion species, and substrate type. The model describes both the steady-state and the time-dependent behaviors and can be applied to general energetic beam epitaxial growth techniques including ion-assisted epitaxy, sputter deposition, direct ion beam deposition, as well as pulsed laser deposition, and can be used for both alloy growth and dopant incorporation.

Bibliography

[1] D.W. Jenkins and J.D. Dow, Phys. Rev. B 36 7994 (1987).

[2] H.A. Atwater, G. He, K. Saipetch, Mat. Res. Soc. Symp. Proc. 355, 123 (1995).

[3] B. Bouhafs, F. Benkabou, M. Ferhat, B. Khelifa, J.P. Dufour, H. Aourag, Infrared Phys. & Tech. 36, 967 (1995).

[4] K.A. Mader, A. Baldereschi, H. von Kanel, Solid State Comm. 69, 1123 (1989).

[5] A. Harwit, P.R. Pukite, J. Angilello and S.S. Iyer, Thin Solid Films 184, 395 (1990).

[6] J. Piao, R. Beresford, T. Licata, W.I. Wang and H. Homma, J. Vac. Sci. Technol. B 8, 211 (1990) .

[7] W. Wegscheider, K. Eberl, U. Menczigar and G. Abstreiter, Appl. Phys. Lett. 57, 875 (1990).

[8] H.-J. Gossmann, J. Appl. Phys. 68, 2791 (1990).

[9] E.A. Fitzgerald, P.E. Freeland, M.T. Asom, W.P. Lowe, R.A. Macharrie, JR., B.E. Weir, A.R. Kortan, F.A. Thiel, Y.-H. Xie, A.M. Sergent, S.L. Cooper, G.A. Thomas and L.C. Kimerling, J. Elec. Mat. 20, 489 (1991).

[10] K. Eberl, W. Wegscheider and G. Abstreiter, J. Crystal Growth 111, 882 (1991).

[11] P. Vogl, J. Olajos, W. Wegscheider and G. Abstreiter, Surface Science 267, 83 (1992).

[12] W. Wegscheider, J. Olajos, U. Menczigar, W. Dondl and G. Abstreiter, J. Crystal Growth 123, 75 (1992).

[13] S.I. Shah, J.E. Greene, L.L. Abels, Q. Yao and P.M. Raccah, J. Crystal Growth 83, 3 (1987).

[14] S. Oguz, W. Paul, T.T. Deutsch, B-Y. Tsaur and D.V. Murphy, Appl. Phys. Lett. 43, 848 (1983).

[15] I.T.H Chang, B. Cantor and A.G. Cullis, J. Non-Crystalline Solids 117/118, 263 (1990).

[16] S.M. Lee, J. Appl. Phys. 75, 1987 (1994).

[17] G. He and H.A. Atwater, Appl. Phys. Lett. 68, 664 (1996)

[18] J. Knall, J.-E. Sundgren, L.C. Markert and J.E. Greene, Surface Science 214, 149 (1989).

[19] G. He and H.A. Atwater, Nucl. Instrum. Methods B 106, 126 (1995).

[20] G. He and H.A. Atwater, Mat. Res. Soc. Symp. Proc. 399, 380 (1996).

[21] J.Y. Tsao, Materials Fundamentals of Molecular Beam Epitaxy, Academic Press, San Diego, 1993, pp. 275.

[22] M.J. Aziz, J. Appl. Phys. 53, 1158 (1982).

[23] L.M. Goldman, M.J. Aziz, J. Mater. Res. 2, 524 (1987).

[24] M.J. Aziz and T. Kaplan, Acta Metall. 36, 2335 (1988).

[25] D.J. Eaglesham, H.-J. Gossmann, M. Cerullo, Phys. Rev. Lett. 65, 1227 (1990).

[26] M.V.R. Murty, H.A. Atwater, Phys. Rev. B 49, 8483 (1994).

[27] M.V.R. Murty, H.A. Atwater, Phys. Rev. B 45, 1507 (1992).

Chapter 5

OPTICAL ANALYSIS OF Sn_xGe_{1-x} ELECTRONIC STRUCTURE

5 .1 Introduction

The most essential electronic property of Sn_xGe_{1-x} is its composition-dependent tunable energy band gap. Tight-binding and pseudopotential calculations have predicted that diamond-cubic Sn_xGe_{1-x} alloys may have a direct band gap that is continuously tunable from E_g=0.55 eV to E_g=0 eV for tin concentrations in the range of x=0.2 to x=0.6 [1]-[4]. A small direct band gap was also suggested by tight-binding, pseudopotential, and density functional theory calculations for ordered zinc-blende structure SnGe [4]-[7]. Quantum-size effect on energy band gap of pure diamond-cubic tin was also investigated theoretically [8] [9].

Experimental characterization of the energy band gap usually involves optical measurements of the material. One previous report of optical characterization of Sn_xGe_{1-x} has been reported using optical transmission measurements of Sn_xGe_{1-x} thin films [10]. Unfortunately, due to the strong Fabry-Perot oscillations in the transmission spectra as a result of thin film interference

effects, quantitative information of the alloy energy band gap was not obtained. In order to quantitatively characterize the Sn_xGe_{1-x} band gap, the optical constants of Sn_xGe_{1-x} were analyzed experimentally as part of this thesis work. The optical constants include both the real and the imaginary parts of the wavelength-dependent complex index of refraction, which completely describes the optical behavior of any linear optical media. Important parameters, such as the absorption coefficient, which is directly related to the band gap as a result of interband optical transition, can be readily calculated from the optical constants. The band gap can be determined quantitatively from the onset of the interband absorption edge in the absorption spectrum. Since Sn_xGe_{1-x} is only available in the form of thin films, thin film interference effects must be considered in the analysis of optical constants from experimental data.

In order to determine the optical constants of Sn_xGe_{1-x} as a function of wavelength (or photon energy) without ambiguities from the thin film interference effects, Sn_xGe_{1-x} films of different thicknesses were fabricated and optical transmission spectra were experimentally measured as a function of the film thickness using Fourier transform infrared spectroscopy (FTIR). A numerical model was also developed to calculate the multilayer thin film interference effects through exact solutions of Maxwell's equations in the multilayer structures. The measured thickness-dependent transmission spectra were then fit to the numerical interference model through a χ^2 (chi-square) minimization analysis [11] to obtain the optical constants spectra with error estimations established through χ^2 error

analyses. The optical constants spectra were used to calculate the optical absorption spectra from which Sn_xGe_{1-x} band gap information was obtained.

5 .2 Determination of Thin Film Optical Constants

The optical constants include the refractive index $n(\omega)$ and the extinction coefficient $k(\omega)$ which are the real and the imaginary parts of the complex index of refraction, respectively [12]:

$$\tilde{n}(\omega) = n(\omega) - i\,k(\omega)$$

where $\tilde{n}(\omega)$ is the complex index of refraction. The wavelength-dependent optical constants completely describe the optical behavior of any linear optical media. The optical constants are simple scalars for isotropic media including crystals with cubic symmetries (e.g., diamond-cubic crystals in this case).

Various methods can be used to measure the optical constants [12]. Most methods involve measurements of quantities such as light intensity, direction, polarization, phase shift, or a combination of the above. Since Sn_xGe_{1-x} is only available in the form of thin films, bulk measurement methods, such as refraction angle measurements, are not applicable. Due to the thin film nature of the material, any quantitative measurements must include thin film interference effects.

Treatment of such an interference effect in absorbing materials such as Sn_xGe_{1-x} requires extensive numerical data analysis.

Since the spectral range of interest for Sn_xGe_{1-x} is the interband absorption region in the infrared, one of the readily measurable optical quantities is its optical transmission coefficient which can be obtained by Fourier transform infrared spectroscopy (FTIR). The transmission spectrum contains both the absorption effect, which is mostly determined by the extinction coefficient, and the thin film interference effect, which is mostly determined by the refractive index.

One widely used method to calculate both the extinction coefficient and the refractive index from a single measured spectrum is to use the Kramers-Kronig relationships [13] which relate the extinction coefficient and the refractive index through a set of integral transformations as

$$n(\varpi) = n_\infty + \frac{2}{\pi} P\int_0^\infty \frac{\varpi' k(\varpi')}{\varpi'^2 - \varpi^2} d\varpi'$$

$$k(\varpi) = -\frac{2\varpi}{\pi} P\int_0^\infty \frac{n(\varpi') - n_\infty}{\varpi'^2 - \varpi^2} d\varpi'$$

where P stands for the principle value of the integral since it contains a singularity at $\varpi' = \varpi$. Unfortunately, the Kramers-Kronig transformations contain integrals over infinite spectral range. Since experimental measurements can only be performed over a finite spectral range, assumptions must be made regarding properties outside the measured range. Kramers-Kronig transformations are often used for measurements of isolated absorption features such as molecular

absorptions since the optical properties outside the measured spectral range are relatively simple to describe. However, for measurement of the interband absorption of a solid such as Sn_xGe_{1-x}, estimation of optical properties outside the measured spectral range is difficult due to the complicated strong absorption features from the various overlapping higher-lying energy bands in the electronic structure.

To calculate the optical constants without the knowledge of optical properties over an infinite (or a very wide) spectral range, optical transmission spectra as a function of film thickness were measured. The thickness-dependent transmission spectra contain extra information from which both the refractive index and the extinction coefficient can be determined [14]. More specifically, since the optical constants provide a complete description of any linear optical media, the optical transmission spectra is uniquely determined by the optical constants of the films in any given film structure with known film thicknesses:

$$T(\omega) = T_d\left(n(\omega), k(\omega), \omega\right)$$

where $T(\omega)$ is the optical transmission and d is the film thickness. Although the exact analytical form of the transmission function $T_d\left(n(\omega), k(\omega), \omega\right)$ is very complicated in the case of multilayer structures, it is at least possible to calculate numerically. In principle, if two transmission spectra are measured for two different film thicknesses d_1 and d_2, then two different equations can be constructed using the transmission function $T_d(n,k)$ as

$$\begin{cases} T_1(\omega) = T_{d1}\left(n(\omega), k(\omega), \omega\right) \\ T_2(\omega) = T_{d2}\left(n(\omega), k(\omega), \omega\right) \end{cases}$$

where $T_1(\omega)$ and $T_2(\omega)$ are transmission coefficients to be measured experimentally for the two different film thicknesses d_1 and d_2. The two unknown variables $n(\omega)$ and $k(\omega)$ can then be solved in principle from the two independent equations.

More generally, if the transmission spectra are measured for more than two different film thicknesses, the optical constants can be determined with even higher accuracy (i.e., better statistical confidence) by fitting the measured spectra to the transmission function through minimizing the χ^2 function which is defined as

$$\chi(\omega)^2 = \sum_{i=1}^{N} \left(\frac{T(\omega)_i - T_{di}\left(n(\omega), k(\omega), \omega\right)}{\sigma_i} \right)^2$$

where N is the total number of different measurements and σ_i are the standard deviations of the transmission measurement errors [11]. An additional advantage of the χ^2 analysis is that errors can be estimated statistically. Assuming a normal error distribution, the standard error of a fitted parameter a (a can be either $n(\omega)$ or $k(\omega)$ in this case) can be estimated as

$$\sigma_a(\omega) = \sqrt{\sum_{i=1}^{N} \left(\sigma_i(\omega) \Big/ \frac{\partial T_{di}}{\partial a}(\omega) \right)^2} \ .$$

Furthermore, in case the measurement uncertainties σ_i are not known in advance, an estimation can be made if we assume that the model fits well and all measurements have the same standard deviation as

$$\sigma_i(\omega) = \sigma(\omega) = \sqrt{\sum_{i=1}^{N} \left(T_i(\omega) - T_{di}\left(n(\omega), k(\omega), \omega\right) \right)^2 \Big/ (N - M)}$$

where M is the number of fitting parameters ($M = 2$ in the case of optical constants).

5 .3 Measurement of Sn_xGe_{1-x} Infrared Transmission

To study the Sn_xGe_{1-x} energy band gap as a function of the alloy composition, four series of epitaxial samples with different alloy compositions were prepared. The alloy compositions are x=0 (pure germanium), x=0.06, x=0.11, and x=0.15. Each sample series contain six samples of the same compositions but different thicknesses ranging approximately from 50 nm to 300 nm at 50 nm intervals (Figure 5.1).

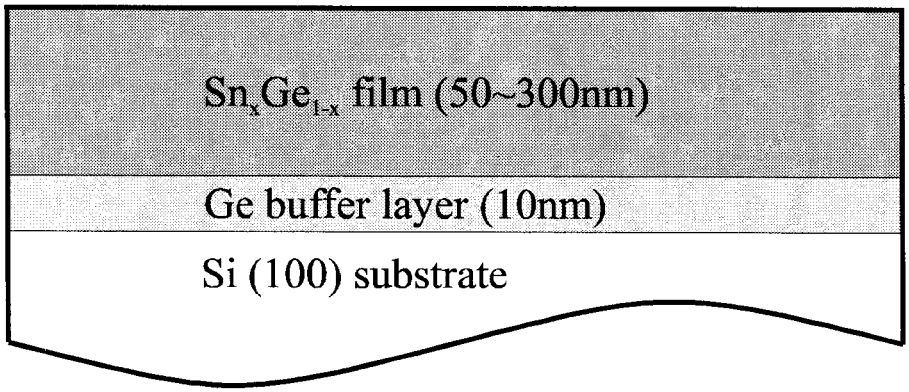

Figure 5.1 Structure of Sn_xGe_{1-x} alloy samples grown for optical analysis.

All samples were grown on double-side polished float-zone n-type (100) silicon substrates with 2000 Ω·cm resistivity by conventional molecular beam epitaxy. The details of the substrate cleaning and preparation procedures are described in the previous chapters. During growth the silicon substrates were first heated up to 550°C to produce a (2×1) reconstructed clean silicon surface as indicated by *in situ* reflection high energy diffraction. For the pure germanium sample series, epitaxial germanium layers were grown at 450°C growth temperature with a growth rate of 0.05 nm/sec. For all the other samples, a 5 nm germanium buffer layer was first grown on the silicon substrate at 450°C with a growth rate of 0.05 nm/sec. The substrate was then cooled down to approximately 180°C. This cooling down process takes about one hour. Another 5 nm of germanium buffer was then grown at 180°C to stabilize the growth rate of 0.05 nm/sec. Following this second germanium buffer layer, growth of epitaxial Sn_xGe_{1-x} alloy layers was started immediately at the same growth temperature and

growth rate. The germanium growth rate was feedback controlled by a quartz crystal thickness monitor adjacent to the sample, and the tin growth rate was controlled by the voltage of the source heater. *In situ* reflection high energy electron diffraction showed spotty diffraction patterns throughout the growth of the alloy films, indicating epitaxial growth with atomically rough surfaces at monolayer scales (Figure 5.2). Optical microscopy showed that all sample surfaces were optically clear (Figure 5.3). Atomic force microscopy over a few 500 nm × 500 nm areas on the $Sn_{0.15}Ge_{0.85}$ sample (300 nm thick) showed that the root-mean-square surface roughness was approximately 0.6 nm and the maximum peak-to-valley roughness was about 4 nm. The exact composition and thickness of the samples were measured by Rutherford backscattering spectroscopy which also confirmed uniform alloy composition in the alloy films (Figure 5.4).

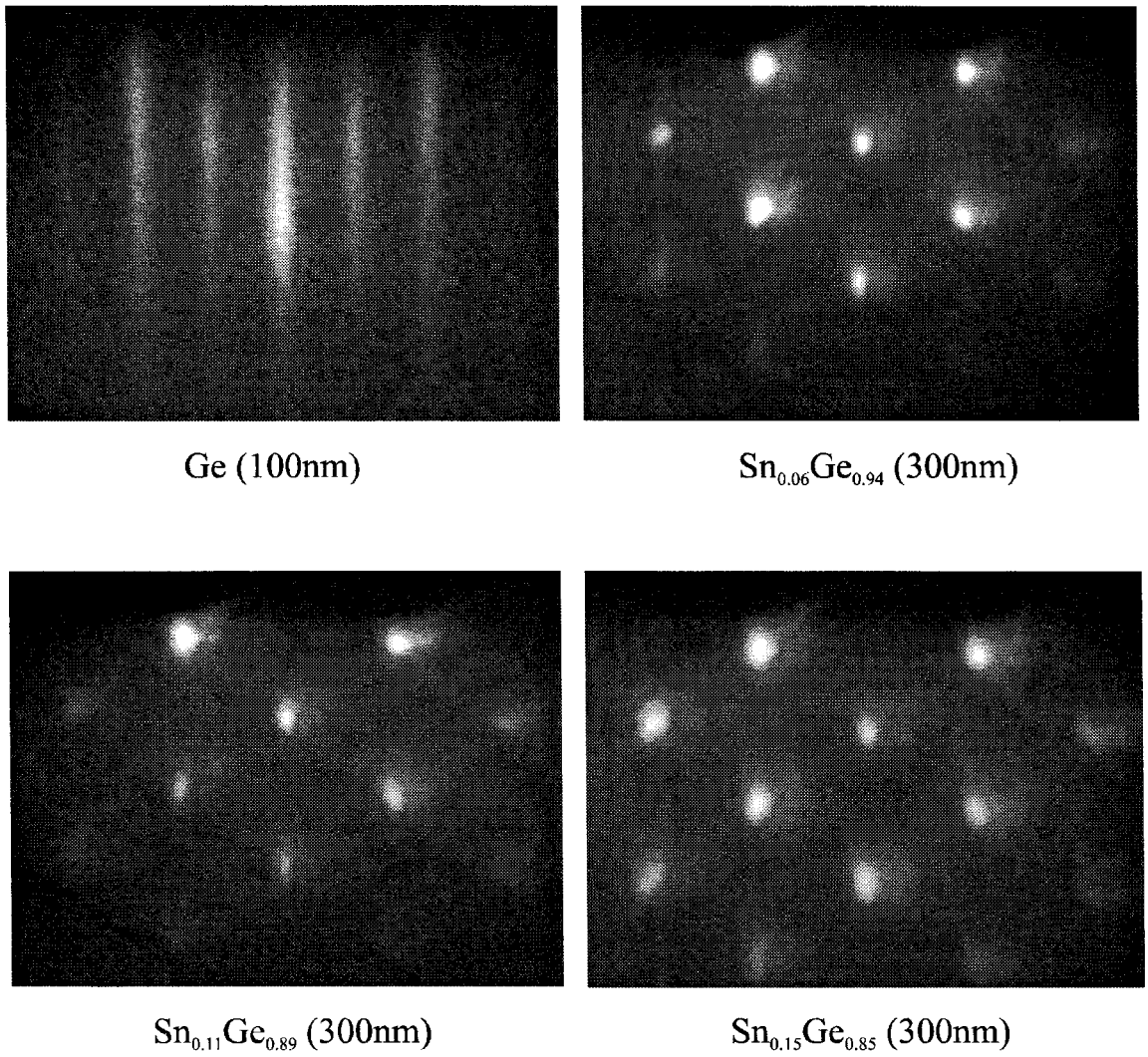

Figure 5.2 Reflection high energy electron diffraction of Sn_xGe_{1-x} samples grown by molecular beam epitaxy for optical analysis.

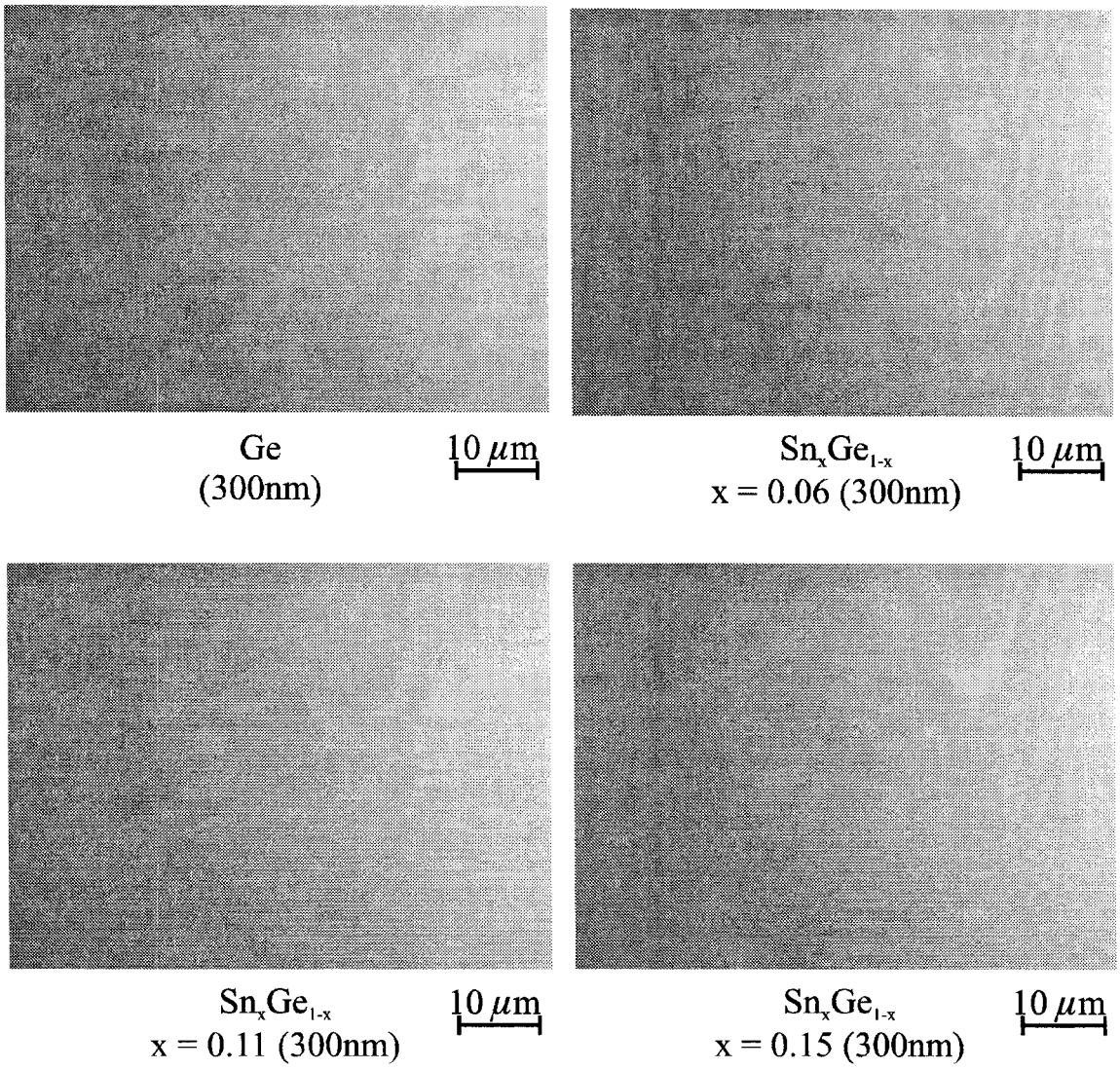

Figure 5.3 Optical micrograph of Sn_xGe_{1-x} samples (300 nm) grown by molecular beam epitaxy for optical analysis.

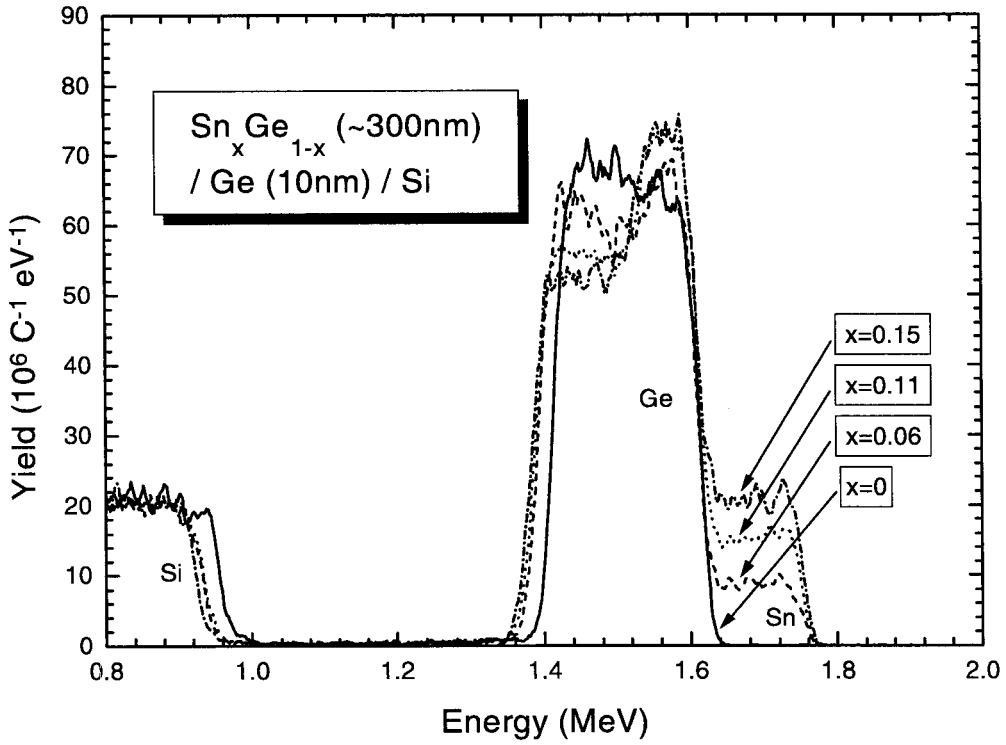

Figure 5.4 Rutherford backscattering spectra of Sn_xGe_{1-x} samples (300 nm) grown by molecular beam epitaxy for optical analysis.

High resolution x-ray diffraction of the (400) and (440) diffraction peaks showed that the alloy films are epitaxial and diamond cubic (Figure 5.5 and Figure 5.6). The (400) and (440) diffraction curves of the same sample were measured at exactly the same location on the sample to assure the consistency between the in-plane and out-of-plane measurements. The diffraction intensities from the alloy films were similar to the diffraction intensity of the pure germanium sample. The

peak widths of the alloy films are slighter wider for higher tin concentrations, which may indicate increased misfit dislocation densities at higher tin concentrations.

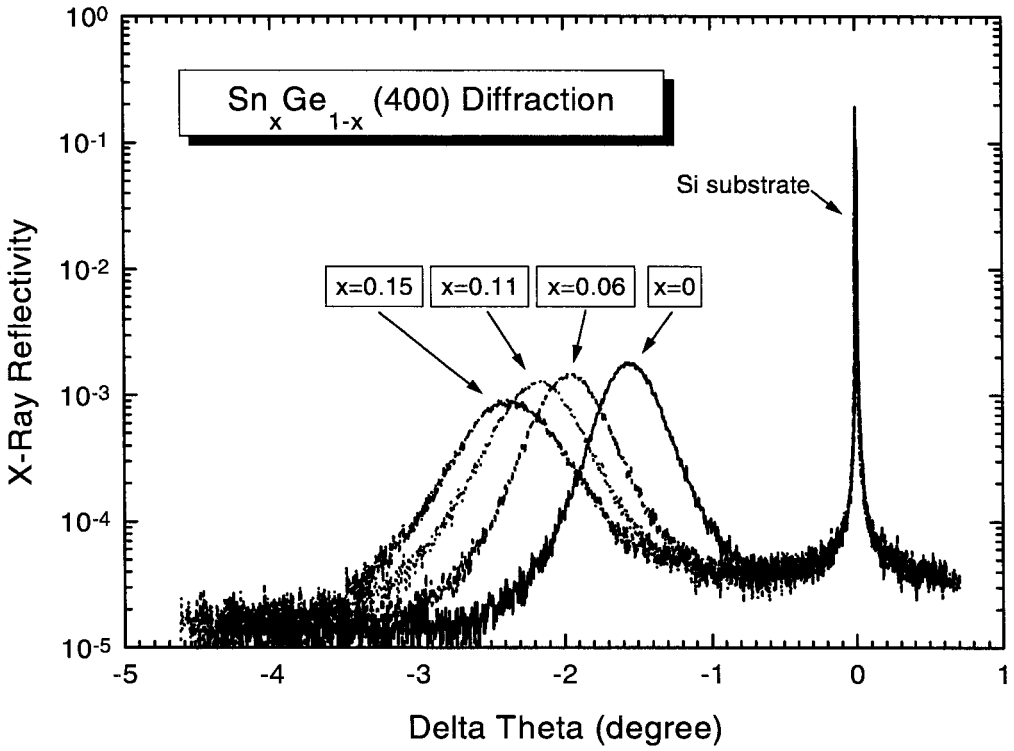

Figure 5.5 High resolution x-ray diffraction of (400) peak of Sn_xGe_{1-x} (300 nm) samples grown by molecular beam epitaxy for optical analysis.

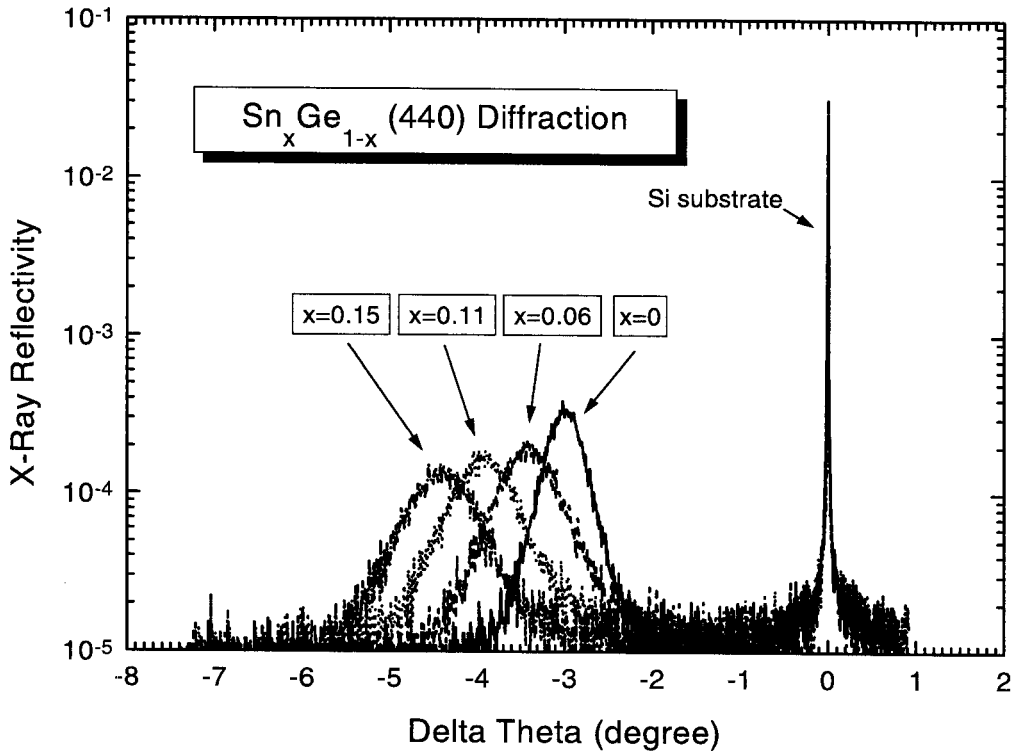

Figure 5.6 High resolution x-ray diffraction of (400) peak of Sn_xGe_{1-x} (300 nm) samples grown by molecular beam epitaxy for optical analysis.

In-plane, out-of-plane, and relaxed lattice parameters of the epitaxial films can be determined from the peak shift relative to the silicon substrate peak in the (400) and (440) x-ray diffraction curves (Figure 5.7). The resulting relaxed lattice parameters match Vegard's law very well, suggesting that Vegard's law is a good approximation for diamond-cubic Sn_xGe_{1-x} alloys with moderate tin concentrations (up to x=0.15). The resulting in-plane and out-of-plane lattice constants indicated

that the alloy films were close to be completely strain relieved, with some small residual strains smaller or close to the error limits of the experiments (about 0.005). There may be some slightly higher residual strain in the lower tin concentration samples which may suggest a slower strain relaxation as a result of smaller lattice mismatch. The germanium reference sample is expected to be almost completely strain relaxed since its growth temperature was much higher (450°C).

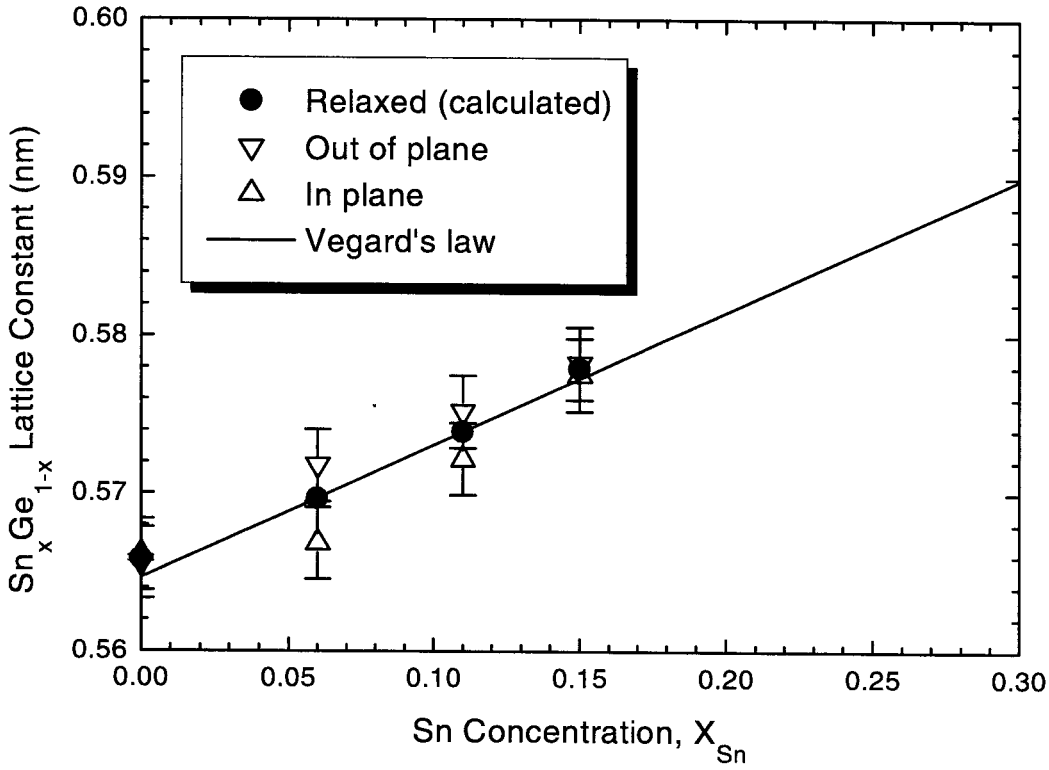

Figure 5.7 Lattice parameters measured by high-resolution x-ray diffraction as a function of tin concentration compared with Vegard's Law.

Room temperature carrier mobility and concentration of the samples were estimated from Hall effect measurements made in a van der Pauw configuration [15] (Table 5.1). Good ohmic contacts between the tungsten probe tips and the alloy films were easily obtained without indium paste. The epitaxial films were found to be relatively heavily doped p-type. The resistivity and carrier type obtained by Hall effect measurements were consistent with spreading resistance

measurements performed on the same samples which also showed uniform resistivity profile across the alloy films within the experimental uncertainties of the spreading resistance measurements (Figure 5.8). The small fluctuations in the spreading resistance profiles near the sample surfaces may be experimental errors.

Composition X	Resistivity (Ω·cm)	Carrier Type (P / N)	Carrier Density (cm^{-3})	Hall Mobility ($cm^2 V^{-1} s^{-1}$)
0	0.092	P	1.0×10^{17}	660
0.06	0.073	P	7.0×10^{17}	120
0.11	0.067	P	1.0×10^{18}	90
0.15	0.036	P	3.1×10^{18}	60

Table 5.1 Carrier transport properties of the Sn_xGe_{1-x} samples obtained by Hall effect measurements.

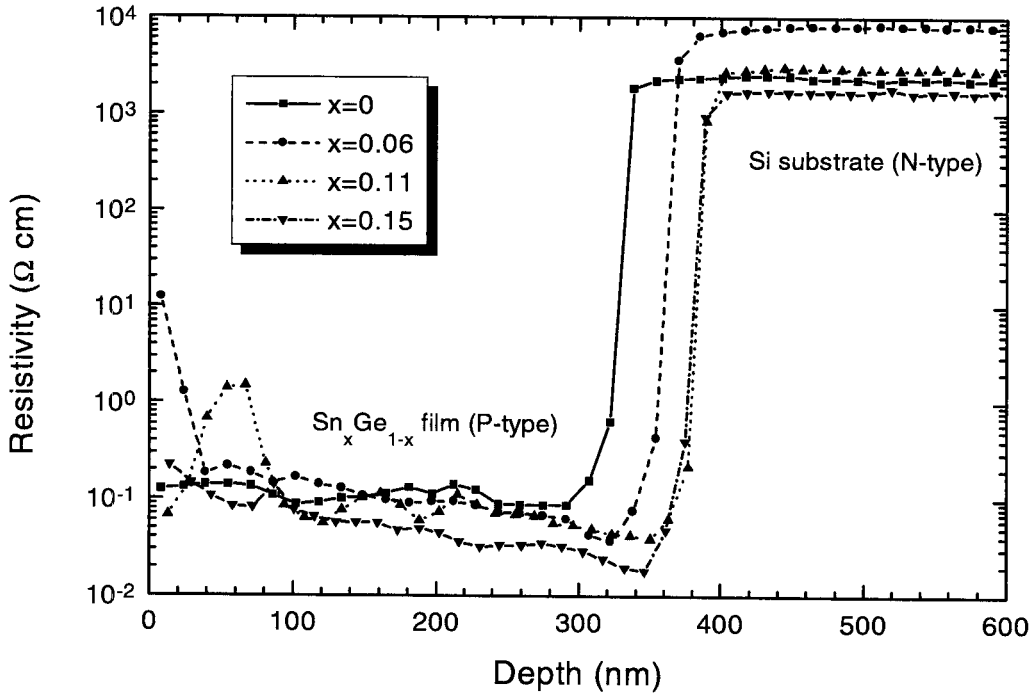

Figure 5.8 Spreading resistance measurements of Sn_xGe_{1-x} samples (300 nm) grown by molecular beam epitaxy for optical analysis.

The carrier densities of the alloy films measured from Hall effects are of the order of 10^{17}~10^{18} cm^{-3}, which is about 1 order of magnitude below the 6×10^{18} cm^{-3} effective density of states in the valence band of pure germanium. This indicates that the alloy films are extrinsic as long as the energy band gaps are significantly larger than the thermal energy (kT). The relatively heavy doping was unintentional and may come from the solid sources of germanium and tin used in

the molecular beam epitaxy growth. Compared to the intrinsic germanium hole mobility of 1900 $cm^2V^{-1}s^{-1}$ at room temperature , the room temperature hole mobility for 1.0×10^{17} cm^{-3} p-type doped germanium is about 900 $cm^2V^{-1}s^{-1}$ [16]. The reduction of carrier mobility with increasing doping concentration in bulk germanium suggest that the measured Hall mobility of 660 $cm^2V^{-1}s^{-1}$ in the germanium films may have a significant contribution from the relatively heavy doping with a measured carrier density of 1.0×10^{17} cm^{-3}. The carrier mobility of the germanium films may also be affected by the misfit dislocations in the epitaxial films as a result of strain relaxation. The samples showed increasing carrier density with increasing tin concentration, suggesting that the tin source may have contained unintentional p-type dopant. The measured Hall mobility of the Sn_xGe_{1-x} alloy films decreased with increasing tin concentration, which may be a result of increased alloy scattering, increased misfit dislocation density, as well as increased dopant scattering since the doping concentration increased with increasing tin concentration (Figure 5.9). The measured conductivity of the Sn_xGe_{1-x} alloy films, which is proportional to the product of carrier mobility and concentration, increased with increasing tin concentration, suggesting that dopant (ionized impurity) scattering is not the only limiting factor in the carrier mobility.

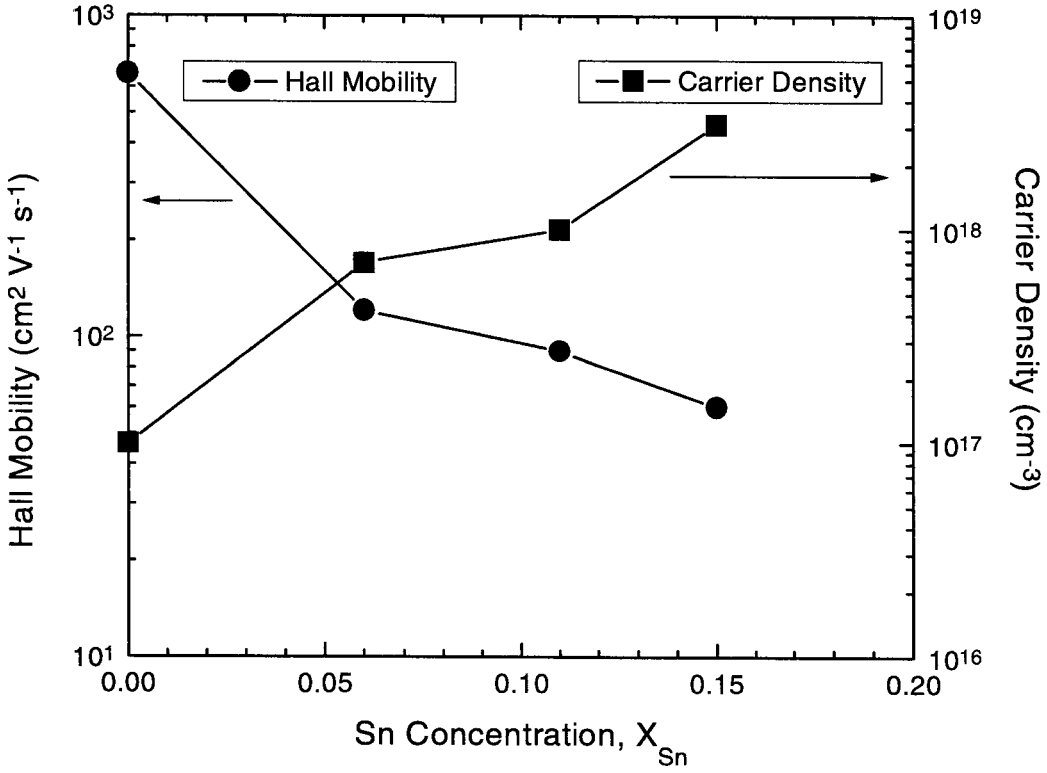

Figure 5.9 Carrier density and Hall mobility from Hall effect measurements of Sn_xGe_{1-x} samples (300 nm) grown by molecular beam epitaxy for optical analysis.

The optical transmission measurements were performed in a Nicolet 60SX Fourier transform infrared spectrometer. The spectrometer was purged continuously with dry nitrogen at approximately 4 liter/min during measurements to avoid ambient vapor (such as water and carbon dioxide) absorption. The source beam was projected to the sample from the back side of the substrate at normal incidence (Figure 5.10). Two sets of apertures were used to restrict the beam size

to about 10 mm (circular) and the beam convergence angle to about 0.1 rad. Each optical transmission spectrum was calculated by dividing the transmitted intensity of the sample by the through-beam intensity measured right after the sample measurement. The through-beam spectra taken right before and after the sample measurement were compared with each other for every sample measurement and were found to match each other within 0.5%, indicating good instrumental stability during the measurements. Note that due to the source configurations of the molecular beam epitaxy system, the tin concentrations in the alloy films have a 10% relative variation across the 10 mm measurement area on the samples.

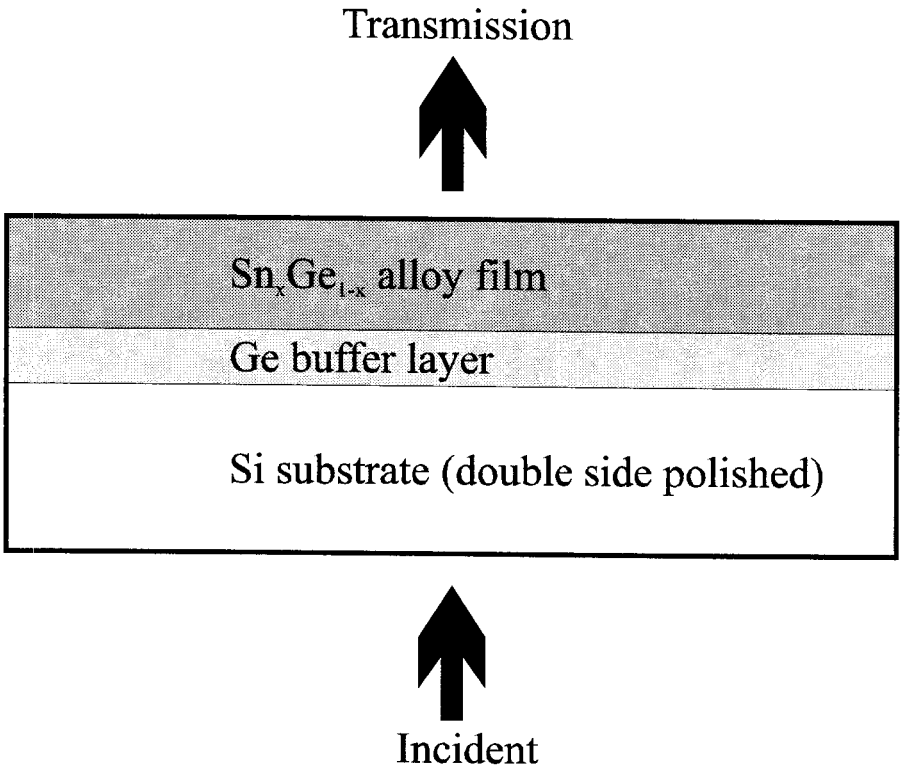

Figure 5.10 Schematic of the Sn_xGe_{1-x} infrared transmission measurement.

The optical transmission spectra were measured with 5 cm^{-1} resolution for each alloy composition and film thickness (Figure 5.11 through Figure 5.14). The small feature at about 0.93 eV is an instrumental artifact caused by a near-zero minimum in the instrument response function. The decrease of transmission above 1.1 eV in the reference silicon wafer is a result of the band-edge absorption of the silicon fundamental band gap. The absorption features below 0.25 eV are results of multi-phonon lattice absorption from the silicon substrate. The systematic decrease of overall transmission with increasing tin concentration is consistent with a decreasing energy band gap with increasing tin concentration. Detailed

optical constant analysis of the sample spectra are required in order to obtain quantitative information about the alloy band gaps.

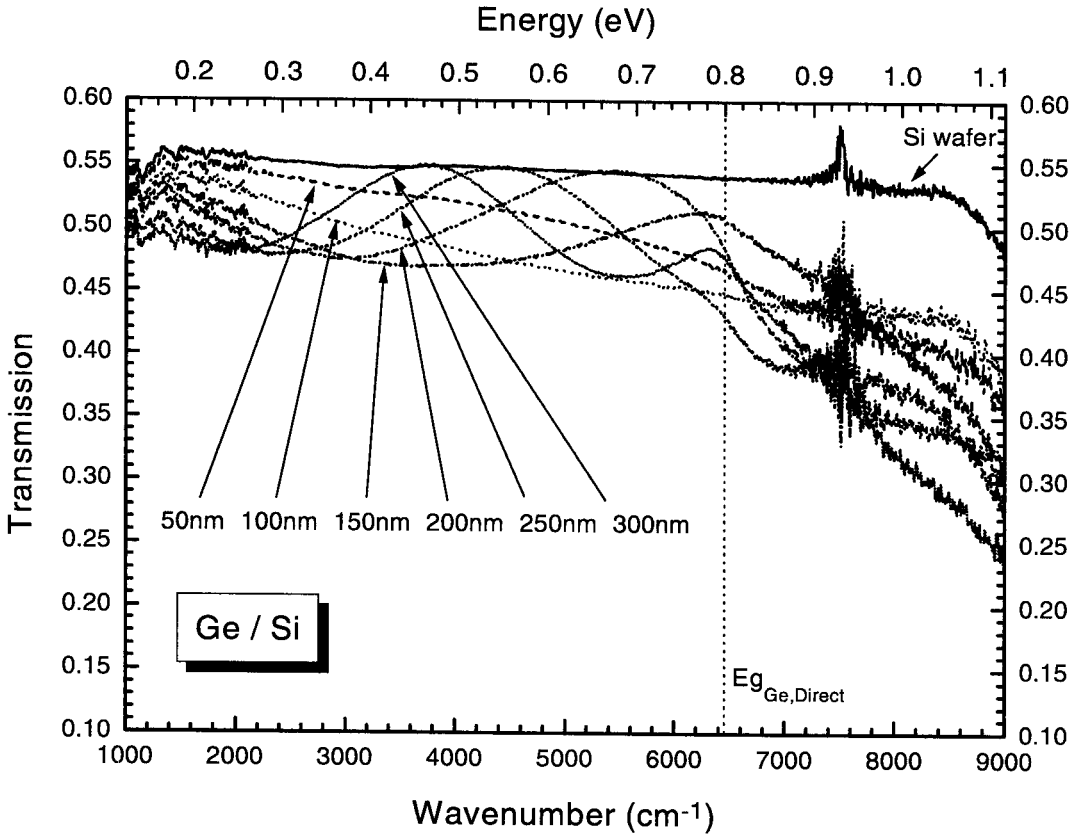

Figure 5.11 Transmission spectra of germanium film of different thicknesses grown on silicon substrates.

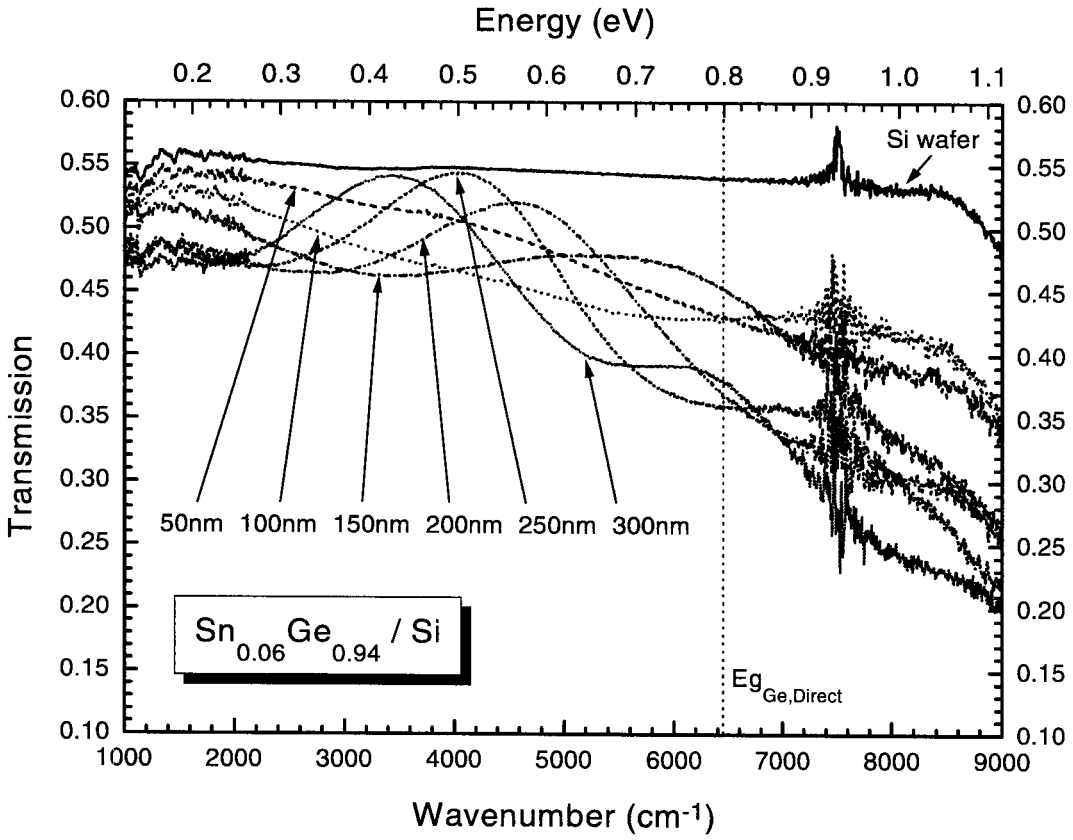

Figure 5.12 Transmission spectra of $Sn_{0.06}Ge_{0.94}$ film of different thicknesses grown on silicon substrates.

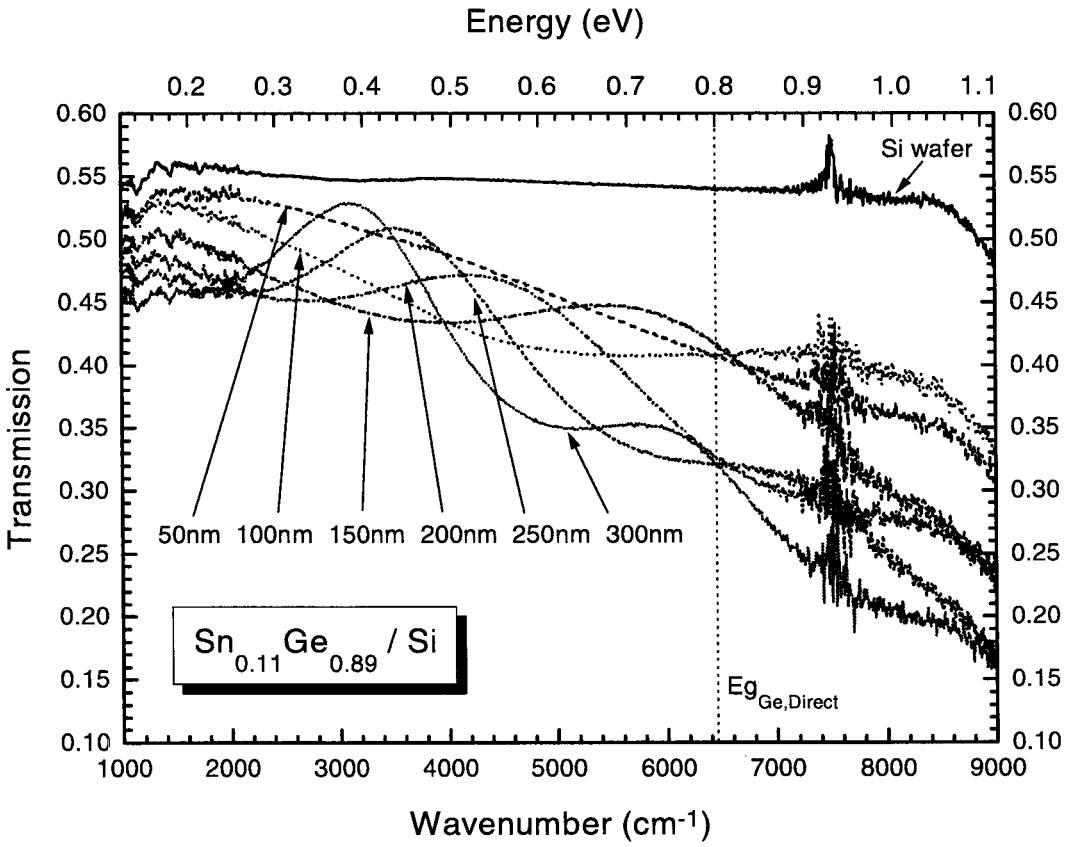

Figure 5.13 Transmission spectra of $Sn_{0.11}Ge_{0.89}$ film of different thicknesses grown on silicon substrates.

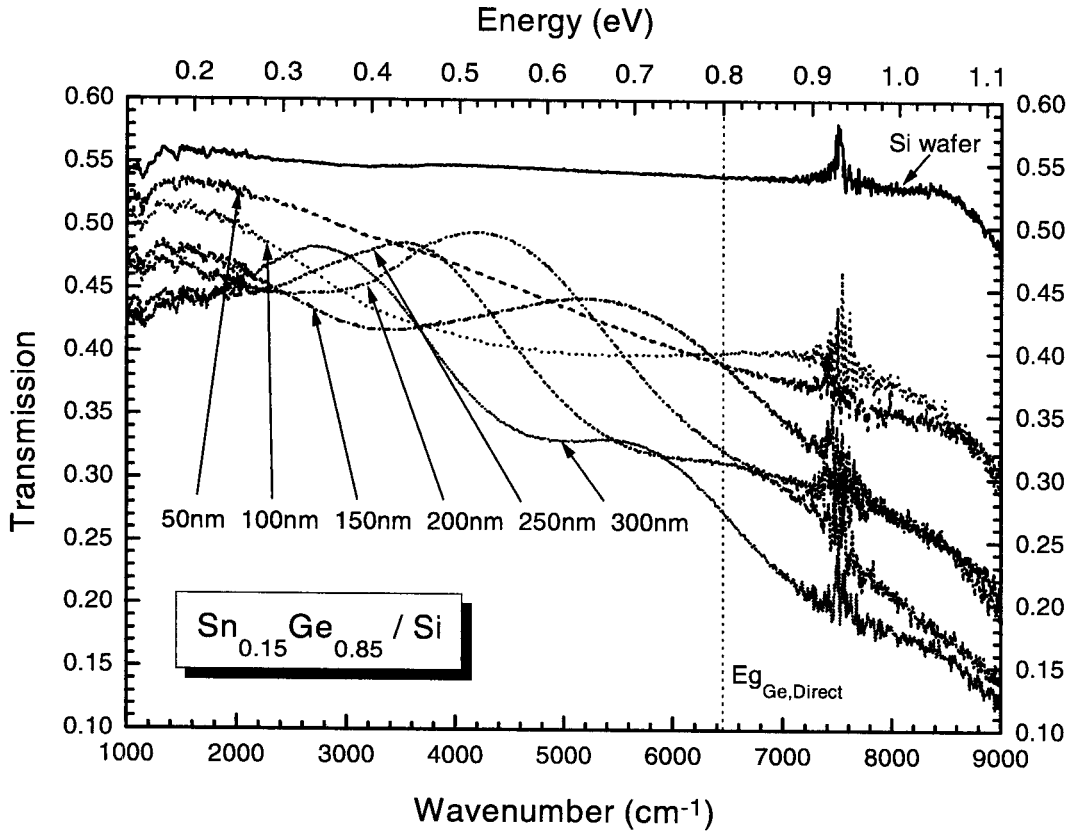

Figure 5.14 Transmission spectra of $Sn_{0.15}Ge_{0.85}$ film of different thicknesses grown on silicon substrates.

5 .4 Optical Constant Analysis of Sn_xGe_{1-x} and Energy Band Gap

Optical constant spectra for the alloy films were calculated by fitting the experimentally measured thickness-dependent transmission spectra to the numerical optical transmission function which includes multilayer interference as described in the previous sections. The transmission spectra were first normalized by the transmission spectra of the reference silicon wafer before the fitting. The fittings were performed numerically using a modified Levenberg-Marquardt method [11]. Fitting of each spectrum took about one hour on a Pentium 100 MHz computer. Details of the computer analysis routines are provided in Appendix A. The 200 nm $Sn_{0.15}Ge_{0.85}$ sample was excluded from the data analysis because it showed a very large discrepancy with the other samples in the same series when it was included in the fitting, which suggested a bad sample quality. This was confirmed by high-resolution x-ray diffraction measurement which showed a very weak diffraction intensity with a very broad angular width, suggesting a bad epitaxial quality of the sample.

The resulting spectra of refractive index showed that the refractive index of the Sn_xGe_{1-x} films increases with increasing tin concentration, from $n \approx 4.0$ for $x=0$ to $n \approx 4.3$ for $x=0.15$ at long wavelengths (Figure 5.15). The measured refractive index spectrum from the pure germanium samples matches the data for pure germanium in literature [17]-[20]. The fluctuations at 0.93 eV are due to an instrument artifact of a near-zero minimum in the instrumental response function and the fluctuations below 0.25 eV are due to the multi-phonon lattice absorption in the silicon substrate. The error analysis of the refractive index spectra estimated maximum standard errors of the order of 0.05 between 2000 cm^{-1} and 8000 cm^{-1},

except for the estimated standard error of the x=0.15 sample which was slightly larger than the other samples with a peak of about 0.15 at 0.78 eV (Figure 5.16).

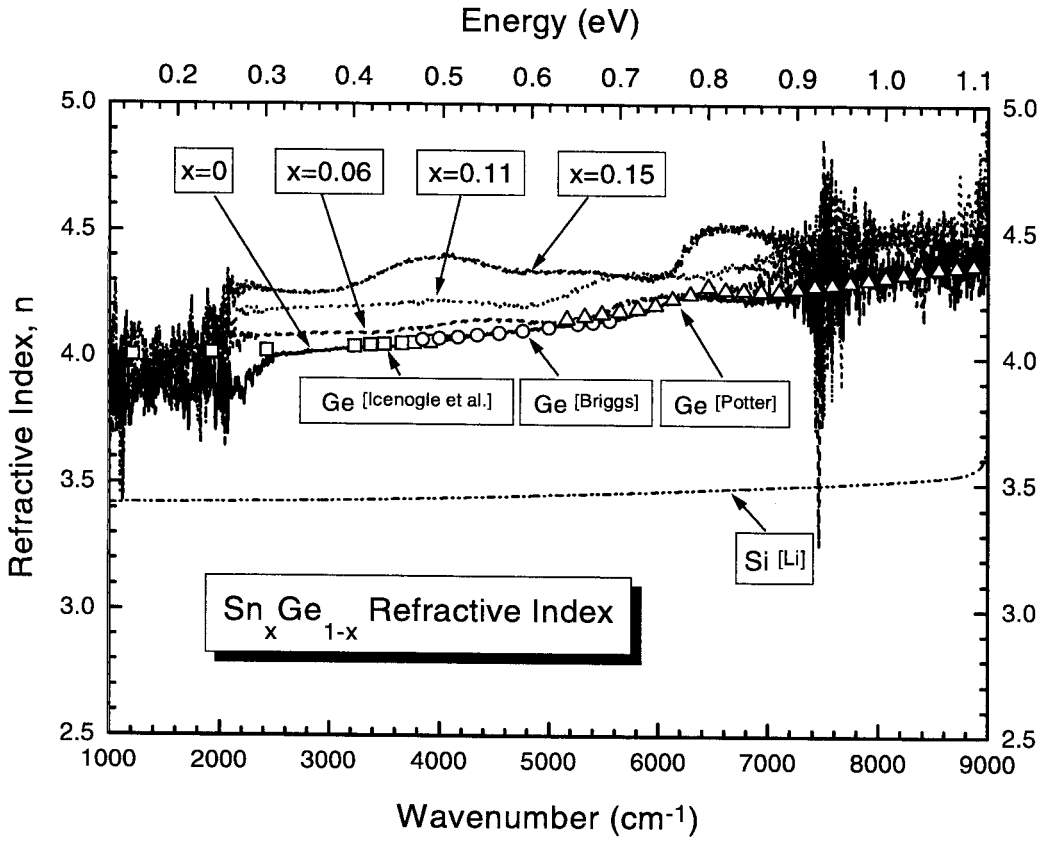

Figure 5.15 Refractive index of Sn_xGe_{1-x} analyzed from thickness-dependent transmission spectra, compared with that of pure silicon and germanium [18]-[21].

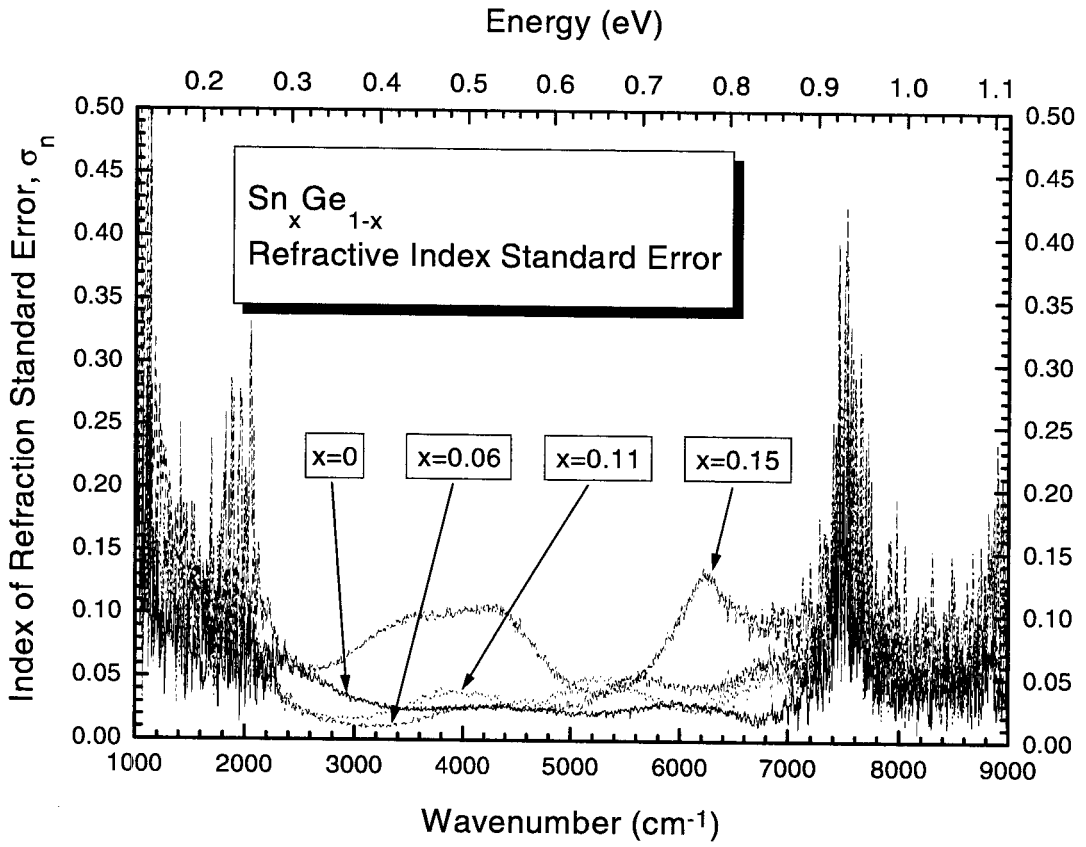

Figure 5.16 Estimated standard error of Sn_xGe_{1-x} refractive index analysis.

The resulting spectra of extinction coefficient showed that the onset energy for strong absorption in Sn_xGe_{1-x} decreases with increasing tin concentration, from about 0.8 eV for x=0 to about 0.25 eV for x=0.15 (Figure 5.17). The measured extinction coefficient from the pure germanium samples matches the data for pure germanium in literature [17],[22]. Similar to that of the refractive index spectra, the fluctuations at 0.93 eV are due to the instrument artifact of a near-zero minimum in the instrumental response function and the fluctuations below 0.25 eV

are due to the multi-phonon lattice absorption in the silicon substrate. The error analysis of the extinction coefficient spectra estimated maximum standard errors of the order of 0.005 between 2000 cm^{-1} and 8000 cm^{-1}, except for the estimated standard error of the x=0.15 sample which was slightly larger than for the other samples with a peak of about 0.015 at 0.54 eV, which may account for a small fluctuation in its extinction coefficient spectrum at the same spectral frequency (Figure 5.18).

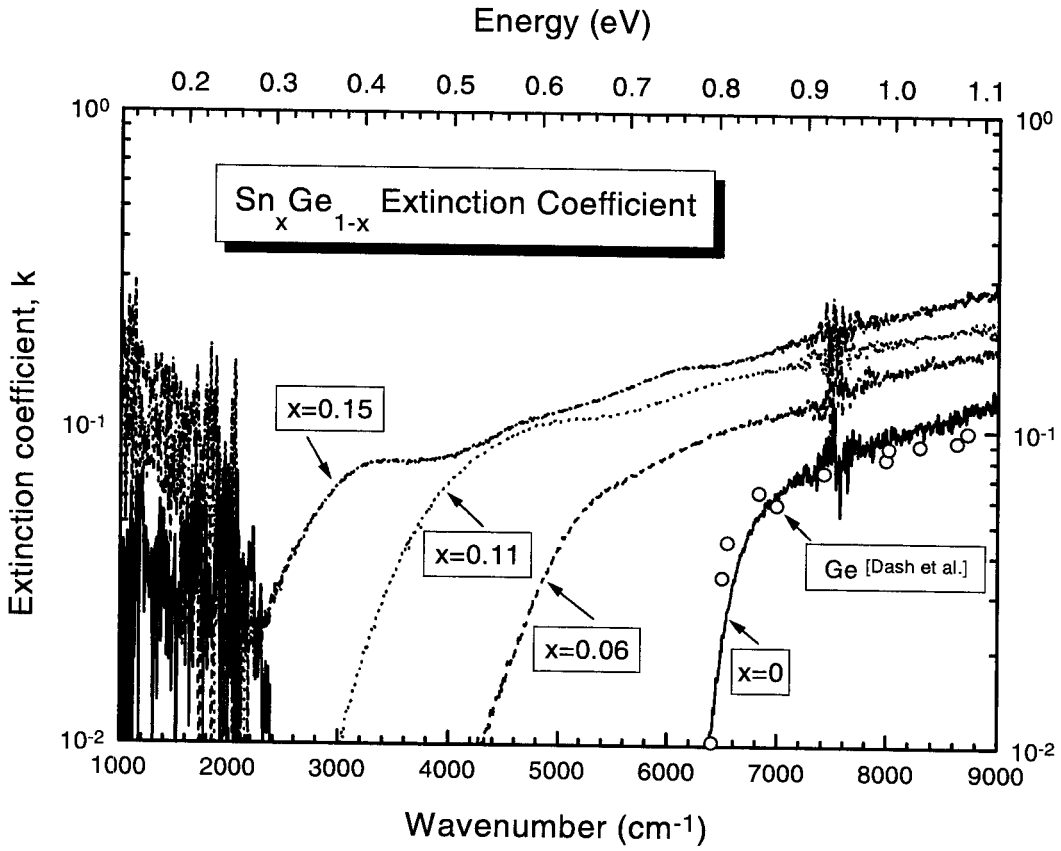

Figure 5.17 Extinction coefficient of Sn_xGe_{1-x} analyzed from thickness-dependent transmission spectra, compared with that of pure germanium [22].

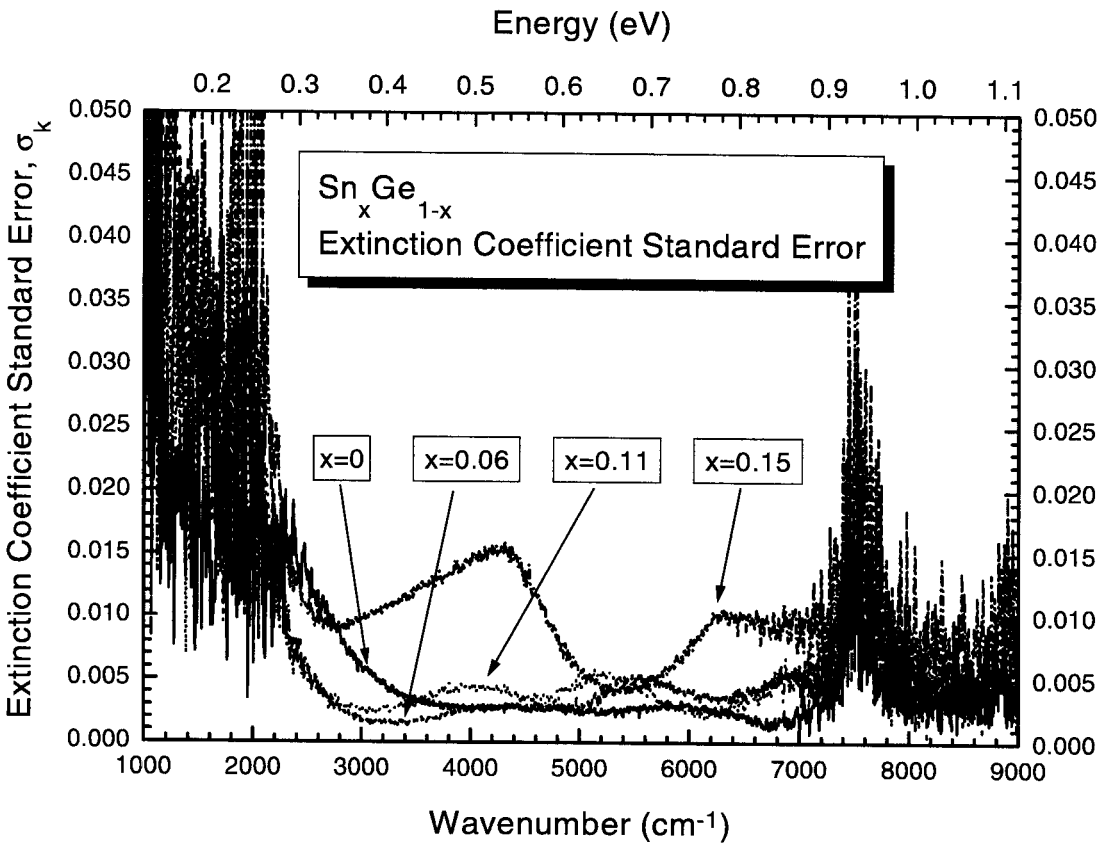

Figure 5.18 Estimated standard error of Sn_xGe_{1-x} extinction coefficient analysis.

Absorption coefficient spectra were calculated from the measured extinction coefficient spectra (Figure 5.19). Note that the absorption onset at 0.8 eV in the measured spectrum of the pure germanium samples corresponds to the 0.8 eV direct band gap of germanium instead of its 0.67 eV indirect fundamental band gap which has a much weaker absorption that is below the detection sensitivity of the Fourier transform infrared spectrometer for a 0~300 nm thick germanium film. This suggests that the absorption onsets indicated by the

measured absorption spectra of the Sn_xGe_{1-x} alloys correspond to an interband transition, but not necessarily a transition between the fundamental band gaps since there might a smaller indirect energy band gap with very weak absorption below the detection limit. Similar to the absorption coefficient from the direct band gap of pure germanium, the measured absorption coefficients of the Sn_xGe_{1-x} alloys are of the order of 10^3~10^4 cm^{-1} near the absorption onset, which are consistent with interband transitions across the direct, but not necessarily the fundamental, energy band gap. Under a parabolic band approximation, the absorption edge is expected to have a power dependence of 0.5 on energy for direct band gaps and a power dependence of 2 for indirect band gaps. Unfortunately, due to the experimental sensitivity limit, absorption coefficients below about 500 cm^{-1} near the absorption edges were not available for such power law fitting. The absorption curves above the detection limit fitted roughly a power dependence of about 1 over a range of about 0.2 eV from the absorption onset, but with a very large uncertainty (~0.5) due to the lack of information at the low absorption regions as well as the uncertainty limitations established by the error analyses. Note that in practice, significant deviations from the ideal power dependence of direct band gap absorption are frequently observed experimentally in semiconductors. Such deviations may result from deviation from the parabolic band approximation, or optical transitions between band tails (especially for heavily doped semiconductors) [23]. It is noted that the Sn_xGe_{1-x} alloy films used for this measurement are relatively heavily doped (10^{17}~10^{18} cm^{-3}), and that there is a 10% relative nonuniformity in tin concentration across the 10 mm optical measurement area which broadens the measured absorption edge hence increasing

the apparent power dependence. These observations suggest that the measured absorption edges of the Sn_xGe_{1-x} alloys are consistent with optical transitions across a direct (but not necessarily fundamental) band gap. Notice that the measured absorption strength and spectral range of the Sn_xGe_{1-x} alloys are comparable with typical narrow direct band gap semiconductors such as InAs and InSb [17] (Figure 5.20). It is noted that the measured energy band gap and refractive index of the Sn_xGe_{1-x} alloys does not follow the Moss rule which states that the fourth power of refractive index scales inversely with the energy band gap ($n^4 \propto E_g^{-1}$) [24]. Such a discrepancy is not surprising considering that the diamond-cubic tin, one of the constituents of the Sn_xGe_{1-x} alloys, does not follow the Moss rule since it has a zero energy band gap and a refractive index of about $n = 4.9$. Narrow band gap semiconductors InAs and InSb are also well known exceptions of the Moss rule.

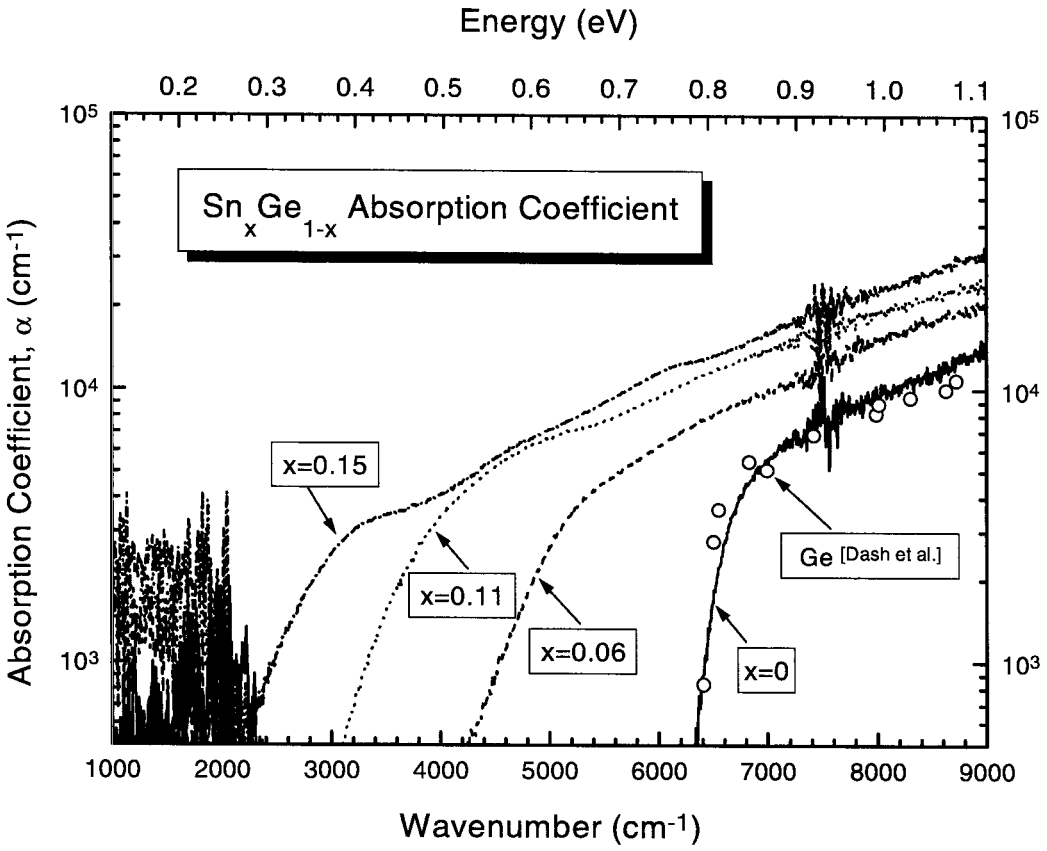

Figure 5.19 Absorption coefficient of Sn_xGe_{1-x} analyzed from the measured extinction coefficient, compared with that of pure germanium [22].

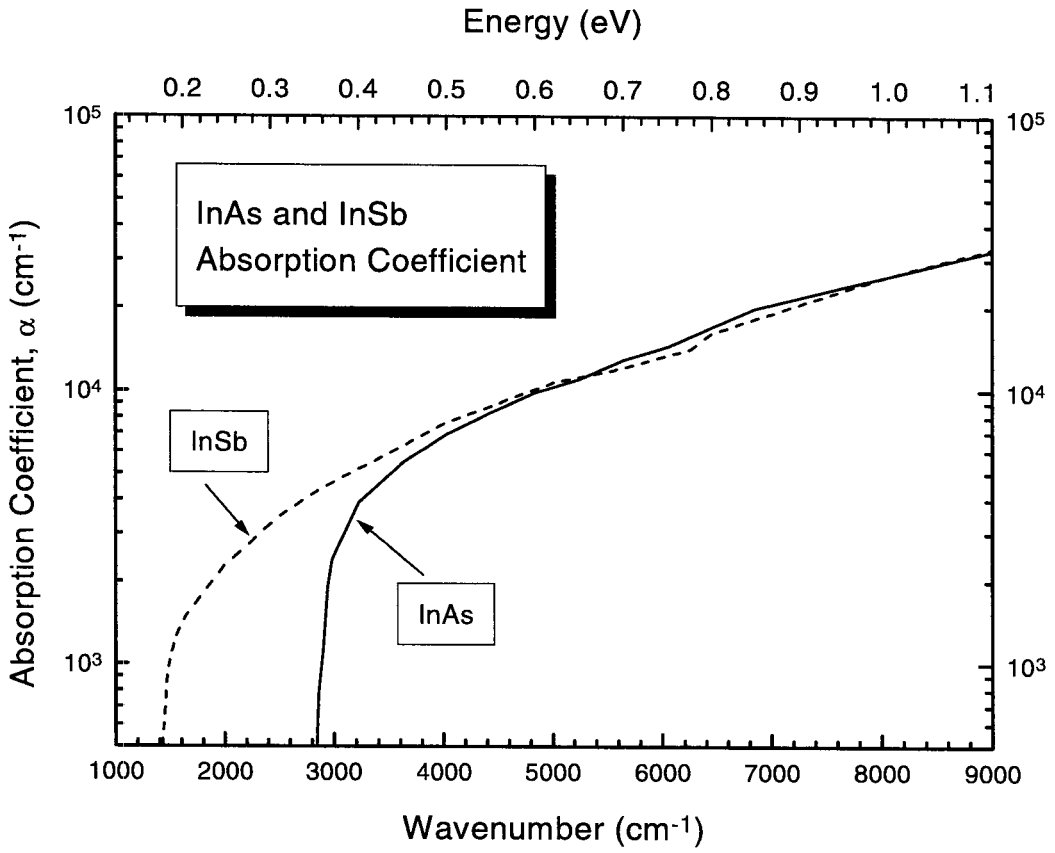

Figure 5.20 Absorption coefficient of InAs and InSb [17].

A plot of the measured onsets of absorption of the Sn_xGe_{1-x} alloys as a function of tin concentration showed that the measured band gap decreases with increasing tin concentration much faster than predicted by the tight-binding and pseudopotential calculations in the virtual crystal approximation [1]-[4] (Figure 5.21). Possible sources of error in the measured energy band gap includes random errors characterized by the χ^2 error analysis as well as the possible band gap shift from small residual epitaxial strains in the alloy films. The random error is

estimated to be within about 40 meV from the χ^2 error analysis, and the error induced by residual strain is estimated to be also within about 40 meV from the x-ray diffraction strain measurements and assuming a deformation potential of pure germanium [25]. Notice that although band filling effects may slightly affect the measured band gaps for heavily doped semiconductors, such effects tend to increase the measured band gaps in general [23]. If the measured band gaps of the Sn_xGe_{1-x} alloys as a function of alloy composition is connected with the established band gap of pure (diamond-cubic) α-tin of E_g=-0.4 eV [26] through a parabolic fit:

$$E_g = E_{g0}(1-x) + E_{g1}x + E_a x(x-1),$$

a bowing parameter E_a [27] of 2.8 eV is obtained, although the value may contain some significant error due to the lack of data points in the mid composition range. This relatively large band bowing effect may be the result of a large random alloy disorder which causes significant deviation from the virtual crystal approximation used in the tight-binding and pseudopotential calculations [28]. Such a deviation is consistent with the results from the first-principles local structure calculations described in chapter 3. The measured energy band gaps of the Sn_xGe_{1-x} alloys suggest that the alloy band gaps may become zero at a tin concentration less than x=0.25 instead of x=0.6 as predicted by the tight-binding and pseudopotential calculations.

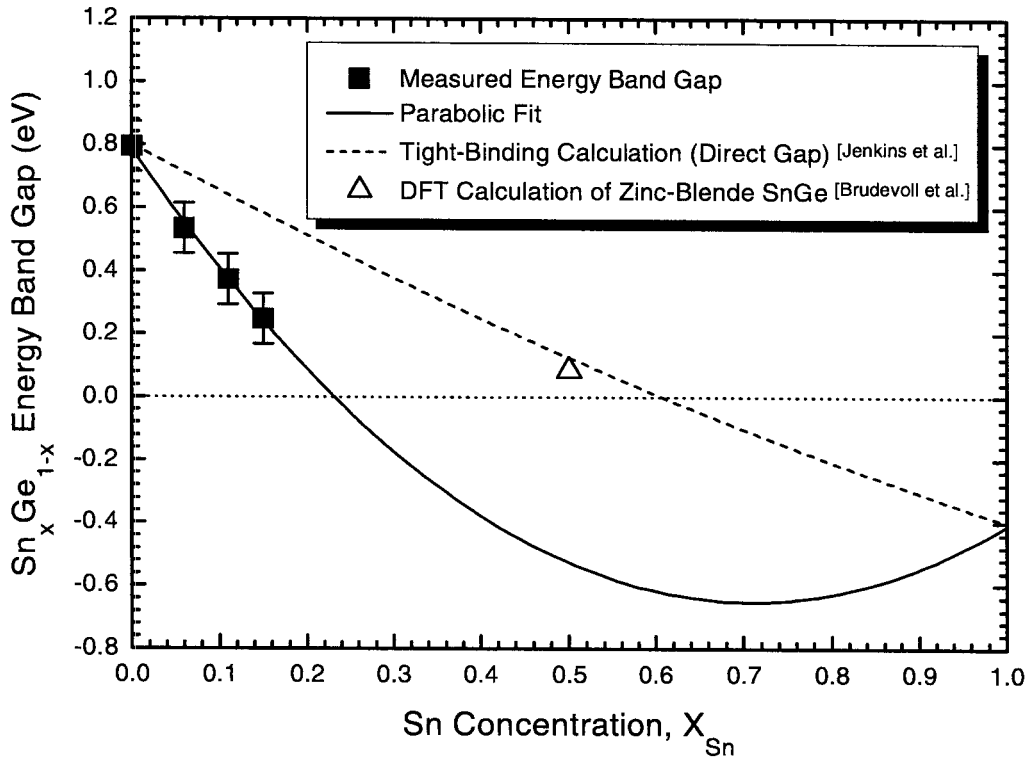

Figure 5.21 Sn_xGe_{1-x} energy band gaps measured from the absorption onset as a function of alloy compositions compared with tight-binding calculations of Sn_xGe_{1-x} alloys [1] and density functional calculation of zinc-blend SnGe [6]. The estimated error in the measured data is given by the error bars in the vertical dimension and by the size of the squares in the horizontal dimension.

5 .5 Conclusions

Optical constants spectra of epitaxial Sn_xGe_{1-x} alloy films grown on silicon substrates as a function of alloy compositions were obtained using thickness-dependent optical transmission measurements. The resulting absorption spectra showed strong interband absorption (of the order of 10^3~10^4 cm^{-1} near the absorption onset) consistent with an optical transition across a direct, but not necessarily fundamental, energy band gap. This is the first systematic experimental measurement of Sn_xGe_{1-x} optical constants and energy band gap to our knowledge. The measured band gap from the onset of absorption decreases with increasing tin concentration much faster than predicted by tight-binding and pseudopotential calculations in the virtual crystal approximation. The measured band gap for $Sn_{0.15}Ge_{0.85}$ was as low as E_g=0.25 eV, and the measurements suggest that zero band gap may be reached with tin concentrations as little as x=0.25 instead of x=0.6 as predicted by the calculations. A parabolic fit of the measured Sn_xGe_{1-x} alloy band gaps as a function of alloy compositions yielded a band gap bowing parameter of 2.8 eV. This relatively large bowing parameter may indicate a significant deviation from the virtual crystal approximation used in the tight-binding and pseudopotential calculations, which is consistent with the first principle structural calculations discussed in Chapter 3. Bowing parameters of similar magnitudes have also been observed in some II-VI ternary alloys such as $ZnS_{1-x}Te_x$ (~3.0 eV) [29].

The measured absorption spectra of the epitaxial Sn_xGe_{1-x} alloy films grown on silicon substrates showed absorption strength and spectral range comparable to typical III-V narrow direct band gap semiconductors such as InAs and InSb, suggesting the possibilities of silicon-based infrared optoelectronic devices using heteroepitaxial Sn_xGe_{1-x} alloy films with performances similar to the current III-V compound infrared devices based on direct narrow band gap semiconductors. The increase of refractive index with increasing tin concentration shown by the optical measurements also suggests the possibilities for fabricating waveguide structures in Sn_xGe_{1-x} alloy layers. Monolithic integration of infrared devices with silicon technology may enable a new array of applications including large-area silicon-based monolithic infrared imaging arrays. The low growth temperature of epitaxial Sn_xGe_{1-x} alloys potentially allows the fabrication of the Sn_xGe_{1-x} alloy layers as the last processing step on an almost fully processed VLSI silicon integrated circuit without affecting the existing devices already fabricated on the wafer. The measured Sn_xGe_{1-x} alloy band gaps as a function of alloy compositions suggest that full access to the complete range of Sn_xGe_{1-x} tunable band gaps may be obtained with tin concentrations much less than previously expected based on the tight-binding and pseudopotential calculations in the virtual crystal approximation. Difficulties in the growth of epitaxial Sn_xGe_{1-x} alloys with high tin concentrations has been regarded as one of the major obstacles for the device application of this alloy material. This study showed that band gaps as low as E_g=0.25 eV can be achieved in Sn_xGe_{1-x} alloys with tin concentrations as little as x=0.15 grown completely by conventional molecular beam epitaxy on silicon substrates. Furthermore, full access of the complete range of Sn_xGe_{1-x} tunable band gap may

have already been achieved with ion-assisted molecular beam epitaxy (described in the previous chapters) which was able to produce Sn_xGe_{1-x} alloys with tin concentrations of more than x=0.3 [2] [30] [31], already exceeding the requirement of x=0.25 suggested by the band gap measurements. Unfortunately, experimental measurements of optical constants for these higher tin concentration samples using the current method is difficult since it requires the growth of a series of samples of relatively large and different thicknesses, which is still relatively difficult to achieve by ion-assisted molecular beam epitaxy. Other measurement methods, such as combined transmission and reflection, as well as photoconductivity, may be better suited for such measurements. Nevertheless, the measurements of energy band gaps from samples grown by conventional molecular beam epitaxy have already shown a very wide range of tunable energies (E_g=0.67 eV to E_g=0.25 eV) for potential device applications.

Bibliography

[1] D.W. Jenkins and J.D. Dow, Phys. Rev. B 36, 7994 (1987).

[2] H.A. Atwater, G. He, K. Saipetch, Mat. Res. Soc. Symp. Proc. 355, 123 (1995).

[3] B. Bouhafs, F. Benkabou, M. Ferhat, B. Khelifa, J.P. Dufour, H. Aourag, Infrared Phys. & Tech. 36, 967 (1995).

[4] K.A. Mader, A. Baldereschi, H. von Kanel, Solid State Comm. 69, 1123 (1989).

[5] Na. Amrane, S. Ait Abderrahmane, H. Aourag, Infrared Phys. & Tech. 36, 843 (1995).

[6] T. Brudevoll, D.S. Citrin, N.E. Christensen, M. Cardona, Phys. Rev. B 48,17128 (1993).

[7] E. Kaxiras, unpublished.

[8] B.I. Craig and B.J. Garrison, Phys. Rev. B 33, 8130 (1986).

[9] B.I. Craig, Superlattices and Microstructures 12, 1 (1992).

[10] A. Harwit, P.R. Pukite, J. Angilello and S.S. Iyer, Thin Solid Films 184, 395 (1990).

[11] W.H. Press, S.A. Teukolsky, W.T. Vetterling, B.P. Flannery, Numerical Recipes in C: The Art of Scientific Computing, Second Edition, Cambridge University Press, Cambridge, 1992.

[12] O.S. Heavens, Optical Properties of Thin Solid Films, Dover Publications, New York, 1991.

[13] T.S. Robinson, Proc. Phys. Soc. 71, 910 (1952).

[14] W.H. Brattain and H.B. Briggs, Phys. Rev. 75, 1705 (1949).

[15] D.K. Schroder, Semiconductor Material and Device Characterization, John Wiley & Sons, New York, 1990.

[16] S.M. Sze, Physics of Semiconductor Devices, Second Edition, John Wiley & Sons, New York, 1981.

[17] Edward D. Palik, Editor, Handbook of Optical Constants of Solids, Academic Press, Orlando, 1985.

[18] H.W. Icenogle, B.C. Platt, and W.L. Wolfe, Appl. Optics 15, 2348 (1976).

[19] H.B. Briggs, Phys. Rev. 77, 287 (1950).

[20] R.F. Potter, Phys. Rev. 150, 562 (1966).

[21] H.H. Li, J. Phys. Chem. Ref. Data 9, 561 (1980).

[22] W.C. Dash and R. Newman, Phys. Rev. 99, 1151 (1955).

[23] J.I. Pankove, Optical Processes in Semiconductors, Dover Publications, New York, 1975.

[24] T.S. Moss, Photoconductivity in the Elements, Academic Press, New York, 1952.

[25] J. Bardeen and W. Shockley, Phys. Rev. 80, 72 (1950).

[26] C.H.L. Goodman, IEEE Proc. 129, 189 (1982).

[27] A.G. Thompson and J.C. Woolley, Can. J. Phys. 45, 255 (1967).

[28] A. Zunger and J.E. Jaffe, Phys. Rev. Lett. 51, 662 (1983).

[29] R. Hill and D. Richardson, J. Phys. C 6, L115 (1973).

[30] G. He and H.A. Atwater, Nucl. Instrum. Methods B 106, 126 (1995).

[31] G. He and H.A. Atwater, Appl. Phys. Lett. 68, 664 (1996).

Chapter 6

CONCLUSIONS AND PROSPECTS

Group IV semiconductor alloys, including $Si_{1-y}(Sn_{1-x}C_x)_y$ and Sn_xGe_{1-x}, are promising new materials for silicon-based high-performance electronic and optoelectronic devices. Epitaxial $Si_{1-y}(Sn_{1-x}C_x)_y$ alloys with tin and carbon concentrations of up to y=0.02 (x=0.5) were successfully synthesized by molecular beam deposition followed by solid phase epitaxy [1]-[3]. Epitaxial Sn_xGe_{1-x} alloys with tin concentrations of up to x=0.2 were successfully synthesized by conventional molecular beam epitaxy, while epitaxial Sn_xGe_{1-x} alloys with concentrations of more than x=0.3 were achieved by ion-assisted molecular beam epitaxy [4]-[7]. The successful synthesis of these metastable alloy materials will enable further exploration of their material and electronic properties as well as their device applications.

The $Si_{1-y}(Sn_{1-x}C_x)_y$ alloys are interesting candidates for the heterojunction layers in high-speed silicon-based heterojunction transistors. The ability to grow epitaxial $Si_{1-y}(Sn_{1-x}C_x)_y$ alloy films by solid phase epitaxy on silicon substrates suggests that a device fabrication process using $Si_{1-y}(Sn_{1-x}C_x)_y$ can be implemented in almost the same way as the process of current $Si_{1-x}Ge_x$ heterojunction bipolar transistors which can be made compatible with current Bi-CMOS (bipolar-complementary-metal-oxide-semiconductor) processes [8]. Compared with

$Si_{1-x}Ge_x$, $Si_{1-y}(Sn_{1-x}C_x)_y$ may offer the advantage of low-strain or unstrained heterojunction layers which may allow large band offsets without introducing elastic metastabilities leading to misfit dislocation generation hence achieving better device performance and reliability. Another ternary group IV alloy system that may have similar applications in high-speed silicon-based heterojunction devices is the $Si_{1-y}(Ge_{1-x}C_x)_y$ system [9]. The $Si_{1-y}(Ge_{1-x}C_x)_y$ alloy system has recently received extensive investigation and may provide similar low-strain or unstrained heterojunction layers on silicon substrates. In either system, one important outstanding issue closely related to device performance is that of band offsets between the heterojunction layers and silicon as a function of alloy composition and epitaxial strain. The answers to this question are still not clear and require further investigation of the detailed electronic properties of both material systems.

The Sn_xGe_{1-x} alloys have interesting potential applications in silicon-based infrared optoelectronic devices due to their continuously tunable band gaps in the infrared region. Tight-binding and pseudopotential calculations in the virtual crystal approximation have predicted a tunable direct band gap between E_g=0.55 eV and E_g=0 eV for tin concentrations between x=0.2 and x=0.6 [4] [10]-[12]. Sn_xGe_{1-x} alloys with tin concentrations up to x=0.2 can be achieved by conventional molecular beam epitaxy. However, when the tin concentration is higher than x=0.2, conventional molecular beam epitaxy growth has faced great difficulty due to the surface tin segregation. The segregation was significantly suppressed and tin concentrations of more than x=0.3 were achieved in ion-

assisted molecular beam epitaxy where the surface of the growing film was irradiated by a low energy (40 eV ~ 50 eV) high flux (~ 0.1 mA/cm^2) Ar^+ ion beam generated by an electron cyclotron resonance ion source. Ion damages to the epitaxial films can be minimized by using low energy ion beams. For example, at higher ion energies of about 100 eV), inclusion of argon atoms of up to 1% were found in the epitaxial films by Rutherford backscattering spectroscopy; when the ion energy is reduced to 40 eV ~ 50 eV, no argon inclusion could be found within the detection limit of Rutherford backscattering spectroscopy, although possibilities of other types of structural defects cannot be completely ruled out yet.

To quantitatively describe the effect of surface segregation suppression by ion irradiation, an analytic model was developed [5] [6]. In addition to the thermal segregation, the model includes the effect of ion-induced recoil-mixing as well as direct-implant-mixing and is applicable to energetic beam epitaxial growth in general. The model predicts the steady-state segregation coefficient k as well as the temporal segregation profile during energetic beam epitaxial growth and is consistent with the results of ion-assisted molecular beam epitaxial growth of Sn_xGe_{1-x}.

The most important electronic property of Sn_xGe_{1-x} regarding its infrared device applications is its predicted tunable band gap. Since the Sn_xGe_{1-x} material is only available in thin films form, measurements of thickness-dependent optical transmission spectra were performed to quantitatively characterize the Sn_xGe_{1-x} band gap as a function of alloy composition from the analysis of optical spectra.

The results showed strong interband absorption and decreasing absorption onset with increasing tin concentration [13]. The absorption was consistent with an optical transition across a direct band gap. Due to the sensitivity limit of the measurements, it was not yet determined whether this is the fundamental band gap of the material. The measured absorption strength and spectral range of Sn_xGe_{1-x} are similar to the typical direct band gap infrared semiconductors such as InAs and InSb. The decrease of the measured band gap with increasing tin concentration was much faster than tight-binding and pseudopotential calculations have predicted. For example, the measured alloy band gap for tin concentration of x=0.15 was as low as 0.25 eV. The measurements suggest a relatively large band-gap bowing parameter of approximately 2.8 eV, so that zero band gap may be reached at tin concentrations no more than x=0.25, instead of x=0.6 as predicted by the tight-binding and pseudopotential calculations in the virtual crystal approximation. The relatively large band-gap bowing parameter may indicate a significant deviation from the virtual crystal approximation which was used in the calculations. Such a deviation is also consistent with first principles density functional theory (DFT) calculations in the local density approximation (LDA).

Another important issue regarding the device applications of Sn_xGe_{1-x} alloys is its doping. Although doping of Sn_xGe_{1-x} alloys was not explicitly investigated in this study, it is noted that the Sn_xGe_{1-x} alloy films obtained in this study are all p-type doped. It has also been reported that pure diamond-cubic tin can be doped as both p-type and n-type by indium and antimony, respectively [14].

The experimental results for the Sn_xGe_{1-x} energy band gap have important implications regarding the device applications of the material. The potential for infrared devices based on Sn_xGe_{1-x} may be far greater than has been previously thought which was mostly based on the tight-binding and pseudopotential calculations in the virtual crystal approximation. The band gap measurements suggest that band gaps as low as 0.25 eV can be achieved by conventional molecular beam epitaxy, and full access to the complete range of the Sn_xGe_{1-x} tunable band gap may have already been achieved with by ion-assisted molecular beam epitaxy which has yielded alloys with tin concentrations of more than x=0.3, exceeding the requirement of x=0.25 suggested by the band gap measurements. The fast decreasing band gap with increasing tin concentration implies a lattice mismatch with the substrate for a given alloy band gap that is smaller than anticipated. If Vegard's law is assumed to be valid, the expected zero band gap composition of x=0.25 should correspond to a lattice mismatch to germanium of approximately 3%, which is slightly smaller than the 4% lattice mismatch between germanium and silicon. Thus high-performance devices based on pseudomorphic Sn_xGe_{1-x} multilayers on silicon or germanium substrates are conceivable. Other substrate materials with larger lattice constants such as InP, SrF_2, or BaF_2 may also be used to produce high-quality pseudomorphic Sn_xGe_{1-x} layers or specialized high-performance devices. The Sn_xGe_{1-x} band gap can be continuously tuned over an extremely wide infrared spectral range, thus optimal device performance can be achieved by custom tailoring its operation wavelength for specific applications. The ability to grow epitaxial Sn_xGe_{1-x} alloy films at very low temperatures (200°C)

implies that it may be possible to fabricate Sn_xGe_{1-x} alloy layers as the last processing step on an almost fully processed wafer without affecting the existing devices already fabricated on the wafer. By building the supporting circuits (e.g., scanning driver and signal amplifier circuits) on the same wafer, integrated high-performance infrared imaging arrays using Sn_xGe_{1-x} may be achievable on silicon substrates.

Bibliography

[1] G. He, M.D. Savellano, and H.A. Atwater, Mat. Res. Soc. Symp. Proc. 298, 229 (1993).

[2] G. He, M.D. Savellano, and H.A. Atwater, Appl. Phys. Lett. 65, 1159 (1994).

[3] G. He, M.D. Savellano, and H.A. Atwater, Section X2.15 Electronic Materials: SiSnC, Handbook of Thin Film Process Technology, Ed. D.A. Golcker and S.I. Shah, Institute of Physics Publishing Ltd. (Bristol and Philadelphia) (1995).

[4] H.A. Atwater, G. He, K. Saipetch, Mat. Res. Soc. Symp. Proc. 355, 123 (1995).

[5] G. He and H.A. Atwater, Nucl. Instrum. Methods B 106, 126 (1995).

[6] G. He and H.A. Atwater, Mat. Res. Soc. Symp. Proc. 399, 380 (1996).

[7] G. He and H.A. Atwater, Appl. Phys. Lett. 68, 664 (1996).

[8] G.L. Patton, J.H. Comfort, B.S. Meyerson, E.F. Crabbe, G.J. Scilla, E. Defresart, J.M.C. Stork, J.Y.C Sun, D.L. Harame, et al., IEEE Elec. Dev. Lett. 11, 171 (1990).

[9] J.W. Strane, H.J. Stein, S.R. Lee, S.T. Picraux, J.K. Watanabe, and J.W. Mayer, J. Appl. Phys. 76, 3656 (1994).

[10] D.W. Jenkins and J.D. Dow, Phys. Rev. B 36, 7994 (1987).

[11] B. Bouhafs, F. Benkabou, M. Ferhat, B. Khelifa, J.P. Dufour, H. Aourag, Infrared Phys. & Tech. 36, 967 (1995).

[12] K.A. Mader, A. Baldereschi, H. von Kanel, Solid State Comm. 69, 1123 (1989).

[13] G. He and H.A. Atwater, in preparation.

[14] C.F. Lavine and A.W. Ewald, J. Phys. Chem. Solids 32, 1121 (1971).

Appendix A Modeling Multi-Layer Thin Film Optical Interference

In order to quantitatively analyze the optical constants from optical measurements, an optical transmission function must be constructed. The transmission function must include thin film interference effects. When multiple layers are contained in the sample structure, the analytical form of the transmission function becomes complicated, therefore a numerical solution was developed.

To construct the transmission function accurately, Maxwell's equations were used as the starting points:

$$\begin{cases} \nabla \cdot \vec{D} = 0 & \nabla \times \vec{E} + \dfrac{1}{c}\dfrac{\partial \vec{B}}{\partial t} = 0 \\ \nabla \cdot \vec{B} = 0 & \nabla \times \vec{H} + \dfrac{1}{c}\dfrac{\partial \vec{D}}{\partial t} = 0 \end{cases}$$

where

$$\begin{cases} \vec{D} = \varepsilon \vec{E} \\ \vec{B} = \mu \vec{H} \end{cases}$$

where ε and μ are the dielectric constant and magnetic permeability, respectively, and are tensors in general.

In the plane-wave basis, Maxwell's equations have the following solutions:

$$\begin{cases} \vec{E}(\vec{x},t) = \vec{E}\exp\left(i\vec{k}\cdot\vec{x} - i\varpi t\right) \\ \vec{H}(\vec{x},t) = \vec{H}\exp\left(i\vec{k}\cdot\vec{x} - i\varpi t\right) \end{cases}$$

where

$$\vec{k} = \tilde{k}\,\hat{k},\ \hat{k}\cdot\hat{k} = 1$$

and where $\vec{k}$ is the wave vector, and $\vec{E}, \vec{H}, \vec{k}, \hat{k}, \tilde{k}$ are complex numbers in general.

In magnetically isotropic media, μ is a scalar, and the plane-wave solutions satisfy the following conditions:

$$\begin{cases} \vec{B} = \dfrac{c}{\varpi}\vec{k}\times\vec{E} \\ \vec{D} = \dfrac{c}{\varpi}\vec{k}\times\vec{H} \end{cases} \quad \Rightarrow \quad \begin{cases} \vec{k}\cdot\vec{B} = 0 \\ \vec{k}\cdot\vec{D} = 0 \end{cases}.$$

The energy flux can be represented by the Poynting vector as

$$\vec{S} = \frac{1}{2}\frac{c}{4\pi}\vec{E}\times\vec{H}^{*},$$

and the amplitude of the wave vector can be determined as

$$\tilde{k} = \tilde{n}\frac{\varpi}{c}$$

where $\tilde{n}$ is the complex index of refraction:

$$\tilde{n}^2 = \mu\frac{\vec{D}\cdot\vec{D}}{\vec{E}\cdot\vec{D}}.$$

For isotropic media, ε is a scalar as well, therefore the complex index of refraction is

$$\tilde{n}^2 = \mu\varepsilon \ .$$

At the interface between two media (media 1 and 2), Maxwell's equations can be represented in the plane-wave basis as the following interface boundary conditions:

$$\begin{cases} \varpi_1 = \varpi_2 \\ \vec{k}_1 \times \hat{z} = \vec{k}_2 \times \hat{z} \ , \end{cases}$$

and

$$\begin{cases} \left(\sum \vec{D}_1 - \sum \vec{D}_2\right) \cdot \hat{z} = 0 & \left(\sum \vec{E}_1 - \sum \vec{E}_2\right) \times \hat{z} = 0 \\ \left(\sum \vec{B}_1 - \sum \vec{B}_2\right) \cdot \hat{z} = 0 & \left(\sum \vec{H}_1 - \sum \vec{H}_2\right) \times \hat{z} = 0 \end{cases}$$

or

$$\begin{cases} \left(\sum \varepsilon_1 \vec{E}_1 - \sum \varepsilon_2 \vec{E}_2\right) \cdot \hat{z} = 0 \\ \left(\sum \vec{k}_1 \times \vec{E}_1 - \sum \vec{k}_2 \times \vec{E}_2\right) \cdot \hat{z} = 0 \\ \left(\sum \vec{E}_1 - \sum \vec{E}_2\right) \times \hat{z} = 0 \\ \left(\sum \frac{1}{\mu_1} \vec{k}_1 \times \vec{E}_1 - \sum \frac{1}{\mu_2} \vec{k}_2 \times \vec{E}_2\right) \times \hat{z} = 0 \end{cases}.$$

At an interface in the x-y plane with plane waves propagating in the x-z plane, the wave vectors satisfy

$$\vec{k}^{\pm} = \begin{bmatrix} k_x \\ k_y \\ k_z \end{bmatrix}^{\pm} = \begin{bmatrix} k_x \\ 0 \\ \pm\sqrt{k^2 - k_x^2} \end{bmatrix}$$

where $k^{\pm}$ are the forward and backward propagating wave vectors, and the phase ϕ of the square root is defined as

$$-\frac{\pi}{4} < \phi\{\sqrt{x}\} \leq +\frac{3\pi}{4} .$$

Since in each layer of a multilayer structure there is a forward and a backward propagating wave (as a result of reflection), the electromagnetic field in a layer can be represented by an amplitude vector which combines the wave amplitude of both the forward and backward propagating waves as

$$\vec{\vec{E}}_{s,p} = \begin{bmatrix} E^+ \\ E^- \end{bmatrix}_{s,p}$$

where s represents the s wave (electric field $\vec{E}$ perpendicular to the plane of incidence x-z), and p represents the p wave (electric field $\vec{E}$ parallel to the plane of incidence x-z).

At the interface between two layers (layer 1 and 2), the boundary conditions can be represented by a matrix equation:

$$\bar{I}_1 \vec{\vec{E}}_1 = \bar{I}_2 \vec{\vec{E}}_2$$

where the interface matrix $\bar{I}$ is defined as

$$\begin{cases} \bar{I}_s = \begin{bmatrix} 1 & 1 \\ k_z^+/\mu & k_z^-/\mu \end{bmatrix} \\ \bar{I}_p = \begin{bmatrix} k_z^+/k & k_z^-/k \\ \tilde{k}/\mu & \tilde{k}/\mu \end{bmatrix} \end{cases}.$$

Within each layer, the propagation of the waves simply follow the plane-wave solution and can be represented in a matrix form as:

$$\vec{\vec{E}}(\vec{x}) = \bar{P}(\vec{x})\vec{\vec{E}}(0)$$

where the propagation matrix $\bar{P}$ is defined as

$$\bar{P}(\vec{x}) = \begin{bmatrix} \exp\left(i\vec{k}^+ \cdot \vec{x}\right) & 0 \\ 0 & \exp\left(i\vec{k}^- \cdot \vec{x}\right) \end{bmatrix}.$$

Combining the interface matrix and the propagation matrix, the electric field amplitude vectors at the beginning of one layer and the next layer can be related by the vector equation

$$\bar{I}_n \bar{P}_n \vec{\vec{E}}_n = \bar{I}_{n+1}\vec{\vec{E}}_{n+1} \ .$$

An equation for amplitude vectors across a multilayer structure can be obtained by combining the equations above across all adjacent layers

$$\vec{\vec{E}}_0 \ = \ \bar{I}_0^{-1} \ \left(\bar{I}_1 \bar{P}_1^{-1} \bar{I}_1^{-1}\right) \ \cdots \ \left(\bar{I}_n \bar{P}_n^{-1} \bar{I}_n^{-1}\right) \ \bar{I}_{n+1} \ \ \vec{\vec{E}}_{n+1}$$

or equivalently,

$$\vec{\vec{E}}_{transmitted} = \bar{F}\ \vec{\vec{E}}_{incident} \quad \text{where } \bar{F} = \begin{bmatrix} \bar{F}^{++} & \bar{F}^{+-} \\ \bar{F}^{-+} & \bar{F}^{--} \end{bmatrix}$$

$$\vec{\vec{E}}_{incident} = \overline{\overline{B}}\ \vec{\vec{E}}_{transmitted} \quad \text{where } \overline{\overline{B}} = \begin{bmatrix} \overline{B}^{++} & \overline{B}^{+-} \\ \overline{B}^{-+} & \overline{B}^{--} \end{bmatrix}$$

where $\overline{F}$ and $\overline{B}$ are the forward and backward transfer matrices across a multilayer structure determined as

$$\overline{F} = \bar{I}_{n+1}^{-1}\left(\bar{I}_n \bar{P}_n \bar{I}_n^{-1}\right)\cdots\left(\bar{I}_1 \bar{P}_1 \bar{I}_1^{-1}\right)\bar{I}_0$$

$$\overline{B} = \bar{I}_0^{-1}\left(\bar{I}_1 \bar{P}_1^{-1} \bar{I}_1^{-1}\right)\cdots\left(\bar{I}_n \bar{P}_n^{-1} \bar{I}_n^{-1}\right)\bar{I}_{n+1}.$$

From the forward and backward transfer matrices, the transmission and reflection amplitudes can be calculated as

$$\begin{cases} t = 1/\overline{B}^{++} \\ r = \overline{B}^{-+}/\overline{B}^{++} \end{cases}.$$

The energy flux transmission, reflection, and absorption are

$$\begin{cases} T^{flux} = t\,t^* \cdot \left(C_{transmitted}/C_{incident}\right) \\ R^{flux} = r\,r^* \\ A^{flux} = 1 - T^{flux} - R^{flux} \end{cases}$$

where

$$C = \mathrm{Re}\left\{\frac{1}{\mu} k_z^{+*}\right\},$$

and the polarization ratios in transmission and reflection are:

$$\begin{cases} t_{p/s} = t_p/t_s \\ r_{p/s} = r_p/r_s \end{cases}.$$

The solutions above are for ideal multilayer structures where the interfaces are exactly parallel to each other and the illumination is coherent both spatially and temporally. These conditions are not necessarily satisfied in practice, especially for epitaxial thin film samples on thick substrates. The substrates are usually very thick compared to the thin films deposited on them, so the interference oscillations from the substrates can have extremely high frequencies which may exceed the experimental resolution of the spectrometer. Also, the two surfaces of the substrate are usually not absolutely parallel, so the interference oscillations from the substrates may be strongly damped. Also moderate reductions in the resolution of the spectrometer cause the interference oscillations from the substrate to be completely suppressed. If these experimental conditions are true, the substrate effectively acts as an incoherent medium, hence the total transmission and reflection from the sample become partially coherent.

The partially coherent mixed state can be described by the polarization density matrix:

$$\bar{\rho} = \begin{bmatrix} \rho_{ss^*} & \rho_{sp^*} \\ \rho_{ps^*} & \rho_{pp^*} \end{bmatrix}.$$

The polarization density matrix of a coherent wave is:

$$\bar{\rho} = \bar{E}\bar{E}^T = \begin{bmatrix} E_s \\ E_p \end{bmatrix} \begin{bmatrix} E_s^* & E_p^* \end{bmatrix} = \begin{bmatrix} E_s E_s^* & E_s E_p^* \\ E_p E_s^* & E_p E_p^* \end{bmatrix}$$

where A^T represents the transpose of vector A.

Using the polarization density matrix representation, an experimental measurement of the polarization state by a linear polarizer $\hat{p}$ and a quarter-wave plate $(\hat{o},\hat{e})$ can be represented by a polarization measurement vector $\bar{M}$:

$$\bar{M} = (\hat{p}\cdot\hat{o})\,\hat{o} + i\,(\hat{p}\cdot\hat{e})\,\hat{e}$$

so that the resulting intensity of the measurement is given by:

$$\begin{aligned} Q_{\bar{M}} &= \bar{M}^T \bar{\rho} \bar{M} \\ &= M_s M_s^* E_s E_s^* + M_p M_p^* E_p E_p^* + M_s M_p^* E_s E_p^* + M_p M_s^* E_p E_s^* . \end{aligned}$$

Here $\hat{p}$ is the unit vector of the polarization direction of the linear polarizer, $\hat{o}$ and $\hat{e}$ are the unit vectors of the ordinary and extraordinary optical axes of the wave plate, respectively.

Similar to the amplitude vector for the coherent state, a polarization density amplitude vector can be defined to describe the total mixed state in a layer with both forward and backward propagating waves:

$$\bar{\bar{\rho}} = \begin{bmatrix} \bar{\rho}^+ \\ \bar{\rho}^- \end{bmatrix}.$$

In analogy to the forward and backward transfer matrices for the coherent state, forward and backward polarization density transfer matrices can be defined for partially coherent mixed state:

$$\bar{\bar{\rho}}_{transmitted} = \bar{\bar{\bar{F}}}\;\bar{\bar{\rho}}_{incident} \qquad \text{where } \bar{\bar{\bar{F}}} = \begin{bmatrix} \bar{\bar{\bar{F}}}^{++} & \bar{\bar{\bar{F}}}^{+-} \\ \bar{\bar{\bar{F}}}^{-+} & \bar{\bar{\bar{F}}}^{--} \end{bmatrix}$$

$$\overline{\overline{\rho}}_{incident} = \overline{\overline{B}}\,\overline{\overline{\rho}}_{transmitted} \qquad \text{where } \overline{\overline{B}} = \begin{bmatrix} \overline{\overline{B}}^{++} & \overline{\overline{B}}^{+-} \\ \overline{\overline{B}}^{-+} & \overline{\overline{B}}^{--} \end{bmatrix}.$$

For multilayer structures with n layers, the polarization density transfer matrices can be constructed as the sequential products of polarization density transfer matrices of all the layers of the multilayer structure:

$$\overline{\overline{F}} = \overline{\overline{F}}_n \overline{\overline{F}}_{n-1} \cdots \overline{\overline{F}}_2 \overline{\overline{F}}_1$$

$$\overline{\overline{B}} = \overline{\overline{B}}_1 \overline{\overline{B}}_2 \cdots \overline{\overline{B}}_{n-1} \overline{\overline{B}}_n \ .$$

From the polarization density transfer matrices, the transmitted, reflected, and absorbed energy flux can be readily calculated as

$$\begin{cases} T_{xy*}^{flux} = \left(1/\overline{\overline{B}}_{xy*}^{++}\right) \cdot \left(C_{transmitted}/C_{incident}\right) \\ R_{xy*}^{flux} = \overline{\overline{B}}_{xy*}^{-+} / \overline{\overline{B}}_{xy*}^{++} \\ A_{xy*}^{flux} = 1 - T_{xy*}^{flux} - R_{xy*}^{flux} \end{cases}$$

where

$$C = \mathrm{Re}\left\{\frac{1}{\mu} k_z^{+*}\right\}.$$

and where x and y may represent either s or p polarizations.

To construct the polarization density transfer matrix of a multilayer structure, polarization density transfer matrices of both incoherent and coherent substructures (group of adjacent layers and interfaces) must be determined. The polarization density transfer matrix across an incoherent medium (such as a thick substrate) is simple since only intensity is of concern:

$$\overline{\overline{F}}(\vec{x}) = \begin{bmatrix} \left|\exp\left(i\vec{k}^{+}\cdot\vec{x}\right)\right|^2 & 0 \\ 0 & \left|\exp\left(i\vec{k}^{-}\cdot\vec{x}\right)\right|^2 \end{bmatrix}$$

$$\overline{\overline{B}}(\vec{x}) = \begin{bmatrix} \left|\exp\left(-i\vec{k}^{+}\cdot\vec{x}\right)\right|^2 & 0 \\ 0 & \left|\exp\left(-i\vec{k}^{-}\cdot\vec{x}\right)\right|^2 \end{bmatrix}.$$

The polarization density transfer matrix across a coherent structure surrounded by incoherent media on both sides (such as a thick substrate on one side and air on the other) can be derived from the coherent transfer matrix across the coherent structure. Since both the polarization density transfer matrix and the coherent transfer matrix must yield the same physical transmission and reflection, the following equations must hold

$$\overline{\overline{F}}_{xy^*} = \begin{bmatrix} \overline{\overline{F}}_{xy^*}^{++} & \overline{F}_x^{+-}\overline{F}_y^{+-*} \\ \overline{\overline{F}}_{xy^*}^{-+} & \overline{F}_x^{--}\overline{F}_y^{--*} \end{bmatrix}$$

$$\overline{\overline{B}}_{xy^*} = \begin{bmatrix} \overline{B}_x^{++}\overline{B}_y^{++*} & \overline{\overline{B}}_{xy^*}^{+-} \\ \overline{B}_x^{-+}\overline{B}_y^{-+*} & \overline{\overline{B}}_{xy^*}^{--} \end{bmatrix}.$$

Since the forward and backward transfer matrices are the inverse matrices of each other, the matrix equations above yields the polarization density transfer matrix across a coherent structure surrounded by incoherent media on both sides:

$$\overline{\overline{F}}_{xy^*} = \begin{bmatrix} \left(1-\overline{F}_x^{+-}\overline{F}_y^{+-*}\overline{B}_x^{-+}\overline{B}_y^{-+*}\right)/\overline{B}_x^{++}\overline{B}_y^{++*} & \overline{F}_x^{+-}\overline{F}_y^{+-*} \\ -\overline{F}_x^{--}\overline{F}_y^{--*}\overline{B}_x^{-+}\overline{B}_y^{-+*}/\overline{B}_x^{++}\overline{B}_y^{++*} & \overline{F}_x^{--}\overline{F}_y^{--*} \end{bmatrix}$$

$$\overline{\overline{B}}_{xy^*} = \begin{bmatrix} \overline{B}_x^{++}\overline{B}_y^{++*} & -\overline{B}_x^{++}\overline{B}_y^{++*}\overline{F}_x^{+-}\overline{F}_y^{+-*}/\overline{F}_x^{--}\overline{F}_y^{--*} \\ \overline{B}_x^{-+}\overline{B}_y^{-+*} & \left(1-\overline{B}_x^{-+}\overline{B}_y^{-+*}\overline{F}_x^{+-}\overline{F}_y^{+-*}\right)/\overline{F}_x^{--}\overline{F}_y^{--*} \end{bmatrix},$$

or

$$\overline{\overline{F}}_{xy^*} = \begin{bmatrix} \begin{pmatrix} \overline{F}_x^{++}\overline{F}_y^{++*} \\ -\dfrac{\overline{F}_x^{++}\overline{F}_x^{--}\overline{F}_y^{+-*}\overline{F}_y^{-+*}}{\overline{F}_x^{--}\overline{F}_y^{--*}} \\ -\dfrac{\overline{F}_x^{+-}\overline{F}_x^{-+}\overline{F}_y^{++*}\overline{F}_y^{--*}}{\overline{F}_x^{--}\overline{F}_y^{--*}} \end{pmatrix} & \overline{F}_x^{+-}\overline{F}_y^{+-*} \\ -\overline{F}_x^{-+}\overline{F}_y^{-+*} & \overline{F}_x^{--}\overline{F}_y^{--*} \end{bmatrix}$$

$$\overline{\overline{B}}_{xy^*} = \begin{bmatrix} \overline{B}_x^{++}\overline{B}_y^{++*} & -\overline{B}_x^{+-}\overline{B}_y^{+-*} \\ \overline{B}_x^{-+}\overline{B}_y^{-+*} & \begin{pmatrix} \overline{B}_x^{--}\overline{B}_y^{--*} \\ -\dfrac{\overline{B}_x^{++}\overline{B}_x^{--}\overline{B}_y^{+-*}\overline{B}_y^{-+*}}{\overline{B}_x^{++}\overline{B}_y^{++*}} \\ -\dfrac{\overline{B}_x^{+-}\overline{B}_x^{-+}\overline{B}_y^{++*}\overline{B}_y^{--*}}{\overline{B}_x^{++}\overline{B}_y^{++*}} \end{pmatrix} \end{bmatrix}.$$

The solutions above are all the equations needed for calculation of optical transmission and reflection for a multilayer structure containing both coherent and incoherent layers. The multilayer structure can be divided into coherent sub-

structures separated by incoherent layers. Polarization density transfer matrices are calculated separately for each of these coherent substructures and incoherent layers and are then combined to form the overall polarization transfer matrices, from which optical transmission and reflection are calculated. The optical constant spectra are calculated by fitting the experimentally measured thickness-dependent transmission spectra to the numerical optical transmission function. The fittings were performed numerically using a modified Levenberg-Marquardt method. Fitting of each spectrum took about one hour on a Pentium 100 MHz computer.

The program for the multilayer optical interference modeling and transmission data analysis is written in C++ using Microsoft Visual C++ Version 4.0. The program consists of eight software modules named as "Analysis", "Fit", "Model", "Film", "Matrix", "Complex", "Stream", "Basis". Each module contains a "*.CPP" file which contains the implementation codes as well as a "*.H" header file which contains the definitions of the class structures in the module. The "Analysis" module handles the data file input and output and coordinates the calculations. The "Fit" module performs the numerical data fit through a modified Levenberg-Marquardt non-linear chi-square analysis. The "Model" module models the optical transmission and reflection functions in multilayer samples with thin film interference effects. The "Film" module defines multilayer objects to represent the structures of multilayer samples. The "Matrix" module defines common operations for matrix linear algebra. The "Complex" module defines common operations for complex numbers. The "Stream" module is an extension to the standard C++ stream class which contains a text search function to allow easy

handling of free format input data files. The "Basis" module contains the definitions of some frequently used basic constants and functions. The source codes of each module are given below.

```
//*************************************************************************
// File: Analysis.H                    - Gang He, 1996
//*************************************************************************
//
// input file format:
//
//        TotalLayers <int>
//        Thickness(nm) <real> .....
//        Coherent(Y/N) .....
//
//        TotalSamples <int>
//        VaryingLayer <int>
//        VaryingThickness(nm) <real> .....
//        StandardDeviation <real> .....
//
//        Nmin <real> Nmax <real>
//        Kmin <real> Kmax <real>
//        ChiSquareError <real>
//
//        SpectralRange <real> <real>
//
//        Wavenumber (N K) Normalize Transmittance
//        <real> <real> <real> ..... <real> <real> .....
//        .....
//
// output file format (default to NUL):
//
//        Wavenumber N K Std-N Std-K ChiSquare Transmittance
//        <Wavenumber> <N> <K> <Std-N> <Std-K> <ChiSquare> <Transmittance> .....
//
// note:
//
//        Layers including enterance and exit media
//        with the first layer as the enterance media.
//
//*************************************************************************
```

```
int main(int argc, char* argv[]);


//*************************************************************************
// File: Analysis.CPP              - Gang He, 1996
//*************************************************************************

#include "Analysis.h"
#include "Model.h"
#include "Fit.h"
#include "Film.h"
#include "Stream.h"
#include <math.h>
#include <fstream.h>

int main(int argc, char* argv[]) {
        if (argc<2) {
                cout<<"Thickness Series Transmission Data Analysis - Gang He 1996"<<endl;
                cout<<"Usage: Analysis <input file> [ <output file> ]"<<endl;
                return 0;
        };
        char* InputFileName=argv[1];
        char* OutputFileName=(argc>=3? argv[2] : "NUL");
        ifstream Input(InputFileName);
        ofstream Output(OutputFileName);
        int i;
        Film Sample;
        Input>>Skip("TotalLayers")>>Sample.TotalLayers;
        Sample.Profile=new Layer[Sample.TotalLayers];
        SimpleMedia* LayerMaterial=new SimpleMedia[Sample.TotalLayers];
        Input>>Skip("(nm)");
        for (i=0; i<Sample.TotalLayers; i++) {
                real t;
                Input>>t;
                Sample.Profile[i].Thickness=t*1e-7;
        };
        Input>>Skip("(Y/N)");
        for (i=0; i<Sample.TotalLayers; i++) {
                char c;
                Input>>c;
                Sample.Profile[i].Coherent=(c!='n' && c!='N');
                Sample.Profile[i].Material=&(LayerMaterial[i]);
        };
        int TotalSamples,VaryingLayer;
        Input>>Skip("TotalSamples")>>TotalSamples;
        Input>>Skip("VaryingLayer")>>VaryingLayer;
        VaryingLayer--;
```

```
real* VaryingThickness=new real[TotalSamples];
real* Transmittance=new real[TotalSamples];
real* StandardDeviation=new real[TotalSamples];
Input>>Skip("(nm)");
for (i=0; i<TotalSamples; i++) {
        real t;
        Input>>t;
        VaryingThickness[i]=t*1e-7;
};
Input>>Skip("Deviation");
for (i=0; i<TotalSamples; i++)
        Input>>StandardDeviation[i];
real Nmin,Nmax,Kmin,Kmax,ChiSquareError,Wmin,Wmax;
Input>>Skip("Nmin")>>Nmin>>Skip("Nmax")>>Nmax;
Input>>Skip("Kmin")>>Kmin>>Skip("Kmax")>>Kmax;
Input>>Skip("Error")>>ChiSquareError;
Input>>Skip("Range")>>Wmin>>Wmax;
if (!(Input>>Skip("Transmittance")).good()) {
        cerr<<"Invalid Input File"<<endl;
        return 1;
};
OpticalModel SampleModel(&Sample,VaryingLayer);
Estimator SampleFit(&SampleModel);
logic Vary[5];
real Parameter[5],P_Min[5],P_Max[5],CovMatrix[5][5],CurMatrix[5][5];
real* (Covariance[5]);
real* (Curvature[5]);
for (i=0; i<5; i++) {
        Covariance[i]=&(CovMatrix[i][0]);
        Curvature[i]=&(CurMatrix[i][0]);
};
Vary[0]=(Nmin<=Nmax);
Vary[1]=(Kmin<=Kmax);
Vary[2]=Vary[3]=Vary[4]=false;
P_Min[0]=Nmin; P_Max[0]=Nmax;
P_Min[1]=Kmin; P_Max[1]=Kmax;
cout<<"Wavenumber N K Std-N Std-K ChiSquare Transmittance"<<endl;
Output<<"Wavenumber N K Std-N Std-K ChiSquare Transmittance"<<endl;
while ((Input>>ws).good()) {
        real Wavenumber,Normalize,ChiSquare;
        Input>>Wavenumber;
        if (Wavenumber>=Wmin && Wavenumber<=Wmax) {
                for (i=0; i<Sample.TotalLayers; i++) {
                        real n,k,u=1;
                        Input>>n>>k;
                        LayerMaterial[i]=SimpleMedia(Complex(n,k),u);
                };
                Complex VaryingN=LayerMaterial[VaryingLayer].
```

```
                    RefractiveIndex(Wavenumber);
                Complex VaryingU=LayerMaterial[VaryingLayer].
                    MagneticPermeability(Wavenumber);
                Parameter[0]=re_part(VaryingN);
                Parameter[1]=im_part(VaryingN);
                Parameter[2]=re_part(VaryingU);
                Parameter[3]=im_part(VaryingU);
                Parameter[4]=Wavenumber;
                Input>>Normalize;
                for (i=0; i<TotalSamples; i++) {
                    real t;
                    Input>>t;
                    Transmittance[i]=t/Normalize;
                };
                if (SampleFit.Fit(
                    TotalSamples,VaryingThickness,Transmittance,StandardDeviation,
                    Parameter,P_Min,P_Max,Vary,
                    Covariance,Curvature,&ChiSquare,ChiSquareError)) {
                    real n=Parameter[0];
                    real k=Parameter[1];
                    real dn=sqrt(Covariance[0][0]);
                    real dk=sqrt(Covariance[1][1]);
                    cout<<Wavenumber<<" "<<n<<" "<<k<<" "
                        <<" "<<dn<<" "<<dk<<" "<<ChiSquare;
                    Output<<Wavenumber<<" "<<n<<" "<<k<<" "
                        <<" "<<dn<<" "<<dk<<" "<<ChiSquare;
                    for (i=0; i<TotalSamples; i++) {
                        real t;
                        SampleModel.Evaluate(VaryingThickness[i],Parameter,&t);
                        t*=Normalize;
                        cout<<" "<<t;
                        Output<<" "<<t;
                    };
                    cout<<endl;
                    Output<<endl;
                } else {
                    cout<<Wavenumber<<" ?"<<endl;
                    Output<<Wavenumber<<" ?"<<endl;
                };
            };
        };
        return 0;
};

//*************************************************************************
// File: Fit.H                  - Gang He, 1996
//*************************************************************************
```

```
#ifndef Included_Fit
#include "Basis.h"

class FitFunction {
public:
        FitFunction(int TotalParameters);
        virtual ~FitFunction();
        int TotalParameters;
        virtual logic Evaluate
                (real x, real* a, real* y, real* dyda, logic* Vary)=NULL;
};

class NumericalFunction : public FitFunction {
public:
        NumericalFunction(int TotalParemeters);
        ~NumericalFunction();
        logic Evaluate(real x, real* a, real* y, real* dyda, logic* Vary);
        virtual logic Evaluate(real x, real* a, real* y)=NULL;
        real* Displacement;
};

class Estimator {
public:
        Estimator(FitFunction* Model);
        ~Estimator();
        FitFunction* Model();
        logic Fit(
                int ndata, real* x, real* y, real* sig,
                real* a, real* a_min, real* a_max, logic* vary,
                real** covar, real** curv, real* chisq, real chisq_error=1e-2);
private:
        logic MarquardtMin(
                int ndata, real* x, real* y, real* sig,
                real* a, real* a_min, real* a_max, logic* vary,
                real** covar, real** curv, real* chisq, real* alamda);
        logic MarquardtCoefficient(
                int ndata, real* x, real* y, real* sig,
                real* a, logic* vary, real** curv, real* beta,
                real* chisq);
        logic GaussJordan(int n, real** a, real* b);
        void CovarianceSort(real** covar, logic* vary);
        void Swap(real& a, real& b);
        FitFunction* Model_;
        int ma,mfit,nfit_data;
        real *atry, *beta, *da, *oneda, *dyda;
        int *indxc, *indxr, *ipiv;
};
```

```
#define Included_Fit
#endif


//*************************************************************************
// File: Fit.CPP          - Gang He, 1996
//*************************************************************************

#include "Fit.h"
#include <stdlib.h>
#include <iostream.h>
#include <iomanip.h>

FitFunction::FitFunction(int TotalParametersIn)
: TotalParameters(TotalParametersIn)
{};

FitFunction::~FitFunction() {};

NumericalFunction::NumericalFunction(int TotalParametersIn)
:       FitFunction(TotalParametersIn)
{
        Displacement=new real[TotalParameters];
};

NumericalFunction::~NumericalFunction() {
        delete Displacement;
};

logic NumericalFunction::Evaluate
(real x, real* a, real* y0, real* dyda, logic* Vary) {
        if (!Evaluate(x,a,y0)) return false;
        for (int Parameter=0; Parameter<TotalParameters; Parameter++) {
                if (Vary[Parameter]) {
                        real a0=a[Parameter];
                        a[Parameter]+=Displacement[Parameter];
                        real y1;
                        if (!Evaluate(x,a,&y1)) return false;
                        a[Parameter]=a0;
                        dyda[Parameter]=(y1-*y0)/Displacement[Parameter];
                } else {
                        dyda[Parameter]=0.0;
                };
        };
        return true;
};
```

```
Estimator::Estimator(FitFunction* ModelIn)
: Model_(ModelIn) {
        ma=Model_->TotalParameters;
        atry=new real[ma];
        beta=new real[ma];
        da=new real[ma];
        oneda=new real[ma];
        dyda=new real[ma];
        indxc=new int[ma];
        indxr=new int[ma];
        ipiv=new int[ma];
};

Estimator::~Estimator() {
        delete atry;
        delete beta;
        delete da;
        delete oneda;
        delete dyda;
        delete indxc;
        delete indxr;
        delete ipiv;
};

FitFunction* Estimator::Model() {
        return Model_;
};

logic Estimator::Fit(
        int ndata, real* x, real* y, real* sig,
        real* a, real* a_min, real* a_max, logic* vary,
        real** covar, real** curv, real* chisq, real chisq_error)
{
        const real max_alamda=1e99;
        real alamda=-1;
        if (!MarquardtMin(ndata,x,y,sig,a,a_min,a_max,vary,
                covar,curv,chisq,&alamda))
                return false;
        real chisq0;
        logic succeed;
        do {
                if (!(alamda<=max_alamda)) return false;
                chisq0=*chisq;
                succeed=MarquardtMin(ndata,x,y,sig,a,a_min,a_max,vary,
                        covar,curv,chisq,&alamda);
        } while (
                (!succeed) ||
                chisq0-*chisq>chisq_error);
```

```
        alamda=0;
        return MarquardtMin(ndata,x,y,sig,a,a_min,a_max,vary,covar,curv,chisq,&alamda);
};

logic Estimator::MarquardtMin(
        int ndata, real* x, real* y, real* sig,
        real* a, real* a_min, real* a_max, logic* vary,
        real** covar, real** curv, real* chisq, real* alamda)
{
        const real init_alamda=1e0, reduce_alamda=0.1, increase_alamda=10;
        int j,k,l,m;
        if (*alamda<0) {
                for (mfit=0,j=0; j<ma; j++)
                        if (vary[j]) mfit++;
                for (nfit_data=0,j=0; j<ndata; j++)
                        if (sig[j]>0) nfit_data++;
                for (j=0; j<ma; j++)
                        atry[j]=a[j];
                *alamda=init_alamda;
                return MarquardtCoefficient(ndata,x,y,sig,a,vary,curv,beta,chisq);
        };
        real ochisq=*chisq;
        for (j=-1,l=0; l<ma; l++) {
                if (vary[l]) {
                        for (j++,k=-1,m=0; m<ma; m++) {
                                if (vary[m]) {
                                        k++;
                                        covar[j][k]=curv[j][k];
                                };
                        };
                        covar[j][j]=curv[j][j]*(1.0+*alamda);
                        oneda[j]=beta[j];
                };
        };
        if (*alamda==0) {
                *chisq+=nfit_data-mfit;
                if (!GaussJordan(mfit,covar,oneda)) return false;
                CovarianceSort(covar,vary);
                return true;
        };
        if (GaussJordan(mfit,covar,oneda)) {
                for (j=0; j<mfit;j++) da[j]=oneda[j];
                for (j=-1,l=0; l<ma; l++)
                        if (vary[l]) {
                                atry[l]=a[l]+da[++j];
                                if (atry[l]<a_min[l]) atry[l]=a_min[l];
                                if (atry[l]>a_max[l]) atry[l]=a_max[l];
                        };
```

```
                if (MarquardtCoefficient(ndata,x,y,sig,atry,vary,covar,da,chisq)) {
                        if (*chisq<=ochisq) {
                                for (j=-1,l=0; l<ma; l++) {
                                        if (vary[l]) {
                                                for (j++,k=-1,m=0; m<ma; m++) {
                                                        if (vary[m]) {
                                                                k++;
                                                                curv[j][k]=covar[j][k];
                                                        };
                                                };
                                                beta[j]=da[j];
                                                a[l]=atry[l];
                                        };
                                };
                                *alamda*=reduce_alamda;
                                return true;
                        };
                };
        };
        *chisq=ochisq;
        *alamda=(*alamda+1)*increase_alamda;
        return false;
};

logic Estimator::MarquardtCoefficient(
        int ndata, real* x, real* y, real* sig,
        real* a, logic* vary, real** curv, real* beta,
        real* chisq)
{
        int i,j,k,l,m;
        real ymod,wt,sig2i,dy,d_chisq=(nfit_data-mfit)/(real)nfit_data;
        for (j=0; j<mfit; j++) {
                for (k=0; k<=j; k++) curv[j][k]=0.0;
                beta[j]=0.0;
        };
        *chisq=0;
        for (i=0; i<ndata; i++) {
                if (sig[i]>0) {
                        if (!Model_->Evaluate(x[i],a,&ymod,dyda,vary))
                                return false;
                        sig2i=1.0/(sig[i]*sig[i]);
                        dy=y[i]-ymod;
                        for (j=-1,l=0; l<ma; l++) {
                                wt=dyda[l]*sig2i;
                                if (vary[l])
                                        for (j++,k=-1,m=0; m<=l; m++) {
                                                if (vary[m])
                                                        curv[j][++k]+=wt*dyda[m];
```

```
                                                beta[j]+=dy*wt;
                                        };
                                };
                                *chisq+=dy*dy*sig2i-d_chisq;
                        };
                };
                for (j=1; j<mfit; j++)
                        for (k=0; k<j; k++)
                                curv[k][j]=curv[j][k];
                return true;
};

logic Estimator::GaussJordan(int n, real** a, real* b) {
        int i,icol,irow,j,k,l,ll;
        real big,dum,pivinv;
        for (j=0;j<n;j++) ipiv[j]=0;
        for (i=0;i<n;i++) {
                big=-1.0;
                for (j=0;j<n;j++)
                        if (ipiv[j] != 1)
                                for (k=0;k<n;k++) {
                                        if (ipiv[k] == 0) {
                                                if (!(absolute(a[j][k]) <= big)) {
                                                        big=absolute(a[j][k]);
                                                        irow=j;
                                                        icol=k;
                                                }
                                        } else if (ipiv[k] > 1) {
                                                return false;
                                        };
                                };
                ++(ipiv[icol]);
                if (irow != icol) {
                        for (l=0;l<n;l++) Swap(a[irow][l],a[icol][l]);
                        Swap(b[irow],b[icol]);
                };
                indxr[i]=irow;
                indxc[i]=icol;
                if (a[icol][icol] == 0.0) {
                        return false;
                };
                pivinv=1.0/a[icol][icol];
                a[icol][icol]=1.0;
                for (l=0;l<n;l++) a[icol][l] *= pivinv;
                b[icol] *= pivinv;
                for (ll=0;ll<n;ll++)
                        if (ll != icol) {
                                dum=a[ll][icol];
```

```
                                        a[ll][icol]=0.0;
                                        for (l=0;l<n;l++) a[ll][l] -= a[icol][l]*dum;
                                        b[ll] -= b[icol]*dum;
                                };
        };
        for (l=n-1;l>=0;l--) {
                if (indxr[l] != indxc[l])
                        for (k=0;k<n;k++)
                                Swap(a[k][indxr[l]],a[k][indxc[l]]);
        };
        return true;
};

void Estimator::CovarianceSort(real** covar, logic* vary) {
        int i,j,k;
        for (i=mfit; i<ma; i++)
                for (j=0; j<=i; j++)
                        covar[i][j]=covar[j][i]=0.0;
        for (k=mfit-1, j=ma-1; j>=0; j--) {
                if (vary[j]) {
                        for (i=0; i<ma; i++) Swap(covar[i][k],covar[i][j]);
                        for (i=0; i<ma; i++) Swap(covar[k][i],covar[j][i]);
                        k--;
                };
        };
};

void Estimator::Swap(real& a, real& b) {
        real temp=a;
        a=b;
        b=temp;
};


//*************************************************************************
// File: Model.H          - Gang He, 1996
//*************************************************************************
//
// Note:
//
//      a[0]=sqrt(n)
//      a[1]=sqrt(k)
//      a[2]=Re[u]
//      a[3]=Im[u]
//      a[4]=Wavenumber
//
//*************************************************************************
```

```
#ifndef Included_Model
#include "Fit.h"
#include "Film.h"

class OpticalModel : public NumericalFunction {
public:
        OpticalModel(Film* Sample, int VaryingLayer);
        logic Evaluate(real x, real* a, real* y);
private:
        Film* Sample;
        int VaryingLayer;
};

#define Included_Model
#endif


//*************************************************************************
// File: Model.CPP                - Gang He, 1996
//*************************************************************************

#include "Model.h"

OpticalModel::OpticalModel(
        Film* SampleIn,
        int VaryingLayerIn)
:       NumericalFunction(5),
        Sample(SampleIn),
        VaryingLayer(VaryingLayerIn)
{
        Displacement[0]=1e-3;
        Displacement[1]=1e-3;
        Displacement[2]=1e-3;
        Displacement[3]=1e-3;
        Displacement[4]=10;
};

logic OpticalModel::Evaluate(real x, real* a, real* y) {
        real OriginalThickness=Sample->Profile[VaryingLayer].Thickness;
        Media* OriginalMedia=Sample->Profile[VaryingLayer].Material;
        Sample->Profile[VaryingLayer].Thickness=x;
        SimpleMedia FittingMedia(Complex(a[0],a[1]),Complex(a[2],a[3]));
        Sample->Profile[VaryingLayer].Material=&FittingMedia;
        real Transmission,r;
        Complex c;
        Sample->Measure(a[4],0,&r,&Transmission,&r,&r,&r,&c,&c);
        Sample->Profile[VaryingLayer].Thickness=OriginalThickness;
        Sample->Profile[VaryingLayer].Material=OriginalMedia;
```

```
        *y=Transmission;
        return (Transmission==Transmission);
};


//************************************************************************
// File: Film.H                    - Gang He, 1996
//************************************************************************
//
// Note:
//
//      The first layer is the entrance media;
//      The last layer is the exit media;
//
//************************************************************************

#ifndef INCLUDED_FILM

#include "matrix.h"

class Media {
public:
        Media();
        virtual ~Media();
        virtual Complex RefractiveIndex(real Wavenumber);
        virtual Complex MagneticPermeability(real Wavenumber);
};

class SimpleMedia : public Media {
public:
        SimpleMedia(Complex RefractiveIndex=1, Complex MagneticPermeability=1);
        Complex RefractiveIndex(real Wavenumber);
        Complex MagneticPermeability(real Wavenumber);
private:
        Complex RefractiveIndex_, MagneticPermeability_;
};

class Layer {
public:
        Layer();
        Media* Material;
        real  Thickness;
        logic  Coherent;
};

class Film {
public:
        Film();
```

```
        int   TotalLayers;
        Layer* Profile;
        void  Measure(
                real   Wavenumber,   real   IncidentAngle,
                real*  RefractionAngle,
                real*  SSTransmission, real*  SSReflection,
                real*  PPTransmission, real*  PPReflection,
                Complex* SPTransmission, Complex* SPReflection);
private:
        Complex K(int Layer, real Wavenumber);
        Complex Kz(int Layer, real Wavenumber, Complex Kx);
        real   FluxFactor(int Layer, real Wavenumber, Complex Kx);
        Matrix2 SInterfaceMatrix(int Layer, real Wavenumber, Complex Kx);
        Matrix2 PInterfaceMatrix(int Layer, real Wavenumber, Complex Kx);
        Matrix2 BackwardPropogation(int Layer, real Wavenumber, Complex Kx);
        Matrix2 DensityMatrix(Matrix2 Bx, Matrix2 By);
};

#define INCLUDED_FILM
#endif


//*************************************************************************
// File: Film.CPP                    - Gang He, 1996
//*************************************************************************

#include <math.h>
#include "Film.h"

Media::Media() {};

Media::~Media() {};

Complex Media::RefractiveIndex(real Wavenumber) {
        return 1;
};

Complex Media::MagneticPermeability(real Wavenumber) {
        return 1;
};

SimpleMedia::SimpleMedia(Complex RefractiveIndexIn, Complex MagneticPermeabilityIn) {
        RefractiveIndex_=RefractiveIndexIn;
        MagneticPermeability_=MagneticPermeabilityIn;
};

Complex SimpleMedia::RefractiveIndex(real Wavenumber) {
        return RefractiveIndex_;
```

```
};

Complex SimpleMedia::MagneticPermeability(real Wavenumber) {
        return MagneticPermeability_;
};

Layer::Layer() {
        Material=NULL;
        Thickness=0;
        Coherent=true;
};

Film::Film() {
        TotalLayers=0;
};

void Film::Measure(
                real  Wavenumber,   real  IncidentAngle,
                real*  RefractionAngle,
                real*  SSTransmission, real*  SSReflection,
                real*  PPTransmission, real*  PPReflection,
                Complex* SPTransmission, Complex* SPReflection) {
        if (TotalLayers<=0) {
                *RefractionAngle=IncidentAngle;
                *SPTransmission=*SSTransmission=*PPTransmission=1;
                *SPReflection=*SSReflection=*PPReflection=0;
                return;
        };
        Complex Kx=re_part(K(0,Wavenumber))   *sin(IncidentAngle);
        Matrix2 BDensitySS=1,BDensityPP=1,BDensitySP=1;
        for (int Interface=1; Interface<TotalLayers; Interface++) {
                Matrix2 Bs=SInterfaceMatrix(Interface-1,Wavenumber,Kx).inverse();
                Matrix2 Bp=PInterfaceMatrix(Interface-1,Wavenumber,Kx).inverse();
                for (; Interface<TotalLayers-1 && Profile[Interface].Coherent; Interface++) {
                        Matrix2 Is=SInterfaceMatrix(Interface,Wavenumber,Kx);
                        Matrix2 Ip=PInterfaceMatrix(Interface,Wavenumber,Kx);
                        Bs=Bs*Is*BackwardPropogation(Interface,Wavenumber,Kx)*Is.inverse();
                        Bp=Bp*Ip*BackwardPropogation(Interface,Wavenumber,Kx)*Ip.inverse();
                };
                Bs=Bs*SInterfaceMatrix(Interface,Wavenumber,Kx);
                Bp=Bp*PInterfaceMatrix(Interface,Wavenumber,Kx);
                BDensitySS=BDensitySS*DensityMatrix(Bs,Bs);
                BDensityPP=BDensityPP*DensityMatrix(Bp,Bp);
                BDensitySP=BDensitySP*DensityMatrix(Bs,Bp);
                if (Interface<TotalLayers-1) {
                        Matrix2 B=BackwardPropogation(Interface,Wavenumber,Kx);
                        Matrix2 BDensity=B*B.conjugate();
                        BDensitySS=BDensitySS*BDensity;
```

```
                    BDensityPP=BDensityPP*BDensity;
                    BDensitySP=BDensitySP*BDensity;
                };
        };
        real KxPhase=re_part(Kx);
        real KzPhase=re_part(Kz(TotalLayers-1,Wavenumber,Kx));
        real KPhase=sqrt(KxPhase*KxPhase+KzPhase*KzPhase);
        *RefractionAngle=asin(KxPhase/KPhase);
        real TransmissionFactor=
                FluxFactor(TotalLayers-1,Wavenumber,Kx)/FluxFactor(0,Wavenumber,Kx);
        *SSTransmission=TransmissionFactor/re_part(BDensitySS.component(0,0));
        *PPTransmission=TransmissionFactor/re_part(BDensityPP.component(0,0));
        *SPTransmission=TransmissionFactor/BDensitySP.component(0,0);
        *SSReflection=re_part(BDensitySS.component(1,0)/BDensitySS.component(0,0));
        *PPReflection=re_part(BDensityPP.component(1,0)/BDensityPP.component(0,0));
        *SPReflection=BDensitySP.component(1,0)/BDensitySP.component(0,0);
        return;
};

Matrix2 Film::SInterfaceMatrix(int Layer, real Wavenumber, Complex Kx) {
        Matrix2 Is;
        Is.component(0,0)=Is.component(0,1)=1;
        Is.component(1,0)=Kz(Layer,Wavenumber,Kx)/
                Profile[Layer].Material->MagneticPermeability(Wavenumber);
        Is.component(1,1)=-Is.component(1,0);
        return Is;
};

Matrix2 Film::PInterfaceMatrix(int Layer, real Wavenumber, Complex Kx) {
        Matrix2 Ip;
        Complex K0=K(Layer,Wavenumber);
        Ip.component(0,0)=Kz(Layer,Wavenumber,Kx)/K0;
        Ip.component(0,1)=-Ip.component(0,0);
        Ip.component(1,0)=Ip.component(1,1)=K0/
                Profile[Layer].Material->MagneticPermeability(Wavenumber);
        return Ip;
};

Matrix2 Film::BackwardPropogation(int Layer, real Wavenumber, Complex Kx) {
        Matrix2 B=0;
        B.component(0,0)=exp(-Complex::i*Kz(Layer,Wavenumber,Kx)*Profile[Layer].Thickness);
        B.component(1,1)=1/B.component(0,0);
        return B;
};

Matrix2 Film::DensityMatrix(Matrix2 Bx, Matrix2 By) {
        Complex X00=Bx.component(0,0), Y00=conjugate(By.component(0,0));
        Complex X01=Bx.component(0,1), Y01=conjugate(By.component(0,1));
```

```
        Complex X10=Bx.component(1,0), Y10=conjugate(By.component(1,0));
        Complex X11=Bx.component(1,1), Y11=conjugate(By.component(1,1));
        Matrix2 Bxy;
        Bxy.component(0,0)=X00*Y00;
        Bxy.component(1,0)=X10*Y10;
        Bxy.component(0,1)=-X01*Y01;
        Bxy.component(1,1)=X11*Y11-(X00*X11*Y01*Y10+X01*X01*Y00*Y11)/(X00*Y00);
        return Bxy;
};

Complex Film::K(int Layer, real Wavenumber) {
        return 2*pi*Wavenumber*
                Profile[Layer].Material->RefractiveIndex(Wavenumber);
};

Complex Film::Kz(int Layer, real Wavenumber, Complex Kx) {
        Complex K0=K(Layer,Wavenumber);
        Complex Kz0=sqrt(K0*K0-Kx*Kx);
        if (re_part(Kz0)<0) Kz0=-Kz0;
        return Kz0;
};

real Film::FluxFactor(int Layer, real Wavenumber, Complex Kx) {
        return re_part(conjugate(Kz(Layer,Wavenumber,Kx))/
                Profile[Layer].Material->MagneticPermeability(Wavenumber));
};


//************************************************************************
// File:  Matrix.H                - Gang He, 1996
//************************************************************************

#ifndef INCLUDED_Matrix

#include "Complex.h"

class Vector2;
class Matrix2;

class Vector2 {
public:
        Vector2();
        Vector2(Complex x0, Complex x1);
        Complex& component(int index);
        Vector2 operator+(Vector2 v);
        Vector2 operator-(Vector2 v);
        Vector2 operator*(Matrix2 m);
        Complex operator*(Vector2 v);
```

```
private:
        Complex comp[2];
};

class Matrix2 {
public:
        Matrix2();
        Matrix2(Vector2 v0, Vector2 v1);
        Matrix2(Complex c);
  Matrix2(real r);
        Vector2& component(int index);
        Complex& component(int index1, int index2);
        Matrix2 transverse();
  Matrix2 inverse();
        Matrix2 conjugate();
        Matrix2 operator+(Matrix2 m);
        Matrix2 operator-(Matrix2 m);
        Matrix2 operator*(Matrix2 m);
        Vector2 operator*(Vector2 v);
private:
        Vector2 comp[2];
};

#define INCLUDED_Matrix
#endif


//************************************************************************
// File: Matrix.CPP                - Gang He, 1996
//************************************************************************

#include "Matrix.h"

Vector2::Vector2() {
 comp[0]=comp[1]=0;
};

Vector2::Vector2(Complex x0, Complex x1) {
 comp[0]=x0; comp[1]=x1;
};

Complex& Vector2::component(int index) {
 return comp[index];
};

Vector2 Vector2::operator+(Vector2 v) {
 return Vector2(comp[0]+v.comp[0],comp[1]+v.comp[1]);
};
```

```
Vector2 Vector2::operator-(Vector2 v) {
 return Vector2(comp[0]-v.comp[0],comp[1]-v.comp[1]);
};

Vector2 Vector2::operator*(Matrix2 m) {
 return Vector2((*this)*m.transverse().component(0),
                                        (*this)*m.transverse().component(1));
};

Complex Vector2::operator*(Vector2 v) {
 return comp[0]*v.comp[0]+comp[1]*v.comp[1];
};

Matrix2::Matrix2() {
 comp[0]=comp[1]=Vector2();
};

Matrix2::Matrix2(Vector2 v0, Vector2 v1) {
 comp[0]=Vector2(v0); comp[1]=Vector2(v1);
};

Matrix2::Matrix2(Complex c) {
 comp[0]=Vector2(c,0);
 comp[1]=Vector2(0,c);
};

Matrix2::Matrix2(real r) {
 comp[0]=Vector2(r,0);
 comp[1]=Vector2(0,r);
};

Vector2& Matrix2::component(int index) {
 return comp[index];
};

Complex& Matrix2::component(int index1, int index2) {
        return comp[index1].component(index2);
};

Matrix2 Matrix2::transverse() {
 return Matrix2(Vector2(component(0,0),component(1,0)),
                                    Vector2(component(0,1),component(1,1)));
};

Matrix2 Matrix2::conjugate() {
        return Matrix2(
                Vector2(::conjugate(component(0,0)),::conjugate(component(1,0))),
```

```
                Vector2(::conjugate(component(0,1)),::conjugate(component(1,1))));
};

Matrix2 Matrix2::inverse() {
 Complex det=
        1/(component(0,0)*component(1,1)-component(0,1)*component(1,0));
 return Matrix2(
        Vector2(det*component(1,1),-1*det*component(0,1)),
        Vector2(-1*det*component(1,0),det*component(0,0)));
};

Matrix2 Matrix2::operator+(Matrix2 m) {
 return Matrix2(comp[0]+m.comp[0],comp[1]+m.comp[1]);
};

Matrix2 Matrix2::operator-(Matrix2 m) {
 return Matrix2(comp[0]-m.comp[0],comp[1]-m.comp[1]);
};

Matrix2 Matrix2::operator*(Matrix2 m) {
 Matrix2 mt=m.transverse();
 return  Matrix2
        (Vector2(comp[0]*mt.comp[0],comp[0]*mt.comp[1]),
        Vector2(comp[1]*mt.comp[0],comp[1]*mt.comp[1]));
};

Vector2 Matrix2::operator*(Vector2 v) {
 return Vector2(comp[0]*v,comp[1]*v);
};


//*************************************************************************
// File:  Complex.H                - Gang He, 1996
//*************************************************************************

#ifndef INCLUDED_Complex

#include "basis.h"

class Complex {
 public:
   Complex();
   Complex(const real re);
   Complex(const real re, const real im);
   Complex operator=(const real re);
        static  const  Complex i;
        real    friend re_part  (const Complex);
   real    friend im_part  (const Complex);
```

```
  real    friend abs      (const Complex);
  real    friend theta    (const Complex);
  Complex friend operator-(const Complex);
  Complex friend operator+(const Complex, const Complex);
  Complex friend operator-(const Complex, const Complex);
  Complex friend operator*(const Complex, const Complex);
  Complex friend operator/(const Complex, const Complex);
  Complex friend operator+(const Complex, const real   );
  Complex friend operator-(const Complex, const real   );
  Complex friend operator*(const Complex, const real   );
  Complex friend operator/(const Complex, const real   );
  Complex friend operator+(const real   , const Complex);
  Complex friend operator-(const real   , const Complex);
  Complex friend operator*(const real   , const Complex);
  Complex friend operator/(const real   , const Complex);
  Complex friend conjugate(const Complex);
  Complex friend exp      (const Complex);
  Complex friend sin      (const Complex);
  Complex friend cos      (const Complex);
  Complex friend sinh     (const Complex);
  Complex friend cosh     (const Complex);
  Complex friend sqrt     (const Complex);
 private:
  real re,im;
};

#define INCLUDED_Complex
#endif


//***************************************************************************
// File :  Complex.CPP     - Gang He, 1993.
//***************************************************************************

#include "Complex.h"
#include <math.h>

real conj(const real r) { return r; };

Complex::Complex()
 { re=im=0; };

Complex::Complex(const real rr)
 { re=rr; im=0; }

Complex::Complex(const real rr, const real ii)
 { re=rr; im=ii; }
```

```
Complex Complex::operator=(const real r)
  { re=r; im=0; return *this; };

const Complex Complex::i=Complex(0,1);

real re_part(const Complex c) { return c.re; }

real im_part(const Complex c) { return c.im; }

Complex conjugate(const Complex c)
  { return Complex(c.re, -c.im); }

real abs(const Complex c)
  { return sqrt(c.re*c.re+c.im*c.im); }

real theta(const Complex c) {
  return atan2(c.im,c.re);
}

Complex operator-(const Complex c)
  { return Complex(-c.re, -c.im); }

Complex operator+(const Complex c1, const Complex c2)
  { return Complex(c1.re+c2.re, c1.im+c2.im); }

Complex operator-(const Complex c1, const Complex c2)
  { return Complex(c1.re-c2.re, c1.im-c2.im); }

Complex operator*(const Complex c1, const Complex c2) {
  return Complex(c1.re*c2.re-c1.im*c2.im,
            c1.re*c2.im+c1.im*c2.re); }

Complex operator/(const Complex c1, const Complex c2) {
  real temp=c2.re*c2.re+c2.im*c2.im;
  return Complex((c1.re*c2.re+c1.im*c2.im)/temp,
            (c1.im*c2.re-c1.re*c2.im)/temp);
}

Complex operator+(const Complex c, const real r)
  { return Complex(c.re+r, c.im); }

Complex operator-(const Complex c, const real r)
  { return Complex(c.re-r, c.im); }

Complex operator*(const Complex c, const real r)
  { return Complex(c.re*r, c.im*r); }

Complex operator/(const Complex c, const real r)
```

```
 { return Complex(c.re/r, c.im/r); }

Complex operator+(const real r, const Complex c)
 { return Complex(c.re+r, c.im); }

Complex operator-(const real r, const Complex c)
 { return Complex(r-c.re, -c.im); }

Complex operator*(const real r, const Complex c)
 { return Complex(c.re*r, c.im*r); }

Complex operator/(const real r, const Complex c)
 { return (r/(c.re*c.re+c.im*c.im))*conjugate(c); }

Complex exp(const Complex c)
 { return exp(c.re)*Complex(cos(c.im),sin(c.im)); }

Complex sin(const Complex c) {
 Complex temp=Complex(-c.im,c.re);
 temp=(exp(temp)-exp(-temp))/2;
 return Complex(temp.im, -temp.re);
}

Complex cos(const Complex c) {
 Complex temp=Complex(-c.im,c.re);
 return (exp(temp)+exp(-temp))/2;
}

Complex sinh(const Complex c)
 { return (exp(c)-exp(-c))/2; }

Complex cosh(const Complex c)
 { return (exp(c)+exp(-c))/2; }

Complex sqrt(const Complex c) {
 real t=theta(c)/2;
 return sqrt(abs(c))*Complex(cos(t),sin(t));
}


//*************************************************************************
// File : Stream.H                    - Gang He, 1996
//*************************************************************************

#ifndef Included_Stream
#include "Basis.h"
#include <iostream.h>
#include <iomanip.h>
```

```
class Manipulator {
 public:
   Manipulator();
   friend  ostream& operator<<(ostream&, Manipulator&);
   friend  istream& operator>>(istream&, Manipulator&);
 protected:
   virtual ostream& Insert (ostream&);
   virtual istream& Extract(istream&);
};

class Skip : public Manipulator {
 public:
   Skip(char* String);
   Skip(char  Character);
 protected:
   istream& Extract(istream&);
 private:
   char* String;
   char  Buffer[2];
};

class Line : public Manipulator {
 public:
   Line(char* String, int Size);
 protected:
   istream& Extract(istream&);
 private:
   char* String;
         int   Size;
};

class SetWP : public Manipulator {
 public:
   SetWP(int Width, int Precision);
 protected:
   istream& Extract(istream&);
   ostream& Insert (ostream&);
 private:
   int Width, Precision;
};

#define Included_Stream
#endif


//*************************************************************************
// File :  Stream.CPP                - Gang He, 1996
```

```
//*****************************************************************************

#include "Stream.h"

Manipulator::Manipulator() {};

ostream& Manipulator::Insert (ostream& s) { return s; };

istream& Manipulator::Extract(istream& s) { return s; };

ostream& operator<<(ostream& s, Manipulator& M)
 { return (&M)->Insert(s); };

istream& operator>>(istream& s, Manipulator& M)
 { return (&M)->Extract(s); };

Skip::Skip(char* StringIn) {
 Buffer[0]='\0';
 String=(StringIn? StringIn: Buffer);
};

Skip::Skip(char Character) {
 Buffer[0]=Character;
 Buffer[1]='\0';
 String=Buffer;
};

istream& Skip::Extract(istream& s) {
 int Matched=0;
 while (String[Matched] && s.good()) {
  char c;
  s.get(c);
  int Matching=Matched;
  logic Match=true;
  while (Matching>=0 && !(Match && c==String[Matching])) {
   Matching--;
   Match=true;
   for (int I=0; I<Matching && Match; I++)
        Match=(String[I]==String[I+Matched-Matching]);
  };
  Matched=Matching+1;
 };
 return s;
};

Line::Line(char* StringIn, int SizeIn) {
 String=StringIn;
 Size=SizeIn;
```

```
};

istream& Line::Extract(istream& s) {
 return s.getline(String,Size);
};

SetWP::SetWP(int WidthIn, int PrecisionIn) {
 Width=WidthIn; Precision=PrecisionIn;
};

istream& SetWP::Extract(istream& s) {
 return s>>setiosflags(ios::showpointlios::fixed)
          >>setprecision(Precision)>>setw(Width);
};

ostream& SetWP::Insert(ostream& s) {
 return s<<setiosflags(ios::showpointlios::fixed)
          <<setprecision(Precision)<<setw(Width);
};


//*************************************************************************
// File : Basis.H            - Gang He, 1996
//*************************************************************************

#ifndef Included_Basis

#define NULL 0

typedef int   logic;
const extern logic true, false;

typedef double  real;
const extern    real pi;

real    absolute      (real r);
int     sign          (real r);
long int closest_long_int(real r);
int     closest_int   (real r);
long int absolute(long int l);
int     sign   (long int l);
int     absolute(int i);
int     sign   (int i);

#define Included_Basis
#endif
```

```
//*************************************************************************
// File : Basis.CPP                    - Gang He, 1996
//*************************************************************************


#include "Basis.h"

const logic false=0;
const logic true =!false;

const real pi=3.14159265358979323846264338 3;

int absolute(int i)
  { return i>=0?i:-i; };

long int absolute(long int l)
  { return l>=0?l:-l; };

real absolute(real r)
  { return r>=0?r:-r; };

int sign(int i)
  { return i==0?0:(i>0?1:-1); };

int sign(long int l)
  { return l==0?0:(l>0?1:-1); };

int sign(real r)
  { return r==0?0:(r>0?1:-1); };

int closest_int(real r)
  { return r>=0? (int)(r+0.5) : -(int)(-r+0.5); };

long int closest_long_int(real r)
  { return r>=0? (long int)(r+0.5) : -(long int)(-r+0.5); };
```

Appendix B High Resolution Encoder Signal Interpolation for High Accuracy Position Measurement

Encoders are widely used for accurate linear and angular position measurements in modern technology. For example, a high resolution high accuracy encoder system is one of the key components in a high resolution x-ray diffractometer system built in the Keck Laboratory at Caltech. The diffractometer is used for all the high resolution x-ray diffraction measurements in this study.

A very common type of encoder is the incremental encoder which generates incremental quadrature pulse signals corresponding to the relative position changes that can be further integrated (counted) to obtain absolute positions. They generally have relatively low costs and are capable of high resolutions. Very high resolution optical incremental encoders usually generate quadrature sinusoidal analog signals by optical diffractometry and interferometry, hence achieve resolutions that approach optical wavelength limit (e.g., Canon Laser Rotary Encoder K-1 that generates 81,000 sinusoidal pulses per revolution). The most straightforward way of obtaining position information from this type of encoder is to directly count the number of the sinusoidal pulses. The maximum resolution from such direct counting is determined by the density of the pulses, which, in the case of optical encoders, is limited by the optical wavelength.

To further increase the encoder resolution, the sinusoidal signals must be interpolated so that additional position information is obtained from the amplitudes of the analog signals. This is commonly achieved by using a hardware circuit to divide each sinusoidal pulse into multiple digital quadrature pulses which can then be integrated to obtain finer positions (e.g., Canon Encoder Interpolator CI40-2 that divides each sinusoidal pulse into 40 divisions to achieve a 0.4 arc second resolution with a K-1 encoder). However, such hardware interpolators are relatively expensive and limited in resolution, accuracy, stability, and flexibility. For example, we have used the combination of Canon Encoder K-1 and Interpolator CI40-2 in a high resolution x-ray diffraction system and experienced severe encoder-interpolator instability problems caused by background noises. The interpolator is inherently sensitive to high frequency noise and such noise can generate high frequency pulse trains that cause the computer to lose track of the encoder position. Also, such hardware interpolators may generate inaccurate results when the encoder signals are not ideal quadrature sinusoidal signals.

To overcome the limitations of such interpolators, a new interpolation scheme was developed and implemented which uses analog-to-digital (A/D) signal conversion followed by software phase calculations to obtain the position information and achieved a resolution of 0.04 arc second when used with the Canon K-1 encoder. When compared with the conventional hardware interpolators, the new interpolation scheme costs much less yet achieves much higher performance in terms of resolution, accuracy, stability and flexibility. For

example, the new interpolation scheme can easily compensate residual errors via software calibrations, increase resolution by using higher dynamic range A/D converters, and accommodate multiple encoders in a single system.

The analog output encoders usually have two sinusoidal wave outputs as phase A and phase B which are phase shifted by $\pi/2$ (90 degrees). The encoder position is proportional to the phase angle θ of the sinusoidal waves. In principle, once the values of phase A and phase B signals are known, the phase angle θ can be numerically calculated from $tan(\theta)=B/A$. In practice, however, A and B signals are not always phase shifted by exactly $\pi/2$. Assuming that the error in the phase shift from $\pi/2$ is δ so that the real phase shift between A and B signals is $\pi/2 + \delta$, then:

$$A = cos(\theta - \delta/2) ,$$

$$B = sin(\theta + \delta/2) .$$

Note that δ is a parameter of a specific encoder system and is obtained from calibration. Define X and Y as the quadrature signals after correcting for the error δ in phase shift:

$$X = cos(\theta) = [A\ cos(\delta/2) - B\ sin(\delta/2)]\ cos(\delta) ,$$

$$Y = sin(\theta) = [\ B\ cos(\delta/2) - A\ sin(\delta/2)\ ]\ cos(\delta)\ .$$

Equivalently, (X,Y) can be viewed as a vector in a two-dimensional space. Define C as the count of cycles that the (X,Y) vector has circled around the origin, and N as the count of quadrants that the (X,Y) vector has passed (Counterclockwise counted as positive and clockwise counted as negative). Define *phase*(X,Y) as the phase angle of (X,Y) in the range of 0 to 2π, and *quadrant*(X,Y) as the quadrant number of (X,Y) ($(0,\pi/2)$, $(\pi/2,\pi)$, $(\pi,3\pi/2)$, and $(3\pi/2,2\pi)$ defined as quadrant 0, 1, 2, and 3, respectively), then:

$$\begin{aligned}\theta &= C \cdot 2\pi + phase(X,Y) \\ &= C \cdot 2\pi + quadrant(X,Y) \cdot \pi/2 + phase(X,Y) - quadrant(X,Y) \cdot \pi/2 \\ &= [\ C \cdot 4 + quadrant(X,Y)\ ] \cdot \pi/2 + [\ phase(X,Y) - quadrant(X,Y) \cdot \pi/2\ ] \\ &= N \cdot \pi/2 + [\ phase(X,Y) - quadrant(X,Y) \cdot \pi/2\ ]\ .\end{aligned}$$

Here *phase*(X,Y) are calculated from X and Y which can be calculated from numeric values of A and B obtained from A/D conversion. N can be obtained by counting the A, B quadrature signals the way standard quadrature encoder signals are counted. To do so, the sinusoidal waves of A and B must be transformed into square waves first. The simplest way is to use the sign bit of digitized A and B as the square wave. However, this would require the A/D converter to be operating at high speed all the time and may also encounter noise problems at the zero-crossing points. A better way is to use a dedicated comparator to digitize the A, B

signals. To obtain large noise margins, standard Schmitt comparators can be used. The quadrant of (X,Y) can then be readily calculated from N as *quadrant*(X,Y) = (N mod 4), provided that the initial value of N is correctly set at initialization so that the counting of N starts from quadrant zero. Note, however, that in general the perfect synchronization of *phase*(X,Y) (from A, B digitization) with quadrature counter N is not guaranteed, especially when quadrature counter N is supported by dedicated comparators. In other words, *phase*(X,Y) may be one quadrant away from quadrature counter N. This problem can be solved by restricting *phase*(X,Y) to be within a $(-\pi,+\pi)$ range from the center of the quadrant indicated by quadrature counter N, i.e.,

$$-\pi < \textit{phase}(X,Y) - [\ (N \bmod 4) \cdot \pi/2 + \pi/4\ ] < +\pi\ .$$

Thus the total phase angle can be expressed as:

$$\begin{aligned}\theta &= N \cdot \pi/2 + [\ \textit{phase}(X,Y) - \textit{quadrant}(X,Y) \cdot \pi/2\ ] \\ &= N \cdot \pi/2 + \pi/4 + [\ \textit{phase}(X,Y) - (\ \textit{quadrant}(X,Y) \cdot \pi/2 + \pi/4\ )\ ] \\ &= N \cdot \pi/2 + \pi/4 + \textit{offset}(\ \textit{phase}(X,Y) - [\ (N \bmod 4) \cdot \pi/2 + \pi/4)\ ]\ ),\end{aligned}$$

where *offset*(α) is a function that folds angle α onto the range of $(-\pi,+\pi)$:

$$\textit{offset}(\alpha) = \alpha - \textit{closest-integer}(\ \alpha/(2\pi)\ ) \cdot 2\pi\ .$$

Finally, the position p of the encoder can be calculated from the total phase angle θ and the encoder displacement L per sinusoidal output cycle as:

$$p = L \cdot \theta / (2\pi) .$$

A schematic of such an encoder signal interpolation system is shown below. The system is very inexpensive to implement. Since in most encoder applications a computer is already part of the system, the only additional cost of the interpolation system is the A/D converters and the quadrature up/down counters with supporting circuits, which is much less than the cost of a conventional hardware interpolator (e.g., Canon Interpolator CI40).

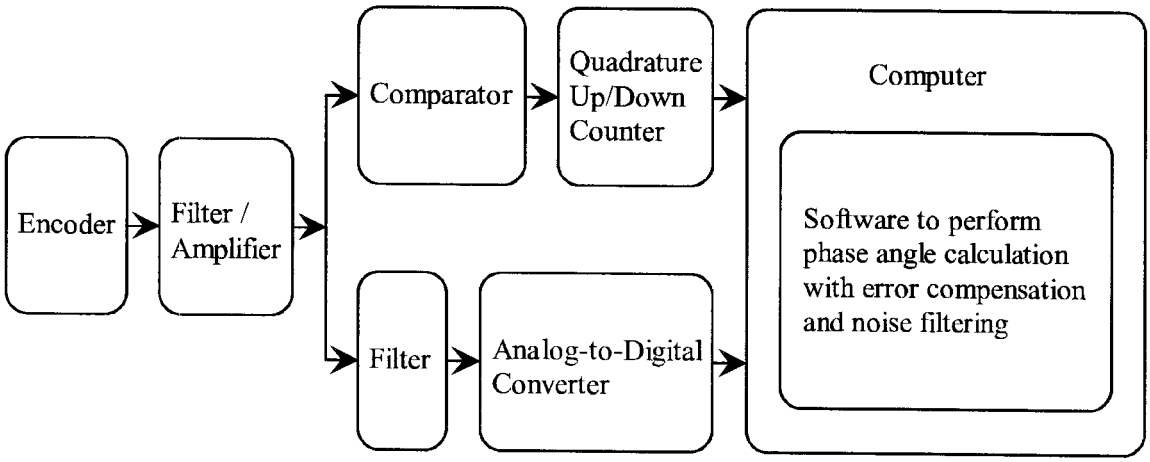

The resolution of the interpolation system is determined by the dynamic range of the A/D converter. With an n-bit A/D converter, the maximum signal

amplitude is 2^{n-1}, and the worst case conversion error is $2^{1/2}$, so the worst case phase error is

$$\Delta\theta = 2^{1/2} / 2^{n-1}$$
$$= 2^{-(n-3/2)} .$$

Therefore, the maximum interpolation resolution (number of divisions) per sinusoidal cycle is:

$$D = 2\pi / \Delta\theta$$
$$= 2\pi / 2^{-(n-3/2)}$$
$$= 2^{n-1/2}\,\pi$$
$$\approx 2.22 \cdot 2^{n} .$$

For example, with an 8-bit A/D converter, the maximum interpolation resolution will be $2.22 \cdot 2^8 \geq 560$ divisions per sinusoidal cycle. This is much better than most conventional hardware interpolators (e.g., Canon Interpolator CI40).

The accuracy of the interpolation system is only limited by the reproducibility of the encoder itself. Any deviation from ideal quadrature sinusoidal wave signals can be easily compensated in software by either analytical calculations (as shown in the previous section) or calibrated lookup tables. Long range instrumental errors can also be compensated similarly. These error

compensations can be implemented through either factory or custom calibrations. Thus the final accuracy can easily surpass those of the conventional hardware interpolators.

The maximum encoder moving speed in the interpolation system is only limited by the bandwidths of the comparators and the quadrature up/down counters, which are usually faster than most hardware phase determination circuits.

The interpolation system is also relatively immune to noise. Unlike the Canon Interpolator CI40, the interpolation system described here does not have instability problems in noisy environments since no high frequency pulse generation is involved. The noise in the signals can be filtered by both hardware and software, resulting in much reduced noise level. With software filtering one can easily trade acquisition speed for lower noise level when needed. This is especially desirable in systems where highly accurate measurements of slow displacements or stopping positions are needed.

The encoder signal interpolation scheme described here can be easily extended to cover encoder signals that are not purely quadrature sinusoidal by simply modifying the software phase calculation algorithm. Multiple encoders can also be accommodated by a single interpolator system. In such a multiple encoder system, while separate comparators and up/down counters are needed for each

encoder, only a single computer and A/D converter is needed to analyze all the encoder signals, so that the total system cost is greatly reduced.

The encoder signal interpolation scheme described above has been successfully implemented in the high resolution x-ray diffractometer system in the Keck Laboratory at Caltech. The encoder signal interpolator is interfaced to a personal computer through a software module written in C++ which is included below.

```
//*************************************************************************
//
// Encoder Interpolation Module     - Gang He, 1993.
//
//*************************************************************************
//
// class Encoder;
// class AnalogEncoder  : public Encoder;
//
//*************************************************************************

#include " <Hardware interface modules> "

// Definition ***************************************************************

class Encoder {
 public:
   Encoder(real Resolution);
   const   real Resolution;
   virtual real Position() =NULL;
};

class AnalogEncoder : public Encoder {
 public:
        AnalogEncoder(real Resolution, real QuadrantSize,
                      DC8* Controller, int  Axis,
                      real OffsetA,    real OffsetB,
```

```
                    real GainA,     real GainB,
                    real PhaseDifference);
        real Position();
 private:
        real    QuadrantSize;
        DC8*    Controller;
        int     Axis;
        real    OffsetA, OffsetB, GainA, GainB, SinDelta, CosDelta;
        long int QuadrantOffset;
};


// Implementation ****************************************************

Encoder::Encoder(real ResolutionIn)
 : Resolution(ResolutionIn)
{};

AnalogEncoder::AnalogEncoder(real ResolutionIn, real QuadrantSizeIn,
                             DC8* ControllerIn, int AxisIn,
                             real OffsetAIn,    real OffsetBIn,
                             real GainAIn,      real GainBIn,
                             real PhaseDifference)
 : Encoder    (ResolutionIn),
   QuadrantSize(QuadrantSizeIn),
   Controller  (ControllerIn),
   Axis        (AxisIn),
   OffsetA     (OffsetAIn),
   OffsetB     (OffsetBIn),
   GainA       (GainAIn),
   GainB       (GainBIn)
{
 real Delta=(PhaseDifference-90)*(pi/180)/2;
 SinDelta=sin(Delta);
 CosDelta=cos(Delta);
 long int LastStep, ThisStep, NextStep;
 logic DigitalA, DigitalB;
 do {
   logic Dummy;
   LastStep=-Controller->Position(Axis,&Dummy,&Dummy);
   ThisStep=-Controller->Position(Axis,&DigitalA,&DigitalB);
   NextStep=-Controller->Position(Axis,&Dummy,&Dummy);
 } while (ThisStep!=LastStep || ThisStep!=NextStep);
 QuadrantOffset=(DigitalA ? (DigitalB? 0:3) : (DigitalB? 1:2));
 QuadrantOffset=(((QuadrantOffset-ThisStep)%4)+4)%4;
};

real AnalogEncoder::Position() {
```

```
 real    AnalogA, AnalogB, PhaseA, PhaseB, X, Y, PhaseAngle;
 logic   DigitalA, DigitalB;
 long int ThisStep, Quadrant, QuadrantError;
 ThisStep=-Controller->Position(Axis,&DigitalA,&DigitalB);
 Controller->GetPhase(Axis,&AnalogA,&AnalogB);
 ThisStep+=QuadrantOffset;
 Quadrant=(DigitalA ? (DigitalB? 0:3) : (DigitalB? 1:2));
 QuadrantError=((((Quadrant-ThisStep)%4)+5)%4)-1;
 PhaseA=(AnalogA-OffsetA)/GainA;
 PhaseB=(AnalogB-OffsetB)/GainB;
 X=PhaseA*CosDelta-PhaseB*SinDelta;
 Y=PhaseB*CosDelta-PhaseA*SinDelta;
 PhaseAngle=atan2(Y,X)/(pi/2)-(Quadrant+0.5);
 PhaseAngle-=closest_long_int(PhaseAngle/4)*4;
 return -(ThisStep+QuadrantError+PhaseAngle)*QuadrantSize;
};
```

Appendix C High Resolution X-ray Diffractometer Control System

The multi-axis high-resolution x-ray diffractometer system built in the Keck Laboratory at Caltech is controlled by an IBM-PC compatible personal computer by a general purpose x-ray diffraction control program running under DOS. The computer is equipped with a Data Translation DT-2819 general purpose counter board for x-ray intensity integration and two Precision Micro Control DC-8 boards to control the motors and encoders. The computer also controls a Compumotor stepper motor for the theta axis via a standard RS-232 interface. The theta axis, which is the most important axis in rocking curve measurement, is monitored by a high resolution Canon laser encoder type K-1. To take full advantage of the laser encoder, a special algorithm along with a laser encoder adapter is developed to replace the Canon encoder interpolator CI40-2, which results in a very stable encoder system with extremely high resolution (Appendix B).

The diffraction system control software is written in C++ using Borland C++ version 4.0. The program is constructed from a set of objects as building blocks which can be easily changed to adapt to any future changes of the hardware or software system. The overall structure of the software is designed with the

following layered modular structure where the higher level layers are built on the basis of the lower level layers for easy modification and expansion:

System Integration Layer
Operation Module Layer
Virtual Device Layer
Physical Device Layer
Hardware Interface Layer

The hardware interface layer handles the machine (binary) level communication with the hardware devices including the DT-2819 counter board, the DC-8 motor control board, and the Compumotor indexer. This layer contains the following files:

DT2819IO.H,	DT2819IO.CPP,
DC8IO.H,	DC8IO.CPP,
COMPUIO.H,	COMPUIO.CPP,
GRAPHICS.H,	EGAVGA.OBJ.

The last two files (GRAPHICS.H and EGAVGA.OBJ) are provided with Borland C++ Version 4.0.

The physical device layer handles the basic operations of the physical devices including the DT-2819 counter board, the DC-8 motor control board, the Compumotor indexer, and the EGA graphic video adapter. This layer contains the following files:

DT2819.H,	DT2819.CPP,
DC8.H,	DC8.CPP,
COMPU.H,	COMPU.CPP,
CONSOLE.H,	CONSOLE.CPP.

The virtual device layer provides the integrated high level control of the various system components including the x-ray detector, various types of motors with encoders, the GUI (graphic user interface) window system, and the x-ray sequence and spectrum data management module. One important feature of the x-ray detector module is that the x-ray intensity integration is running as a background process on the DT-2819 counter board so that the detector can integrate the x-ray intensity while the CPU is working on other things such as making multiple position measurement for increased precision and quick response of user requests. The virtual device layer contains the following files:

DETECTOR.H,	DETECTOR.CPP,
MOTOR.H,	MOTOR.CPP,
WINDOW.H,	WINDOW.CPP,

DATAPOOL.H, DATAPOOL.CPP.

The operation module layer performs high level operations for x-ray diffraction control and measurement. These operations including x-ray diffraction main control, axis alignment, sequence editing, sequence scanning, sequence information memo, real time axis position and x-ray intensity monitoring, and equipment initialization and integration. This layer contains the following files:

XRAYMENU.H, XRAYMENU.CPP,
ALIGN.H, ALIGN.CPP,
EDIT.H, EDIT.CPP,
SCAN.H, SCAN.CPP,
MEMO.H, MEMO.CPP,
MONITOR.H, MONITOR.CPP,
EQUIP.H, EQUIP.CPP.

The system integration layer integrates all the operation modules and build the control program. This layer contains the following files:

XRAYSYS.H, XRAYSYS.CPP,
XRAY.H, XRAY.CPP.

Besides all the layers described above, there is also a language extension layer which serves as the common basis of the other layers. The language

extension layer defines the basic data types used throughout the program and contains the following files:

BASIS.H, BASIS.CPP.

If testing of the program on a stand alone computer is desired, a hardware interface simulation layer can be used to replace and simulate the hardware interface layer. The simulation layer simulates a set of "perfect" motors which always follows the motions commands immediately, as well as an x-ray intensity with sinusoidal oscillation. The simulation layer shares the same header files with the hardware interface layer and contains the following files:

DT2819IO.H, DT2819SI.CPP,
DC8IO.H, DC8SI.CPP,
COMPUIO.H, COMPUSI.CPP.

If open loop operation (with encoder bypassed) is desired, simply go to the EQUIP.CPP file and replace the corresponding encoder pointers with NULL pointers. The EQUIP.CPP file also contains all the motor parameters.

The DT-2819 interface is implemented via the DT2819Board object defined in file DT2819IO.H and DT2819IO.CPP. The TTL pulse signal from the x-ray detector single channel analyzer should be connected to the Source-1 port on the terminal box of the DT-2819 board. The board has five 16-bit general purpose

counters labeled 1-5. Counters 1 and 2 are combined to form a 32 bit counter to count the x-ray pulse signal from source-1, and counters 3, 4, and 5 are combined to form a 48 bit counter to count a 5MHz internal frequency reference signal in order to obtain the x-ray rate. All the counters are set to count up on high pulses repeatedly.

The DC-8 interface is implemented via the DC8Board object defined in file DC8IO.H and DC8IO.CPP. The DC-8 boards are the most unstable component in the system and are most likely to cause trouble, if any. No complete description of the DC-8 board communication protocol is available. The only information available is a demo program (in BASIC) from the company that demonstrates the communication with the DC-8 board. The demo routine had problems communicating with the DC-8 board occasionally. After the routine is ported to C++, it had an even greater problem, presumably due to the faster speed of the C++ code. To address this problem, the hand shake process has been modified such that at least ten continuous hand shake signals must be successfully received before the hand shake is complete. Further testing and analysis showed that there are also some kind of "dead loop" pattern during the communication where the board will be trapped. Extra codes are therefore added to detect these patterns and restart the communication process. After these refinements, the communication process with the DC-8 boards is now much more stable and no problem has occurred yet.

The theta axis of the diffraction system is the most important axis for rocking curve measurement. It is monitored by a Canon rotary laser encoder type K-1. Unlike most optical encoders which generate quadrant square-wave outputs, the Canon laser encoder is capable of generating quadrant sinusoidal-wave outputs at 81000 periods per revolution, or 1/225 degree (16 arc-second) per period. To achieve even higher resolution, a Canon encoder interpolator CI40-2 was originally used to divide each sine wave signal into 10 pulse trains and obtained a resolution of 1/9000 degrees (0.4 arc-second). However, this set up was extremely unstable and often halted the whole system unless the Canon laser encoder was bypassed. And indeed the original control program was later modified to bypass the encoder.

We found that this instability was caused by the fact that the interpolator was inherently sensitive to noise, especially to high frequency noise. When a very high frequency noise is coupled into the encoder output signal, the encoder interpolator will be driven by this noise to generate pulse trains at the same high frequency and consequently cause the computer to lose track of the encoder position. In fact, we found that there is indeed a very large noise in the mega-Hertz range in the x-ray lab caused by the switching action of a 20kHz switching power supply for the Compumotor stepper motor. Unfortunately, that power supply has to be on when the system is working and there is no easy replacement of it. A noise suppresser has been installed in the AC power line of the switching power supply to prevent the noise from going back into the AC power line.

However, it has been very difficult to completely shield the noise for the Canon laser encoder.

A much better method is then developed to analyze the encoder signal. The new method combines a software algorithm with a hardware laser encoder adapter designed to replace the Canon encoder interpolator. The new method is insensitive to noise and is capable of much higher resolution than the old method. The resulting system has been very stable and has achieved a resolution of about 1/50000 degree (0.072 arc-second). Note that there still may be an accumulated long range error in the encoder which can be calibrated by a standard encoder. Such a long range error is specified to be less than about 20 arc-second per revolution by Canon.

The output from the Canon laser encoder is a sine wave with an amplitude of 1 volt p-p. The signal is amplified to 4 volts p-p and centered at 2.5 volts. It is then passed through four low pass RC filter bands each with a 3db point at 16kHz. The filtered signal is then sent to a DC-8 board for A/D conversion (8-bits, 0 to 5 volts). A quadrant signal is also generated from the filtered signal by a Schmitt comparator with triggering point set at 1.7 volts and 3.3 volts, a big enough error margin. The following is the circuit diagram of the signal amplification and filtering board.

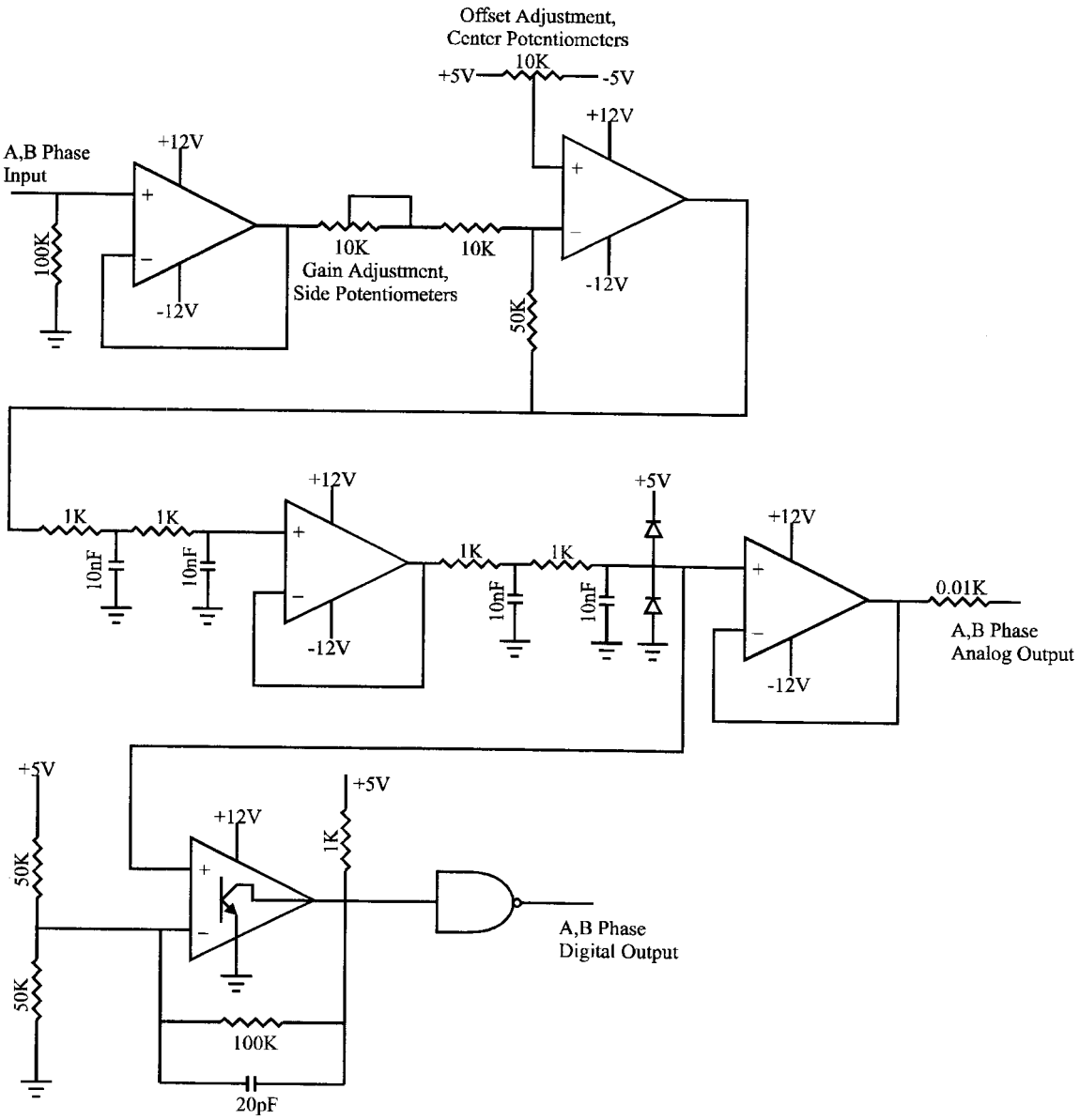

The gain and offset of the signal should be calibrated in the laser encoder adapter. The calibration requires a well calibrated oscilloscope and should be carried out in the following steps:

1. Turn on the laser encoder adapter.

2. Connect the X and Y axes of the oscilloscope to the A phase and B phase analog outputs of the adapter You can either use pin M and N on the circuit board, or use pin 3 and 4 of the DB-9 output socket. Common ground is pin 1-22 on the circuit board and pin 7-8 in the DB-9 socket.

3. Turn the oscilloscope into x-y DC mode. Make sure that ground level is correct.

4. Rotate the theta axis by the motor, adjust the gain and offset potentiometers on the adapter circuit board so that the amplitudes of both x and y are 4 volts p-p and both x and y are centered at 2.5 volts. The potentiometers are located at a corner of the circuit board. The two center potentiometers are for offset adjustments of the two phases, and the two side ones are for gain adjustments of the two phases. The two that are closer to the center are for phase A, and the two that are closer to the side are for phase B.

For most of the high precision measurements, the hardware calibration above is good enough. Nevertheless, an even more precise calibration can be carried out by a software calibration, in which any remaining small error in gain, offset as well as phase shift can be corrected. The software calibration can be carried out as the following:

1. Collect a large number of (A,B) values from the DC-8 A/D converter for different theta motor positions.

2. Do a least square fit of the obtained (A,B) values for equations

$$A = \text{Gain A} \cos(\text{theta} - \text{Delta}/2) + \text{Offset A}$$

$$B = \text{Gain B} \sin(\text{theta} - \text{Delta}/2) + \text{Offset B}$$

where

$$\text{Delta} = \text{Phase Delay} - 90^\circ$$

to obtain parameters

{ Gain A, Gain B, Offset A, Offset B, Phase Delay }.

3. Write the fit parameters into a calibration file using the following format:

Phase A Offset : < value >
Phase B Offset : < value >
Phase A Gain : < value >
Phase B Gain : < value >
Phase Difference : < value >

The offsets are in units of V_{offset} / $V_{reference}$ ($V_{reference}$ = 5 volts) with a standard value of 0.5. The gains are in units of $V_{amplitude}$ / $V_{reference}$ with a standard value of 1 (only the relative gain of A and B matters). And the phase difference is in unit of degrees with a standard value of 90.

The calibration file should be named XRAY.INI and stored in director C:\XRAY or in the directory specified by a DOS environment variable XRAY so that it can be accessed by the x-ray diffraction control program every time it starts. If the program is not able to find the calibration file, the standard values will be used.

The following are the pin specifications for the circuit boards related to the Canon laser encoder circuits.

Adapter plug in board (44 pins):

1-22	GND	
A	GND	
B	Not Used	
C	A Phase	<- Canon Encoder
D	B Phase	<- Canon Encoder
E	Z Phase	<- Canon Encoder

F	+5V	-> Canon Encoder
H	-5V	-> Canon Encoder
J	Not Used	
K	A Phase Digital	-> DC8
L	B Phase Digital	-> DC8
M	A Phase Analog	-> DC8
N	B Phase Analog	-> DC8
P	+5V Reference	-> DC8
R	Z Phase	-> DC8
S	+5V	-> Not Used
T	-5V	-> Not Used
U	+12V	-> Not Used
V	-12V	-> Not Used
W	Not Used	
X	+12V	<- DC Power Supply
Y	-12V	<- DC Power Supply
Z	Not Used	

Adapter input from the DC Power Supply (3 Pins):

1	+12V	<- DC Power Supply
2	-12V	<- DC Power Supply
3	DC GND	<- DC Power Supply

GND	Earth Ground	<- DC Power Supply

Adapter input from the Canon encoder (12 Pins):

1	A Phase	<- Canon encoder
2	GND	
3	B Phase	<- Canon encoder
4	GND	
5	Z Phase	<- Canon encoder
6	GND	
7	+5V	-> Canon encoder
8	GND	
9	-5V	-> Canon encoder
10	GND	
11	Shield	
12	Case	

Adapter output to the DC8 (9 Pins):

1	A Phase Digital	-> DC8
2	B Phase Digital	-> DC8
3	A Phase Analog	-> DC8
4	B Phase Analog	-> DC8

5	+5V Reference	-> DC8
6	Z Phase	-> DC8
7	GND	
8	GND	
9	Shield	

Adapter output adapter to the DC8#1 Axis 1 Encoder/Motor Connector (9 Pins):

1	Not Used
2	Not Used
3	B Phase Digital
4	GND
5	A Phase Digital
7	Not Used
8	Not Used
9	Not Used

Adapter output adapter to the DC8#1 I/O Connector (15 Pins) :

1	A Phase Digital
2	B Phase Digital
3	Not Used
4	Not Used

5	A Phase Analog
6	B Phase Analog
7	Not Used
8	Not Used
9	+5V Reference
10	GND
11	Not Used
12	Not Used
13	Not Used
14	Not Used
15	Not Used

DC8#1 Axis 1 Encoder/Motor Connector (9 Pins):

1	Motor Control M1
2	Motor Control M2
3	Channel B Encoder
4	GND
5	Channel A Encoder
6	+5V Encoder Power Supply

DC8#1 I/O Connector (25 Pins):

1 GND

2 Analog Input #01

3 Digital I/O Channel 16 Keyboard In #4

4 Analog Input #03

5 Digital I/O Channel 15 Keyboard In #3

6 Digital I/O Channel 14 Keyboard In #2

7 Digital I/O Channel 13 Keyboard In #1

8 Digital I/O Channel 12 Keyboard Out #4

9 Digital I/O Channel 11 Keyboard Out #3

10 Digital I/O Channel 10 Keyboard Out #2

11 Digital I/O Channel 09 Keyboard Out #1

12 Digital I/O Channel 08 Reference Switch Axis #4

13 Digital I/O Channel 07 Reference Switch Axis #3

14 Digital I/O Channel 06 Reference Switch Axis #2

15 Digital I/O Channel 05 Reference Switch Axis #1

16 Digital I/O Channel 04 Limiting Switch Axis #4

17 Digital I/O Channel 03 Limiting Switch Axis #3

18 Digital I/O Channel 02 Limiting Switch Axis #2

19 Digital I/O Channel 01 Limiting Switch Axis #1

20 Analog Input #04

21 Not Used

22 Analog Input #02

23 Analog Reference Input

24 Not Used

25 Not Used

DC8#1 I/O Connector adapter to the Adapter (15 Pins):

1 Digital I/O Channel 01 Limiting Switch #1

2 Digital I/O Channel 05 Reference Switch #1

3 Digital I/O Channel 09 Keyboard Out #1

4 Digital I/O Channel 13 Keyboard In #1

5 Analog Input #01

6 Analog Input #02

7 Analog Input #03

8 Analog Input #04

9 Analog Reference Input

10 GND

11 Not Used

12 Not Used

13 Not Used

14 Not Used

15 Not Used

DC8#1 I/O Connector adapter to the SunX Reference Switches (15 Pins):

1 Digital I/O Channel 02 Limiting Switch #2

2 Digital I/O Channel 06 Reference Switch #2

3 Digital I/O Channel 10 Keyboard Out #2

4 Digital I/O Channel 14 Keyboard In #2

5 Digital I/O Channel 03 Limiting Switch #3

6 Digital I/O Channel 07 Reference Switch #3

7 Digital I/O Channel 11 Keyboard Out #3

8 Digital I/O Channel 15 Keyboard In #3

9 Digital I/O Channel 04 Limiting Switch #4

10 Digital I/O Channel 08 Reference Switch #4

11 Digital I/O Channel 12 Keyboard Out #4

12 Digital I/O Channel 16 Keyboard In #4

13 GND

14 Not Used

15 Not Used

Note: The A, B Phase outputs from the adapter are inverted relative to the corresponding outputs from the Canon encoder.

Appendix D Operation of the Fourier Transform Infrared Spectrometer over a Wide Spectral Range

The Nicolet 60SX Fourier Transform Infrared (FTIR) Spectrometer in Lab 249 Watson is equipped with sources, detectors, and beam splitters that are designed to cover a spectral range from 50 cm^{-1} to 5000 cm^{-1}. With proper modifications and operations of the instrument, however, a much wider spectral range from 50 cm^{-1} to as high as 9000 cm^{-1} can be covered. The following is a summary of modifications as well as instrument operation procedures that were developed during this thesis study. Note that a lot of useful information regarding the operation and maintenance of the spectrometer is provided in the Nicolet 60SX service manual, and information regarding the FTIR software is provided in the Nicolet 60SX FTIR reference manual.

The spectrometer is equipped with two sources: a globar source (infrared source) designed to cover 50 cm^{-1} to 6000 cm^{-1}, and a tungsten-halogen source (visible source) designed to cover 6000 cm^{-1} to 25000 cm^{-1}. The actual spectral ranges of these two sources have a very large overlap, with the tungsten source capable of covering as low as 2000 cm^{-1} and the globar source capable of covering as high as 10000 cm^{-1}. The intensities of the sources are, of course, somewhat lower outside their designed operation ranges. In general, the rule of thumb to

choose the sources is that the globar source should be used if the entire spectral range of interest is below 6000 cm^{-1}, and the visible source should be used if the spectral range of interest extends considerably above 6000 cm^{-1}. These two sources are both installed in the spectrometer and can be selected by software. Two deuterated triglycine sulfate (DTGS) pyroelectric detectors are available with the spectrometer: a DTGS-A detector with a KBr window designed to cover 400 cm^{-1} to 5000 cm^{-1}, and a DTGS-B detector with a polyethylene window designed to cover 10 cm^{-1} to 500 cm^{-1}. The DTGS-A detector has small but usable detectivity up to about 9000 cm^{-1}. Both the detectors can be mounted to the spectrometer at the same time and can be selected by software. There are two types of beam splitters available: the Ge on KBr beam splitter designed to cover 400 cm^{-1} to 5000 cm^{-1} and the six Mylar beam splitters of various thicknesses designed to cover 10 cm^{-1} to 500 cm^{-1}. The beam splitter is one of the key components that determines the spectral range of the spectrometer. The Ge on KBr beam splitter has very small but usable efficiency up to about 9000 cm^{-1}. Only one beam splitter can be installed in the spectrometer at a time, and after each reinstallation the interferometer must be realigned.

When the spectrometer is used to cover spectral ranges above 5000 cm^{-1}, the biggest problem is that the Ge on KBr beam splitter has an efficiency minimum of near zero at about 7400 cm^{-1}, which may be a result of the constructive thin film interference in the Ge coating. The exact location of the efficiency minimum may vary slightly (up to a few tens of cm^{-1}) from sample to sample and may even vary for the same sample when the sample is remounted. Since the instrument

efficiency is near zero at this minimum, a slight shift in the minimum location can cause very large artifacts in the resulting normalized spectrum (which is the ratio of the raw sample spectrum to the raw through-beam spectrum). One possible source of the shift is some small thickness nonuniformity in the interferometer beam splitter which produces spatial variations in the minimal efficiency wavelength. The spatial variation can then be translated into angular variations by the convergent mirror in front of the sample compartment, and is then selectively transmitted by the sample. It is therefore conceivable, and was also experimentally confirmed, that such slight shifts in the efficiency minimum location can be eliminated by putting a small aperture between the interferometer and the sample compartment to restrict the total beam diameter and convergence angle hence reducing the spatial and angular variations. Currently an aperture of 3/8 inch diameter is installed at the entrance of the sample compartment. While the total signal intensity has been reduced by about a factor of five, the spectral shift has been largely eliminated by the aperture. The aperture is essential if spectral range above 5000 cm^{-1} is to be covered. If only spectral range below 5000 cm^{-1} is needed, the aperture can be removed to achieve better signal to noise ratio. Normally no realignment is needed when the aperture is installed or removed.

Instrument stability is a very important issue that affects data quality. A good method to check instrument stability is the 100% line defined as the ratio of two through-beam spectra taken with identical instrument parameters. The 100% line would contain, of course, random noise but should not have any systematic deviation (tilt) from unity. A tilted 100% line indicates poor instrument stability,

which can be caused by many factors, including poor interferometer and detector alignment, acoustic vibrations from the environment, too high a purge rate, variations in air pressure of the air bearing, thermal drift, etc.. It is important to minimize any acoustic vibrations in the lab during operations of the spectrometer, and definitely avoid touching the spectrometer during data collection. Since the spectrometer signal is modulated in audio frequencies, acoustic vibrations have huge effects on the data quality. The instrument is supplied with continuous dry nitrogen at all times for instrument bench purging and air bearing pressure. The supply to the air bearing is controlled by an external regulator which is set at 45 psi. Make sure that the pressure does not drop below this setting. The purge supply is controlled by a flow meter. The purge keeps water vapor out of the bench since some important optics in the bench (e.g., KBr) can be damaged by moist air. The purge also keeps out species such as water vapor and carbon dioxide to eliminate absorption features from these species. The spectrometer cover should be tightly closed during normal operation to assure good purging efficiency. When transferring samples in and out of the sample compartment, it is desirable to use a high purge (higher than 10 l/m) rate to minimize the back flow of ambient air into the spectrometer. The high purge rate should be kept for another 10~15 minutes after sample transferring to drive out the residual ambient air in the spectrometer. During data collection, a purge rate of 3~4 l/m is found to be satisfactory. The purge rate must be reduced to the rate used for data collection at least for half an hour before data collection begins to achieve thermal equilibrium and to avoid thermal drift in the spectrometer. A special sample holder has been designed and installed in the spectrometer. The sample holder allows mounting of about six

samples together and switching among the samples without having to open the sample compartment. Thus the purge rate does not need to be changed when switching among the samples mounted on the same sample holder. Another source of thermal drift is the sources. The sources should be turned on about half a day before data collection to achieve thermal equilibrium with the rest of the spectrometer. For measurements where very high instrument stability is required, through beam spectra can be taken both before and after the sample spectrum. The ratio of the through beam spectra before and after the sample spectrum can then be used to estimate the amount of instrument instability.

Optical alignment in the spectrometer affects not only the instrument stability but also the signal to noise ratio as well as the usable spectral range. If the signal level is found to be noticeably lower than the usual level, a realignment of the interferometer may be needed. The easiest way to align the interferometer is to use the TUN macro in the FTIR software. To run the macro, simply enter TUN in the "SX>" mode. Then set the parameter "MOTOR" to 1, which means aligning the fixed mirror of the interferometer. Then go to the tuning mode. The interferogram, the maximum and minimum signals, the FFT average of the interferogram, and the X and Y positions of the fixed mirror are displayed in the tuning mode. The goal of the alignment is to maximize the signal by varying the X and Y positions of the fixed mirror. The easiest way to do so is to use the built-in simplex tuning algorithm, which in general does quite a good job. If manual tuning is desired, one can also vary the X and Y positions of the fixed mirror by the arrow keys. After the fixed mirror alignment, go back to the FTIR software and

run the ZPD macro by entering ZPD in the "SX>" mode. This macro will automatically find the zero path length difference and store it in the "PEAK LOC" parameter. This parameter is the location of the interferogram peak and can be displayed by selecting "#DATA POINTS" on the bench touch panel. In the event of a power interruption, the value in the "PEAK LOC" is sometimes lost, causing the spectrometer to scan in the wrong location so that no signal in the interferogram can be seen. This can be corrected by simply running the ZPD macro again. The fixed mirror alignment is also required after each change of beam splitter. In such cases, the starting position of the fixed mirror may be so far out of alignment that no signal can be seen at all. Therefore manual scanning of the mirror position may be needed initially to find the interferogram peak. It is also possible that the peak location in the interferogram is significantly changed after a beam splitter change so that interferogram peak is far out of the display range. In such cases a dual channel oscilloscope can be used to find the interferogram peak. The procedure to do so is provided in section 2.2.17 of the 60SX service manual. Note that it should be possible to make custom interferometer beam splitters to expand the spectral range of the detector. The beam splitter consists of two identical substrates of the same material and thickness. One of the substrate is coated with beam splitter coating while the other is not coated and acts as a phase compensator. The two substrates are held together with an air gap in between. The air gap is of the order of half a millimeter thick. The coating side of the coated substrate should be facing the compensator. When designing the custom beam splitter, it is important to note that the beam splitter efficiency is strongly determined by the thin film interference in the beam splitter coating, and a detailed

transmission/reflection simulation that includes the multilayer thin film interference effect must be performed to determine the optimal coating structure. Such simulations can be performed using the algorithm and software codes described in appendix A.

The detectors do not need to be aligned routinely. If the signal level is lower than the usual level even after a careful interferometer fixed mirror alignment, the detectors may need to be realigned. The alignment can not be done automatically. Manual adjustment of the detector position is illustrated in section 6.4 (page 6-13) of the Nicolet 60SX service manual. Note that very fine adjustments of the detector position (better than a fraction of a millimeter) in all three dimensions is required to properly align the detector. Before removing and installing the detectors, the power to the detector must be turned off by deselecting the detector. A flexible detector mount has been designed and installed on the spectrometer. The flexible detector mount has an x-y-z micrometer driven translation stage to ease the detector alignment. It can be used to mount non-standard detectors as well as to do photoconductivity measurements. A 12V peak-to-peak differential signal should be fed to the detector electrical connector through 20 Ω 1/8 watt impedance matching resistors. The following is the drawing of the flexible detector mount with its critical dimensions (note that the optical axis is 2 inches above the center of the dowel pins).

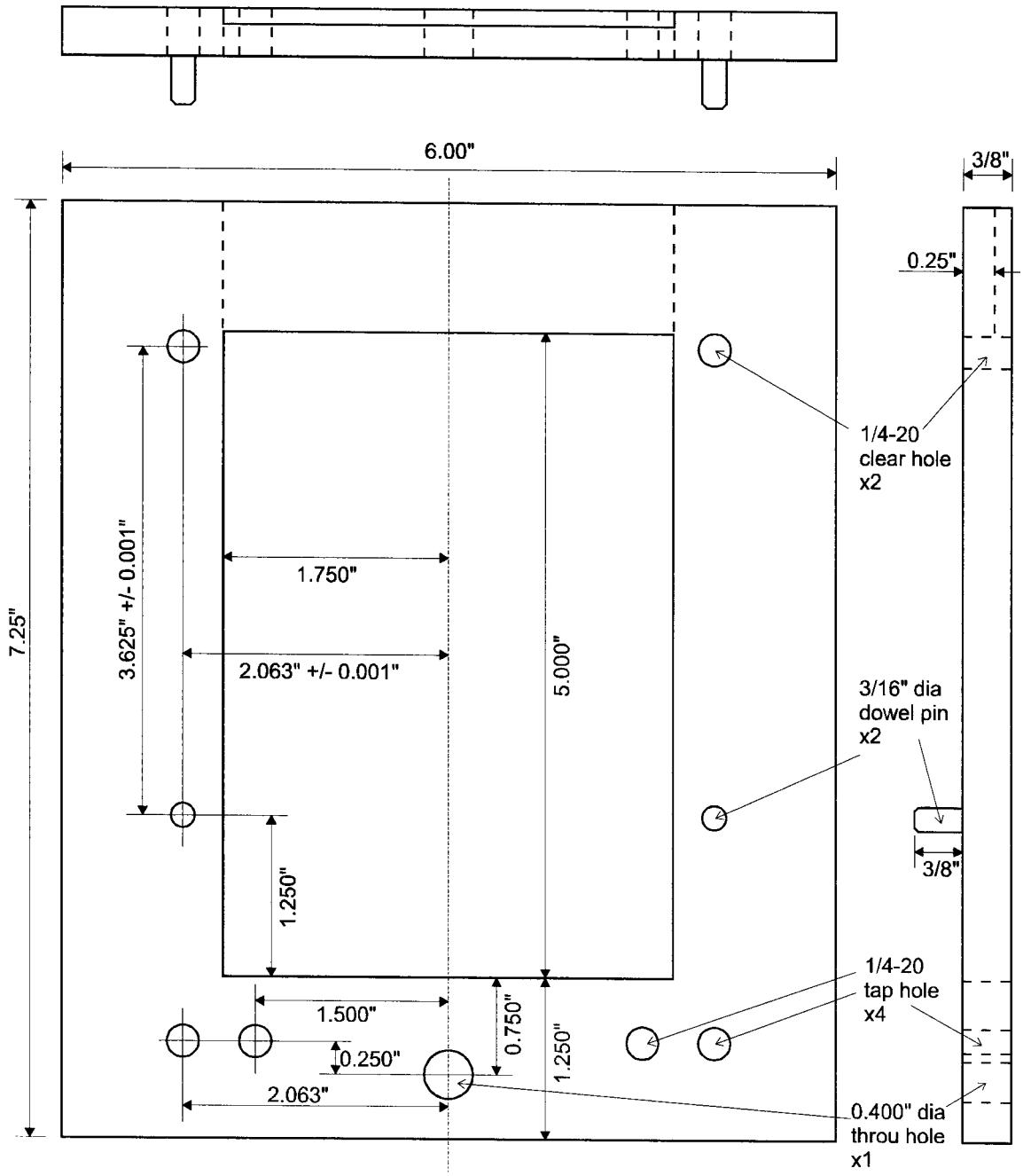

The Nicolet 60SX FTIR reference manual provides a very complete description of the FTIR software operation. When choosing the parameters of

sampling spacing and electronic filters, it is important to be aware of the possible aliasing effect which folds all the high frequency signals into the measurement bandwidth through the Fourier transform process. Such effects can be avoided with proper values of sampling spacing and electronic filters, and sometimes optical filters can be used to better block the unwanted frequencies. Note that it is in principle possible to take advantage of the aliasing effect and obtain spectral information outside the measurement bandwidth.

The software of the FTIR system is protected through a software key protection system and cannot operate without the software key. The software key is usually remembered by the computer, even if there is a short power interruption. However, if power to the computer is lost for a long time (a few weeks), the computer may lose the software key so that the FTIR software is not functional. In such an event, simply boot the computer from the software key floppy disk to restore the software key.

There are two serial connections between the Nicolet spectrometer computer and an IBM-PC compatible personal computer. One is a standard RS-232 serial connection which connects the "SPARE" communication port of the Nicolet computer to the "COM1" port of the IBM-PC, and the other is a special high-speed serial port which connects the "High Speed Serial Link 1" of the Nicolet computer to the "COM2" port of the IBM-PC. Note that the high speed serial interface is not standard RS-232 (although the interface used in the IBM-PC

is standard RS-232) and the connection cable is custom made with the following pin specifications.

IBM-PC (RS232)	1	2	3	4	5	6	7	8	9
Nicolet (High Speed Serial)	NC	6	2	NC	4	NC	NC	NC	NC

The standard RS-232 connection is used to enable console control of the spectrometer computer from the IBM-PC. The connection is 9600 BPS, 7 data bits, 1 stop bit, mark parity, no hardware handshaking. To enable console control from the IBM-PC, enter "CD -RB" on the Nicolet computer in NICOS mode, and run the Terminal program on the IBM-PC which is in the FTIR program group of the program manager. The Nicolet computer can then be controlled from the Terminal window from the IBM-PC. To disable console control from the IBM-PC, enter "CD -I0" on the Nicolet computer in NICOS mode, and exit the terminal program on the IBM-PC.

The high-speed serial link is used to transfer data files (spectra) from the Nicolet computer to the IBM-PC through the KERMIT protocol. The connection is 38400 BPS, 8 data bits, 1 stop bit, no parity, no hardware handshaking. To establish the connection, run the Transfer program on the IBM-PC (the program icon is in the FTIR group in program manager), and run the KERMIT program on the Nicolet computer and set the communication port at "J" and communication baud rate at 38400 BPS. The KERMIT program on the Nicolet computer automatically acts as a KERMIT server. The Transfer program on the IBM-PC is a

KERMIT session with a special script to communicate with the Nicolet computer. To transfer a file from the Nicolet computer to the IBM-PC, simply move to the desired directory and enter "get <filename>" in the Transfer program on the IBM-PC. After closing the connection, simply enter "exit" to exit the Transfer program on the IBM-PC and type "x" to exit the KERMIT program on the Nicolet computer.

The spectrum file from the Nicolet computer is in Nicolet binary file format. A program has been written to translate the binary files to ASCII files which can then be read by generic data analysis software. The program is written in C++ using Microsoft Visual C++ Version 4.00. To run the program, simply enter "nic2dat <binary file name> <ASCII file name>" in a command prompt. The following is the source code of the program.

```
//**************************************************************************
// File :  Nic2Dat.CPP - Gang He, 1996.
//**************************************************************************
// Note : Spectrum File Format defined in FT-IR Software Chapter 18.
//**************************************************************************

#include <fstream.h>
#include <iomanip.h>
#include <math.h>

typedef int logic;
const logic false=0;
const logic true =!false;

class NicFile {
 public:
        NicFile(char* FileName);
        logic Valid();
        long int NextWord();
```

```
 private:
        ifstream File;
        logic EvenWord;
        char SharedByte;
};

NicFile::NicFile(char* FileName)
 :File(FileName,ios::binary) {
 EvenWord=true;
};

logic NicFile::Valid() {
 return File.good();
};

long int NicFile::NextWord() {
 union { long int Word; char Byte[4]; } NicWord;
 NicWord.Word=0;
 if (EvenWord) {
        File.get(NicWord.Byte[3]).get(NicWord.Byte[2]).get(SharedByte);
        (NicWord.Byte)[1]=SharedByte&(char)0xF0;
 } else {
        File.get(NicWord.Byte[2]).get(NicWord.Byte[1]);
        (NicWord.Byte)[3]=SharedByte&(char)0x0F;
        NicWord.Word=NicWord.Word<<4;
 };
 EvenWord=!EvenWord;
 return NicWord.Word/(long int)0x1000;
};

int main(int argc, char* argv[]) {
 const double Laser=15798.00;
 if (argc<2) {
        cerr<<"Nicolet FTIR Spectrum File to ASCII Data File Converstion"<<endl
                <<"By Gang He, 1996"<<endl
                <<"Usage: NIC2DAT Nicolet-Spectrum-File [ ASCII-Data-File ]"<<endl;
        return 1;
 };
 const int FSBLength=352;
 long int FSB[FSBLength];
 int Word;
 NicFile NicSpectrum(argv[1]);
 if (!NicSpectrum.Valid()) {
        cerr<<"File < "<<argv[1]<<" > not found"<<endl;
        return 1;
 };
 for (Word=0; Word<FSBLength; Word++)
        FSB[Word]=NicSpectrum.NextWord();
```

```
if (FSB[1]!=(long int)(01234321)) {
        cerr<<"File < "<<argv[1]<<" > is not a valid Nicolet Spectrum File"<<endl;
        return 1;
};
ostream* DataFile;
if (argc<3)
        DataFile=&cout;
else {
        DataFile=new ofstream(argv[2]);
        if (DataFile? !*DataFile : true) {
                cerr<<"Could not open file < "<<argv[2]<<" > for output"<<endl;
                return 1;
        };
};
(*DataFile)<<"##TITLE = ";
for (Word=67; Word<=106 && ((FSB[Word]&0x7F) != 13); Word++)
        (*DataFile)<<(char)(FSB[Word]&0x7F);
(*DataFile)
        <<endl<<"##DATATYPE = "
        <<(FSB[6]==0? "Emission Spectrum":
                FSB[7]==0? "Interferogram":
                FSB[8]==0? "Transmission Spectrum":
                FSB[9]==0? "Absorbtion Spectrum":
                                                "Unknown");
(*DataFile)<<endl<<"##DATE = ";
for (Word=48; Word<=55; Word++)
        (*DataFile)<<(char)(FSB[Word]&0x7F);
(*DataFile)<<endl<<"##TIME = ";
for (Word=57; Word<=64; Word++)
        (*DataFile)<<(char)(FSB[Word]&0x7F);
(*DataFile)<<endl<<"##XUNITS = "<<(FSB[7]==0?"MICRON":"1/CM");
(*DataFile)
        <<endl<<"##YUNITS = "
        <<(FSB[6]==0? "Emission":
                FSB[7]==0? "Interferogram":
                FSB[8]==0? "Transmittance":
                FSB[9]==0? "Absorbance":
                                                "Unknown");
logic Interferogram=FSB[7]==0;
long int EXP=FSB[5], Nscan=FSB[2], NSK=FSB[12],
                        NTP256=FSB[14], NDP256=FSB[15], SSP=FSB[16];
if (NSK<=0) NSK=NDP256*128;
if (NSK>3300) NSK=3300;
long int Npoints=(Interferogram? NDP256*256: NTP256*128);
double DeltaX=(Interferogram? SSP*1e4/Laser: Laser/SSP/Npoints);
double SCL=(Interferogram? 640/(double)Nscan: 1);
double Yfactor=SCL*exp(log(2)*(EXP-19));
double Resolution=Laser/(NDP256*256-NSK);
```

```
 (*DataFile)<<endl<<"##NPOINTS = "<<Npoints;
 (*DataFile)<<endl<<"##MAX-RES = "<<setw(4)<<setprecision(2)<<Resolution
          <<" (1/CM)"<<endl<<endl;
 for (long int Point=0; Point<Npoints; Point++)
          (*DataFile)<<setw(9)<<setprecision(3)<<Point*DeltaX<<" "
                   <<setw(9)<<setprecision(6)<<Yfactor*NicSpectrum.NextWord()<<endl;
 if (argc>2 && DataFile) delete DataFile;
 return 0;
};
```

Appendix E Modifications, Operations and Maintenance of the Molecular Beam Epitaxy System

The molecular beam epitaxy (MBE) system in Lab 247 Watson is capable of growing various group IV alloy materials. It contains solid sources for carbon, silicon, germanium, tin, as well as a rod fed electron-beam evaporation source that can be used for dopants. It also has an electron cyclotron resonance ion source for ion-assisted molecular beam epitaxy. Many components of the MBE system were added or modified during the course of this thesis study and will be described in this appendix.

E .1 Silicon and Germanium Electron Beam Evaporation Sources

The silicon and germanium sources are electron beam evaporation sources. The silicon source is a Thermionics HM^2 75cc 10kV source, and the germanium source is a Temescal SFIH-270-1 7cc 10kV source. Both sources are connected to the same 10kV high voltage power supply which is interlocked to the cooling water supplies. The power supply sometimes may trip off by itself, for uncertain reasons. If high voltage trips off very quickly after it is turned on, check the cables

connecting the upper control cabinet and the lower high voltage cabinet. The connectors of these cables are somewhat loose and can cause the high voltage to trip off if the contact is intermittent. The electron beam sweep (positioning) coils of both sources are powered by the sweep unit of the high voltage power supply. Due to the limited sweep current range of the power supply, the electron beam of the silicon source can only cover part of the crucible. It would be desirable to be able to cover the whole silicon source crucible, in which case a sweeping power supply of wider current range would be needed. The filament power (or more precisely, the voltage across the filament) of both the silicon and germanium sources are supplied by separate custom-made power supply circuits. The filament power can be controlled, depending on the emission control select switch, either manually by a front panel ten-turn potentiometer or automatically (feedback control) by a crystal thickness monitor. The source shutter of both silicon and germanium sources are pneumatically driven and can be controlled, depending on the shutter control select switch, either by a front panel switch or by the crystal thickness monitor. Three crystal thickness monitor can be installed in the system, one close to the substrate and the other two directly above the silicon and germanium sources. The crystal thickness monitors of either the substrate or the source, depending on the sensor select switch, can be used to control the silicon and germanium sources. The control mode of the silicon and germanium sources are selected through the front panel switches. When operating the sources, keep an eye on the emission current meter on the high voltage power supply unit. The emission current for normal operation with silicon or germanium is less than about 0.1 mA. When the filament power is controlled manually, constant adjustment is

needed to compensate the slow drift in emission current (and hence growth rate). When filament power is feedback-controlled by the crystal thickness monitor, it is preferable to ramp the filament power through the crystal thickness monitor instead of the panel potentiometer to avoid the power surge which may occur when switching over the control from panel to monitor at high filament power. The feedback loop gain of the crystal thickness monitor is usually set to 0 to 20, and the "approach" parameter of the monitor is usually set to 0. Note that too high a loop gain may cause loop oscillations. The following is the circuit diagram of the silicon and germanium source control system. Note that the circuits for the silicon and germanium sources are identical.

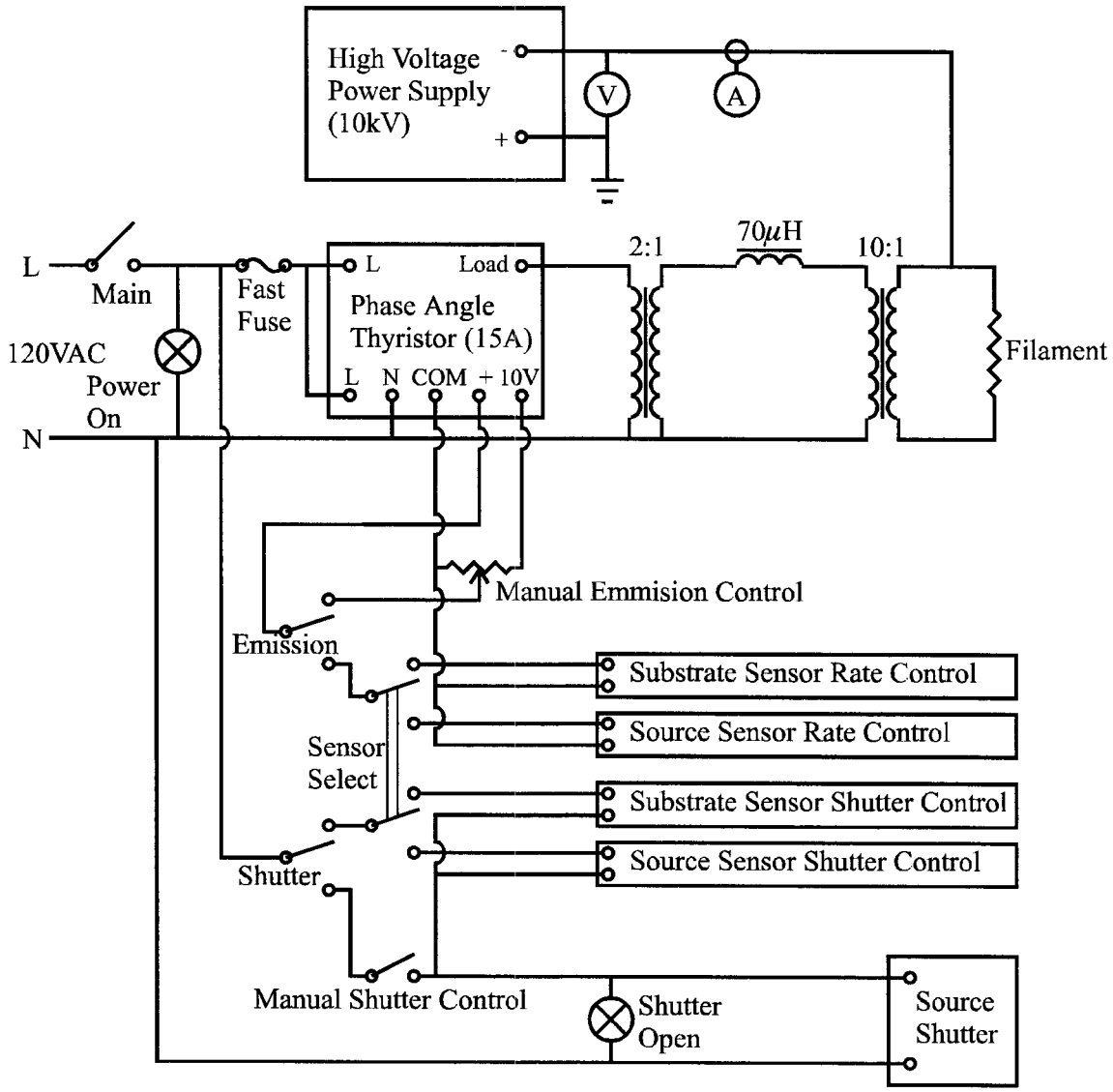

E .2 Carbon Filament Source

The carbon source is a resistively heated graphite filament source and has a water-cooled shroud. The filament is mounted on two molybdenum rods which are

connected to two copper rods of the electric feedthroughs. Be aware that the connectors between the molybdenum rods and copper rods are very close to the source wall, and care must be taken to electrically insulate the connectors from the wall. If no insulating material is used, the spacing between the connectors and wall must be big enough so that they will not be in contact even after thermal expansion during operation. Although there is a type C thermocouple in the carbon source, the source should be controlled by the filament voltage in open loop since the response of the thermocouple is quite slow. The following is a circuit diagram of the carbon source.

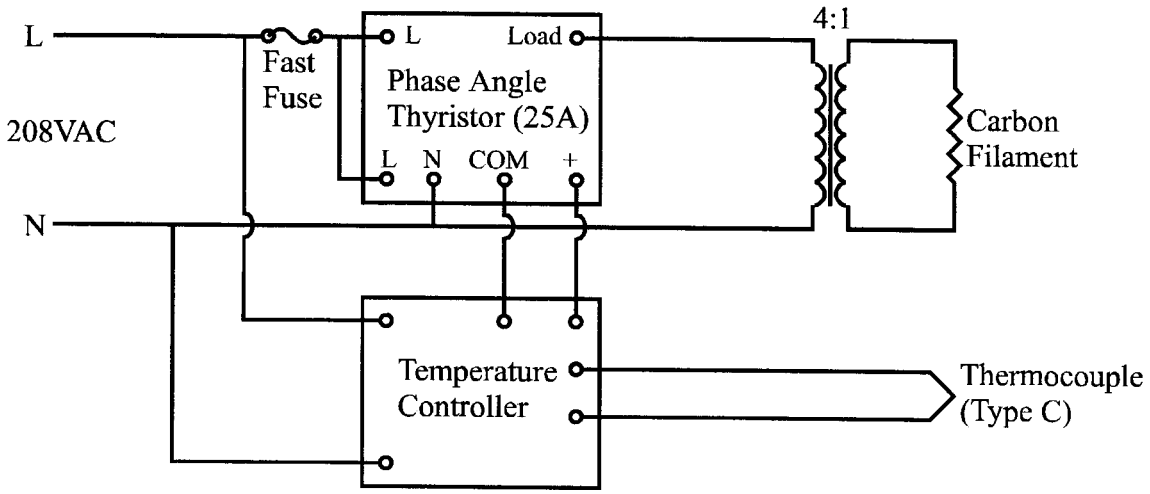

E .3 Tin Effusion Cell

The tin source is a Knudsen effusion cell. Tin is contained in a pyrolytic boron nitride (PBN) crucible which is heated by the surrounding heater coil. The heater coil is enclosed by a metal foil to reduce radiative heat loss. Care must be taken to electrically insulate the heater coil from the metal foil. Ceramic paper can be used to assure good electric insulation. Note that the ceramic paper contains some organic material and must be treated before being used in ultrahigh vacuum environment. To treat the ceramic paper, first cut and, if needed, bend the ceramic paper to the desired shape. Then put the ceramic paper in the outer flame of a high temperature torch. The ceramic paper in the flame will first turn black and start to give off smoke. After it is red hot and stops giving off smoke, the organic material in the ceramic paper is mostly burned out and the paper should be white and somewhat brittle after cooling down and can then be used in ultrahigh vacuum environment. When burning one region of the ceramic paper, a metal tweezer can be used to hold the paper at another region. The ceramic paper is not a good thermal conductor and therefore heating is very localized. When treating the ceramic paper, one should wear ultraviolet and infrared eye protection glasses (such as welder's glasses). Although there is a type C thermal couple in the tin source, the source is better controlled by the heater voltage in open loop since the feedthrough of the thermocouple is a normal electric feedthrough which results in drift in the thermocouple reading when the feedthrough is warmed up. Also be aware of the spatial nonuniformity of the tin growth flux across the substrate. The calibration of growth rate and flux nonuniformity are posted on the side of the instrument bench. The tin source is usually kept at 300~400°C (10.0% to 20.0% power setting) between growths to keep tin in liquid form to avoid the stress to the

crucible as a result of tin solidification at 230°C. Before venting the chamber, the tin source should be slowly cooled down to room temperature. The following is a circuit diagram of the tin source.

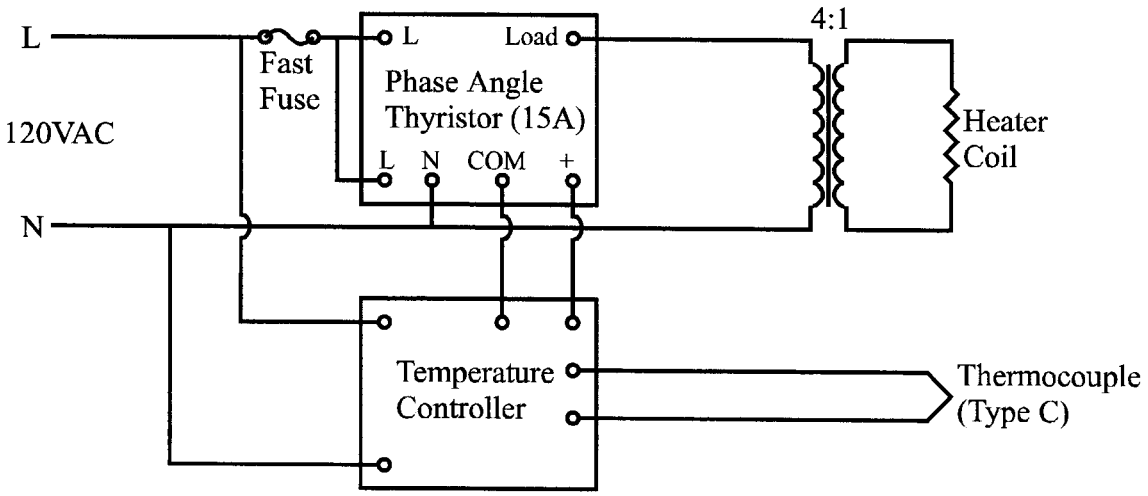

E .4 Electron Cyclotron Resonance Ion Source

The electron cyclotron resonance (ECR) ion source uses permanent magnets which must be removed during chamber baking. When removing and installing the magnets, care must be taken not to break the copper contact fingers on the magnet and on the short/antenna assembly. These contact fingers make electric contact with the metal wall to form the microwave resonant cavity. During operation or when the ion source is heated by baking or by other components in the chamber, cooling air must be turned on. The exit air temperature should be

below 50°C. The microwave resonant cavity can be mechanically tuned by a micrometer. Tuning is needed each time the ion source is operated. The goal of the tuning is to minimize the reflected microwave power which is displayed on the reflected power meter. The substrate ion current measured at a negative substrate bias (a few tens of volts) is sometimes more sensitive to tuning than the reflected microwave power and can therefore also be used to guide the tuning. At very low processing gas pressures, the plasma is sometimes difficult to ignite. In such cases, the processing gas pressure can first be increased to ignite the plasma and then be reduced to the desired operation pressure. The plasma is usually visible from the view port of the chamber. Be aware of the possible ultraviolet radiation from the plasma.

E .5 Reflection High Energy Electron Diffraction System

The reflection high energy electron diffraction (RHEED) pattern is monitored by a CCD video camera. A green filter has been added to the lens system of the camera. The green filter is 50 mm diameter and is fitted into a 52 mm standard camera lens mount. The green filter can significantly enhance the diffraction image contrast since the screen is made of green phosphor. This is especially important when the chamber is in a very bright light environment (e.g., when the carbon source is in operation). When using the reflection high energy

electron diffraction, the chamber baking must be turned off since the AC baking current deflects the electron beam.

E .6 Cryopump

The main chamber is normally pumped by the cryopump. Routine maintenance of the cryopump includes replacement of the compressor absorber and the cold head displacer which is recommended by the factory to be performed every 10000 hours. A very complete step-by-step description of the maintenance procedures is provided in the manuals. The temperature of the cold head is measured by a silicon diode cryogenic temperature sensor. The temperature calibration curve is provided in the manual of the sensor. The following is a circuit diagram of the temperature sensor driving circuit. Note that the negative signal output from the silicon diode sensor is connected to ground because a single-ended amplifier is used in the circuit. The measurement error introduced by such an arrangement is very small (much less than 1 mV).

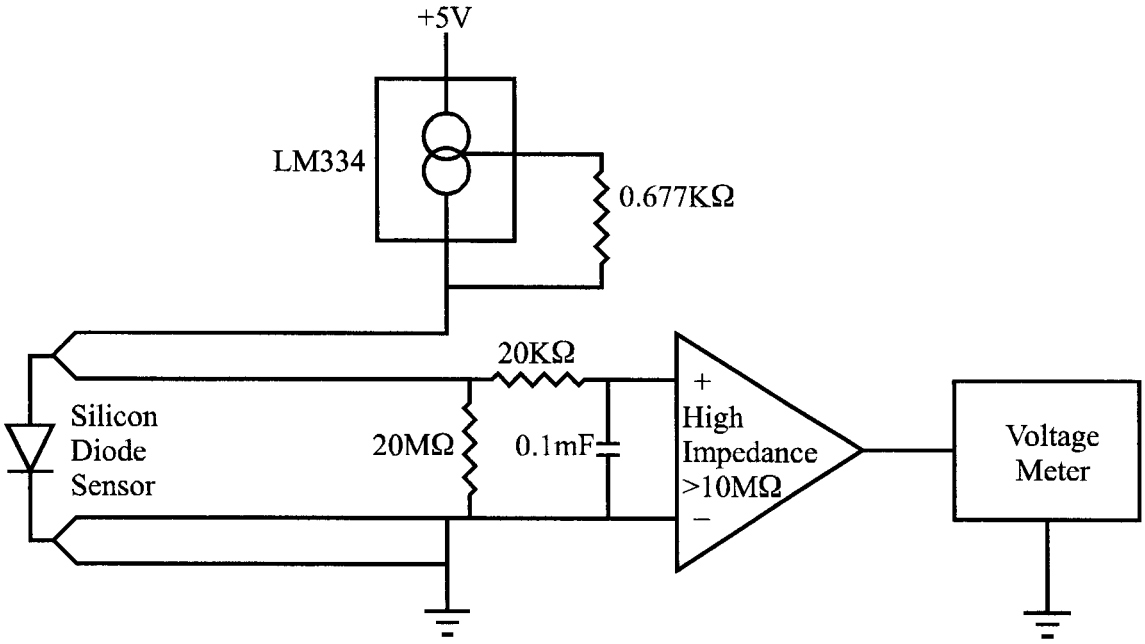

E .7 Bake Out System

The chamber is baked by heating tapes to reach ultrahigh vacuum. Before baking out the chamber, make sure that the cooling water from the electron guns is purged out completely. The baking power is provided by an on-off controller with a type J thermocouple and a high current (40A or more) solid state relay. Since the thermocouple is installed right underneath a heating tape, the temperature setting in the controller is systematically higher than the average chamber temperature. For example, the controller setting of 300°C corresponds to an average chamber wall temperature of approximately 200°C. When rearranging the heating tapes, distribute the tape power evenly among the power connectors since each connector

is rated and protected for 20A maximum current. The solid state relay and the protecting circuit breakers are located on the wall behind the instrument benches. The following is a circuit diagram of the baking power control circuit.

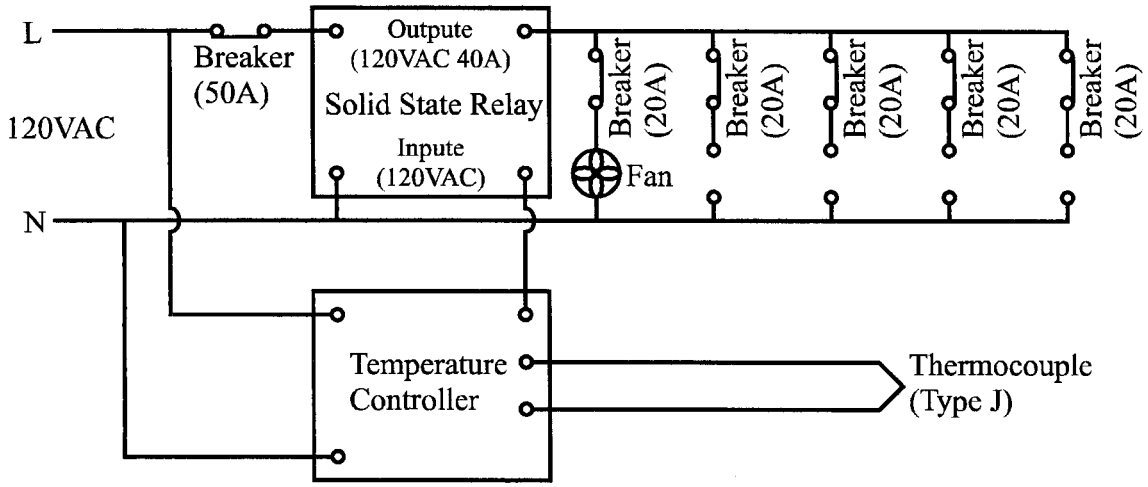

E .8 Routine Maintenance

The routine maintenance of the system includes changing the thickness monitor crystal and adding the source materials. Before venting the chamber, make sure that all hot filaments (ion gauge, mass spectrometer, sources, etc.) in the chamber are turned off. Turn off all cooling water supplies. Disconnect cooling water to the silicon and germanium sources and shroud. If necessary, disconnect cooling water to other sources (e.g., carbon source if it is to be maintained) as well. Note that before disconnecting any water lines, both supply and return valves

must be closed first. For the water lines that are not to be disconnected, only supply valves should be closed to avoid over pressuring. The chamber can be vented with or without turning off the cryopump. For short maintenance, the cryopump can be left on and the chamber can be vented with the cryopump gate valve closed. For long maintenance, the cryopump can be turned off with the cryopump gate valve open. When servicing the components, it is preferable to work from the upper level to the lower level so that falling particles do not contaminate the lower level components such as the sources of silicon and germanium. Before working on any components at the upper level, first cover the silicon and germanium sources with clean aluminum foil to avoid particles falling onto the sources. Loose deposits on any surfaces, especially on surfaces close to the sources (such as shutters and the source itself) should be removed by a vacuum cleaner through a clean steal tube. The cooling shrouds of the silicon and germanium sources should be cleaned with metal wire brushes. It is preferable to use separate brushes to clean the silicon and germanium source shrouds to avoid cross contamination. Also clean or replace the silicon mirror (a 3 inch silicon wafer) used to see the silicon and germanium sources if necessary. If the mirror is moved, it must be realigned to assure that the silicon and germanium sources are visible from the view port. Check the level of tin material in the tin source with an inspection mirror to determine whether addition of tin is needed (usually tin does not need to be added very often). If additional tin is needed, add tin from the front opening of the crucible. Do not apply any pressure to the crucible or any other parts of the source since it is very easy to cause the heater wire to short circuit. After replacing the thickness monitor crystals, check to make sure that the crystal

sensors are working before they are reinstalled into the chamber (check "crystal" on the Inficon controller). The mass spectrometer head has a relatively tight fit in the port and may be shorted to the chamber wall when mounted at some orientations. So before sealing the port, check all the electric feedthrough pins to assure that mass spectrometer head is not shorted to the chamber wall.

E .9 Pump Down

When pumping down the chamber, first use the turbo pumps. Make sure the lid of the load lock is closed when starting pumping. Slowly increase the chamber baking temperature controller setting (over half a day) to 100°C if the cryopump is still on or to 300°C if the cryopump is off and all the gate valves are open. Open the cryopump gate valve or turn on the cryopump when the chamber pressure is in the low 10^{-7} Torr range. Slowly increase the chamber baking temperature controller setting (over half a day) to 300°C if one has not done so. After the chamber pressure reaches low 10^{-8} Torr to high 10^{-9} Torr range, slowly decrease the baking temperature controller setting (over half a day) to 100°C or lower. Close the gate valves to the REELS system and the load lock, and the chamber should be in ultrahigh vacuum.

After the chamber is pumped down to ultrahigh vacuum from ambient pressure, the sources must first be out-gassed before any growth by powering up

the sources to their operation powers. When out-gassing the silicon and germanium sources, the position of the electron beam where it hits the source material in the crucible should be watched through the mirror to assure that the beam is properly positioned and the sweeping range is adequate. Since the crucible of the germanium e-gun is rather small, the whole charge of the germanium source material can usually be melted without sweeping the electron beam. The silicon source, on the other hand, is much bigger and only part of the charge melts. Some degree of sweeping is needed to produce a large melt region. This is usually desirable during the out-gassing so that the charge can be used more uniformly. Make sure that the electron beam does not hit the crucible at any time to avoid contamination of the source. During normal operation, the position and range of the sweeping, if any, should be fixed to assure consistency between growths.